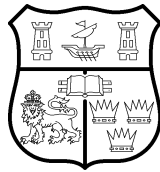


Title	Mutually coupled lasers in photonic integrated circuits
Authors	Dubois, Fabien
Publication date	2018
Original Citation	Dubois, F. 2018. Mutually coupled lasers in photonic integrated circuits. PhD Thesis, University College Cork.
Type of publication	Doctoral thesis
Rights	© 2019, Fabien Dubois. - <a href="http://creativecommons.org/licenses/by-nc-nd/3.0/">http://creativecommons.org/licenses/by-nc-nd/3.0/</a>
Download date	2023-05-04 21:35:17
Item downloaded from	<a href="http://hdl.handle.net/10468/8567">http://hdl.handle.net/10468/8567</a>

# Mutually coupled lasers in photonic integrated circuits

Fabien Dubois  
PHD



NATIONAL UNIVERSITY OF IRELAND, CORK

SCHOOL OF SCIENCE

DEPARTMENT OF PHYSICS

**Thesis submitted for the degree of  
Doctor of Philosophy**

June 2018

Head of Department: Prof. John McInerney

Supervisors: Prof. Frank H. Peters

Research supported by Science Foundation Ireland

# Contents

List of Figures . . . . .	iv
List of Tables . . . . .	xvi
Acknowledgements . . . . .	xxiv
List of Publications . . . . .	xxvii■
Conferences . . . . .	xxix
Abstract . . . . .	xxxii■
<b>1 Introduction</b>	<b>1</b>
1.1 Introduction to optical communications . . . . .	2
1.2 Internet usage projections . . . . .	5
1.3 Introduction to photonic integration . . . . .	7
1.3.1 Hybrid integration . . . . .	8
1.3.2 Monolithic integration . . . . .	8
1.4 Introduction to lasers . . . . .	9
1.4.1 Semiconductor lasers . . . . .	11
1.4.2 Types of semiconductor lasers . . . . .	16
1.4.2.1 Fabry-Pérot (FP) Laser . . . . .	16
1.4.2.2 Distributed Bragg grating (DBR) laser . . . . .	18
1.4.2.3 Distributed feedback (DFB) laser . . . . .	18
1.4.2.4 Vertical cavity surface emitting laser (VCSEL) . . . . .	19
1.4.2.5 Slotted Fabry-Pérot (SFP) Laser . . . . .	20
1.5 Introduction to injection locking . . . . .	21
1.6 Introduction to mutually coupled lasers . . . . .	24
1.6.1 Formal definition of the bifurcation parameters in the mutually coupled arrangement . . . . .	24
1.7 Breakdown of bifurcations observed . . . . .	25
1.7.1 Saddle-Node bifurcation . . . . .	28
1.7.2 Pitchfork Bifurcation . . . . .	29
1.7.3 Hopf bifurcation . . . . .	30
1.7.4 Period-doubling bifurcation . . . . .	32
1.7.5 Torus bifurcation . . . . .	33
<b>2 Literature review</b>	<b>36</b>
2.1 Experimental investigations of mutually coupled semiconductor lasers . . . . .	37
2.2 Theoretical investigations of mutually coupled semiconductor lasers . . . . .	40■
<b>3 Experimental Work</b>	<b>46</b>
3.1 Introduction . . . . .	47
3.2 Device Design . . . . .	47
3.3 Device Testing . . . . .	49
3.3.1 Testing Outline . . . . .	49
3.3.2 Tuning characterisation of SFP Lasers . . . . .	50
3.3.3 VOA Transparency Measurements . . . . .	52
3.3.4 Facet Loss Calculation . . . . .	53

3.3.5	First Coupling Test . . . . .	55
3.3.6	VOA affecting lasing . . . . .	58
3.3.6.1	Current Leakage . . . . .	59
3.3.6.2	Effective Cavity Length Measurement . . . . .	60
3.3.7	700 $\mu\text{m}$ VOA Coupling test . . . . .	61
3.3.8	On Chip Master/Slave Injection . . . . .	64
3.3.9	External Injection Locking of On Chip Lasers . . . . .	66
3.3.10	Future Device Design . . . . .	68
3.4	Experimental conclusion . . . . .	71
<b>4</b>	<b>Single mode model for identical lasers</b>	<b>73</b>
4.1	Model introduction . . . . .	73
4.1.1	Introduction . . . . .	74
4.1.2	The model . . . . .	74
4.1.3	Analytical bifurcations of the no delay, no detuning system	78
4.1.3.1	Model simplifications and CW solutions . . . . .	78
4.1.3.2	Linearization of the equations . . . . .	79
4.1.3.3	Deriving the Characteristic Equation of the CW System . . . . .	80
4.1.3.4	Zero Delay Pitchfork and Hopf Bifurcations . . . . .	81
4.1.4	Analytical bifurcations of the delayed, no detuning system	84
4.1.5	Saddle-node bifurcation . . . . .	91
4.1.6	Analytical solutions of one colour states in the zero detuning case . . . . .	92
4.1.6.1	Symmetric in phase/anti-phase one colour solutions . . . . .	93
4.1.6.2	Symmetry broken one colour states . . . . .	96
4.1.7	Analytical solutions of two colour states in the zero detuning case . . . . .	100
<b>5</b>	<b>Including detuning</b>	<b>105</b>
5.1	Analytical approach to the single mode model with detuning . . . . .	105
5.1.1	Introduction . . . . .	106
5.1.2	Analytical solutions of one colour states in the detuned case . . . . .	106
5.1.3	Analytical solutions of two colour states in the detuned case . . . . .	110
5.1.4	Analytical attempts to study bifurcations of the detuned, delayed model . . . . .	111
5.1.5	Bifurcations of the no delay detuned system . . . . .	113
5.2	Attractor diagram study of the detuned model . . . . .	118
5.2.1	Attractor diagram methodology introduction . . . . .	119
5.2.2	Time series analysis method . . . . .	119
5.2.3	FFT analysis methods . . . . .	120
5.2.4	Nine point grid comparison method . . . . .	125
5.2.5	Interpolation Expansion Method . . . . .	128
5.2.6	Attractor Diagram Study of the Model with Detuning . . . . .	129



5.2.6.1	$(\phi, \eta)$ Parameter Space Study . . . . .	130
5.2.7	$(\phi, \delta)$ Parameter Space Study . . . . .	135
5.3	Recreation of experimental methods . . . . .	138
5.3.1	Dependence on the injection parameter . . . . .	138
5.3.2	Dependence on detuning . . . . .	142
5.4	Self-Pulsations . . . . .	143
5.4.1	Experimental results . . . . .	149
5.4.1.1	Results from 2 <sup>nd</sup> generation MCL devices . . .	149
5.4.1.2	Results from 3 <sup>rd</sup> generation MCL devices . . .	152
5.5	Conclusion . . . . .	156
<b>6</b>	<b>Multimode approach to modelling mutually coupled lasers</b>	<b>158</b>
6.1	Introduction . . . . .	159
6.2	Model introduction . . . . .	159
6.3	Bifurcation study of two mode coupled laser model . . . . .	163
6.3.1	Study of the $(\phi, \eta)$ space bifurcations . . . . .	163
6.3.2	Study of the detuning space bifurcations . . . . .	171
6.4	Introducing non symmetric modes . . . . .	178
6.4.1	Alteration of multi-mode gain terms . . . . .	178
6.5	Bifurcation study of the unbalanced mode arrangement . . . . .	180
6.6	Recreation of experiment using multi-mode model . . . . .	182
6.6.1	Individual VOA bias sweeps . . . . .	182
6.6.2	Data summary of a collection of VOA sweeps . . . . .	195
6.7	Comparison with experiment . . . . .	197
6.8	Conclusion . . . . .	200
<b>7</b>	<b>Conclusion and future work</b>	<b>201</b>
<b>A</b>	<b>Breakdown of the epitaxial composition of the wafers used</b>	<b>204</b>
<b>B</b>	<b>Model for improved handling of VOA section</b>	<b>207</b>
B.1	Model basis . . . . .	208
B.2	Adapted model . . . . .	209
<b>C</b>	<b>Comb injection rate equation model development</b>	<b>211</b>
C.1	Model development . . . . .	212
C.2	Experimental recreation . . . . .	214

## List of Figures

1.1	Example of the constellation diagram for 16QAM, showing the corresponding binary number associated with each point. . . .	4
1.2	Increases in the number of internet users per year from 1995 to 2013. . . . .	6
1.3	Predicted data traffic of different video formats (ultra high definition (UHD) in blue, high definition (HD) in green and standard definition (SD) in navy) each year from 2016 to 2021. . . . .	6
1.4	Nielsen's law of predicting internet speeds vs. measured speeds.	7
1.5	Layout of an ideal laser cavity, where a gain medium is surrounded on one side by a perfect reflector and on the other by a partial reflector. . . . .	9
1.6	Example of an LI (light output-current) plot for a semiconductor diode laser. . . . .	10
1.7	Plots of lattice constant versus band gap for varying compositions of various III-V and III-VI semiconductor compounds. . . . .	11
1.8	Example of a quantum well made by sandwiching a layer of lower band-gap material between to higher band-gap cladding layers, forming a potential well. Electrons/holes in the wells occupy discrete quantum states, so that the energy of the photon emission is no longer the band-gap, but the difference between the quantum states in the wells, as shown. . . . .	12
1.9	Time trace of $N_p$ from solving Eqn. 1.1-1.2. Here the gain is assumed linear, using the expression in Eqn. 1.4. The parameters used are $\Gamma = 0.8$ , $a = 5.34 * 10^{-16} \text{ cm}^2$ , $\tau_p = 2.77 \text{ ps}$ , $\beta = 1$ , $\tau_r = 2.71 \text{ ns}$ , $I = 2 \text{ mA}$ , $e = 1.6 * 10^{-19} \text{ C}$ , $V = 4 * 10^{-12} \text{ cm}^2$ and $\tau_n = 1.57 \text{ ns}$ . . . . .	15
1.10	A simulated IV curve, tracking the steady state value of $N_p$ , from Eqn. 1.1 vs. injected current, $I$ . The parameters used are $\Gamma = 0.8$ , $a = 5.34 * 10^{-16} \text{ cm}^2$ , $\tau_p = 2.77 \text{ ps}$ , $\beta = 1$ , $\tau_r = 2.71 \text{ ns}$ , $e = 1.6 * 10^{-19} \text{ C}$ , $V = 4 * 10^{-12} \text{ cm}^2$ and $\tau_n = 1.57 \text{ ns}$ . . . . .	16
1.11	Schematic of a basic FP laser. Here the lasing cavity of length $L_{fp}$ , uses the air-material interface to provide reflectivities $r_{1,2}$ .	17
1.12	Airy functions of Fabry P�rot resonators with different reflectivities, $R$ . . . . .	17
1.13	Schematic of a DBR laser. The device contains a gain section of length $L_a$ , a phase section of $L_b$ and a grating of length $L_{gr}$ . This has an effective length of $L_{eff}$ and a reflectivity of $r_{gr}$ . On the other side of the device there is a facet, providing a reflectivity of $r_f$ . The length $L_{DBR}$ is an indication of the length of the resonant cavity of the light emitted. . . . .	18

1.14	Schematic of a DFB laser. The active region of the laser is fabricated to have the grating profile. This is a "shifted" DFB, as at the centre there is a perturbation twice the size of a normal grating perturbation i.e. $\lambda/2$ . The ends are coated with anti-reflection coating to encourage the light to exit the cavity, as the grating provides the internal feedback needed to cause lasing. . . . .	19
1.15	Schematic diagram of a VCSEL. Here the active region of width, $L_a$ is surrounded by two passive regions of length $L_p$ , this is then surrounded by stacks of layers of alternating refractive index, forming a grating. Each grating has a physical length of $L_{g1,2}$ but an effective length of $L_{eff1,2}$ and a reflectivity $r_{g1,2}$ . . . . .	20
1.16	Schematic of a SFP laser. The gain section has a length of $L_{fp}$ , the section with a series of etched slots acts as a grating of length $L_g$ and provides a reflectivity of $r_g$ , with an effective length of $L_{eff}$ . $r_1$ is the reflectivity provided by the facet. . . . .	21
1.17	Bifurcation diagram of the injected slave case from Eqn. 1.7-1.8 in the $(\omega, k)$ space. The Hopf bifurcation is by H and the saddle-node is denoted by SN. The points that these bifurcations intersect at two codimension-two saddle-node-Hopf points $G_1$ and $G_2$ . . . . .	23
1.18	Example of periodic orbits, $\bar{x}_k$ , intersecting with the transverse surface, $S$ , after one rotation at $\bar{x}_{k+1}$ . The fixed point, $\bar{x}^*$ , meets itself after one rotation. . . . .	26
1.19	Example of a saddle-node bifurcation, showing the solutions of Eqn. 1.15 for varying $r$ . Solid lines are stable solutions and dashed lines are unstable. . . . .	28
1.20	Example of a supercritical pitchfork bifurcation, showing the solutions of Eqn. 1.16 for varying $r$ . Solid lines are stable solutions and dashed lines are unstable. . . . .	29
1.21	Example of a subcritical pitchfork bifurcation, showing the solutions of Eqn. 1.17 for varying $r$ . Solid lines are stable solutions and dashed lines are unstable. . . . .	30
1.22	Example of a supercritical Hopf bifurcation showing phasor diagrams of Eqn. 1.18 and 1.19 for $\mu < 0$ (showing a stable fixed point) and $\mu > 0$ (showing a stable limit cycle). The Hopf bifurcation occurs at $\mu = 0$ . . . . .	31
1.23	Example of a subcritical Hopf bifurcation showing Phasor diagrams of Eqn. 1.20 and 1.21 for $\mu < 0$ (showing a stable fixed point and stable limit cycle, with a unstable limit cycle between them) and $\mu > 0$ (showing a stable limit cycle and an unstable fixed point). The Hopf bifurcation occurs at $\mu = 0$ . . . . .	32
1.24	Unit circle in the complex plane, with a red dot highlighting the eigenvalue causing a period-doubling bifurcation . . . . .	33
1.25	Example of a torus formed by a torus bifurcation. . . . .	34
1.26	Unit circle in the complex plane, with red dots highlighting the eigenvalues causing a torus bifurcation. . . . .	34

3.1	Schematic of the first generation MCL devices designed. . . . .	48
3.2	First generation MCL device under testing. . . . .	48
3.3	Wavelength tuning Optical Spectrum Analyser (OSA) intensity plots. . . . .	51
3.4	Photocurrent(A) vs. Reverse Bias (V) for the 100 $\mu\text{m}$ VOA Mutually Coupled Laser (MCL) device. The photocurrent measured using one section is shown in red and three sections in blue. . . . .	52
3.5	Photocurrent(A) vs. Reverse Bias (V) for the 700 $\mu\text{m}$ VOA MCL device. The photocurrent measured using one section is shown in red and three sections in blue. . . . .	53
3.6	Photocurrent (A) measured using two separate sources vs. reverse bias (V). The two sources are placed on the VOA (red) and the adjacent mirror section (blue). . . . .	53
3.7	. . . . .	54
3.8	Circuit diagram for the facet loss experiment. TLS - tunable laser source, PC - Polarisation Controller. . . . .	55
3.9	Circuit diagram for the mutual coupling experiment. The arrows represent optical isolators, while the black lines represent optical fibre. EDFA - Erbium doped fibre amplifier, HSPD - High speed photodiode, ESA- Electrical spectrum analyser, OSA - Optical spectrum analyser. . . . .	56
3.10	An animation of the device under testing. . . . .	56
3.11	Zero detuning arrangement of both lasers before coupling. . . . .	56
3.12	Coupled OSA intensity graph of varying VOA bias for the zero detuning arrangement seen in figure 3.11. . . . .	57
3.13	Coupled ESA intensity graph of varying VOA bias for the zero detuning arrangement seen in figure 3.11. . . . .	57
3.14	Example laser spectrum, with no VOA bias (red), and with $-6\text{ V}$ applied to VOA (blue). . . . .	58
3.15	Effective circuit of a three section laser and the VOA section on the MCL PIC. . . . .	59
3.16	Reverse bias sweep of VOA, measuring the current. . . . .	60
3.17	Fourier transform of OSA traces for a laser when there are $-6\text{ V}$ on the VOA (blue) and $0\text{ V}$ on the VOA (red). . . . .	60
3.18	Schematic of a single laser, along with VOA, and waveguide leading to AR bend. . . . .	61
3.19	Zero detuning arrangement with $-6\text{ V}$ across the VOA. . . . .	62
3.20	Coupled OSA intensity graph for the 700 $\mu\text{m}$ VOA device. . . . .	63
3.21	Coupled ESA intensity graph for the 700 $\mu\text{m}$ VOA device. . . . .	63
3.22	Fourier transform of OSA traces for a laser when there are $-7\text{ V}$ on the VOA (blue) and $0\text{ V}$ on the VOA (red) from the mutual coupling experiment results outlined in figure 3.21. . . . .	64
3.23	Coupled OSA intensity graph for on chip master/slave on the 100 $\mu\text{m}$ VOA device. . . . .	65
3.24	Coupled ESA intensity graph for on chip master/slave on the 100 $\mu\text{m}$ VOA device. . . . .	66

3.25	External injection locking test circuit. TLS - tunable laser source, PC - Polarisation Controller, EDFA - Erbium doped fibre amplifier, HSPD - High speed photodiode, ESA- Electrical spectrum analyser, HSO - High speed oscilloscope. . . . .	66
3.26	ESA intensity plot for external injection of the on chip laser with a TLS. The TLS power was fixed at 7 dBm, and the wavelength was swept across the peak of the slave laser. . . . .	67
3.27	High Speed Oscilloscope (HSO) plots of different dynamic regimes in figure 3.26. . . . .	68
3.28	An improved design of MCL devices schematic. . . . .	69
3.29	Diagram illustrating different etch depths of ridges on a PIC. The bottom picture shows the deep etch used, which goes through the quantum wells. . . . .	70
3.30	Later generation MCL chips tested by my colleague. . . . .	72
4.1	Example of a pair of mutually coupled lasers on a PIC. Here the intermediate section's (VOA) transparency is a measure of $\eta$ and can be controlled by applying a voltage to the gold contact pad connected to this section. The time of flight between the lasers ( $\tau$ ) is the VOA length. This propagation induces a phase change of $\phi$ . The difference in the frequencies emitted is $\delta$ and the current injected, $J$ , is through the gold contact pads on the top of the device. . . . .	76
4.2	3D plot of Eqn. 4.23, for varying $(\phi, \eta)$ (blue) along with $f(\eta, \phi) = 0$ plane (red). . . . .	82
4.3	3D plot of Eqn. 4.24, for varying $(\phi, \eta)$ (blue) along with $f(\eta, \phi) = 0$ plane (red). . . . .	83
4.4	Diagrams of the Hopf (blue) and Pitchfork (red) bifurcations for zero delay. . . . .	84
4.5	Example of multiple roots of $\omega_s$ from solving Eqn. 4.26, with $\eta = 0.42$ , $\phi = 2\pi$ and $\tau = 20$ . . . . .	85
4.6	Examples of main and middle root algorithms. . . . .	86
4.7	Delayed pitchfork bifurcations for varying $\tau$ values. . . . .	87
4.8	Plot of the real part of the eigenvalue of Eqn. 4.22 for varying $\phi$ and $\eta = 0.3$ and $\tau = 1$ . Where this curve crosses the $y = 0$ axis, a Hopf bifurcation occurs. . . . .	88
4.9	Delayed Hopf bifurcations for varying $\tau$ values. . . . .	89
4.10	Diagram of the $(\phi, \eta)$ space, showing stable CW states (green), unstable CW states (red), pitchfork bifurcation (blue), Hopf bifurcation (Orange), for $\tau = 1$ . . . . .	90
4.11	Diagram of the $(\phi, \eta)$ space, showing stable CW states (green), unstable CW states (red), pitchfork bifurcation (blue), Hopf bifurcation (Orange), for $\tau = 2$ . . . . .	91
4.12	Plot of the pitchfork bifurcation (blue), Hopf bifurcation (orange) and the saddle-node bifurcation (green) for $\tau = 2$ over the $(\phi, \eta)$ space. . . . .	92

4.13	FFT of $\tilde{E}_{1,2}$ (left) and time trace of $ \tilde{E}_{1,2} $ (right) for $\eta = 0.1$ , $\phi = 0$ , $\tau = 0$ and $\delta = 0$ . . . . .	93
4.14	Plot of $\omega_a$ from Eqn. 4.34 (blue), peak wavelength of FFT of $E_1$ from solving Eqn. 4.6-4.9 (with $\tau = 0$ and $\delta = 0$ ) (orange)) along with the stability of the in-phase one colour solution (stable in green, unstable in red), for $\eta = 0.1$ and varying $\phi$ from $0 - 2\pi$ . . . . .	94
4.15	Plot of $\omega_a$ from Eqn. 4.34 (blue), peak wavelength of FFT of $E_1$ from solving Eqn. 4.6-4.9 ( $\delta = 0$ ) (orange)) along with the stability of the in-phase one colour solution (stable in green, unstable in red), for $\tau = 0.5$ , $\eta = 0.1$ and varying $\phi$ from $0 - 2\pi$ . . . . .	95
4.16	Plot of $\omega_a$ from Eqn. 4.34 (blue), peak wavelength of FFT of $E_1$ from solving Eqn. 4.6-4.9 ( $\delta = 0$ ) (orange)) along with the stability of the in-phase one colour solution (stable in green, unstable in red), for $\tau = 2$ , $\eta = 0.1$ and varying $\phi$ from $0 - 2\pi$ . . . . .	95
4.17	Plot of symmetry broken one colour solution, $\omega_a$ from solving Eqn. 4.57 (blue), and peak wavelength of FFT of $E_1$ from solving Eqn. 4.6-4.9 (with $\tau = 0$ and $\delta = 0$ ) (orange)), for $\eta = 0.1$ and sweeping $\phi$ from $0 \rightarrow 2\pi$ . . . . .	98
4.18	Plot of symmetry broken one colour solution, $\omega_a$ from solving Eqn. 4.60 and 4.61 (blue), and peak wavelength of FFT of $E_1$ from solving Eqn. 4.6-4.9 (with $\delta = 0$ ) (orange)), for $\tau = 0.5$ , $\eta = 0.1$ and sweeping $\phi$ from $0 \rightarrow 2\pi$ . . . . .	99
4.19	Plot of symmetry broken one colour solution, $\omega_a$ from solving Eqn. 4.60 and 4.61 (blue), and peak wavelength of FFT of $E_1$ from solving Eqn. 4.6-4.9 (with $\delta = 0$ ) (orange)), for $\tau = 2$ , $\eta = 0.1$ and sweeping $\phi$ from $0 \rightarrow 2\pi$ . . . . .	100
4.20	FFT of $\tilde{E}_{1,2}$ (left) and time trace of $ \tilde{E}_{1,2} $ (right) for $\eta = 0.1$ , $\phi = 0.5\pi$ , $\tau = 0$ and $\delta = 0$ . . . . .	101
4.21	Parametric plot of $N_1(\omega_a)$ , $N_2(\omega_a)$ and $N_1(\omega_b)$ , $N_2(\omega_b)$ , from Eqn. 4.66 and 4.67, for $\eta = 0.1$ , $\phi = 1.26$ and $\tau = 0.5$ . . . . .	102
4.22	Analytical solutions for $\omega_{a,b}$ (blue) compared with simulated results (orange), for $\eta = 0.1$ , a) $\tau = 0$ , b) $\tau = 0.5$ , while varying $\phi$ from $0 - \pi$ . . . . .	103
5.1	Plot of symmetry broken one colour solution, $\omega_a$ from solving Eqn. 5.22 and 5.23 (blue), and peak wavelength of FFT of $E_1$ from solving Eqn. 4.6-4.9 (orange), for $\delta = 0.05$ , $\tau = 0.5$ and $\eta = 0.1$ and sweeping $\phi$ from $0 \rightarrow 2\pi$ . . . . .	109
5.2	Plot of symmetry broken one colour solution, $\omega_a$ from solving Eqn. 5.22 and 5.23 (blue), and peak wavelength of FFT of $E_1$ from solving Eqn. 4.6-4.9 (orange), for $\delta = 0.2$ , $\tau = 2$ and $\eta = 0.1$ and sweeping $\phi$ from $0 \rightarrow 2\pi$ . . . . .	109
5.3	Analytical solutions for $\omega_{a,b}$ (blue) compared with simulated results (orange), for $\eta = 0.1$ , $\tau = 0.5$ and $\delta = 0.05$ , while varying $\phi$ from $0 - \pi$ . . . . .	111

5.4	Plot of L2 Norm from Eqn. 4.6-4.9 for $\eta = 0.2$ , $\delta = 0.05$ and $\tau = 0$ , versus coupling phase ( $\phi$ ). Showing stable steady states (orange), unstable steady states (blue), stable periodic orbits (green), saddle node bifurcation (red dot), Hopf bifurcation (black dot), and change in system detected by attractor diagram (purple). . . . .	113
5.5	Hopf (blue) and saddle-node (orange) bifurcation lines in the $(\phi, \eta)$ space for a) $\delta = 0.05$ and b) $\delta = 0.1$ . . . . .	115
5.6	a) shows the bifurcation diagram for $\delta = 0.05$ with the $\eta$ values of interest highlighted by the dashed green lines, b) The L2 Norm for varying $\phi$ with the stable and unstable parts of the three types of periodic solutions that exist (labelled A, B and C), with the bifurcations between them being as follows: saddle node in purple, period-doubling in yellow and torus in black for $\eta = 0.0275$ c) The L2 Norm for varying $\phi$ with the stable steady state in blue, unstable steady state in orange, and the stable periodic solution in green. The saddle node bifurcation is given by the purple dots and the Hopf-fold bifurcation given by the grey dots. . . . .	116
5.7	Time traces of the different periodic behaviours shown in figure 5.6b. . . . .	117
5.8	Plot of $a_{1,2}(=  E_{1,2} )$ vs time, showing the slope of the line between the max and min value of the time trace, for a steady state (a), and a limit cycle (b). . . . .	120
5.9	Plot of the $(\phi, \eta)$ space, where the steady states are in blue, the analytically found Hopf bifurcation line is in orange, and the pitchfork bifurcation is in green. . . . .	121
5.10	$\tilde{E}_{1,2}$ for $\eta = 0.1$ , $\phi = 1.721$ , $\tau = 2$ and $\delta = 0$ for two different integration times. a) 20000 and b) 100000. . . . .	122
5.11	Time trace of $ E_{1,2} $ for $\eta = 0.1$ , $\phi = 1.721$ , $\tau = 2$ and $\delta = 0$ for two different time periods. a) between 19000 and 20000 and b) between 99000 and 100000. . . . .	123
5.12	Plot of $\tilde{E}_1$ , for a) one colour and b) two colour states, with the result of peak detection on the solution (black dots). . . . .	124
5.13	Graphical representation of 9 point grid comparison method. Here the example bifurcation line is in green, the point of interest is in orange, and it is being compared with the 8 points directly around it (red) for a change in behaviour. The blue arrows represent the algorithm detecting a change in behaviour as the bifurcation line is crossed, and the purple dots are the mid-points saved for further bisection. . . . .	125
5.14	Output of the nine point grid comparison method, for finding the pitchfork (green dots) and hopf (red dots) bifurcations, for the model with $\delta = 0$ and $\tau = 1$ . The result is compared with previously calculated bifurcations for this system (pitchfork (blue line) and hopf (orange line)). . . . .	126

5.15	Output of the nine point grid comparison method, for finding the pitchfork (green dots) and hopf (red dots) bifurcations, for the model with $\delta = 0$ and $\tau = 2$ . The result is compared with previously calculated bifurcations for this system (pitchfork (blue line) and hopf (orange line)). . . . .	127
5.16	Plots of the Imaginary parts of $\tilde{E}_{1,2}$ on either side of the Hopf bifurcation in figure 5.14. . . . .	128
5.17	Graphical representation of Interpolation Expansion method. Here the example bifurcation line is in green, the interpolated point is in orange. The blue arrows represent expanding left and right around the interpolated point in steps of $\epsilon$ . . . . .	129
5.18	Results of nine point grid comparison method for defining the boundaries of the one colour region, O.C., (blue) and two colour, T.C., (orange) for $\delta = 0.1$ and varying $\tau$ . . . . .	130
5.19	$\tilde{E}_{1,2}$ and time traces of $ E_{1,2} $ for $\eta = 0.25, \phi = 1.26, \tau = 1$ and $\delta = 0.1$ ( $\tilde{E}_2$ is inverted for clarity). . . . .	131
5.20	Results of nine point grid comparison method for defining the boundaries of the one colour region, O.C., (blue) and two colour, T.C., (orange) for $\delta = 0.2$ and varying $\tau$ . . . . .	132
5.21	Results of nine point grid comparison method for defining the boundaries of the one colour region, O.C., (blue) and two colour, T.C., (orange) for $\delta = 0.3$ and varying $\tau$ . . . . .	133
5.22	$\tilde{E}_{1,2}$ and time traces of $ E_{1,2} $ for $\eta = 0.07, \phi = 2.2, \tau = 0.5$ and $\delta = 0.3$ ( $\tilde{E}_2$ is inverted for clarity). . . . .	134
5.23	$\tilde{E}_{1,2}$ and time traces of $ E_{1,2} $ for $\eta = 0.1, \phi = 2.83, \tau = 2$ and $\delta = 0.3$ ( $\tilde{E}_2$ is inverted for clarity). . . . .	134
5.24	Results of nine point grid comparison method for detecting change from one colour $\rightarrow$ not one colour (Orange) and two colour $\rightarrow$ not two colour (Blue), in the $(\phi, \delta)$ parameter space, for $\tau = 0.5$ and varying $\eta$ . The areas of one colour states are highlighted by O.C. and the two colour regions are denoted by T.C. . . . .	135
5.25	$\tilde{E}_{1,2}$ for $\tau = 0.5, \eta = 0.025, \delta = 0.05$ and $\phi = 1$ ( $\tilde{E}_2$ is inverted for clarity). . . . .	136
5.26	$\tilde{E}_1$ for $\eta = 0.025, \phi = 0.94, \tau = 0.5$ and (a) $\delta = 0.1$ , (b) $\delta = 0.2$ . . . . .	136
5.27	$\tilde{E}_{1,2}$ and time traces of $ E_{1,2} $ for $\eta = 0.1, \phi = 3.3, \tau = 0.5$ and $\delta = 0.2$ ( $\tilde{E}_2$ is inverted for clarity). . . . .	137
5.28	Results of nine point grid comparison method for detecting change from one colour $\rightarrow$ not one colour (Orange) and two colour $\rightarrow$ not two colour (Blue), in the $(\phi, \delta)$ parameter space, for $\tau = 1$ and varying $\eta$ . The areas of one colour states are highlighted by O.C. and the two colour regions are denoted by T.C. . . . .	138
5.29	Logarithmic contour plots of $\tilde{E}_1$ and the FFT of $ E_1 ^2$ for varying coupling coefficient, for $\delta=0.01, \tau = 0.5$ , and $\phi = 0.4\pi$ . . . . .	139
5.30	Logarithmic contour plots of $\tilde{E}_1$ and $ E_1 $ for varying coupling coefficient, for $\delta=0.2, \tau = 2$ , and $\phi = 0.2\pi$ . . . . .	140



5.31	Logarithmic contour plots of $\tilde{E}_1$ and $ E_1 $ for varying coupling coefficient, for $\delta=0.2$ , $\tau = 2$ , and $\phi = 0.4\pi$ . . . . .	141
5.32	Logarithmic contour plots of $\tilde{E}_1$ and $ E_1 $ for varying coupling coefficient, for $\delta=0.2$ , $\tau = 2$ , and $\phi = 0.7\pi$ . . . . .	141
5.33	Time trace of $ E $ and $\tilde{E}$ for $\eta = 0.1$ , $\phi = 0.4\pi$ , $\tau = 2$ and $\delta = 0.2$ . . . . .	141
5.34	Logarithmic contour plots of $ E_1 ^2$ for varying detuning ( $\delta=-0.2-0.2$ ), for $\eta=0.2$ , $\tau = 0.5$ , and a) $\phi = 0.2\pi$ , b) $\phi = 0.4\pi$ . . . . .	142
5.35	Logarithmic contour plots of $ E_1 ^2$ for varying detuning ( $\delta=-0.2-0.2$ ), for $\eta=0.025$ , $\tau = 0.5$ , and $\phi = 0.2\pi$ . . . . .	143
5.36	Solving the model with $\phi = \frac{\pi}{2}$ simplification for $\eta = 0.1$ and $\tau = 0.5$ . a) Shows parametric plots of $a_1$ vs $a_2$ , while b) shows the time trace of $a_1$ for $\delta = 0.5$ . . . . .	145
5.37	Solving the model with $\phi = \frac{\pi}{2}$ simplification for $\eta = 0.4$ and $\tau = 0.5$ . a) Shows parametric plots of $a_1$ vs $a_2$ , while b) shows the time trace of $a_1$ for $\delta = 0.5$ . . . . .	145
5.38	Solving the model with $\phi = \frac{\pi}{2}$ simplification for $\eta = 0.4$ and $\tau = 2$ , for various $\delta$ values. a) $\delta = 0.1$ , b) $\delta = 0.6$ , c) $\delta = 0.7$ . . . . .	146
5.39	Solving the model with $\phi = \frac{\pi}{2}$ simplification for $\eta = 0.1$ and $\tau = 8$ , for various $\delta$ values. a) $\delta = 0.15$ , b) $\delta = 0.5$ , c) $\delta = 0.7$ d) $\delta = 1$ . . . . .	147
5.40	Solving the model with $\phi = \frac{\pi}{2}$ simplification for $\eta = 0.4$ and $\tau = 8$ , for various $\delta$ values. a) $\delta = 0.45$ , b) $\delta = 0.6$ , c) $\delta = 0.8$ . . . . .	148
5.41	Contour plots of $a_1$ from the model with $\phi = \frac{\pi}{2}$ simplification for varying $\eta$ and a) $\delta = 0.05, \tau = 0.5$ , b) $\delta = 0.05, \tau = 2$ , c) $\delta = 0.8, \tau = 0.5$ d) $\delta = 0.8, \tau = 2$ . . . . .	149
5.42	Second generation of MCL on chip devices. . . . .	150
5.43	Measurement of injection parameter $\eta$ vs. VOA bias for various mirror section biases of the SFP laser. . . . .	150
5.44	Experimental result for varying VOA bias, for a device separation of 1 mm and various detunings. . . . .	152
5.45	Third generation of MCL on chip devices. . . . .	153
5.46	Density plot of ESA traces for varying VOA bias for 385 $\mu\text{m}$ VOA device in figure 5.45, with the lasers tuned to have a detuning of 15 GHz. . . . .	154
5.47	Measurement of the amount of light reaching one laser from the other ( $\eta$ parameter) for the 385 $\mu\text{m}$ device in figure 5.45 for different currents applied to the mirror section of the laser. . . . .	154
5.48	HSO trace of one of the MCL lasers in the harmonic region of figure 5.46, between 1.6V and 1.8V. . . . .	155
5.49	Density plot of optical spectrum analyser (OSA) traces for varying VOA bias for 385 $\mu\text{m}$ VOA device in figure 5.45, with the lasers tuned to have a detuning of 15GHz. . . . .	156
5.50	Cavity lengths present in the optical spectra, for varying VOA bias, for 385 $\mu\text{m}$ VOA device in figure 5.45, with the lasers tuned to have a detuning of 15 GHz. . . . .	157

6.1	Bifurcation diagrams, showing saddle-node bifurcations in orange and hopf in blue, for varying symmetric values of $\Delta\omega_{1,2}$ for the multimode model. . . . .	164
6.2	Plots of the L2 Norm from the multimode model, for varying $\phi$ from $0 - 2\pi$ , for $\eta = 0.1$ and $0.3$ . The stable steady states are in orange, unsteady stable states are blue, steady periodic solutions are green dots and unsteady periodic solutions are in red. . . .	166
6.3	Plots of the L2 Norm from the multimode model, for varying $\phi$ from $0 - 2\pi$ , for $\eta = 0.1$ and $0.3$ . The stable steady states are in orange, unsteady stable states are blue, steady periodic solutions are green dots and unsteady periodic solutions are in red. Saddle-node bifurcations are shown by purple dots, Hopf given by black, and the Hopf-fold is highlighted in grey. . . . .	166
6.4	L2 Norm from the multimode model, for varying $\eta$ , for $\phi = 0.7$ and $\Delta\omega_{1,2} = 0.05$ . The stable steady states are in blue, unsteady stable states are orange, steady periodic solutions are green dots and unsteady periodic solutions are in red. Saddle-node bifurcations are shown by purple dots, Hopf given by black, and the torus bifurcations is highlighted in brown. . . . .	167
6.5	Bifurcation diagram over the $(\phi, \eta)$ parameter space, showing saddle-node bifurcations in orange and hopf in blue, for non-symmetric values of $\Delta\omega_1 = 0.05$ and $\Delta\omega_2 = 0.07$ for the multimode model. . . . .	168
6.6	Plots of the L2 Norm from the multimode model, for varying $\phi$ , with $\Delta\omega_1 = 0.05$ , $\Delta\omega_2 = 0.07$ and a) $\eta = 0.1$ b) $\eta = 0.3$ . The stable steady states are in orange, unsteady stable states are blue, steady periodic solutions are green dots and unsteady periodic solutions are in red. Saddle-node bifurcations are shown by purple dots, Hopf given by black, and the Hopf-fold is highlighted in grey. . . . .	168
6.7	Bifurcation diagram over the $(\phi, \eta)$ parameter space, showing saddle-node bifurcations in orange and hopf in blue, for non-symmetric values of $\Delta\omega_1 = 0.07$ and $\Delta\omega_2 = 0.05$ for the multimode model. . . . .	170
6.8	Plots of the L2 Norm from the multimode model, for varying $\phi$ , with $\Delta\omega_1 = 0.07$ , $\Delta\omega_2 = 0.05$ and a) $\eta = 0.1$ b) $\eta = 0.3$ . The stable steady states are in orange, unsteady stable states are blue, steady periodic solutions are green dots and unsteady periodic solutions are in red. Saddle-node bifurcations are shown by purple dots, Hopf given by black, and the Hopf-fold is highlighted in grey. . . . .	170

6.9	Plot of the L2 Norm from the multimode model, for varying $\Delta\omega_1$ , with $\Delta\omega_2 = 0$ , $\eta = 0.01$ and $\phi = 2.5$ . The stable steady states are in orange, unsteady stable states are blue, steady periodic solutions are green dots and unsteady periodic solutions are in red. Saddle-node bifurcations are shown by purple dots, Hopf given by black and period doubling bifurcations are in yellow. .	172
6.10	Plot of the L2 Norm from the multimode model, for varying $\Delta\omega_2$ , with $\Delta\omega_1 = 0$ , $\eta = 0.01$ and $\phi = 2.5$ . The stable steady states are in orange. . . . .	173
6.11	Plot of the L2 Norm from the multimode model, for varying $\Delta\omega_1$ , with $\Delta\omega_2 = 0.2$ , $\eta = 0.01$ and $\phi = 2.5$ . The stable steady states are in orange, unsteady stable states are blue, steady periodic solutions are green dots and unsteady periodic solutions are in red. Saddle-node bifurcations are shown by purple dots, Hopf given by black, period doubling bifurcations are in yellow, Hopf-fold bifurcations in grey and taurus bifurcations are in brown. .	174
6.12	Time trace of $R_1$ from the multimode model, with the parameter values equal to the regions B and J in figure 6.11. . . . .	175
6.13	Plot of the L2 Norm from the multimode model, for varying $\Delta\omega_1$ , with $\Delta\omega_2 = 0.05$ , $\eta = 0.01$ and $\phi = 2.5$ . The stable steady states are in orange, unsteady stable states are blue, steady periodic solutions are green dots and unsteady periodic solutions are in red. Saddle-node bifurcations are shown by purple dots, Hopf given by black, period doubling bifurcations are in yellow, Hopf-fold bifurcations are in grey and taurus bifurcations are in brown.	176
6.14	Plot of the L2 Norm from the multimode model, for varying $\Delta\omega_1$ , with $\Delta\omega_2 = -0.05$ , $\eta = 0.01$ and $\phi = 2.5$ . The stable steady states are in orange, unsteady stable states are blue, steady periodic solutions are green dots and unsteady periodic solutions are in red. Saddle-node bifurcations are shown by purple dots, Hopf given by black, period doubling bifurcations are in yellow and Hopf-fold bifurcations are in grey. . . . .	177
6.15	Plot of the L2 Norm from the multimode model, for varying $\Delta\omega_2$ , with $\Delta\omega_1 = 0.05$ , $\eta = 0.01$ and $\phi = 2.5$ . The steady periodic solutions are green dots and unsteady periodic solutions are in red. Torus bifurcations are in brown . . . . .	178
6.16	Time series of $ E_{L1} $ and $ E_{L2} $ from the multimode model, for $\beta_{11} = \beta_{22} = 1$ , $\beta_{12} = 0.1$ and $\beta_{21} = 0.9$ . . . . .	179
6.17	Bifurcation diagrams of the multimode model, showing saddle-node bifurcations in orange and hopf in blue, $\Delta\omega_{1,2} = 0.05$ , for a) non symmetric modes b) symmetric modes. . . . .	180
6.18	Bifurcation diagrams of the multimode model, showing saddle-node bifurcations in orange and hopf in blue, for $\Delta\omega_{1,2} = 0.1$ , for a) non symmetric modes b) symmetric modes. . . . .	180

6.19	Bifurcation diagrams of the multimode model, showing saddle-node bifurcations in orange and hopf in blue, for $\Delta\omega_{1,2} = 0.15$ , for a) non symmetric modes b) symmetric modes. . . . .	181
6.20	Bifurcation diagrams of the multimode model, showing saddle-node bifurcations in orange and hopf in blue, $\Delta\omega_1 = 0.05$ and $\Delta\omega_2 = 0.07$ , for a) non symmetric modes b) symmetric modes. .	181
6.21	Bifurcation diagrams of the multimode model, showing saddle-node bifurcations in orange and hopf in blue, $\Delta\omega_1 = 0.07$ and $\Delta\omega_2 = 0.05$ , for a) non symmetric modes b) symmetric modes. .	182
6.22	Measurement of $\eta$ for the $385\mu m$ device in figure 5.45, for various tuning arrangements. . . . .	183
6.23	Logarithmic contour plot of a)FFT of $ E_{L_1} $ , b) FFT of $\tilde{E}_{L_1}$ from the multimode model, for varying VOA bias (using associated $\eta$ values in figure 5.43). $\Delta\omega_{1,2} = 0.1$ and $\phi = 1.57$ . . . . .	183
6.24	Time trace of $ E_{L_1} $ from the multimode model, for $\eta = 0.3$ , $\phi = 1.57$ and $\Delta\omega_{1,2} = 0.1$ . . . . .	184
6.25	a) $\log_{10}$ of the FFT and b) time trace of $ E_{L_1} $ from the multimode model, for $\eta = 0.32$ , $\phi = 2.51$ and $\Delta\omega_{1,2} = 0.1$ . . . . .	184
6.26	$\log_{10}$ of the FFT of $ E_{L_1} $ from the multimode model, for $\eta = 0.32$ , $\phi = 2.51$ and $\Delta\omega_{1,2} = 0.1$ , with the max frequency cut at $80GHz$ . .	185
6.27	Logarithmic contour plot of FFT of $ E_{L_1} $ from the multimode model, for linearly varying $\eta$ . $\Delta\omega_{1,2} = 0.1$ and $\phi = 1.57$ . . . . .	185
6.28	Logarithmic contour plot of a)FFT of $ E_{L_1} ^2$ , b) FFT of $\tilde{E}_{L_1}$ from the multimode model, for varying VOA bias (with $\eta$ values associated with the lower $\eta$ of the second generation MCL devices). $\Delta\omega_{1,2} = 0.1$ and $\phi = 2.51$ . . . . .	186
6.29	Time trace of $ E_{L_1} $ from the multimode model, for $\eta = 0.05$ , $\phi = 2.51$ and $\Delta\omega_{1,2} = 0.1$ . . . . .	186
6.30	Experimental density plot of the wavelength versus the current applied for a simple FP laser. . . . .	187
6.31	Plot of the wavelength of the main mode of the FP device test, versus the current applied. . . . .	188
6.32	Plot of current measured versus voltage applied for the FP device. .	188
6.33	Plot of current measured versus power applied for the FP device. .	189
6.34	Plot of power applied to the FP versus the wavelength of the main mode of the FP device. . . . .	189
6.35	Plot of refractive index ( $n$ ) versus power applied to the FP device. .	190
6.36	Plot of change in refractive index ( $\Delta n$ ) versus power applied to the FP device. . . . .	190
6.37	Plot of current measured versus voltage applied to the different length VOAs in the third generation MCL devices. . . . .	191
6.38	Plot of the change in optical path length for the $385\mu m$ VOA device versus the voltage applied. . . . .	191
6.39	Plot of phase change for the $385\mu m$ VOA device versus the voltage applied. . . . .	192

6.40	Plot of phase change for the various VOA lengths versus the voltage applied. . . . .	193
6.41	$(\phi, \eta)$ curves found from experimental results (black), placed over the bifurcation diagrams of the multimode model, for $\Delta\omega_{1,2} = 0.05$ . . . . .	193
6.42	Logarithmic contour plots of the FFT of $E_{L_1}$ and $ E_{L_1} $ from the multimode model, for a) $\phi = 0$ b) $\phi = 0.3\pi$ start values of the $(\phi, \eta)$ curves highlighted in figure 6.41. . . . .	194
6.43	$(\phi, \eta)$ curves found from experimental results (black) for the $835\mu m$ VOA device, placed over the bifurcation diagrams of the multimode model, for $\Delta\omega_{1,2} = 0.05$ . . . . .	195
6.44	Logarithmic contour plots of the FFT of $E_{L_1}$ and $ E_{L_1} $ from the multimode model, for a) $\phi = 0$ b) $\phi = 0.4\pi$ start values of the $(\phi, \eta)$ curves highlighted in figure 6.43 for the $835\mu m$ VOA devices. . . . .	196
6.45	Hopf (blue) and saddle-node (orange) bifurcations for the $(\Delta\omega, \text{VOA bias})$ parameter space for the $385\mu m$ VOA MCL device, for two initial phase values, a) $\phi = 0$ and b) $\phi = 0.3\pi$ . . . . .	197
6.46	Hopf (blue) and saddle-node (orange) bifurcations for the $(\Delta\omega, \text{VOA bias})$ parameter space for the $835\mu m$ VOA MCL device, for two initial phase values, a) $\phi = 0$ and b) $\phi = 0.3\pi$ . . . . .	197
6.47	ESA contour plots for varying VOA bias for different generation MCL devices . . . . .	198
6.48	Summary of a number of experimental sweeps, where for each sweep, a detuning was fixed and the VOA bias was swept. The different behavioural regimes are given by the colour legend in the plot . . . . .	199
B.1	Schematic of situation modelled by Eqn. B.1-B.3. The middle region is the active region of the laser, labelled 1, and this is surrounded by absorbing regions, labelled 2. The bottom two graphs show the carrier distribution and the power distribution in transition between active and absorbing regions. . . . .	208
B.2	Schematic of MCL device where the region labelled 1, is one of the active regions and the region labelled 3 is the other, and in between them is the absorbing region, labelled 2. The bottom two graphs show the carrier distribution and the power distribution in transition between active regions and absorbing region. . . . .	209
C.1	Experimental diagram for comb injection. . . . .	212
C.2	Frequency space diagram of a three line comb (green) injected into a single mode laser (black), where the frequency difference between each line and the laser is highlighted in purple. . . . .	213
C.3	Contour diagram of the FFT of $ E $ , for solving Eqn. C.13 and C.14 with a comb spacing of $d\omega = 2\omega_R$ , and an injection strength of $K = 0.1$ . . . . .	215

C.4	Contour diagram of the FFT of $ E $ , for solving Eqn. C.13 and C.14 with a comb spacing of $d\omega = 3\omega_R$ , and an injection strength of $K = 0.1$ . . . . .	216
C.5	Contour diagram of ESA traces for a comb spacing of $10GHz$ . .	216

## List of Tables

1.1	Breakdown of data traffic rates worldwide by year. . . . .	5
1.2	Breakdown of the terms in Eqn. 1.1 and 1.2 and what physical laser process they represent . . . . .	13
2.1	A breakdown of the range of delay times and detunings considered in each study of MCLs . . . . .	42
A.1	Epitaxial structure of the material used. A right arrow ( $\rightarrow$ ) indicates a gradient in composition, from lower layer numbers to higher layer numbers. . . . .	205
A.2	Epitaxial structure of the substrate on which the material in table A.1 was grown on. . . . .	205

I, Fabien Dubois, certify that this thesis is my own work and I have not obtained a degree in this university or elsewhere on the basis of the work submitted in this thesis.

*Fabien Dubois*





This thesis is dedicated to anyone who dares to be who they are.





"You might think that you're ruined, you might think you're defeated, if you  
love what you're doing you've already succeeded"

-George Watsky



# Acknowledgements

This thesis would not have been possible without many people but I would like to start by thanking my supervisor, Prof. Frank Peters. His patience, insight and encouragement were instrumental throughout. His visits to our office to vent on frustrations or celebrate minor victories were always welcome. Our discussions on the latest happenings in rugby or basketball were a welcome reprieve. His generosity was always on display in his willingness to welcome the entire research group into his home for food and board games a number of times throughout the year. Here special mention has to be made to his wife Jo Peters, your cooking was always spectacular and your generosity was always appreciated.

To anyone I have shared office 1.16F in the Kane building with goes a special thank you. Starting with the Joseph Cashell and Justin Alexander, who have since moved on to foreign lands and may not read this, your support and friendship were invaluable. To Kieran Cooney, your time here was brief but your encouragement and friendship were appreciated. To the man who has been beside me the longest (at the desk beside me the longest anyway) Kevin Shortiss, you were always a source of advice, knowledge and motivation. No question was too small to ask and you always had a helpful suggestion. To all final year project/summer interns who shared the office with me I hope I was of some help and you were all a pleasure to work with. To the rest of the integrated photonics group member (past and present) a sincere thank you. I always felt welcomed and respected. To all the post-docs who were instrumental in my early days as a PhD student, in offering advice, guidance and a friendly face, Padraic Morrissey, Eddie Cotter, Rob Sheehan and Ehsan Souudi, a heart felt thank you for taking the time out of your day to help me. A particular thank you to Masoud Seifkar, since you started in the group your help and support was instrumental. To my fellow PhD students, past and present, Shane Duggan, Alison Perrott, Ludovic Caro, Mohomad Dernaika, Moises Jezzini, Francesco Azzarello, you were always friendly faces and a great support system, be it technical assistance or just coffee and a chat. To all other members of IPG past or present, though you were not named in person you were a pleasure to work with.

To my parents, your unwavering support and encouragement was a constant motivator. Though you did not understand my work your constant interest always brought a smile to my face. I would not be where I am today without your efforts and I just hope to make you proud with what I do.

To my girlfriend Katie, you have stood beside me through this whole process (as close as beside me can be when you were at the opposite end of the country). Despite the physical distance between us, I always felt your full support and encouragement. They say behind every great man there is a great woman, I may not be a great man, but with you in my corner I feel like I could be.

Finally to my longest standing group of friends Joey, Mike, Susan, Sarah, Saul, Andrew, Grace, James, Alan and Aaron (a.k.a. the group). Thank you for your



support and inability to plan activities.

## List of Publications

- "Modeling mutually coupled non-identical semiconductor lasers on photonic integrated circuits"; **Fabien M. Dubois**, Masoud Seifikar, Alison H. Perrott, and Frank H. Peters, *Applied Optics*, Vol. 57, Issue 22, E154-E162 (2018).
- "Study of the dynamics of a system of two mutually coupled, detuned lasers, using attractor diagrams" **Fabien M. Dubois**, Masoud Seifikar, Alison H. Perrott, and Frank H. Peters, Publication under review, 2019
- "A Multimode Approach To Modelling Mutually Coupled Lasers in Photonic Integrated Circuits"; **Fabien M. Dubois**, Masoud Seifikar, Alison H. Perrot, Frank H. Peters, Publication under review, 2019
- "Deeply Etched Inner-Cavity Pit Reflector"; Mohamad Dernaika, Ludovic Caro, Niall P. Kelly, Justin K. Alexander, **Fabien Dubois**, Padraic E. Morrissey, Frank H. Peters, *IEEE Photonics Journal*, Volume 9, Issue 1, February, 2017.
- "The Devil's Staircase in the Frequency and Amplitude Locking of Nonlinear Oscillators with Continuous Periodic Forcing"; Benjamin Lingnau, Kevin Shortiss, **Fabien Dubois**, Bryan Kelleher and Frank Peters, Publication under review, 2019

# Conferences

## Talks

- "Modeling Mutually Coupled Non-Identical Semiconductor Lasers on Photonic Integrated Circuits"; **Fabien M. Dubois**, Masoud Seifikar, Alison H. Perrot, Frank H. Peters, Conference on the Numerical Simulations of Optoelectronic Devices (NUSOD), Wednesday, 26th July 2017 (WB5), Copenhagen, Denmark.
- "A Multimode Approach To Modelling Mutually Coupled Lasers in Photonic Integrated Circuits"; **Fabien M. Dubois**, Masoud Seifikar, Alison H. Perrot, Frank H. Peters, Photonics North Conference, Wednesday 6th June (TD-5-21-2), Montreal, Canada.

## Posters

- "Mutually Coupled Semiconductor Lasers In Photonic Integrated Circuits"; **F.M. Dubois**, E. Sooudi, R.N. Sheehan, E. Clerkin, M. Yang, J.K. Alexander, H. Yang and F.H. Peters, Photonics Ireland Conference, Thursday 3rd September 2015, Cork, Ireland.
- "Mutually Coupled Semiconductor Lasers In Photonic Integrated Circuits"; **F.M. Dubois**, E. Sooudi, R.N. Sheehan, E. Clerkin, M. Yang, J.K. Alexander, H. Yang and F.H. Peters, Institute of Physics (IOP) Spring Meet, 2016, Belfast, Northern Ireland.
- "Mutually Coupled Semiconductor Lasers in Photonic Integrated Circuits"; **Fabien M. Dubois**, Masoud Seifikar, Alison H. Perrot, Frank H. Peters, European Conference on Integrated Optics (ECIO), Wednesday 18th May 2016 (p-28), Warsaw, Poland.
- "Modelling Non Identical Mutually Coupled Semiconductor Lasers in Photonic Integrated Circuits"; **F.M. Dubois**, A.H. Perrott, M. Seifiker, and F.H. Peters, Photonics Ireland Conference, 13th-15th September 2017, Galway, Ireland.
- " A Multi-mode Approach To Modelling Mutually Coupled Lasers In Photonic Integrated Circuits"; **F.M. Dubois**, A.H. Perrott, M. Seifiker, and F.H. Peters, Photonics Ireland Conference, Tuesday 4th September (p10), Cork, Ireland.
- "Injection Locking of Mutually Coupled SFP Lasers on a PIC"; A.H. Perrott, P.E. Morrissey, **F.M. Dubois**, M. Dernaika, L. Caro, N. Kelly and F.H. Peters, Photon16 Conference, 2016, Leeds, United Kingdom.

- "Mutual Injection Locking of Lasers in a Photonic Integrated Circuit";  
A.H. Perrott, L. Caro, M. Dernaika, N.P. Kelly, **F.M. Dubois**, and F.H.  
Peters, Institute of Physics (IOP) Spring Meet, 2017, Dublin, Ireland.

# **Abstract**

Photonic integration has proven to be a technology with the potential to meet the seemingly unceasing increase in demand for information in an efficient and cost effective way. As the size of optical components shrinks certain challenges must be overcome. This thesis addresses the lack of an optical isolator in our integrated platform. Without this component any system requiring one will have an added feedback when realised in an integrated format. Specifically we deal with the process of injection locking lasers, which is a common process used in spectral filtering. Without the optical isolator the system becomes what is called mutually coupled. When dealing with mutually coupled lasers, the physical separation of the lasers is a key parameter. This system is well understood for large separations between the lasers (on the order of metres), limited studies are available for the short separation regime associated with photonic integration. In this thesis initial experiments into understanding mutually coupled lasers on a photonic integrated circuit will be shown, followed by a theoretical study. This study will focus on a rate equation based approach, using both ordinary and delay differential equation systems. Two different models will be studied, initially the single mode model of previous studies will be analysed, and following this, motivated by comparison of results with experimental results, a multi-mode model will be developed and studied.



# **Chapter 1**

## **Introduction**

Since the laser's inception in the early 1960s, it has become the unseen backbone of modern society. Never has something so ubiquitous in its use in everyday items, been a source of fear for the general populous. Indeed Hollywood has dramatised the laser as the weapon of choice for a myriad of generic mad scientists and though their power is used for such purposes as nuclear fusion and industrial scale welding; the death rays of Doctor Evil are far from common uses. In fact away from the silver screen the laser is universal in its applications and modern developments are removing the barriers of price and size.

Lasers still are a key component of optical storage and disc reading, despite the increased usage of solid state drives. Increasingly the medical industry has become more dependent upon laser technology, through the development of new scanning and treatment techniques. The race for the development of driver-less vehicles has required the implementation of lasers for ranging and scanning purposes, through the use of light detecting and ranging (LIDAR). Ironically the very thesis you are reading was brought into a physical form through the use of laser printers. Gas sensing for safety purposes has also pushed the laser to be used as a powerful tool in the line of spectroscopy.

## 1.1 Introduction to optical communications

Though the laser's use is only limited in its applicability by the creativity of the developer, no industry has flourished and benefited more from it's invention than the area of communications. Since the internet became a global utility in the early 1990s the world's thirst for knowledge and media has forced a ceaseless development in the technology used to transfer data. The earliest dial up connection to the home gave people a taste of access to a world of information. However with maximum speeds of 56 kbps, people were left craving more. At these speeds a low quality feature length film file would take a day to download. This underwhelming speed created a hunger that could not be satisfied through the use of analog phone lines. As has become the story of the laser, the drive for faster, better, more robust technology left it as an ideal candidate to meet this rising need. Thus the fibre optic broadband of modern times came into being, pushing data speeds further and further. In 2015 the Federal Communications Commission in the USA defined basic broadband as having a minimum download speed of 25 Mbps and upload speed of 3 Mbps; a thousand times increase over dial-up.

The backbone of this modern network is the silica optical fiber. Silica has transmission windows (a wavelength span of low attenuation) centred around the wavelengths of 1310 nm and 1550 nm. Modern broadband utilises what is called the C and L bands (wavelength range of 1530 to 1625 nm) as these bands have the lowest attenuation, allowing low loss, long distance transfer. Initial development was focused around making each individual wavelength channel have higher data rates, while spacing them out to reduce channel cross-talk, a process called coarse wavelength division multiplexing (CWDM). As advancements in modulation speeds saturated, research then moved to increase the number of channels, by moving them closer together, leading to dense wavelength division multiplexing (DWDM). State of the art technology has pushed the development of orthogonal frequency wavelength division multiplexing (OFDM). Here the channels are closely packed together and worries of crosstalk are assuaged by maintaining a fixed phase relation between the channels, which can be decoded on the receiver end. The modern standard for using OFDM is called data over cable service interface specification (DOCSIS). The latest version (3.1) utilises 4096-QAM modulated 25 kHz sub carrier spacing to achieve a throughput of 1.89 Gbps per 192 MHz upstream. QAM refers to quadrature amplitude modulation, which is a modulation format incorporating a phase relation. For example a 16QAM would have two possible amplitudes and four phase angles, creating a constellation of 16 points, as shown in figure 1.1.

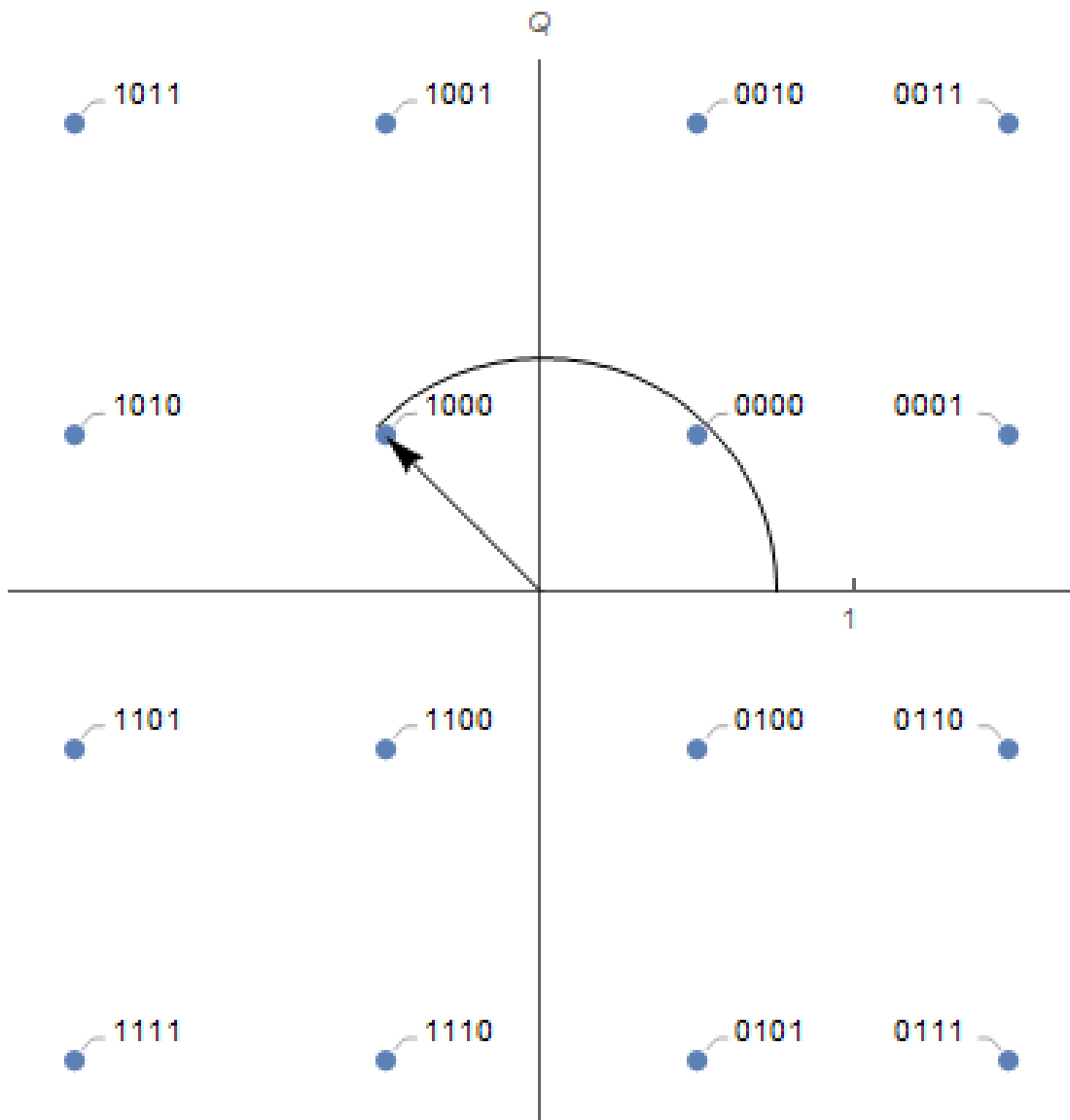


Figure 1.1: Example of the constellation diagram for 16QAM, showing the corresponding binary number associated with each point.

To achieve these low channel spacings, a highly monochromatic light source is required, one which is highly directional to suit the need for long distance communication. All these desired characteristics made the laser the obvious choice.

There are a number of ways to create an OFDM system. For example, through the use of a frequency comb, a number of closely spaced frequency lines can be generated with a fixed phase relation between them. Then these comb lines are demultiplexed, i.e. the comb is split and each frequency line isolated. These demultiplexed lines are then modulated to encode data, and

multiplexed back into a comb, before transmitted to the user.

## 1.2 Internet usage projections

Despite these great speeds that have now been achieved, modern society now desires more and more data at ever faster speeds. A comparison of this demand with the early days of public use of the internet can be seen in Table 1.1. Here the increase in the amount of total global internet traffic from 1992 to 2016 can be seen, with a projection of the increase for 2021.

Year	Global internet traffic
1992	100 GB per day
1997	100 GB per hour
2002	100 GB per second
2007	1000 GB per second
2016	26600 GB per second
2021	105800 GB per second

Table 1.1: Breakdown of data traffic rates worldwide by year<sup>1</sup>.

This is a dramatic increase in a thirty year period and it is only predicted to increase. Many factors contributed to this rise, for example increased numbers of users (see figure 1.2), but also the size of media being consumed. For example, the quality of video files being demanded by consumers has pushed development from standard definition video, to high definition video to now ultra-high definition and 4K video. The breakdown of the resulting traffic can be seen in figure 1.3. Popularity of websites like and Youtube and Netflix are the main driving forces of this demand. Growing industries such as the internet of things and the daily prevalence of social media seems to make demand for data unending. The predictor of this increase is Nielsen's law. The predicted trend line of available data transfer rates from Nielsen's vs. actual realised values can be seen in figure 1.4.

<sup>1</sup><https://www.cisco.com/c/en/us/solutions/collateral/service-provider/visual-networking-index-vni/vni-hyperconnectivity-wp.html>

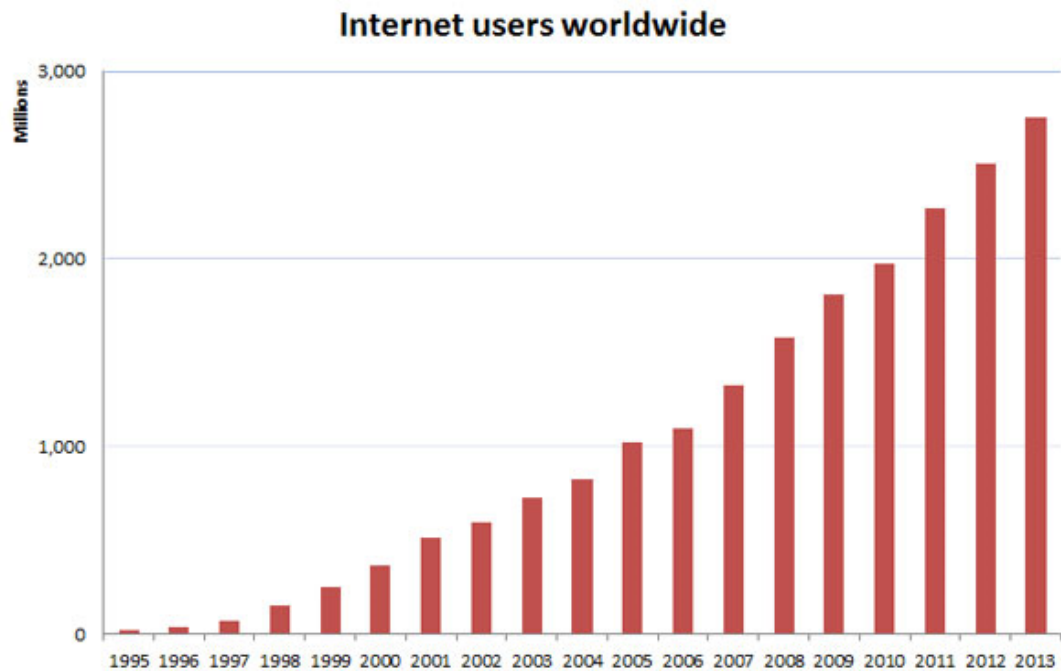


Figure 1.2: Increases in the number of internet users per year from 1995 to 2013<sup>2</sup>.

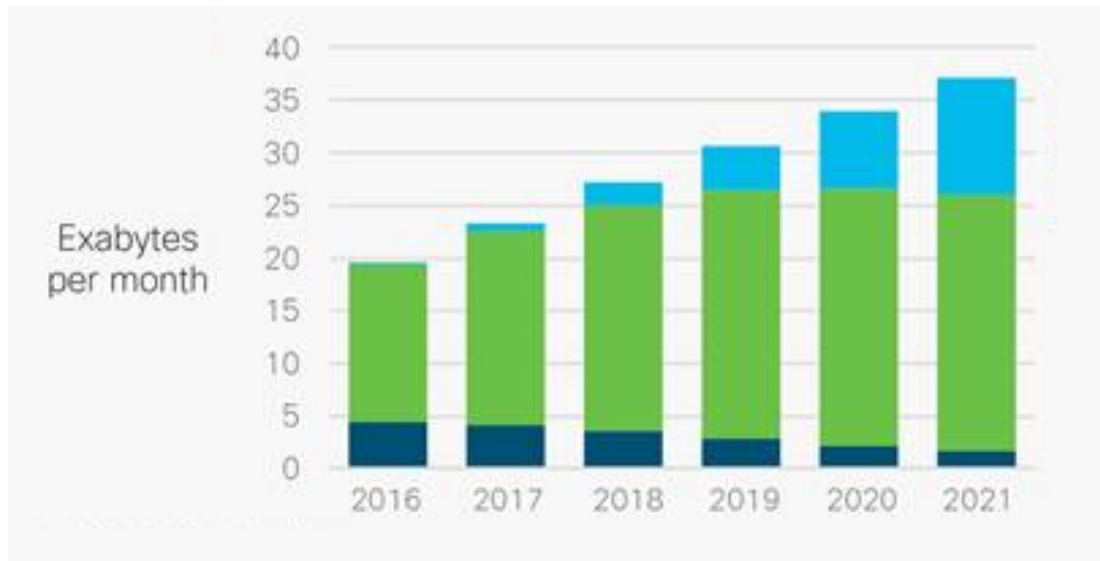


Figure 1.3: Predicted data traffic of different video formats (ultra high definition (UHD) in blue, high definition (HD) in green and standard definition (SD) in navy) each year from 2016 to 2021<sup>3</sup>.

<sup>2</sup><http://www.open.edu/openlearn/money-management/management/business-studies/history-online-retail>

<sup>3</sup><https://www.cisco.com/c/en/us/solutions/collateral/service-provider/visual-networking-index-vni/vni-hyperconnectivity-wp.html>

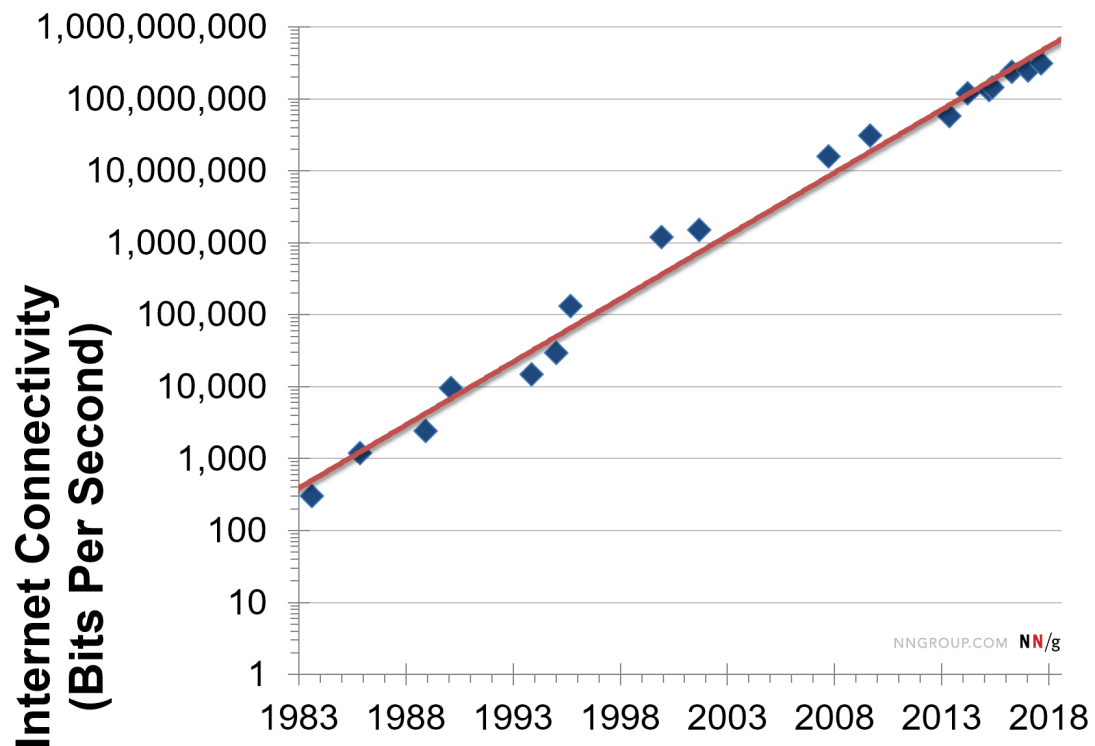


Figure 1.4: Nielsen's law of predicting internet speeds vs. measured speeds<sup>4</sup>.

### 1.3 Introduction to photonic integration

As has been shown, demand for faster data rates has been increasing and current technology has advanced to meet this need. However as the technology continues to advance, one must be concerned with the spatial and energy efficiency of the processes needed to transfer these increasingly large amounts of data. In fact the internet is estimated to currently use 10% of the worlds energy<sup>5</sup>. All projections point to this increasing with rising demand, unless the energy efficiency of the platform can be improved. One solution to this problem is the idea of photonic integration. Instead of linking individual discrete components via optical fibres, a version of each component is fabricated out of semiconductor material and all combined onto one chip. Taking what could occupy an entire bench top experiment, is now all on one chip smaller than a finger nail. There are a number of advantages to this process. Firstly and most obviously the smaller footprint of these systems

<sup>4</sup><https://www.nngroup.com/articles/law-of-bandwidth/>

<sup>5</sup>[https://www.researchgate.net/publication/320225452\\_Total\\_Consumer\\_Power\\_Consumption\\_Forecast](https://www.researchgate.net/publication/320225452_Total_Consumer_Power_Consumption_Forecast)

allows for a denser collection of transmitters in a given location. Secondly, the amount of energy required to power these chips is much lower than power the discretised components. Thirdly, losses associated with fibre coupling of components are avoided. By having the components next to each other on a single semiconductor chip there is a low optical loss between them, improving the overall energy efficiency.

Different schools of thought exist on the best way to achieve photonic integration, each using an array of different material and processes and each having their own advantages and drawbacks.

### 1.3.1 Hybrid integration

The holy grail of photonic integration is to be able to have an entire photonic integrated circuit (PIC) made out of silicon. This would allow the use of the well-established foundry processes and infrastructure of the microelectronics industry, markedly reducing production costs. Also, silicon is transparent at both the 1300 nm and 1550 nm wavelengths desired for optical communications, ensuring low loss operation. However, due to silicon being an indirect band-gap semiconductor, a laser cannot be made of silicon, which means a light source on a pure silicon chip does not exist. To overcome this, hybrid integration fabricates all the passive components of a photonic system on a silicon chip; while making the active components, like lasers, out of a different material that has the desired band-gap structure to produce laser light, e.g. III-V semiconductors. These two chips are then combined to create a "hybrid" chip. The advantage of this method is that the base of the chip is silicon which, as mentioned, has a well-researched manufacturing process that is low cost. The disadvantages are that the hybridisation is a complex process that requires specialised equipment and can result in poor optical coupling between the silicon and active material.

### 1.3.2 Monolithic integration

Monolithic integration is the process of combining all active and passive components of a photonic system on a single epitaxial structure. These components can be formed via processing of the original epitaxy, or through regrowth of extra material onto the chip. This makes the process simpler as it uses one single chip, processed a single time, leading to faster production. Also



making a laser out of these materials is possible as they are direct band-gap semiconductors. However, there are drawbacks; less foundries are compatible with processing these chips and the processes themselves are less researched. All this means more expensive mass production.

## 1.4 Introduction to lasers

The word laser is an acronym for light amplification by the stimulated emission of radiation and within a laser cavity this is the major process that creates the highly monochromatic, directionalised, in phase photons desired. The basic layout of a laser can be seen in figure 1.5.



Figure 1.5: Layout of an ideal laser cavity, where a gain medium is surrounded on one side by a perfect reflector and on the other by a partial reflector.

Here a material, known as the gain medium, provides the amplification. At an atomic level it is the transitions of electrons from the conduction band (the first empty energy level) to the valence band (the outer most energy level containing electrons) that creates a photon of light. By injecting the conduction band with electrons, they fall to conduction band releasing photons of frequency proportional the fixed energy gap between the bands. The gain medium is surrounded by some variation of reflectors, one partial one full in the ideal case, causing the majority of photons to bounce back and forth within the gain medium, with a small percentage exiting the cavity as output. As a photon passes though, an existing electron decays in response to the EM field of the passing photon resulting in an additional photon at the same energy, direction and phase There is also another method by which photons can be generated in a laser cavity. This is called spontaneous emission.

Spontaneous emission is the random emission of photons from within the gain medium. These photons have random direction and phase compared to the photons produced by stimulated emission and therefore contributes to the

noise present in a laser. To achieve laser operation, stimulated emission must exceed spontaneous emission. This happens when enough electrons/photons are injected into the gain medium for stimulated emission to be the predominant process. The point at which stimulated emission overcomes spontaneous emission is referred to as laser threshold. Figure 1.6 shows a plot of light output versus the current applied to a semiconductor laser, which is called an LI (light-current) plot of a laser.

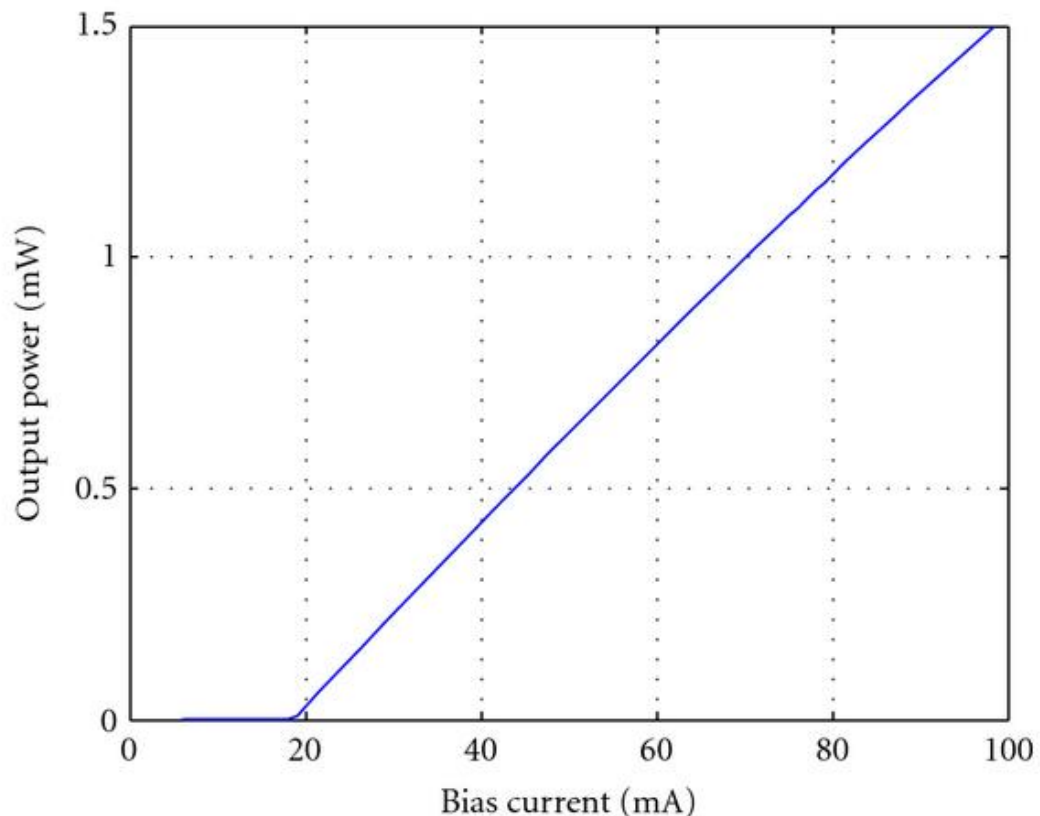


Figure 1.6: Example of an LI (light output-current) plot for a semiconductor diode laser<sup>6</sup>.

The x-axis shows the injected current, and the y-axis shows the laser output. For low currents, there are not enough electrons being injected for stimulated emission to overcome spontaneous emission, so the predominant emission is randomly generated photons. The light output increases slowly as more current is injected, until the threshold current is achieved, after which the light output increases linearly with increased current.

<sup>6</sup><https://www.hindawi.com/journals/aoe/2011/780373/fig4/>

### 1.4.1 Semiconductor lasers

There are many different types of laser, such as gas or solid state lasers, however, for photonic integration; the lasers are made of semiconductor material. Here, the gain material is the semiconductor material itself, and various types of reflectors can be made during the processing of the laser to provide enough reflectivity to form a laser cavity. A further discussion of these reflectors can be found in Sec. 1.4.2. The commonly used materials for semiconductor lasers are compounds of group III and group V elements, known as III-V semiconductors. These compounds are carefully engineered in their compositions to achieve the desired band-gap (which defines the frequency of the output light). Common ternary compounds include GaAs and InP. It is also possible to use quaternary compounds such as InGaAsP or AlInGaAs. For example, figure 1.7 shows how the band-gap and lattice constant of various III-V compounds vary with changing composition. This allows designers to customise the emission wavelength of their devices.

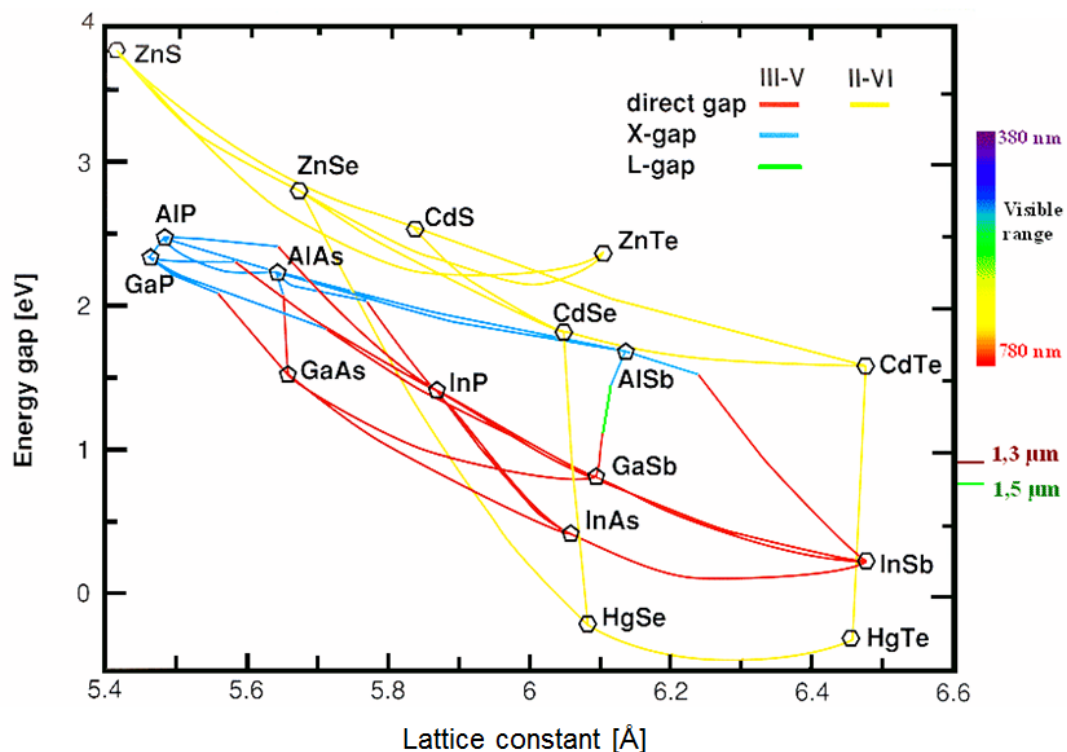


Figure 1.7: Plots of lattice constant versus band gap for varying compositions of various III-V and III-VI semiconductor compounds<sup>7</sup>.

<sup>7</sup>[https://www.tf.uni-kiel.de/matwis/amat/semitech\\_en/kap\\_2/backbone/r2\\_3\\_1.html](https://www.tf.uni-kiel.de/matwis/amat/semitech_en/kap_2/backbone/r2_3_1.html)

However, further engineering can be done to alter the emission wavelength of the laser, rather than simply depending on the composition of the material. Through using alternating layers of two different band-gaps, a series of quantum wells can be made. Here the mathematics of the finite potential well in quantum mechanics comes into play, as can be seen in figure 1.8. Electrons pumped into the conduction band flow into the upper well and occupy one of the quantum energy levels of the well. Now the energy of the photon emitted is not the difference from the bottom of conduction band to the top of the valence band, but rather the energy difference between the first allowed energy state of the top well and first energy state of the lower well. This design also improves the efficiency of the laser as photons are efficiently directed to the well encouraging stimulated emission.

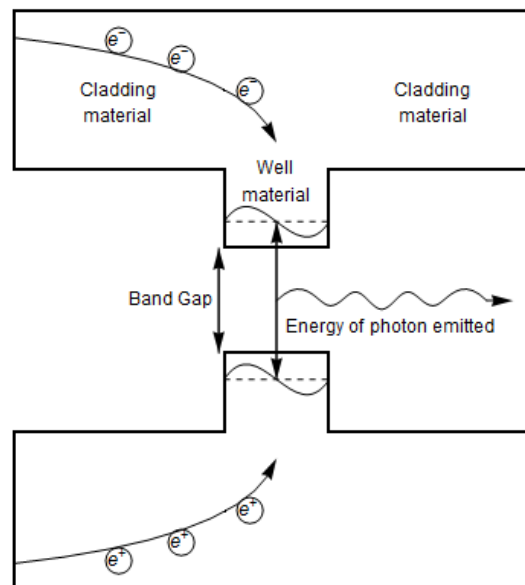


Figure 1.8: Example of a quantum well made by sandwiching a layer of lower band-gap material between two higher band-gap cladding layers, forming a potential well. Electrons/holes in the wells occupy discrete quantum states, so that the energy of the photon emission is no longer the band-gap, but the difference between the quantum states in the wells, as shown.

The quantum well region is made of an un-doped semiconductor, i.e. no impurities have been introduced. This region of quantum well(s) is known as the active region of the laser. To encourage electron flow through this region, it is surrounded by a p-doped semiconductor (by introducing an impurity with excess holes, it introduces an energy level within the band-gap near the valence band) on one side, and on the other side by an n-doped semiconductor (introducing impurity with excess carriers, generates an energy level within

the band-gap near the conduction band). This epitaxial structure forms a PIN diode semiconductor laser structure.

Models to describe the behaviour of semiconductor lasers have been extensively studied. The basic rate equations to model laser behaviour can be seen in Eqn. 1.1 and 1.2, [1]. These describe the temporal evolution of the photon density ( $N_s$ ) and carrier density ( $N$ ).

$$\frac{dN_s}{dt} = (\Gamma G - \frac{1}{\tau_p})N_s + \beta \frac{N}{\tau_r} \quad (1.1)$$

$$\frac{dN}{dt} = \frac{I}{eV} - \frac{N}{\tau_n} - \Gamma G N_s \quad (1.2)$$

Each term describes a different process within the laser. These are broken down in Table 1.2.

Term	Process	Terms
$(\Gamma G - \frac{1}{\tau_p})$	Photons produced by gain - photons lost through non-radiative processes	$\Gamma$ is the confinement factor (volume of active region/volume of cavity). $G$ is the gain term. $\tau_p$ is the average photon lifetime.
$\beta \frac{N}{\tau_r}$	Spontaneous emission	$\beta$ is the spontaneous emission factor, $\tau_r$ is the radiative recombination time constant.
$\frac{I}{eV}$	Electron pumping term	$I$ is the current, $e$ is the charge of an electron. $V$ is the volume of the laser cavity.
$\frac{N}{\tau_n}$	Carrier loss	$\tau_n$ is the average lifetime of a carrier.
$\Gamma G N_s$	Carriers lost through photon generation	Terms described above

Table 1.2: Breakdown of the terms in Eqn. 1.1 and 1.2 and what physical laser process they represent

The terms of the form  $N/\tau$  account for the natural decay of photons and carriers out of the laser that is not part of the production of laser light, i.e. losses. The loss term in the carrier equation, can be re-written to account for a number of processes. The three most common of these processes can be

accounted for by writing this term in the form:

$$\frac{N}{\tau} = AN + BN^2 + CN^3 \quad (1.3)$$

Here the terms represent defect, spontaneous emission ( $R_{sp}$ ) and Auger recombination<sup>8</sup> respectively. Direct Auger recombination is a non-radiative process where when an electron and a hole recombine instead of a photon being produced either the electron is pushed higher into conduction band or the hole is pushed deeper into the valence band. This process is more common for high temperatures and low bandgaps. The gain term  $G$  can be written in various forms, based on the gain profile of the laser. The most basic gain shape is to assume a linear dependence on carrier density  $N$ .

$$G \approx a(N - N_{tr}) \quad (1.4)$$

Here,  $a$  is  $\frac{dG}{dN}$  and  $N_{tr}$  is the transparency carrier density of the material, or a more advanced formulation can be employed which uses a logarithmic representation.

$$G = g'_0 \ln \frac{N + N_s}{N_{tr} + N_s} \quad (1.5)$$

$g'_0$  is an empirical gain coefficient and  $N_s$  is a shift to force the natural logarithm to be finite at  $N = 0$ , such that the gain equals the unpumped absorption. Eqn. 1.5 could also, for example, be multiplied by  $1/(1 - \epsilon N_p)$ . This is accounting for a phenomena known as gain compression. This accounts for how the gain rolls off at higher power output. The gain term in the photon density equation (Eqn. 1.2) is multiplied by  $\Gamma$ , this is known as the confinement factor and accounts for the fact that the volume occupied by photons,  $V_p$ , is generally larger than the active region volume occupied electrons,  $V$ . The photon density is scaled by this ration  $V/V_p = \Gamma$ .

Figure 1.9 shows an example time trace of the photon density from solving Eqn. 1.1 and 1.2. One can see a series of decaying oscillations settling down into steady output. These decaying oscillations are referred to as the relaxation oscillations (RO).

---

<sup>8</sup><https://ocw.mit.edu/courses/electrical-engineering-and-computer-science/6-720j-integrated-microelectronic-devices-spring-2007/lecture-notes/lecture4.pdf>

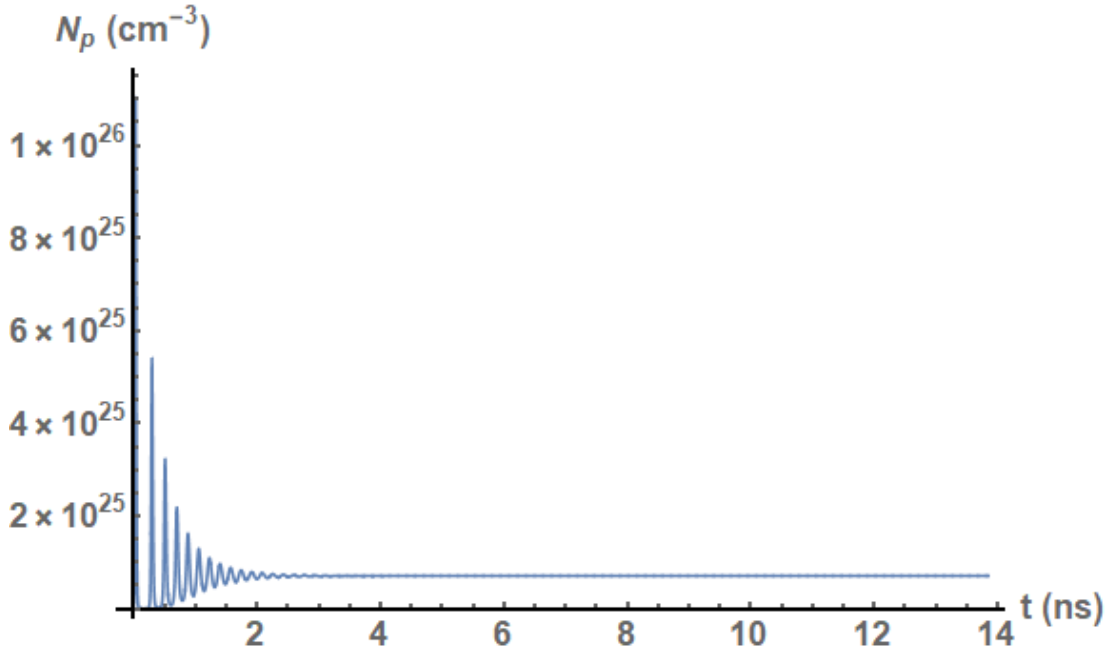


Figure 1.9: Time trace of  $N_p$  from solving Eqn. 1.1-1.2. Here the gain is assumed linear, using the expression in Eqn. 1.4. The parameters used are  $\Gamma = 0.8$ ,  $a = 5.34 \times 10^{-16} \text{ cm}^2$ ,  $\tau_p = 2.77 \text{ ps}$ ,  $\beta = 1$ ,  $\tau_r = 2.71 \text{ ns}$ ,  $I = 2 \text{ mA}$ ,  $e = 1.6 \times 10^{-19} \text{ C}$ ,  $V = 4 \times 10^{-12} \text{ cm}^2$  and  $\tau_n = 1.57 \text{ ns}$ .

The basic laser equations can also be used to simulate an LI curve of a laser. Here the power output,  $N_p$ , is tracked while varying the current,  $I$ . An example of this can be seen in figure 1.10. As mentioned previously, for low current there is not enough gain to overcome the losses of the system and there is a low power output. At a certain current value the losses are overcome and the power now increases dramatically with increasing current. This is called the threshold current.

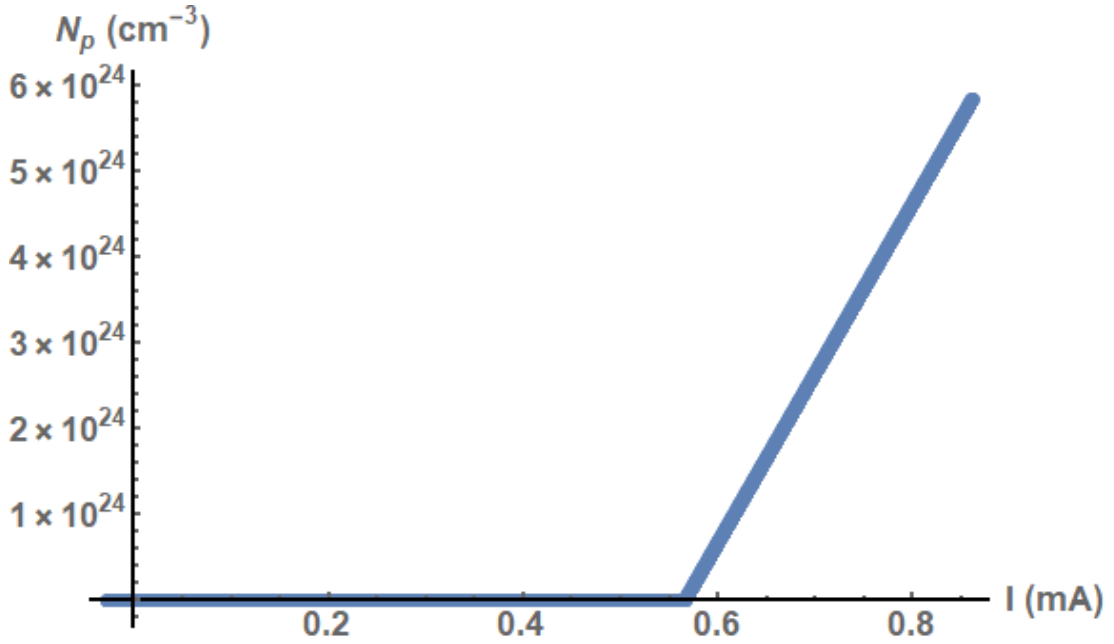


Figure 1.10: A simulated IV curve, tracking the steady state value of  $N_p$ , from Eqn. 1.1 vs. injected current,  $I$ . The parameters used are  $\Gamma = 0.8$ ,  $a = 5.34 \times 10^{-16} \text{ cm}^2$ ,  $\tau_p = 2.77 \text{ ps}$ ,  $\beta = 1$ ,  $\tau_r = 2.71 \text{ ns}$ ,  $e = 1.6 \times 10^{-19} \text{ C}$ ,  $V = 4 \times 10^{-12} \text{ cm}^2$  and  $\tau_n = 1.57 \text{ ns}$ .

### 1.4.2 Types of semiconductor lasers

A number of laser types and designs exist in semiconductor lasers to meet the needs of those designing systems. Here, each shall be outlined and discussed before introducing the lasers considered in this thesis.

#### 1.4.2.1 Fabry-Pérot (FP) Laser

The FP laser is the most basic of laser designs, and the schematic of one can be seen in figure 1.11. The lasing cavity has a cavity of length  $L_{fp}$ , and the required reflectors are provided by the air-material interface (facet) at the ends of the cavity. These are not highly reflective, this can be calculated using the Fresnel equation for normal incidence (Eqn. 1.6). Assuming the refractive index of the material,  $n_1 = 3.5$  and using the refractive index of air,  $n_2 = 1$ , gives a reflectance of  $R = 0.3$ .

$$R = \left| \frac{n_1 - n_2}{n_1 + n_2} \right|^2 \quad (1.6)$$

But the high gain of the semiconductor material overcomes this to achieve laser threshold.



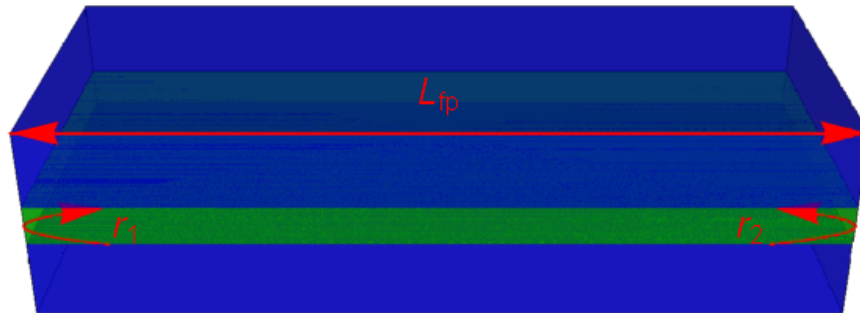


Figure 1.11: Schematic of a basic FP laser. Here the lasing cavity of length  $L_{fp}$ , uses the air-material interface to provide reflectivities  $r_{1,2}$ .

The mirrors of the FP laser are not frequency selective, so a broad range of wavelengths can be outputted. The allowed output wavelengths are dictated by the Fabry P rot resonances of the cavity. The Airy functions of a Fabry P rot interferometer with low reflectivity mirrors are quite broad as seen in figure 1.12. The broadness of these resonances combined with the gain profile of the semiconductor material means a highly multi-wavelength output is achieved.

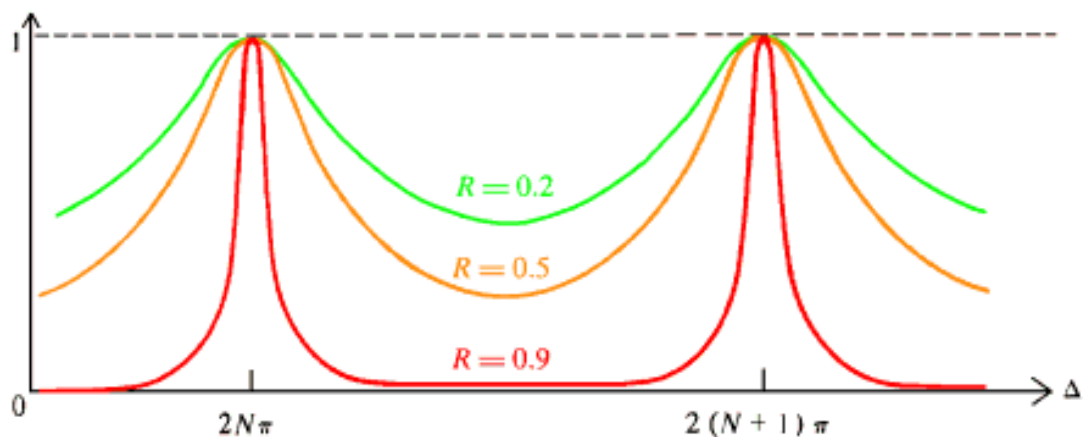


Figure 1.12: Airy functions of Fabry P rot resonators with different reflectivities,  $R^9$ .

### 1.4.2.2 Distributed Bragg grating (DBR) laser

A DBR laser is one where at least one of the mirrors on either end of the cavity is replaced by a grating type reflector, as can be seen in figure 1.13.

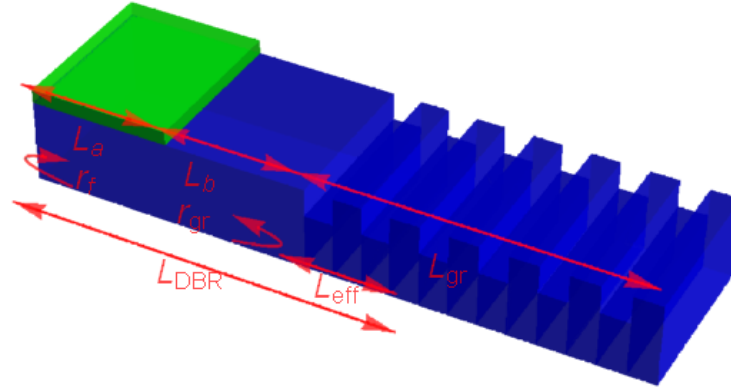


Figure 1.13: Schematic of a DBR laser. The device contains a gain section of length  $L_a$ , a phase section of  $L_b$  and a grating of length  $L_{gr}$ . This has an effective length of  $L_{eff}$  and a reflectivity of  $r_{gr}$ . On the other side of the device there is a facet, providing a reflectivity of  $r_f$ . The length  $L_{DBR}$  is an indication of the length of the resonant cavity of the light emitted.

In general a grating is a periodic array of index variations. At a specific frequency, called the Bragg frequency the period of the grating is half the average optical wavelength of the material. A high number of small reflections can combine to form a high reflectivity grating and at the Bragg frequency, these reflections add up in phase. The cascading nature of small reflections provides what is called an effective length. This is the distance away from the start of the grating a single reflector of reflectivity equal to the total reflectivity of the grating, would need to be placed to provide a reflector of equal characteristics. This effective length is highlighted in figure 1.13. Combining this with the length of the active region and phase region give the length of the DBR. The nature of the grating is that any frequency away from Bragg frequency, does not combine in phase in the grating, and will not reflect off the grating.

### 1.4.2.3 Distributed feedback (DFB) laser

A DFB laser is similar to a DBR, but rather than having the gain section and grating reflector in separate sections, these are incorporated in the same

section, as seen in figure 1.14. The grating is similarly designed as in the DBR, requiring a period of half the Bragg frequency. The central perturbation of the grating can be  $\lambda/4$  or  $\lambda/2$  for what are called "standard" and "shifted" DFBs respectively.

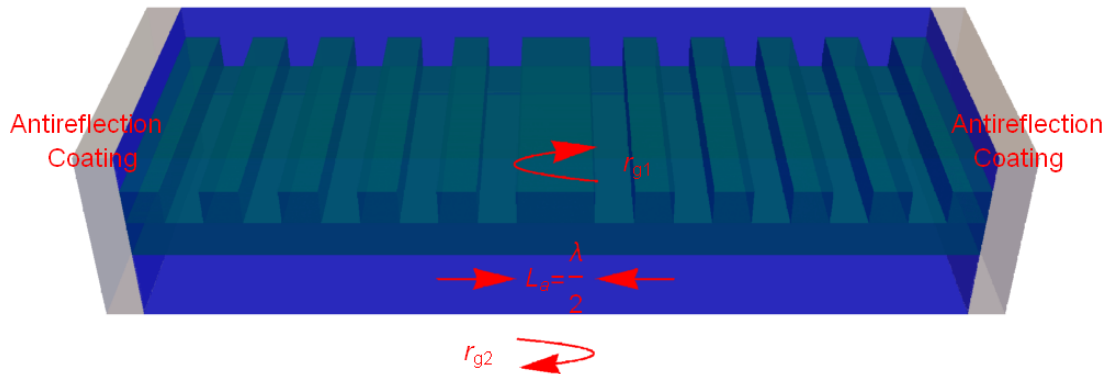


Figure 1.14: Schematic of a DFB laser. The active region of the laser is fabricated to have the grating profile. This is a "shifted" DFB, as at the centre there is a perturbation twice the size of a normal grating perturbation i.e.  $\lambda/2$ . The ends are coated with anti-reflection coating to encourage the light to exit the cavity, as the grating provides the internal feedback needed to cause lasing.

#### 1.4.2.4 Vertical cavity surface emitting laser (VCSEL)

The VCSEL laser is essentially a DBR rotated  $90^\circ$ . The active region has a "grating" vertically above it, here the layers are two alternating layers of varying refractive index, which have to be accurately grown to be  $\lambda/4$  thick for the stack to act as a reflective Bragg grating. This alternating layer structure provides very high reflectivity. This vertical design trades off the single axial-mode operation in favour of this high reflectivity. The reflectivity of one of the gratings is made higher by either including more layers, or putting a metal coating at the end of the stack. This encourages light to be emitted from the other end of the device. A schematic of a VCSEL can be seen in figure 1.15.

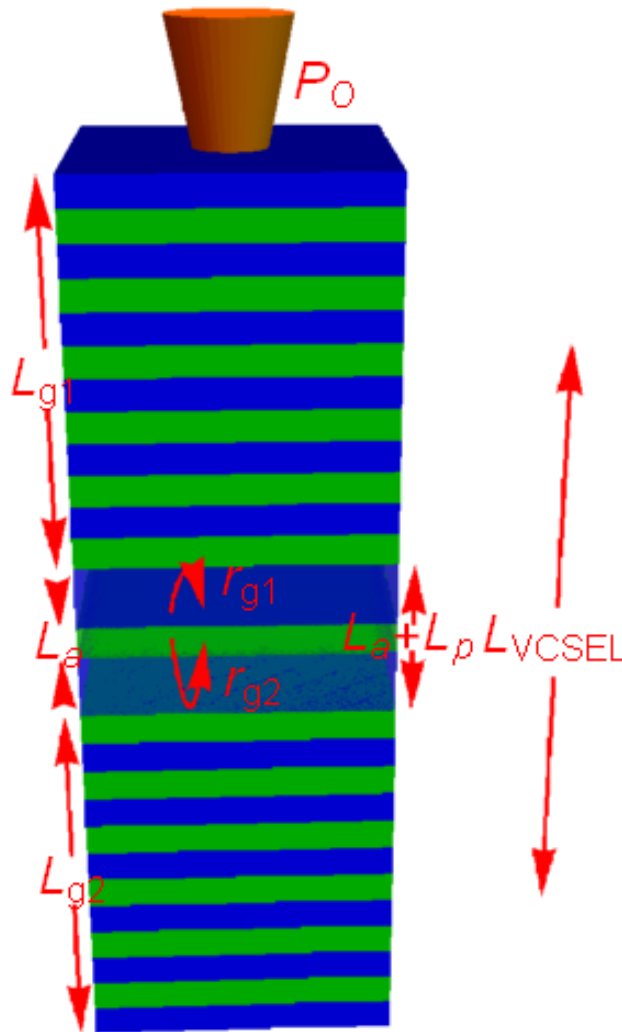


Figure 1.15: Schematic diagram of a VCSEL. Here the active region of width,  $L_a$  is surrounded by two passive regions of length  $L_p$ , this is then surrounded by stacks of layers of alternating refractive index, forming a grating. Each grating has a physical length of  $L_{g1,2}$  but an effective length of  $L_{eff1,2}$  and a reflectivity  $r_{g1,2}$ .

#### 1.4.2.5 Slotted Fabry-Pérot (SFP) Laser

The SFP laser is an advancement on the basic FP laser, where rather than using the facet reflections to define the lasing cavity, an extra section containing periodic etches replaces the cleaved facet(s). The schematic of this can be seen in figure 1.16. This works by modulating the FP modes, where the slots form weakly coupled subcavities[2]. An effective layout of the slots results in single wavelength emission and variation of the current applied to the different sections (as defined by the slots) provides fine tuning of this wavelength.

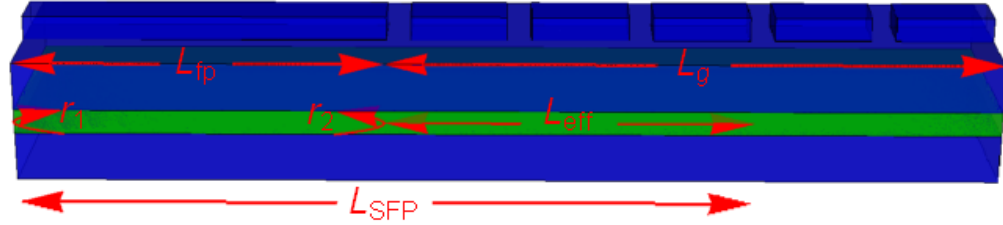


Figure 1.16: Schematic of a SFP laser. The gain section has a length of  $L_{fp}$ , the section with a series of etched slots acts as a grating of length  $L_g$  and provides a reflectivity of  $r_g$ , with an effective length of  $L_{eff}$ .  $r_1$  is the reflectivity provided by the facet.

## 1.5 Introduction to injection locking

An interesting process using lasers that is utilised in photonics is what is called injection locking of lasers. Here the output of one laser, referred to as a master, is injected into a second laser, referred to as a slave, through what is called an optical isolator. This isolator only allows light to pass in one direction, so no light is fed back into the master. If the frequencies of the two lasers are close enough, and the sufficient power reaches the slave from the master, the two lasers will both lase and the frequency of the master, with a suppression of all side modes in the slave. Both lasers also then have a fixed phase relation. This feature is used as an optical filter in many photonic processes, able to pick out a desired frequency from a range of signals, while suppressing any unwanted frequency. Injection locked lasers can also be used in signal generation [3] and in WDM [4] for example.

Injection locked lasers have been extensively studied, both theoretically and experimentally [5]. There was motivation to study this so extensively using theoretical methods because this is an example of a driven complex harmonic oscillator, where any theoretical results can be tested on a real world system. This allows for confirmation of results. The model used can be seen in Eqn. 1.7-1.8. This differs from the previous rate equation model by describing the complex electric field  $E$  instead of the photon density. This give a more complete model allow for a description of the phase behaviour of the laser,

rather than just the intensity.

$$\dot{E} = k + \left[ \frac{1}{2}(1 + i\alpha)n - i\omega \right] E \quad (1.7)$$

$$\dot{n} = -2\Gamma n - (1 + 2Bn)(|E|^2 - 1) \quad (1.8)$$

Here  $\alpha$  is the linewidth enhancement factor which describes the change in refractive index with injected carriers at a given frequency,  $\Gamma$  is the ratio of the photon lifetime to the carrier lifetime,  $B = \frac{\omega_R \tau_p}{2}$  ( $\omega_R$  is the frequency of the ROs and  $\tau_p$  is the photon lifetime). The bifurcation parameters (the parameters that cause a qualitative change in behaviour) of interest in this model are the injection strength  $k$  and the frequency detuning of the master and the slave  $\omega$ . A common bifurcation diagram of this system can be seen in figure 1.17, [5].

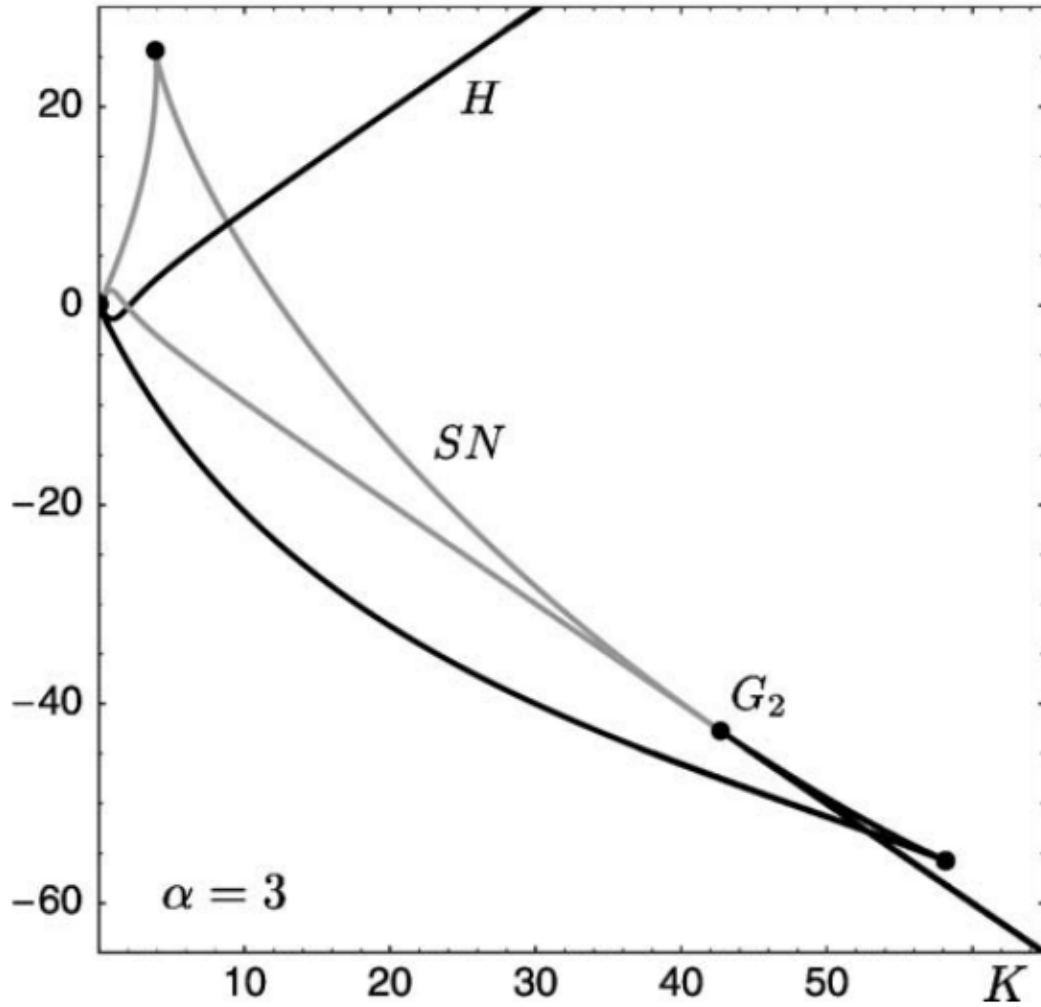


Figure 1.17: Bifurcation diagram of the injected slave case from Eqn. 1.7-1.8 in the  $(\omega, k)$  space. The Hopf bifurcation is by  $H$  and the saddle-node is denoted by  $SN$ . The points that these bifurcations intersect at two codimension-two saddle-node-Hopf points  $G_1$  and  $G_2$ .

The Hopf bifurcations defines a width around the zero detuning mark where the two lasers are in stable locked behaviour. Outside the two hopf lines ( $H$ ), the system is in an oscillatory behaviour. The width of this region between the Hopf lines, in the  $\omega$  parameter, is defined as the locking range and dictates how far the lasers can be apart in terms of frequency for locking to occur. This width increases as more power is injected into the slave by the master, i.e. higher  $k$ . One can also observe that there is an asymmetry in the locking width, i.e. not the same for positive and negative detuning. This is because of the  $\alpha$  parameter. The saddle-node bifurcation creates extra steady state solutions. Within the grey triangle formed by the saddle-node bifurcation line

(SN), there are two fixed point solutions. More complicated dynamics have been reported as the lasers approach locking behaviour where the system will undergo period doubling bifurcations, to produce more complex oscillations, and even generate windows of chaotic behaviour [5].

## 1.6 Introduction to mutually coupled lasers

This model has been used and tested against experimental evidence extensively and has provided good agreement. However when the optical isolator is removed this model is no longer valid as there is now light being fed back into the master laser as well. This is what is referred to as the mutually coupled regime. In monolithic integration a viable optical isolator does not exist. Therefore any system that was realised using injection locked lasers as a filter, now become a mutually coupled system. This is the main motivation behind this thesis: a desire to understand this mutually coupled arrangement of lasers on the short separation scale commonly associated with PICs (100s of  $\mu\text{m}$  to  $\text{mm}$ ). This will mainly be done through experiments on specially designed devices containing mutually coupled pairs of lasers and comparing this with a bifurcation study of different models attempting to describe this short separation interaction.

### 1.6.1 Formal definition of the bifurcation parameters in the mutually coupled arrangement

Throughout this thesis there are recurring parameters of interest that will be used in bifurcation studies. Here these will be formally defined to allow for easier future reference.

- **Injection strength/Coupling strength** -  $\eta$  - This is the percentage of light reaching one laser from the other. Depending on the experimental arrangement considered this can vary from 1 – 2% to 40 – 50%. When using a set of discrete semiconductor lasers coupled through a series of lenses the coupling is inherently low. But when both devices are fabricated on the same chip, separated by a short waveguide section (on the order of  $\text{mm}$ 's), a higher proportion of the light will reach the other laser. It is possible to have an asymmetric coupling, i.e. a higher percentage of power from one laser reaches the other laser than the opposite direction. This is however neglected in the photonic integrated



circuit (PIC) environment, as it requires the use of a Faraday rotator, which has not been realised in our integrated platform.

- **Coupling phase/Phase difference** -  $\phi$  - This is the phase difference between the laser related to the propagation between the lasers. This can be expressed mathematically by

$$\phi = 2\pi(D \bmod(\lambda_0)) \quad (1.9)$$

Here the optical path length between the lasers,  $D$ , is written in modulo of the single mode emission wavelength,  $\lambda_0$ , then multiplied by  $2\pi$ . This is a trivial calculation when the lasers are coupled via a passive element, as the optical path length is unchanging. In the integrated environment it is more complex as the refractive index of the active material is voltage dependent. Changes in this voltage, alters the optical path length.

- **Frequency detuning** -  $\delta$  - This is the difference in frequency between the main modes of the laser, and is defined as  $\delta = \omega_1 - \omega_2$ , where  $\omega_{1,2}$  are the frequencies of the two lasers. The main model used assumes both lasers are single moded, i.e. emit at a single frequency, which allows the definition of this single frequency difference. Experimentally, to measure the quality of how single moded a laser is, the side mode suppression ratio (SMSR) is measured. This is the difference between power between the highest power frequency peak in the optical spectrum and the next highest peak. An acceptable value when seeking single mode emission is an SMSR of approximately 30dB.

In the next section a background introduction to bifurcations will be introduced, and a description of the common bifurcations that will be discussed throughout the thesis. After this a formal definition of the bifurcation parameters being considered will be presented.

## 1.7 Breakdown of bifurcations observed

A bifurcation is when a change in a parameter of a system causes a topological change in the behaviour of that system. If a system of differential equations is given by  $\frac{dx}{dt} = f(\bar{x}(t))$ , where  $\bar{x}(t)$  is a vector of variables and  $f$  is system of equations. To study these bifurcations the steady states of the system is established, i.e. values of  $\bar{x}(t)$  for which  $f(\bar{x}) = 0$ . The Jacobian matrix is then

found by evaluating the derivatives of  $f(\bar{x})$ . Note all definitions, equations and diagrams in this section come from a seminal text in the area of non-linear dynamics [6].

$$A = \begin{bmatrix} \frac{df_1}{d\bar{x}_1} & \cdots & \frac{df_1}{d\bar{x}_n} \\ \vdots & \ddots & \vdots \\ \frac{df_n}{d\bar{x}_1} & \cdots & \frac{df_n}{d\bar{x}_n} \end{bmatrix}$$

Next the Jacobian is evaluated at the steady state values of  $\bar{x}(t)$  and the eigenvalues of this matrix is found using a characteristic equation derived from equation 1.10.

$$\text{Det}[\lambda I - A] = 0 \quad (1.10)$$

This forms an equation dependent on the parameters in the model  $\xi(\lambda, \nu)$ , where  $\nu$  is the parameter of interest. Solving the characteristic equation for  $\lambda$  for a given parameter value, the stability of the solution can be determined based on the sign of  $\lambda$ . If  $\lambda$  is  $> 0$  the solution is unstable and if it is  $< 0$  the solution is stable. The form of  $\lambda$  governs what kind of bifurcation is encountered. Each bifurcation has a different topological change associated with it. These are the bifurcations of the steady states, or where  $f(\bar{x}) = 0$ . There also exist bifurcations of periodic behaviours. A periodic solution is defined by  $f(\bar{x}) = f(\bar{x} + T)$  for  $T$  being some real number. Here a different approach must be used to analyse the stability of the solutions and find the bifurcations. If the system  $f(\bar{x})$  is an  $n$ -dimensional system,  $S$  is defined to be an  $n - 1$  dimensional surface, which is transverse to the solution, as outlined in figure 1.18.

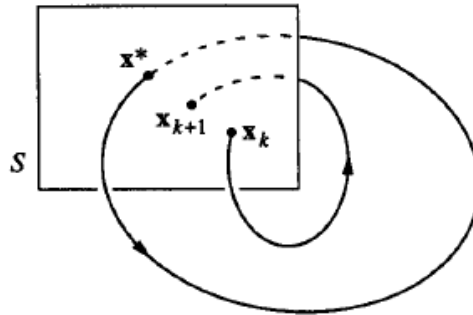


Figure 1.18: Example of periodic orbits,  $\bar{x}_k$ , intersecting with the transverse surface,  $S$ , after one rotation at  $\bar{x}_{k+1}$ . The fixed point,  $\bar{x}^*$ , meets itself after one rotation.

The Poincaré map,  $P$  is a mapping from  $S$  to itself, by following the solutions from one intersection with  $S$  to the next. If  $\bar{x}_k \in S$  is the  $k$ th intersection, then the Poincaré map is defined by:

$$\bar{x}_{k+1} = P(\bar{x}) \quad (1.11)$$

For fixed points  $P(\bar{x}^*) = \bar{x}^*$ , or starting at  $\bar{x}^*$ , the solution will return to  $\bar{x}^*$  after some time  $T$ , forming a closed orbit. Analysis of  $P$  near fixed points can give the stability of the associated closed orbit. Essentially the Poincaré map converts the problem from analysing periodic orbits, to analysing fixed points of a mapping.

If a fixed point is perturbed by adding an infinitesimal amount  $\nu_0$ , such that  $\bar{x}^* + \nu_0$  is in  $S$ , then after one return to  $S$ :

$$\bar{x}^* + \nu_1 = P(\bar{x}^* + \nu_0) \quad (1.12)$$

This expression is then expanded:

$$\bar{x}^* + \nu_1 = P(\bar{x}^*) + [DP(\bar{x}^*)]\nu_0 + O(||\nu_0||^2) \quad (1.13)$$

This process results in the matrix  $DP(\bar{x}^*)$  called the linearised Poincaré map at  $\bar{x}^*$ . Because  $\bar{x}^* = P(\bar{x}^*)$  this results in:

$$\nu_1 = [DP(\bar{x}^*)]\nu_0 \quad (1.14)$$

If it is assumed that the higher order terms  $O(||\nu_0||^2)$  are negligibly small. The stability is analysed by the eigenvalues of  $DP(\bar{x}^*)$ ,  $\lambda_j$ . The solution is stable if  $|\lambda_j| < 1$  and unstable if  $|\lambda_j| > 1$  for all  $j$ . Bifurcations occur when the largest eigenvalue  $|\lambda_m| = 1$ . These eigenvalues are referred to as Floquet multipliers. As they can be complex, to analyse the bifurcations a unit circle in the complex domain is usually considered, and how the eigenvalue crosses this circle defines the bifurcation.

Below is a breakdown of the common bifurcations that were observed throughout this study, what change they cause and the associated eigenvalue form.

### 1.7.1 Saddle-Node bifurcation

The saddle node bifurcation is the most basic bifurcation and is simply how fixed points are created and destroyed. The most basic equation to demonstrate this bifurcation is:

$$\dot{x} = r + x^2 \quad (1.15)$$

Figure 1.19 shows the different solutions of  $x$  for varying  $r$ . For  $r < 0$  there is an unstable and stable fixed point, these collide and annihilate at  $r = 0$ , and no solutions exist for  $r > 0$ .

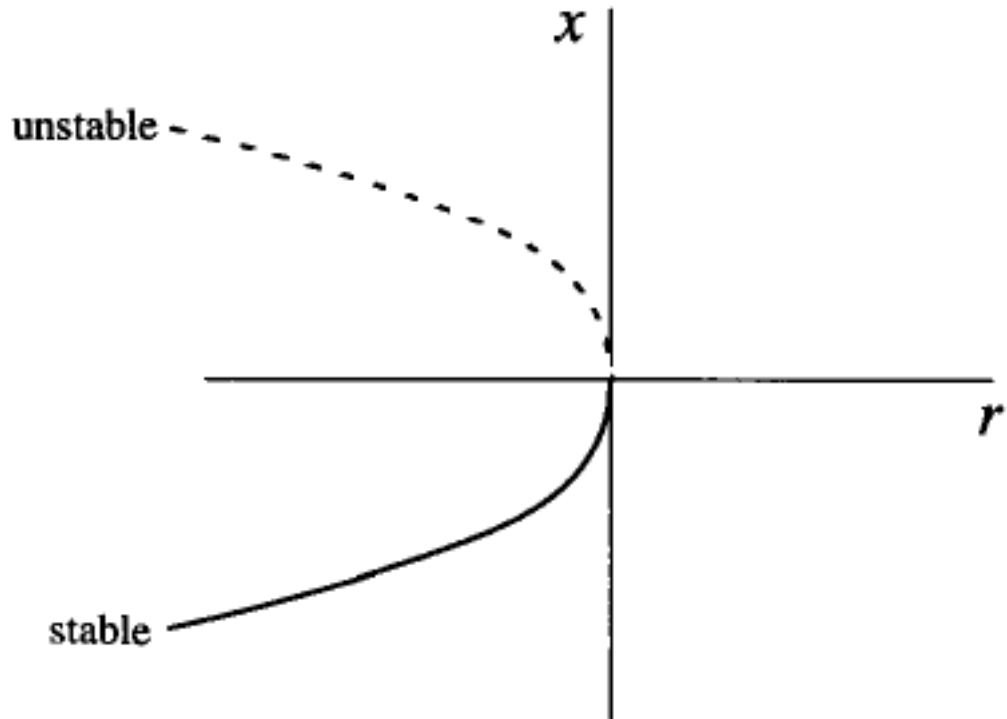


Figure 1.19: Example of a saddle-node bifurcation, showing the solutions of Eqn. 1.15 for varying  $r$ . Solid lines are stable solutions and dashed lines are unstable.

This bifurcation occurs when there is a zero eigenvalue of the characteristic equation 1.10. There also exists a saddle-node bifurcation of cycles, similar to this case with fixed points, where limit cycles collide and annihilate. This is also referred to as a fold bifurcation.

### 1.7.2 Pitchfork Bifurcation

The pitchfork bifurcation is similar to the saddle-node however the solution is not destroyed when the two solutions collide. Instead they create a single solution. This bifurcation has a supercritical and subcritical variant. The supercritical variant is exhibited by the equation:

$$\dot{x} = rx - x^3 \quad (1.16)$$

As shown in figure 1.20, for  $r < 0$  a single stable solution exists, at  $r = 0$  two new stable solutions are created at the original stable solution becomes unstable.

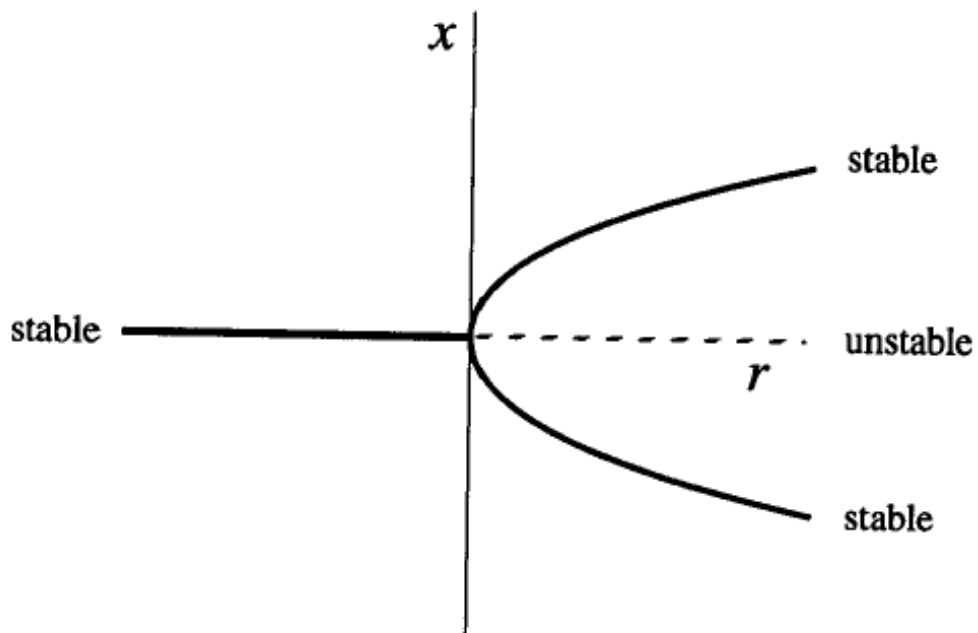


Figure 1.20: Example of a supercritical pitchfork bifurcation, showing the solutions of Eqn. 1.16 for varying  $r$ . Solid lines are stable solutions and dashed lines are unstable.

A subcritical pitchfork bifurcation can be demonstrated using:

$$\dot{x} = rx + x^3 \quad (1.17)$$

The solutions of this equation can be seen in figure 1.21. When  $r < 0$  one stable solution is surrounded by two unstable solutions, as  $r$  is increased these solutions collide at  $r = 0$  and for  $r > 0$  a single unstable solution exists.

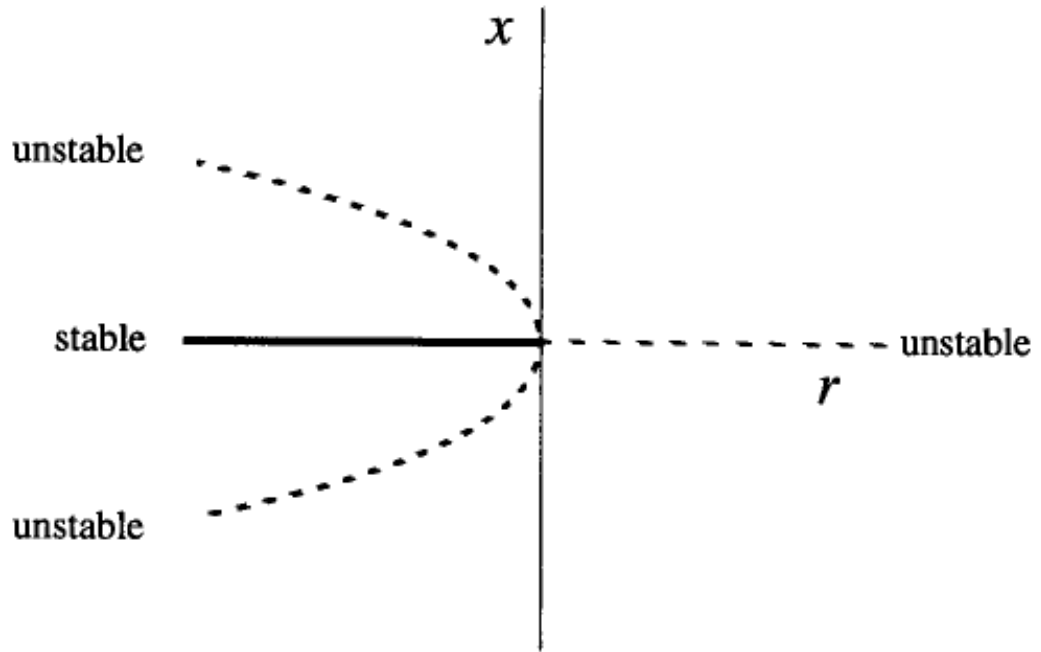


Figure 1.21: Example of a subcritical pitchfork bifurcation, showing the solutions of Eqn. 1.17 for varying  $r$ . Solid lines are stable solutions and dashed lines are unstable.

This bifurcation also occurs when there is a zero eigenvalue of the characteristic equation 1.10.

### 1.7.3 Hopf bifurcation

This bifurcation is associated with the birth and death of oscillations as a parameter is varied. This bifurcation occurs when the eigenvalue  $\lambda$  is purely imaginary, i.e. of the form  $\lambda = i\Omega$ . For example in the system:

$$\dot{r} = \mu r - r^3 \quad (1.18)$$

$$\dot{\theta} = \omega + br^2 \quad (1.19)$$

When  $\mu < 0$  the system is in a stable fixed point behaviour at  $r = 0$ , where nearby values spiral down to this point, however when  $\mu > 0$  a stable limit cycle appears, where the origin now becomes unstable and now spirals towards the stable limit cycle. This is called a supercritical Hopf bifurcation and is demonstrated in figure 1.22

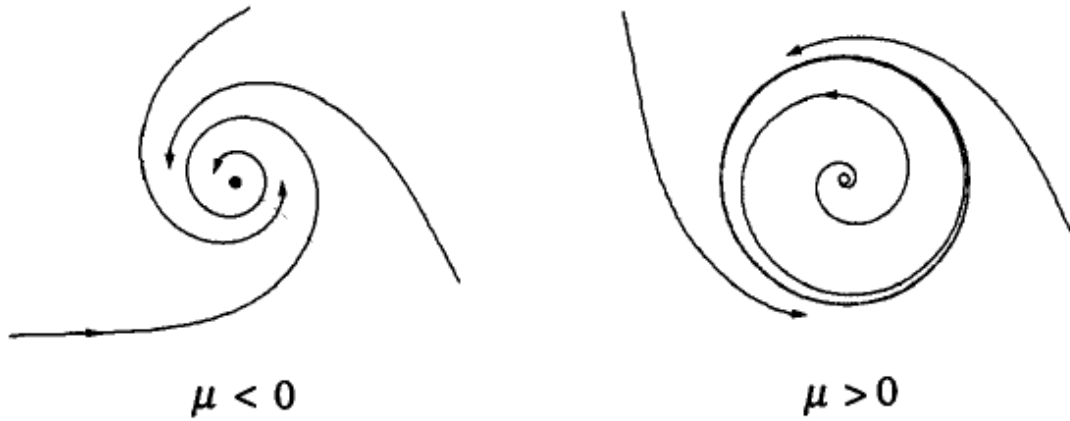


Figure 1.22: Example of a supercritical Hopf bifurcation showing phasor diagrams of Eqn. 1.18 and 1.19 for  $\mu < 0$  (showing a stable fixed point) and  $\mu > 0$  (showing a stable limit cycle). The Hopf bifurcation occurs at  $\mu = 0$ .

A subcritical variant can be exhibited by adjusting Eqn. 1.18 and 1.19 to:

$$\dot{r} = \mu r + r^3 - r^5 \quad (1.20)$$

$$\dot{\theta} = \omega + br^2 \quad (1.21)$$

Now when  $\mu < 0$  There is a stable fixed point at the origin and a stable limit cycle, with an unstable limit cycle between them. As  $\mu$  is increased the stable fixed point and unstable limit cycle collide and makes an unstable fixed point. This forces solutions that were at the fixed point to suddenly jump to the only remaining attractor feature, the stable limit cycle. This process is demonstrated in figure 1.23.

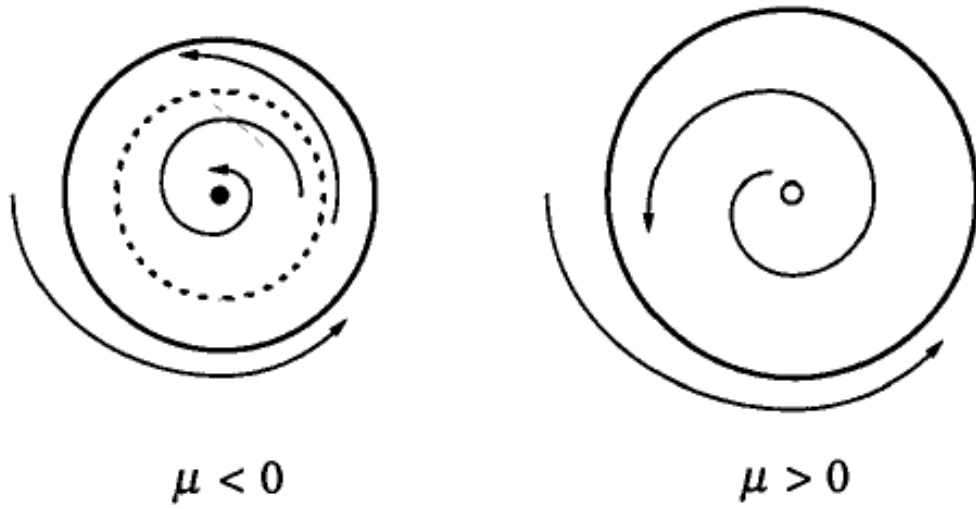


Figure 1.23: Example of a subcritical Hopf bifurcation showing Phasor diagrams of Eqn. 1.20 and 1.21 for  $\mu < 0$  (showing a stable fixed point and stable limit cycle, with an unstable limit cycle between them) and  $\mu > 0$  (showing a stable limit cycle and an unstable fixed point). The Hopf bifurcation occurs at  $\mu = 0$ .

This bifurcation occurs when there is a purely complex pair of conjugate eigenvalues of the characteristic equation 1.10.

#### 1.7.4 Period-doubling bifurcation

This is a bifurcation of limit cycle behaviours, unlike those previously discussed, and its presence is found through the analysis of the Floquet multipliers. This bifurcation causes the system to switch to a new behaviour with twice the period of the original periodic solution. It occurs when one real Floquet multiplier crosses the complex unit circle at  $-1$  on the real axes as seen in figure 1.24. This can also be referred to as a flip bifurcation.



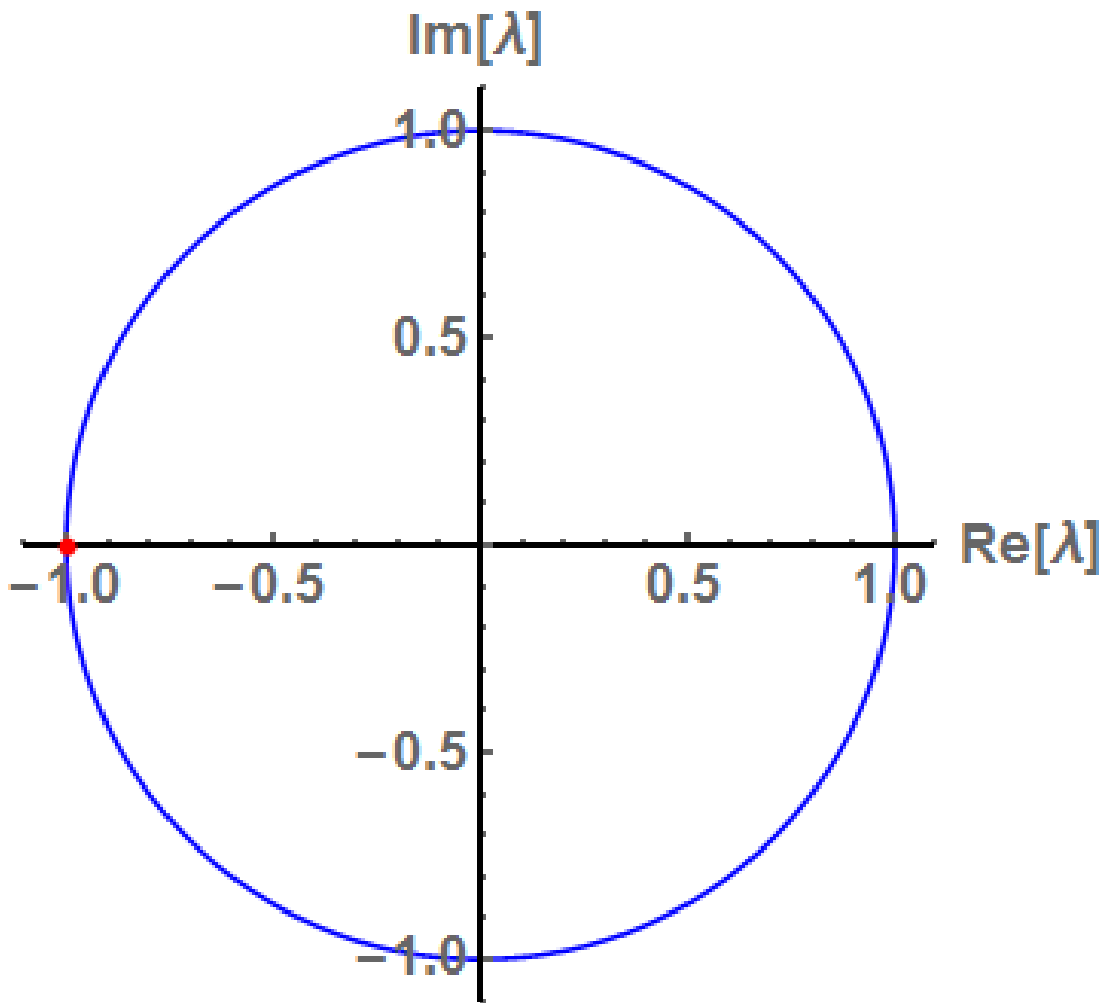


Figure 1.24: Unit circle in the complex plane, with a red dot highlighting the eigenvalue causing a period-doubling bifurcation

### 1.7.5 Torus bifurcation

A torus bifurcation is when a two-dimensional invariant torus is formed from the original limit cycle, as seen in figure 1.25. This bifurcation occurs when there are a pair of complex conjugate Floquet multipliers,  $\lambda_{1,2} = e^{\pm i\theta_0}$ . An example of the pair of eigenvalues on the unit circle can be seen in figure 1.26. This bifurcation is also called a Neimark-Sacker or secondary Hopf bifurcation.



Figure 1.25: Example of a torus formed by a torus bifurcation.

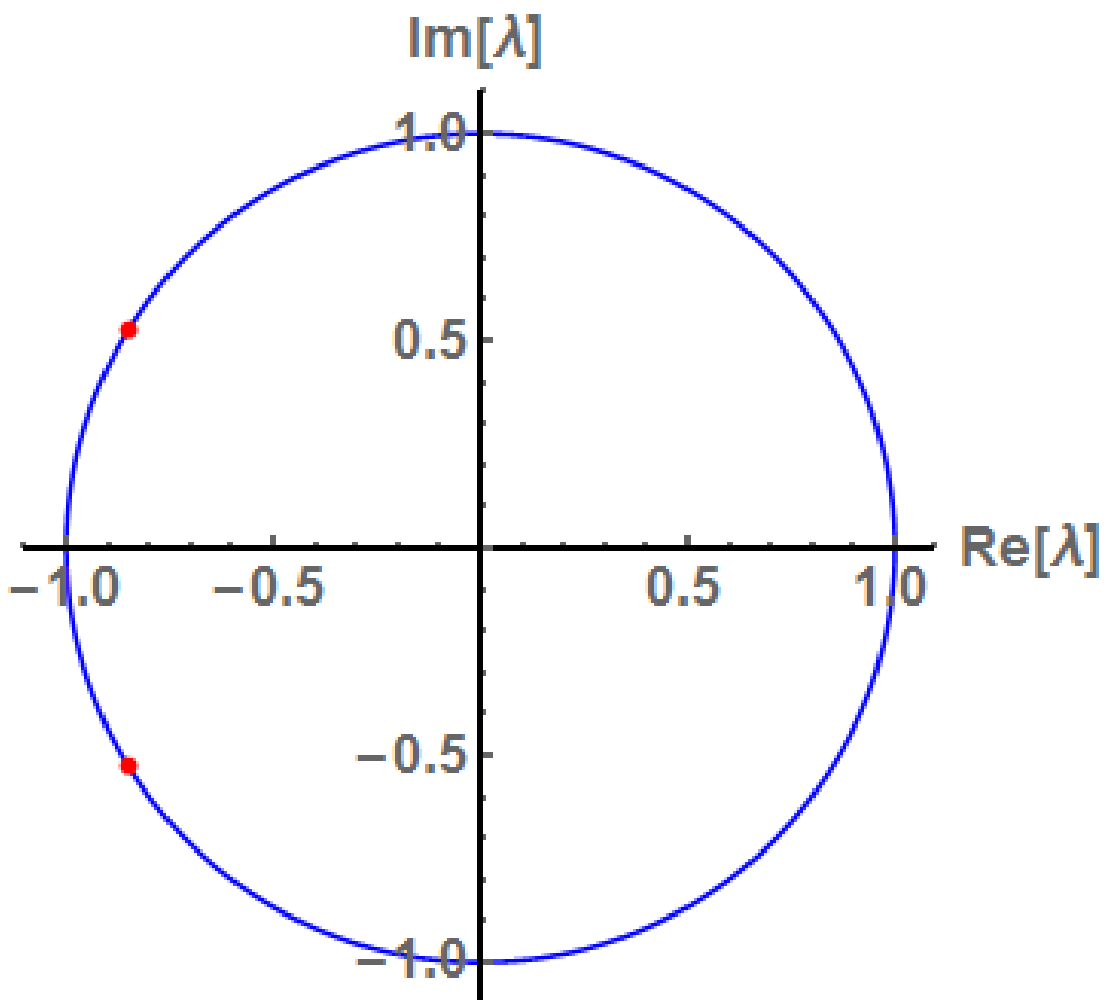


Figure 1.26: Unit circle in the complex plane, with red dots highlighting the eigenvalues causing a torus bifurcation.

In the next chapter a literature review of previous seminal works in the area of mutually coupled semiconductor lasers will be presented. Starting with previously reported experiments and then following this the seminal

theoretical works will be discussed. This will then be used to highlight the novelty of the work undertaken in this thesis.

## **Chapter 2**

### **Literature review**

This thesis is comprised of three distinct approaches to understanding how semiconductor lasers interact when mutually coupled on a single PIC and if the stable behaviour of master-slave injection locked lasers can be re-created on a PIC without on-chip optical isolation. This will allow integrated versions of systems that require a master-slave pair of injection locked lasers to be realised in our integrated platform. In this chapter an overview of previous work in this area is presented, which will provide a background and help to highlight the novelty of the research undertaken. Firstly a review of the limited experimental investigations of mutually coupled lasers on a PIC will be presented, followed by a brief review of injection locked semiconductor lasers. This is to highlight the differences and similarities between the uni-directional case of injection locking and the bi-directional case of mutual coupling. Finally the seminal theoretical studies of mutually coupled semiconductor lasers will be reviewed.

## 2.1 Experimental investigations of mutually coupled semiconductor lasers

There have been a variety of experiments carried out involving the mutual coupling of discrete semiconductor lasers, which have been free space coupled, or coupled through fibre. In one experiment, two commercially available single mode lasers were coupled using collimating lenses over a distance of 20 cm [7, 8]. The lasers were tuned to have the same output wavelength. This arrangement led to very low coupling between the lasers, with less than  $10^{-4}$  of the intensity of one laser reaching the other. This study demonstrated a form of local synchronisation, where one laser is forced to oscillate at the relaxation oscillation frequency of the other laser. A regime of self-initiated and self-sustained oscillations was also discovered.

In another work [9], the authors designed and fabricated two identical DFB lasers and coupled their optical fields via a system of lenses and beam splitters, which resulted in an optical path length of approximately 51 mm. The measured coupling strength was approximately 5%. This study focused on studying the effect of having a varying spectral detuning between the outputs of the lasers. It was found that for small detunings multi-stable compound laser modes were formed, which is where both lasers lock to an identical optical frequency, with stable emission. As detuning was increased, this stable

output was replaced with oscillatory behaviour. Interestingly it was discovered that the width of the locked regime was not symmetric in detuning, i.e. different width for positive and negative detuning.

An alternative way to create a pair of coupled lasers is to split a single output into two beams. This was done with an Ar-laser-pumped  $LiNdP_4O_{12}$  laser which was also modulated, to study the mutual coupling of modulated lasers [10]. In this particular experiment through the variation of the attenuation of one beam and the coupling distance, a regime of chaos synchronisation was discovered, where both laser's power fluctuate chaotically, but with a high level synchronicity. The level of synchronisation is measured through the calculation of what is called the correlation coefficient,  $\rho$ , using Eqn. 2.1. Here  $I_{A,B}^i$  are the instantaneous intensities of the two lasers. Values of  $\rho \geq 0.91$  were achieved in this investigation.

$$\rho = \frac{\sum^i (I_A^i - \langle I_A \rangle)(I_B^i - \langle I_B \rangle)}{\sqrt{\sum^i (I_A^i - \langle I_A \rangle)^2 (I_B^i - \langle I_B \rangle)^2}} \quad (2.1)$$

An experiment comparing bidirectionally coupled and unidirectional coupled laser yielded some interesting results [11]. Using commercially available semiconductor lasers coupled over a distance of 120 cm, the synchronisation of the lasers in the unidirectionally and bidirectionally coupled case was studied while varying self-feedback, coupling and detuning. It was found that the unidirectional case proved to be very sensitive to fluctuations in feedback and detuning while the mutually coupled case proved to have increased robustness to deviations in these parameters.

A regime of time delayed synchronisation has also been observed, where the lasers exhibit identical chaotic fluctuations, but one laser lags behind the other, by a time corresponding to the delay time between the lasers [12]. This was observed when two commercially available semiconductor lasers were coupled over a distance of one meter, with a coupling strength that was varied over a range of 0 – 6.6%. This time shifted dynamical regime has been reported elsewhere. In an experiment containing two discrete semiconductor lasers, with varying delay times between the lasers, (varying between 3.8ns and 5ns) and approximately 5% coupling strength the time series of each individual laser displayed time shifted chaotic oscillations [13]

Along with chaotic fluctuations, locked regimes have also been observed in

certain instances. Through the use of two distributed feedback (DFB) coupled over a distance of 51 mm, with weak coupling (1 – 2%), an area of stable compound laser mode (CLM) behaviour was found for low frequency detuning between the lasers, which transitioned to oscillatory behaviour for higher detuning [14].

Larger laser separations have also been studied. With a system of fibres and attenuators a distance of 12.6 m was introduced between two semiconductor lasers produced by Eblana Photonics [15]. This system also allowed a reasonably high maximum possible coupling of 40%. Through varying the pumping of the lasers a number of different dynamical regimes were observed, such as low frequency fluctuations (LFFs) and continuous wave (CW) operation for 1.02 times threshold. When the pump current was increased to 1.25 times threshold, more complex behaviours were observed such as chaotic emission and significant linewidth broadening.

The effect of asymmetric coupling between mutually coupled lasers has also been studied [16]. Through the use of Faraday rotators between two lasers, with a temporal separation of approximately 15 ns, the coupling from laser A to laser B can be made different to the coupling from laser B to laser A. Additionally laser B received self-feedback in this experimental arrangement. Similarly to previous studies, a regime of highly synchronised chaotic fluctuations was observed. The level of synchronicity was studied for varying feedback levels received by laser B and various levels of asymmetry of the coupling.

There have been a limited number of experiments involving semiconductor lasers fabricated on the same chip and mutually coupled. One such chip consisted of two, four section distributed Bragg reflector (DBR) lasers, fabricated to be side by side. The output of each laser were then combined through the use of a multi-mode interferometer, whose output port enters an angled semiconductor optical amplifier (SOA) section leading to the edge of the chip [17]. The cleaved facet reflection causes a small percent of the light to couple back, causing the mutual coupling. This resulted in a delay time of 30 ps between the lasers. The lensed fibre at the output also acts as an additional reflector to increase the coupling. By adjusting the detuning between the lasers, various non-linear phenomena were observed, such as four wave mixing (FWM), locking, period doubling and chaotic behaviour.

Another such device contained two monolithically integrated distributed

feedback (DFB) lasers in a face to face arrangement, separated by a  $400\text{ }\mu\text{m}$  phase section [18]. Similarly to the previous case, through the variation of the detuning various phenomena were observed such as FWM, locking, period 1 oscillations, quasi-periodic behaviour and chaos.

A third such study was reported, using a chip containing colliding pulse mode locked lasers coupled through an absorber [19]. Non-linear dynamics such as period-four, period-three and period-one limit cycles were observed when varying the pump current.

## 2.2 Theoretical investigations of mutually coupled semiconductor lasers

There have been many theoretical studies of mutually coupled lasers for various parameter regimes. Here the regimes covered and the dynamics reported will be highlighted. Table 2.1 gives a breakdown of the ranges of the critical bifurcation parameters of laser separation and frequency detuning of the MCLs in these studies. Following this, it will be highlighted how the research undertaken in this thesis, is in a parameter space which remains unreported. At this point it is important to define some nomenclature for when referring to the delay between the lasers. This separation will be compared to the photon lifetime of the laser cavities,  $\tau_p$ . A short delay refers to when the separation is on this time scale, while a long delay refers to a separation significantly longer, an order of magnitude longer.

Reference	Laser separation	Frequency difference ( $\delta$ )
Synchronization and Spontaneous Symmetry-Breaking in Symmetrically Delay-Coupled Semiconductor Lasers, T. Heil et al. [13]	$\approx 1.4\text{ m}$	0
Synchronization in Two Couple Nonidentical Semiconductor Lasers, A. Hohl et al. [7]	20 cm	0



Mutually Delay Coupled Semiconductor Lasers: Mode Bifurcation Scenarios, H. Erzgraber et al. [9]	51 mm	$\neq 0$
Synchronization Scenario of Two Distant Mutually Coupled Semiconductor Lasers, J. Mulet et al. [20]	1.2 m - 1.5 m	0
Anticipating Synchronization of Two Chaotic Laser Diodes by Incoherent Optical Coupling and its Application to secure communications, F. Rogister et al. [21]	6 m	0
Bifurcation to Square-Wave Switching in Orthogonally Delay-Coupled Semiconductor Lasers: Theory and Experiment, C. Massoller et al. [22]	0.9 m	0
Bubbling in Delay-Coupled Lasers, V. Flunkert et al. [23]	3 m	0
Chaos Synchronization and Encoding in Coupled Semiconductor Lasers of Multiple Modulated Time Delays, J. Hu et al. [24]	0.9 m and 1.5 m	0
Dynamics of Two Mutually Coupled Semiconductor Lasers: Instantaneous Coupling Limit, S. Yanchuk et al. [25]	0/1 – 2 mm	$\neq 0/0$
Symmetry Breaking and High-Frequency Periodic Oscillations in Mutually Coupled Laser Diodes, F. Rogister et al. [26]	7 mm	$\neq 0$
Dynamical Properties of Mutually Delayed Coupled Semiconductor Lasers, H. Erzgraber et al. [27]	21 mm/51 mm	$\neq 0$

Amplitude-Phase Dynamics Near the Locking Region of Two Delay-Coupled Semiconductor Lasers, H. Erzgraber et al. [28]	21 mm/51 mm	$\neq 0$
Mode Structure of Delay-Coupled Semiconductor Lasers: Influence of the Pump Current, H. Erzgraber et al. [29]	21 mm/51 mm	$\neq 0$
Dynamics of Two-Laterally Coupled Semiconductor Lasers: Strong and Weak-Coupling Theory, H. Erzgraber et al. [30]	21 mm/51 mm	$\neq 0$
Dynamics of Two Semiconductor Lasers Coupled by a Passive Resonator, H. Erzgraber et al. [31]	21 mm/51 mm	$\neq 0$
E. Clerkin [32]	0	0
M. Seifikar [33]	1 – 2 mm	0

Table 2.1: A breakdown of the range of delay times and detunings considered in each study of MCLs

Various experimental investigations in the previous section also contained theoretical studies to match the experiment. The time delayed chaotic synchronisation of two mutually coupled lasers (MCLs) was confirmed using a rate equation based model [13]. The synchronisation of two lasers coupled weakly over a distance of 20 cm observed experimentally, was also observed theoretically [7]. The same author in another publication also presented a numerical and analytical bifurcation study for varying the coupling strength between their lasers, which were separated by an optical path length of 20 cm. Different forms of synchronisation of the laser behaviours were documented.

In the study highlighted in the previous section that used a system of two discrete lasers separated by an optical path length of  $\approx 51$  mm a theoretical study along with the experimental investigation was provided [9]. Using their model they studied the CLMs of the coupled system; how they depend on the detuning of the lasers and the bifurcations that lead to their creation/destruction. The reporting of the experiment where semiconductor lasers were mutually coupled over a time delay of 4 – 5 ns, (which translates

to 1.2 – 1.5 m) also included a theoretical recreation of the time-delayed synchronisation [20].

There have also been various purely theoretical studies of MCLs in different arrangements. One particular study investigated the effect of having incoherent optical coupling between a pair of lasers [21]. The proposed schematic a transmitter laser's output was rotated  $90^\circ$  using a Faraday rotator and the beam was then split. One part was reflected back into the transmitter laser and the second part was injected into a receiver laser. This led to the transmitter laser receiving incoherent feedback and the receiver was subject to incoherent optical injection. The separation was on the order of 20 ns. As with other studies, excellent time delayed synchronisation between the chaotic power outputs of the lasers was observed. This synchronisation was then studied for having mismatched parameters in the model to test its robustness. The authors then propose using this system as a way of cryptographically encoding a data stream, by encoding a series of 1s and 0s on the chaotic output of one laser and using the time delayed matching signal as a cryptographic key to recover the bit-stream.

A similar study modelled the situation where two lasers were orthogonally coupled, and where the dominant transverse electric (TE) mode was rotated  $90^\circ$  before being coupled to the other laser [22]. This model produced a polarisation switch square wave in the output, the characteristics of which the authors studied along with the bifurcations associated with this regime.

A phenomena called bubbling in a system of MCLs, which is a noise induced desynchronisation, has also been reported [23]. This arises from LFFs or coherence collapse (CC) regimes of behaviour. The time delay in this MCL system was approximately 1000 times the photon lifetime.

In another work, the effect of extra time delay on a mutually coupled pair of semiconductor lasers was investigated [24]. The multiple delays were modulated to incur chaotic fluctuations in the lasers.

These studies have all focused on distantly coupled lasers. There have been some studies which are closer to the subject of concern of this thesis, where two lasers are coupled on a single device on a PIC. There are two main models used to model laser dynamics, a rate equation based model, using a modified version of a laser under feedback [34], or a composite cavity mode model based on Maxwell's equations, to create a wave equation type model [12].

This thesis is concerned with the rate equation based model. However there have been some studies of MCLs using the composite cavity model.

One such study presented results of this model for different regimes, such as weak coupling as well as the full general case [12]. The steady states of the model were found and characterised.

Another study using this wave equation based model has been reported, wherein a system of MCLs was proposed, which contained an air gap between the lasers, acting as a passive resonator [35]. The locking behaviour of the lasers and the influence of the separation and  $\alpha$  parameter on the behaviour of the system was presented. Finally the model was expanded to describe an array of three coupled lasers.

Using the rate equation based model several studies have been performed on short delay MCLs. One such study presented a study of the CLMs for zero and short separations (on the order of mm's) initially with no detuning, and then introduced detuning while assuming zero separation between the lasers. The author presents a study of the bifurcations of the CLMs under these conditions. When detuning was then included, a region of self-pulsations was studied for a small parameter range of the fixed phase difference between the lasers.

Another study focused on a longer separation between the MCLs of 7 mm, while also neglecting detuning [26]. The proposed arrangement also had inherently low coupling strength (from approximately  $10^{-4} - 0.16$ ), while also maintaining a fixed phase difference between the lasers. This study discovered periodic solutions, the breaking of their symmetry at low coupling and their high frequency at higher coupling.

In another study by the same author, the detuning and the coupling phase were made dynamic variables, and the model was studied by varying these parameters. The separation of the lasers considered was still approximately 7 mm. Similar to their previous study, the authors only considered very low coupling rates between the lasers, which never exceed a value of 0.1. The bifurcation study revealed a quasi-periodic route to chaos with some period doubling routes to chaos also existing. Periodic regions were also studied.

Erzgräber has performed a number of studies on short separation MCLs. In these studies the lasers are detuned, while various delay distances are considered, varying from 21 mm to 51 mm [27, 28, 29, 30, 31]. The arrangements considered had very low coupling strengths, with only

approximately 5% of light from one laser reaching the other. In these studies a detailed investigation of the CLMs and their bifurcations is shown.

Another approach to modelling short separation MCLs is to consider the delay time to be zero. A study which made this assumption proved the existence of one colour states along with two-colour states, while assuming zero frequency difference between the lasers. This work was then continued by Seifika [33], where short delay times were considered (on the order of mm's).

This thesis will focus on a detailed study of the one and two colour states of the model, when the laser separation is on the order of 100's of  $\mu$  m up to a couple of mm, with a frequency difference included between the lasers. High rates of coupling between the lasers will also be considered for these short delay times. Since both lasers are integrated onto the same chip a high percentage of the light can be coupled from one laser to the other. Furthermore the study will then proceed to develop a multi-mode model for MCLs and perform a bifurcation study on this new model. In each case a comparison with experimental work carried out on MCL devices will be shown, and how well these theoretical investigations re-create the dynamics observed in the experiment. This thesis will focus on the unexplored parameter region of short but non zero laser separation, on the order of a couple of mms, while including detuning. In the next chapter some initial experimental results from MCL pairs in a PIC will be presented. After this the next chapter will focus on theoretically studying the single mode model for the specified parameter range, along with a comparison with experimental results. In the last chapter a new model will be developed which simulate lasers that have multiple modes, rather than using the single mode assumption of all studies in MCLs mentioned previously.

## **Chapter 3**

# **Experimental Work**

## 3.1 Introduction

This study began by testing a series of MCLs on a PIC. It was hoped that by performing these experiments, insight would be given into the kind of dynamics present when mutually coupling lasers with very short time delays, while also providing context to physical values of parameters used within the model. These experiments were the first of their kind. Little was known of design flaws or restrictions in the PIC design, so initial designs were kept basic so as to set a baseline for future devices. These initial tests were as much about characterising the design as they were to test the mutual coupling of lasers on PICs. Each individual part of the device was characterised from the performance of the individual lasers, to the absorbing section between them, to the interaction of connected sections. First, the design of the devices will be outlined, and then characterisation results will be presented. Some results of coupling the lasers will be shown, followed by how design flaws were affecting the testing. Methods for overcoming these flaws will be proposed for future devices.

## 3.2 Device Design

To experimentally analyse MCL dynamics, various arrangements were designed on a PIC using a commercially available InP quantum well based material, designed for emission around  $1.55\ \mu\text{m}$ . The material was grown by a company called IQE and the exact layer epitaxial structure can be seen in Appendix A. The fabricated lasers were designed to be identical; however, the emission properties may change due to variations in process and fabrication parameters.

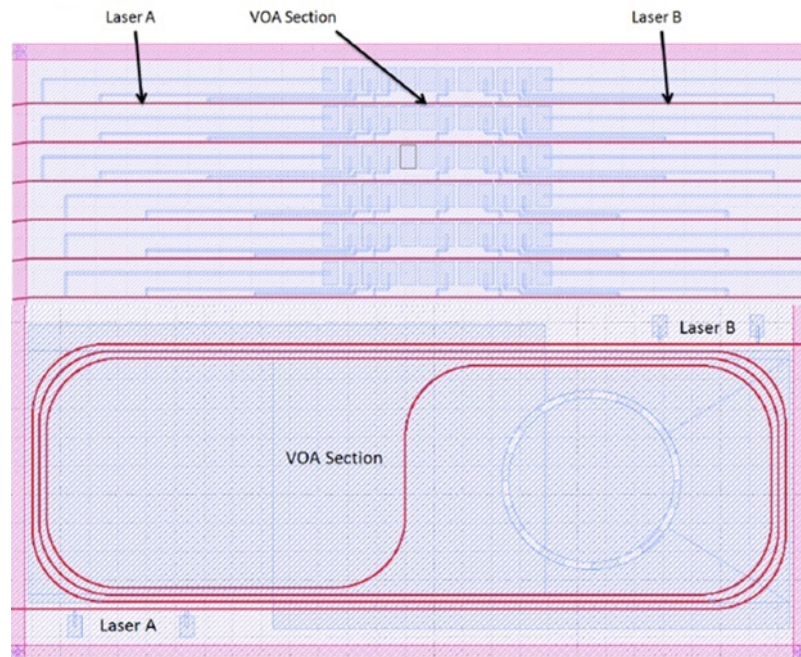


Figure 3.1: Schematic of the first generation MCL devices designed.

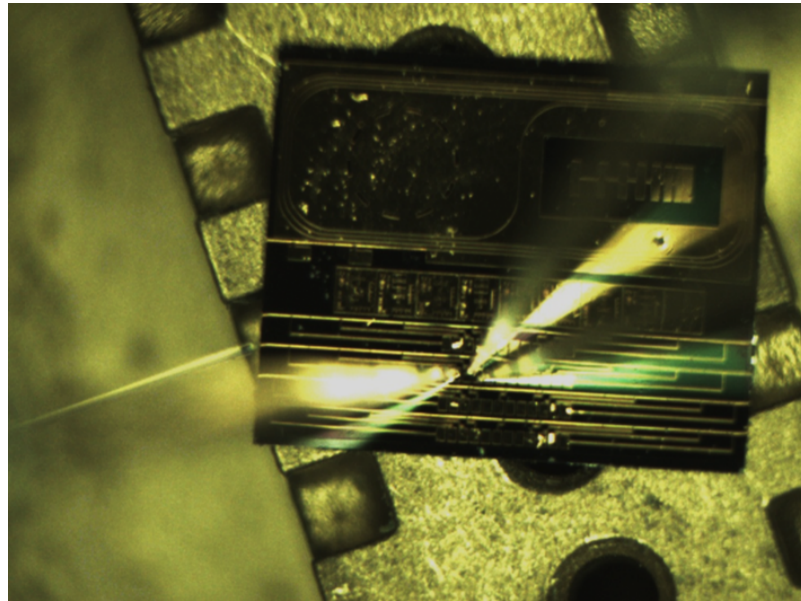


Figure 3.2: First generation MCL device under testing.

A schematic and a picture of the devices under test can be seen in figures 3.1 and 3.2 respectively. The mutually coupled laser pairs were separated using an active waveguide section that can be biased independently to control the attenuation, thus acting as a Variable Optical Attenuator (VOA). The material acts as a basic PIN junction, so by applying a reverse bias the structure can be made to absorb light. There was a concern that this waveguide section could



itself become an independent laser, or become a part of the lasing cavity. However steps were taken to avoid this. Firstly, the sections were kept short to limit the possible gain of the section. Secondly, only small forward biases ( $<1$  V) would be applied, hence inhibiting its ability to become an independent laser. Though this intermediate section is treated as a passive section, it would have more effects on this system, such as adding extra reflections/resonances to the system, however these were considered negligible and the assumption was made to treat it purely as a passive element. In theoretical work on MCLs [25, 32] a key parameter is the injection strength, which is the fraction of power from one laser that reaches the other. By controlling the attenuation of the VOA, this is analogous to varying the strength.

The MCLs were fabricated with VOA separations of 100 , 700  $\mu\text{m}$ , 4500  $\mu\text{m}$  and 9000  $\mu\text{m}$ . To accommodate the larger separations a spiralling waveguide structure was used. Another key theoretical parameter is the frequency detuning, which is the difference in the frequency output of the lasers. To control this facet of the experiment a tuneable on-chip laser design was used, specifically a facetless Slotted Fabry-Perot Laser (SFP), which has been the most commonly used single mode tuneable laser in our research group [36].

### 3.3 Device Testing

#### 3.3.1 Testing Outline

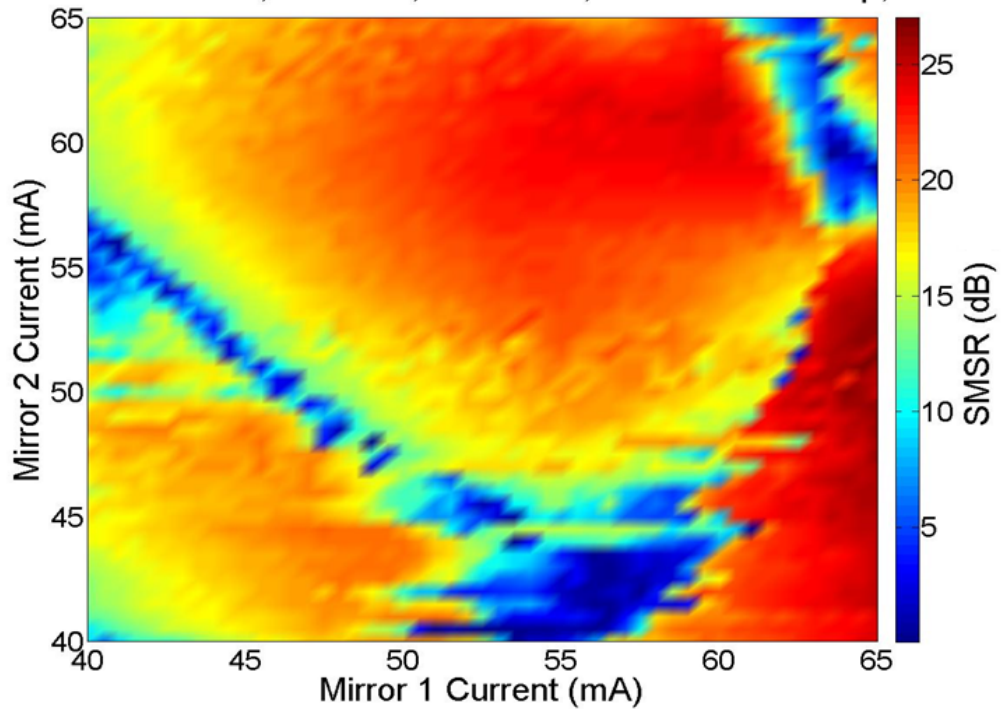
To allow comparison with theoretical work, an appropriate testing method had to be employed. The aforementioned theoretical work was initially focused on mixing of identical lasers, observing their temporal evolution, and studying the bifurcations of the system. A bifurcation occurs when a small smooth change made to the parameter values (the bifurcation parameters) of a system causes a sudden "qualitative" or topological change in its behaviour [37]. To experimentally study bifurcations, an appropriate choice of bifurcation parameters is key, along with the right diagnostic equipment. For this system the best two bifurcation parameters are the injection strength (related to the VOA reverse bias) and the detuning (down to the individual properties of the lasers). To observe the bifurcations an Electronic Spectrum Analyser (ESA) and a High Speed Oscilloscope (HSO) were chosen. The HSO shows the temporal behaviour of the system. The ESA shows the Fourier transform of the HSO, allowing the study of frequencies present in the system. Before coupling

the lasers on the PIC a study of these two parameters had to be done.

### 3.3.2 Tuning characterisation of SFP Lasers

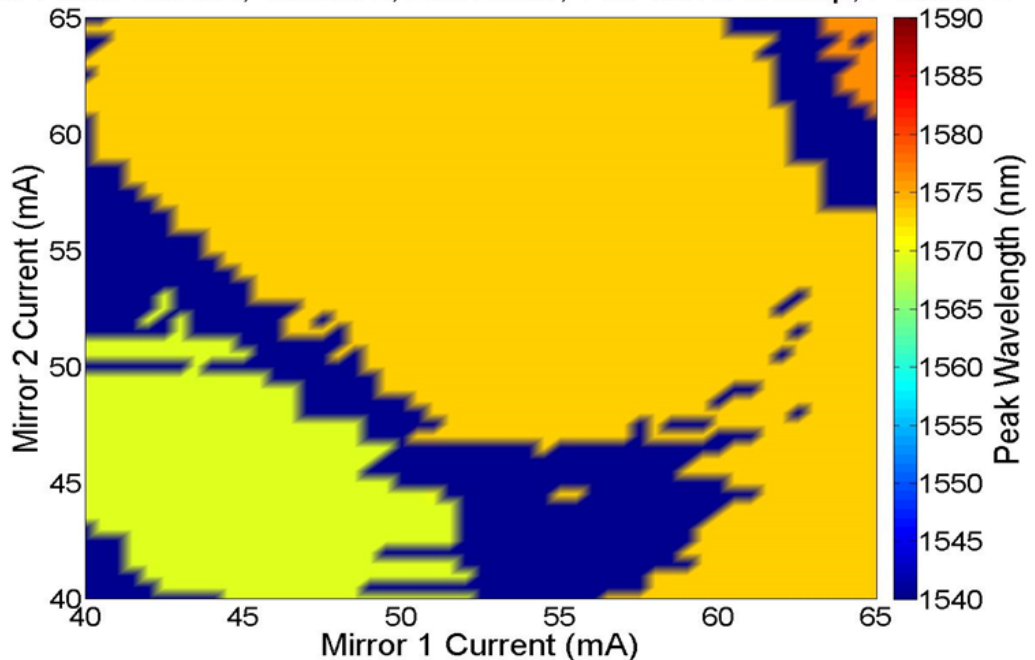
The facetless Slotted Fabry P rot (SFP) lasers on this chip have three sections per laser (one gain, two slotted mirror sections). By fixing the bias of the gain section and changing the mirror currents, single mode regimes on the optical spectrum could be found by measuring the side mode suppression ratio (SMSR), figure 3.3a. The peak wavelength of these single mode regimes was also noted (figure 3.3b), so the lasers can be tuned to have the same output wavelength. Note that figure 3.3b was made by taking figure 3.3a and only considering the regions where the SMSR was  $> 15$  dB and observing the peak wavelengths. The areas in dark blue are the regions deemed to be not singled-moded, or where the SMSR was  $< 15$  dB. The analysis was repeated on both lasers for each device, allowing both lasers to be frequency matched when the coupling experiment was done. Doing this test also allows the lasers to be tuned to a single mode regime. The model at this time still assumed a single mode laser, so adhering to this restriction was important.

50mA Gain Current, Device 2, Left Laser, Two Mirror Sweep, SMSR



(a) Example SMSR vs. Mirror Currents intensity plot of the lasers from the first generation MCL device.

50mA Gain Current, Device 2, Left Laser, Two Mirror Sweep, Peak WL



(b) Example Peak Wavelength (w/ SMSR > 15dB) vs. Mirror Currents intensity plot of the lasers from the first generation MCL device.

Figure 3.3: Wavelength tuning Optical Spectrum Analyser (OSA) intensity plots.

### 3.3.3 VOA Transparency Measurements

The power being absorbed by the VOA as the reverse bias is varied can be calculated by measuring the photocurrent generated in the VOA section when one of the lasers is on and using the following equation.

$$P = \frac{Ihc}{q\lambda} \quad (3.1)$$

The next section after the VOA (the mirror section of the other laser) can also be reverse biased at the same time, connecting it to the same voltage source to see if any light is making it through the VOA. The laser was set to a high SMSR regime discovered in section 3.3.2, then the VOA was reverse biased and the photocurrent was measured. The measurement of the 100  $\mu\text{m}$  long VOA PIC can be seen in figure 3.4.

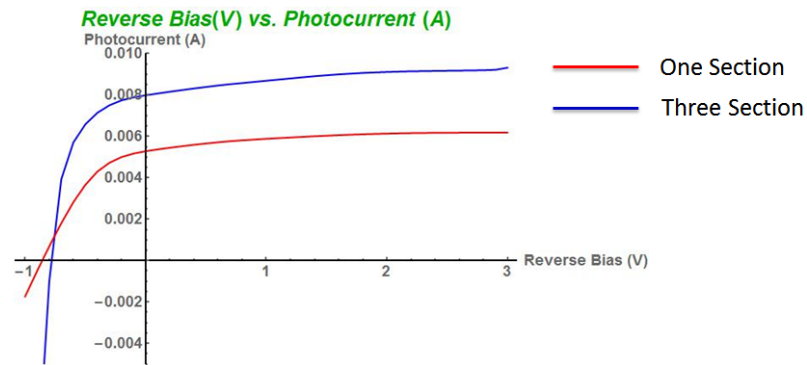


Figure 3.4: Photocurrent(A) vs. Reverse Bias (V) for the 100  $\mu\text{m}$  VOA Mutually Coupled Laser (MCL) device. The photocurrent measured using one section is shown in red and three sections in blue.

In the case where only the VOA was reverse biased the photocurrent saturates at around 6 mA, while when both the VOA and the next section were biased the photocurrent saturates at over 8 mA. This suggested that the 100  $\mu\text{m}$  VOA is not long enough to optically isolate one laser from the other. Moving to the 700  $\mu\text{m}$  VOA device and repeating the test, the results can be seen in figure 3.5.

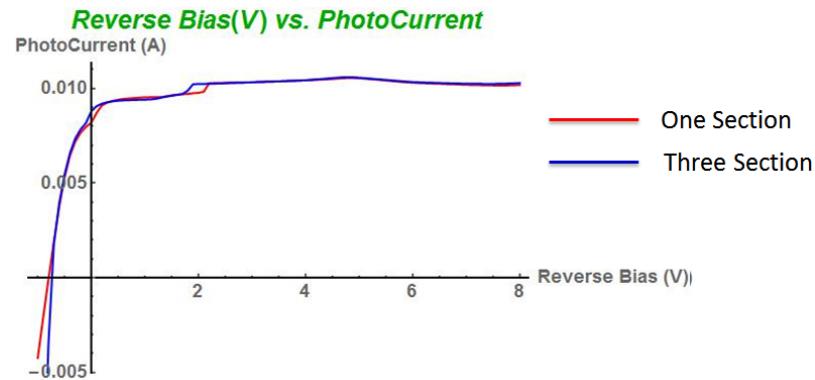


Figure 3.5: Photocurrent(A) vs. Reverse Bias (V) for the 700  $\mu\text{m}$  VOA MCL device. The photocurrent measured using one section is shown in red and three sections in blue.

There was no change in the peak photocurrent absorbed when another absorbing section was added. Therefore unlike the 100  $\mu\text{m}$  long VOA variant this one could optically isolate one laser from another. This was confirmed by another test where a second independent voltage source was used on the section after the VOA and both sources were reverse bias swept at the same time, giving figure 3.6. It can be seen that the blue curve measures zero photocurrent once the VOA has reached its peak absorption, showing that no light is reaching the section after the VOA.

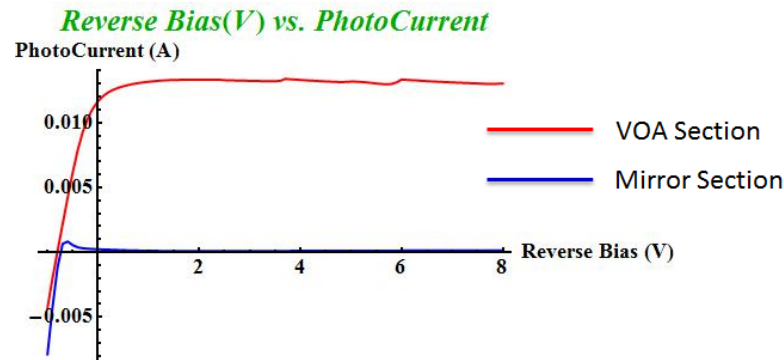
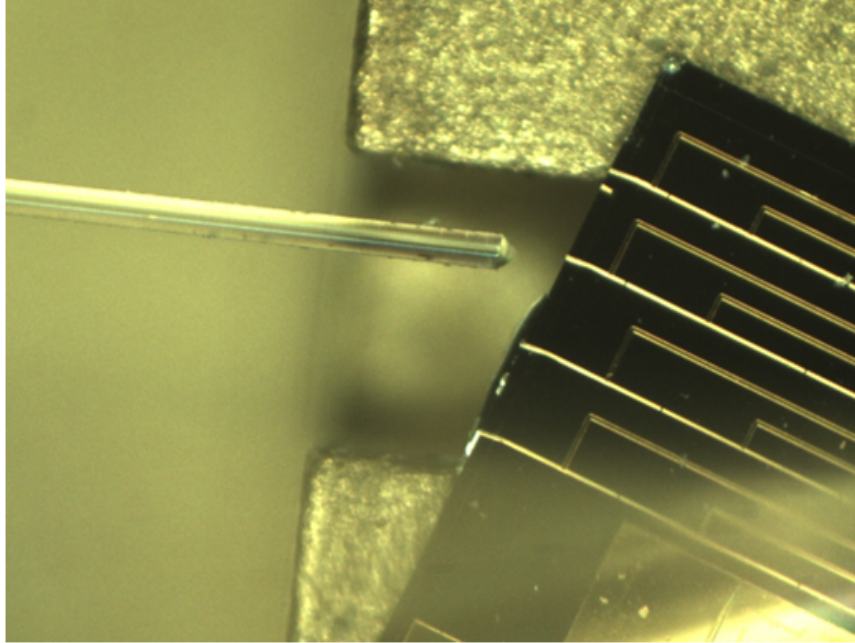


Figure 3.6: Photocurrent (A) measured using two separate sources vs. reverse bias (V). The two sources are placed on the VOA (red) and the adjacent mirror section (blue).

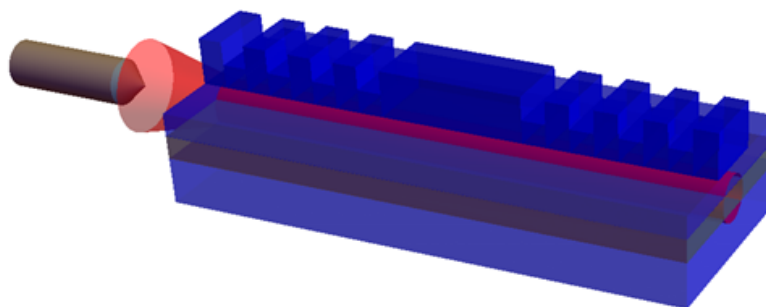
### 3.3.4 Facet Loss Calculation

From the results shown in section 3.3.3 the percentage of power being absorbed by the VOA could be calculated if the power being produced by the laser was known. To measure light output from a PIC, a lensed fibre is used as

seen in figure 3.7. Using a lensed fibre does not result in an accurate measure of the total power emitted by the laser, as it is impossible to couple all the light emitted from the facet into the fibre.



(a) Schematic of a laser on a PIC being fibre coupled.



(b) Simulation of a laser on a PIC being fibre coupled.

Figure 3.7

By injecting an external tunable laser source (TLS) through the circuit diagram in figure 3.8 and reverse biasing the first three waveguide sections on the PIC

(in a similar process to what was described in section 3.3.3) the power being absorbed by the facet was calculated. Comparing that to the power in the fibre before the facet, the loss associated with the facet was found. In this experiment the polarisation controller (PC) is very important as measurements can change dramatically with the alignment of the polarisation between the lasers. With the third port of the circulator connected to a power meter, any back reflections from the facet could also be measured, however this value never exceeded  $-80$  dBm and can be taken as insignificant. The loss associated with the facet/lensed fibre arrangement varied from device to device between  $-4$  dBm to  $-9$  dBm.

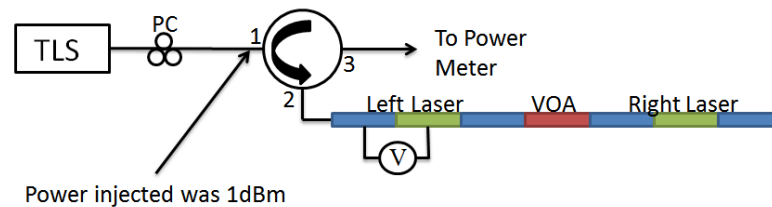


Figure 3.8: Circuit diagram for the facet loss experiment. TLS - tunable laser source, PC - Polarisation Controller.

### 3.3.5 First Coupling Test

Following the preliminary characterisation from sections 3.3.2 and 3.3.3, coupled laser testing began. The circuit diagram for the preliminary experiment can be seen in figure 3.9. The power out of the chip was initially found to be too low to generate a signal on the ESA. An Erbium doped fibre amplifier (EDFA) was added to boost the signal received by the High Speed Photo Diode (HSPD), giving clear features on the ESA. Each laser was individually tuned to closely matching frequencies with a reasonable SMSR, using results from section 3.3.2, figure 3.11. The VOA was reversed biased to  $-6$  V and then the lasers were turned to the zero-detuning arrangement established. The VOA bias was incrementally increased and OSA and ESA traces recorded. This test was first carried out on the PIC incorporating the  $100\ \mu\text{m}$  VOA device.



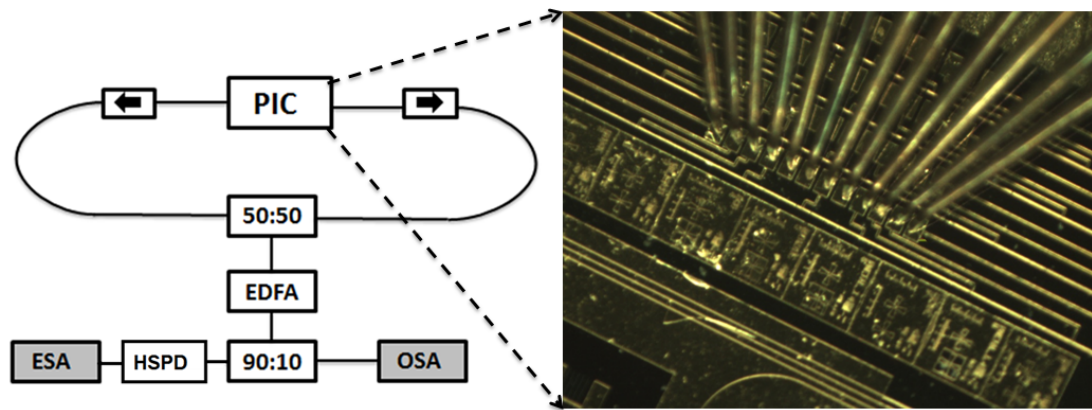


Figure 3.9: Circuit diagram for the mutual coupling experiment. The arrows represent optical isolators, while the black lines represent optical fibre. EDFA - Erbium doped fibre amplifier, HSPD - High speed photodiode, ESA- Electrical spectrum analyser, OSA - Optical spectrum analyser.

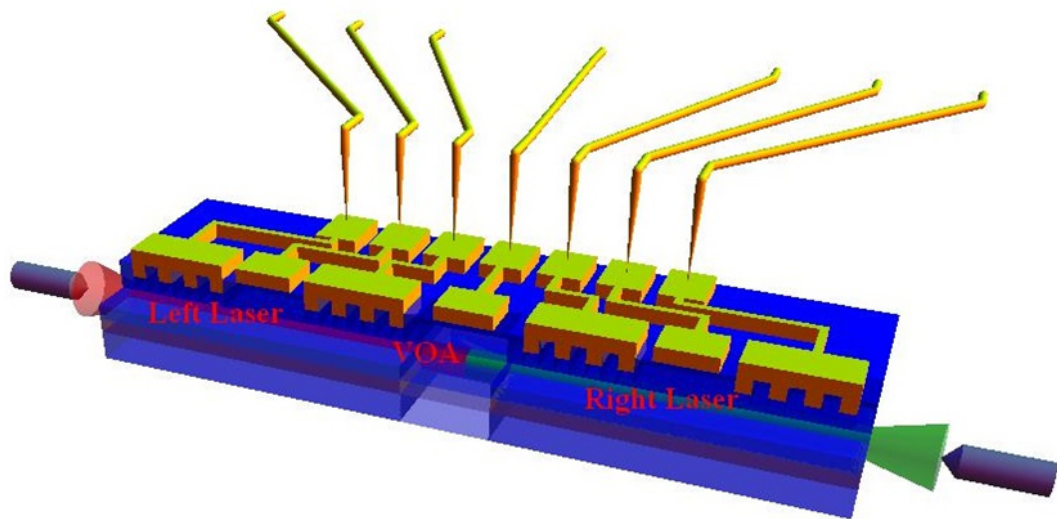


Figure 3.10: An animation of the device under testing.

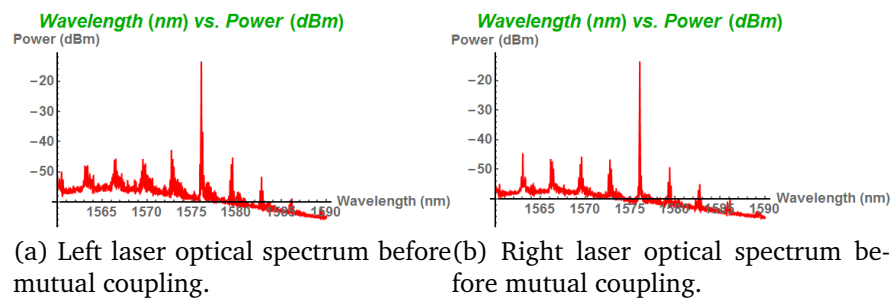


Figure 3.11: Zero detuning arrangement of both lasers before coupling.



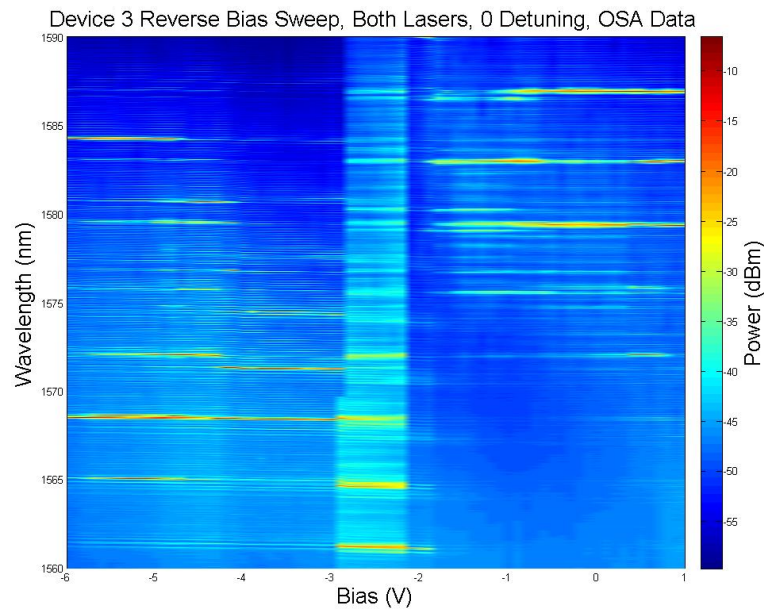


Figure 3.12: Coupled OSA intensity graph of varying VOA bias for the zero detuning arrangement seen in figure 3.11.

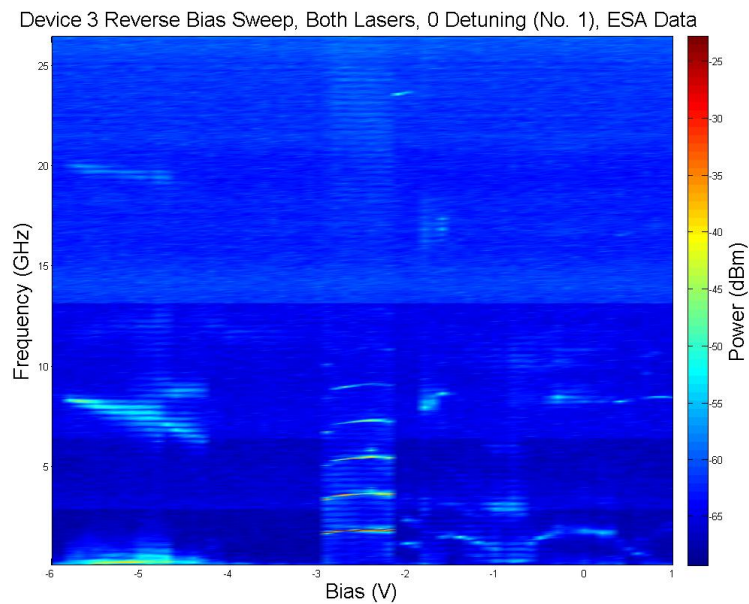


Figure 3.13: Coupled ESA intensity graph of varying VOA bias for the zero detuning arrangement seen in figure 3.11.

A region of single mode operation can be seen in the OSA intensity graph in figure 3.12 between  $-4V$  and  $-3V$ . When this region is examined on the ESA intensity graph in figure 3.13 a quiet region associated with CW phase locked

behaviour can be observed. Additionally for larger reverse biases there is a single frequency beat note of decreasing frequency which can be interpreted as the two laser's frequencies approaching each other, before locking together. As the laser's frequencies were tuned within 0.01 nm, this would generate a beat note  $< 10$  GHz. This was a promising initial result for these devices, showing that phase locked CW operation could be achieved.

This is however, when a strange behaviour was observed on the PIC. Reverse biasing the VOA section was impacting the frequency behaviour of the laser. What was thought to be a zero detuning arrangement of the two lasers was being altered when the VOA was reverse biased. An investigation of this unintended effect was carried out next.

### 3.3.6 VOA affecting lasing

The lasers were individually set to the same tuning as in section 3.3.5, and then  $-6$  V was put across the VOA. A dramatic shift in lasing was observed, as shown in figure 3.14.

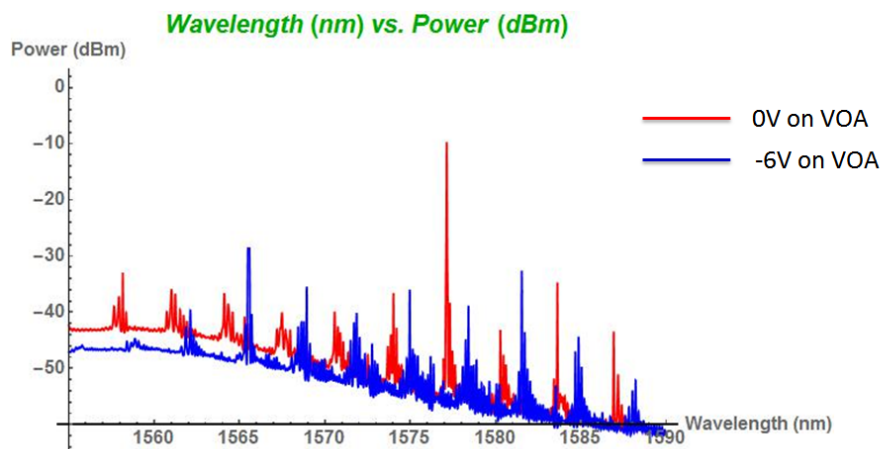


Figure 3.14: Example laser spectrum, with no VOA bias (red), and with  $-6$  V applied to VOA (blue).

The two most likely explanations for this are either current leakage or the VOA has become part of the lasing cavity, as was mentioned previously, due to the limitation of the assumption that this section was purely a passive attenuator.

### 3.3.6.1 Current Leakage

Considering the effective circuit diagram in figure 3.15, the resistance between each section is the resistance between the contact pads on top of the PIC. Applying  $-6\text{ V}$  through the VOA and then using a current source on the mirror section next to it to provide  $60\text{ mA}$  results in a forward voltage of  $\approx 1.6\text{ V}$ . This results in a potential difference of  $\approx 7.6\text{ V}$  through the effective "resistor". Using a multimeter attached to the probes the resistance between the mirror section and the VOA was measured to be  $\approx 12\text{ k}\Omega$ . This means there would be a leakage current of  $0.6\text{ mA}$ , which theoretically is not enough to cause such a dramatic shift in the lasing spectrum.

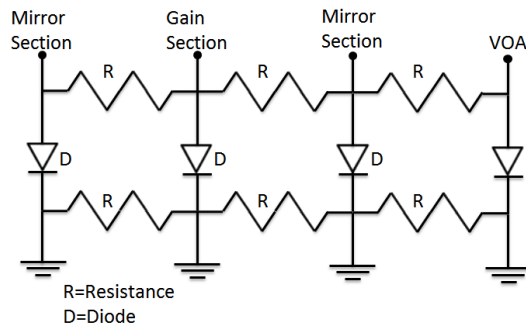


Figure 3.15: Effective circuit of a three section laser and the VOA section on the MCL PIC.

This result needed to be tested experimentally. The laser was set up in the same tuning arrangement as section 3.3.5 using three current sources as normal. However in the mirror section next to the VOA the voltage used to source the current was noted. The current sources were removed and a single voltage source was placed on the mirror section and set at the noted value. A sweep from  $1$  to  $-6\text{ V}$  on the VOA and the next mirror on the other side with two separate voltage sources was done, noting the current, as seen in figure 3.16. At  $-6\text{ V}$  the total current in the VOA and next mirror is over  $1.5\text{ mA}$ . This exceeds the theoretical value and may have caused a change in lasing behaviour, but is unlikely to have caused as dramatic a change in the laser behaviour as observed. All devices were tested and similar results were obtained. This shift in current could cause a shift in the spectrum, depending on the tuning arrangement. If in figure 3.3b the laser was tuned near the border of a high SMSR region (in yellow/orange), a  $1.5\text{ mA}$  increase could push it to a region of multi-wavelength behaviour (dark blue). In the next section it will be determined if through the altering of the VOA bias the length

of the lasing cavity changed in turn. This would alter the Fabry P  rot resonances.

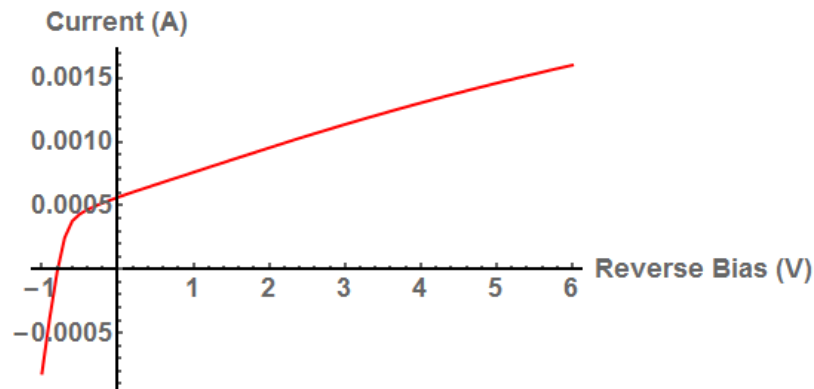


Figure 3.16: Reverse bias sweep of VOA, measuring the current.

### 3.3.6.2 Effective Cavity Length Measurement

The design of the SFP lasers incorporates a number of sub-cavities (the gain section along is one cavity and between each etched slot a smaller sub-cavity is formed). The lengths of the resonating cavity can be observed by taking the Fourier transform of the optical spectrum. There should be a peak in this transform at the length corresponding to a single laser, when the laser is operating in isolation. Repeating this process when  $-6$  V was applied to the VOA will show whether there is any shift in the cavity length that is resonating. figure 3.17 shows the results of this process.

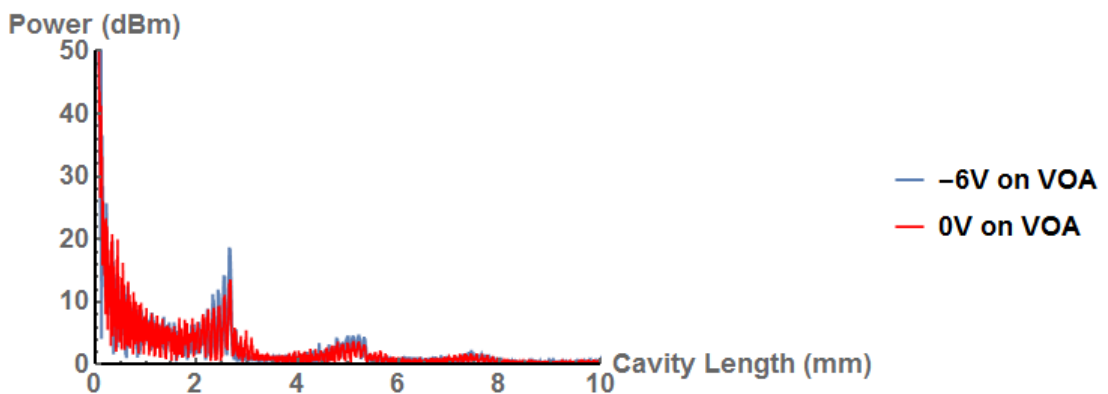


Figure 3.17: Fourier transform of OSA traces for a laser when there are  $-6$  V on the VOA (blue) and  $0$  V on the VOA (red).

In the case of  $0$  V on the VOA (red curve) there is a peak at approximately  $2.6$  mm. The schematic of a single laser along with the lengths of the sections of interest can be seen in figure 3.18. Combining the laser length of  $2150 \mu\text{m}$  and

the waveguide section leads to a length corresponding to the peak in figure 3.17 at approximately 2.6 mm.

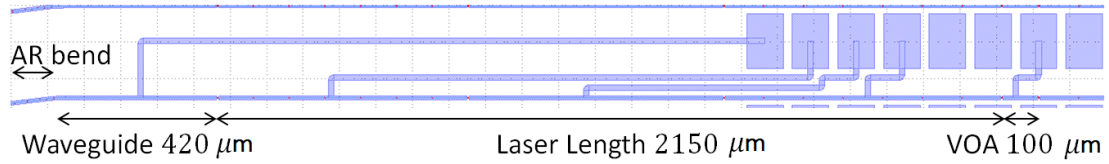


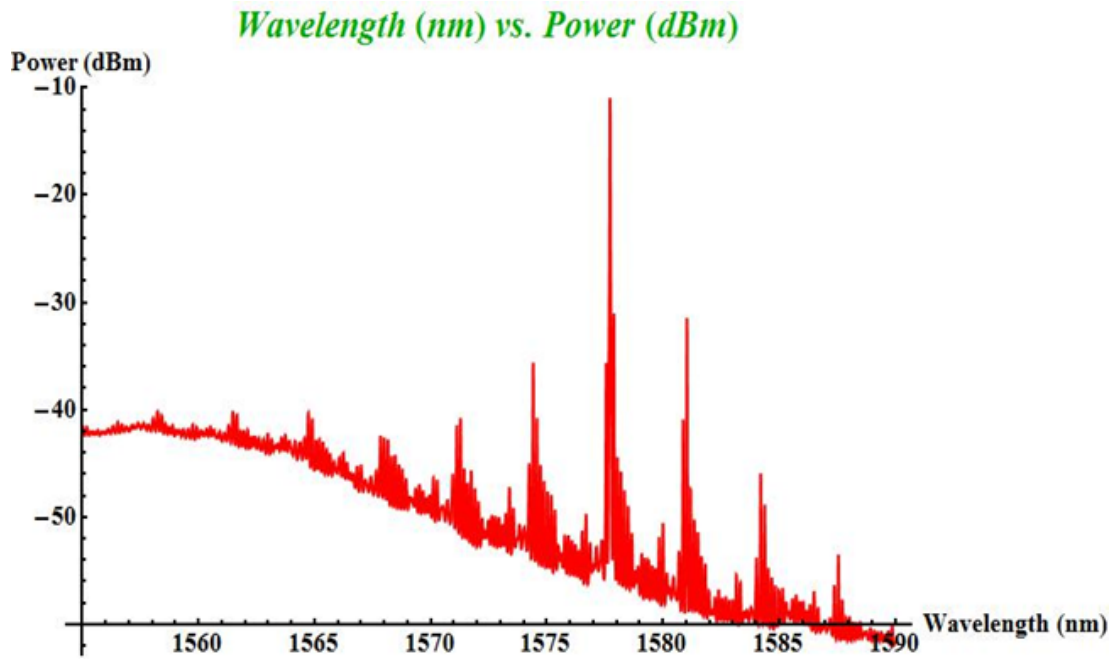
Figure 3.18: Schematic of a single laser, along with VOA, and waveguide leading to AR bend.

The voltage was then changed to  $-6$  V resulting in the blue curve. No shift is observed in the peak at 2.6 mm. In this device the VOA length was  $100\text{ }\mu\text{m}$  and if this VOA was part of the lasing cavity, a shift of  $100\text{ }\mu\text{m}$  would have been observed as  $-6$  V would remove this section from the resonating cavity, shortening the FFT of the spectrum by  $100\text{ }\mu\text{m}$ . Therefore this eliminates a change in the lasing cavity causing the change in lasing when  $-6$  V is applied to the VOA.

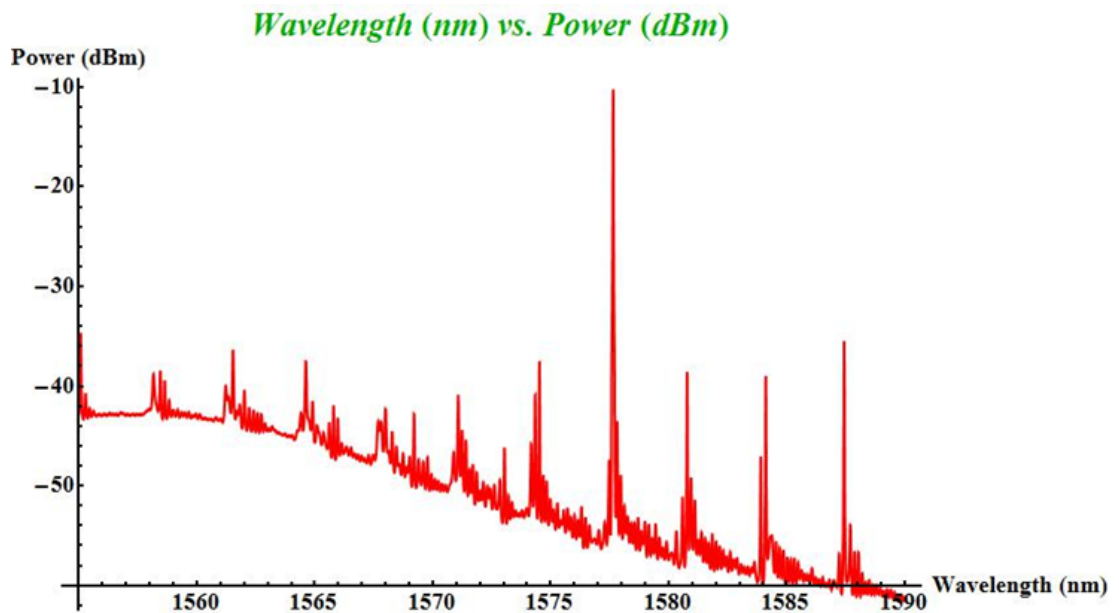
### 3.3.7 $700\text{ }\mu\text{m}$ VOA Coupling test

Next the  $700\text{ }\mu\text{m}$  VOA devices were tested. The effect of the VOA bias on lasing was taken into account, by tuning the lasers before coupling, with  $-6$  V across the VOA.

The experiment from section 3.3.5 was then repeated for the  $700\text{ }\mu\text{m}$  VOA device.



(a) Left laser before mutual coupling.



(b) Right laser before mutual coupling.

Figure 3.19: Zero detuning arrangement with  $-6$  V across the VOA.



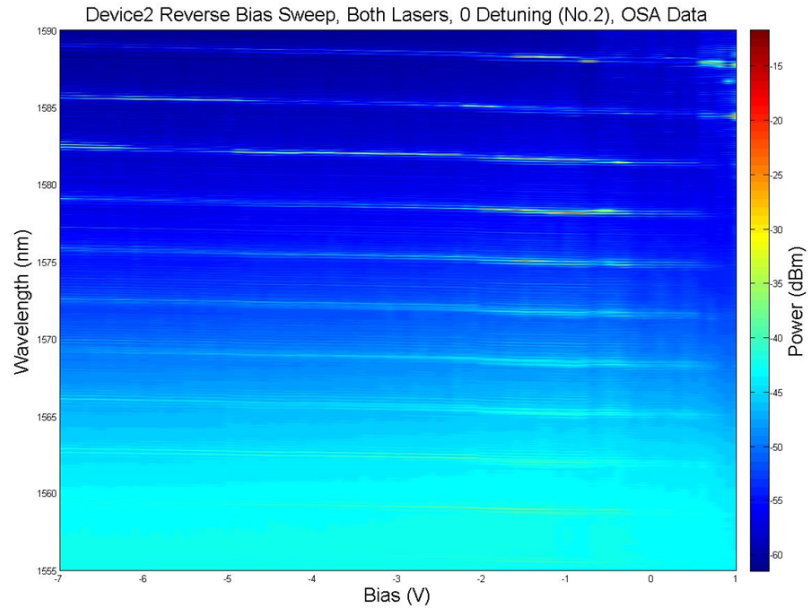


Figure 3.20: Coupled OSA intensity graph for the 700  $\mu\text{m}$  VOA device.

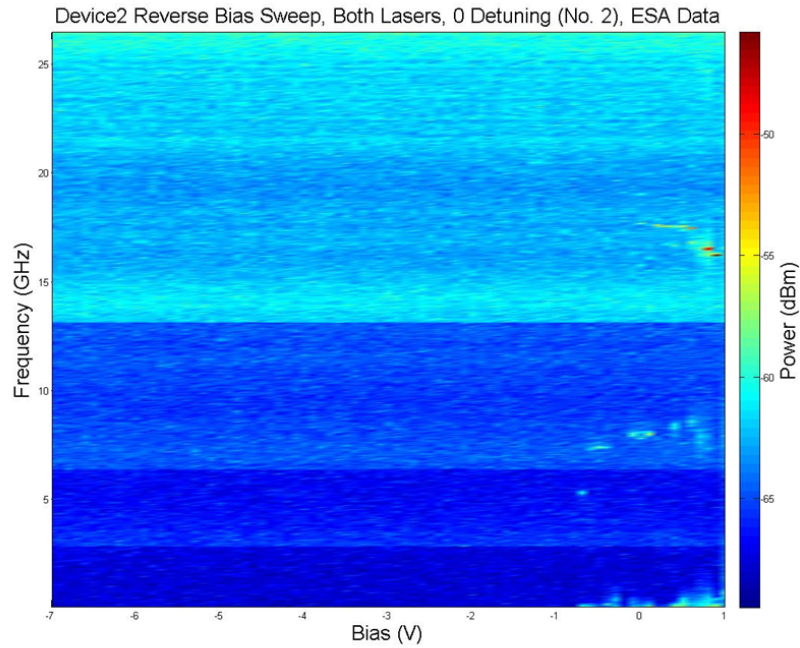


Figure 3.21: Coupled ESA intensity graph for the 700  $\mu\text{m}$  VOA device.

On this longer VOA device a single, a high SMSR regime exists between  $-6\text{ V}$  and  $-4.5\text{ V}$  on the OSA intensity plot in figure 3.20, which is the desired regime. However there is a lack of any features on the ESA intensity plot in figure 3.21. As in section 3.3.5 there is no beat note between the lasers, as

they are introduced to each other. This ESA data would suggest that the whole device has become a single laser; the VOA has just made a coupled cavity laser (CCL). To test this hypothesis the FFT of the OSA traces were analysed, as was done in Sec. 3.3.6.2. The result of this analysis can be seen in figure 3.22.

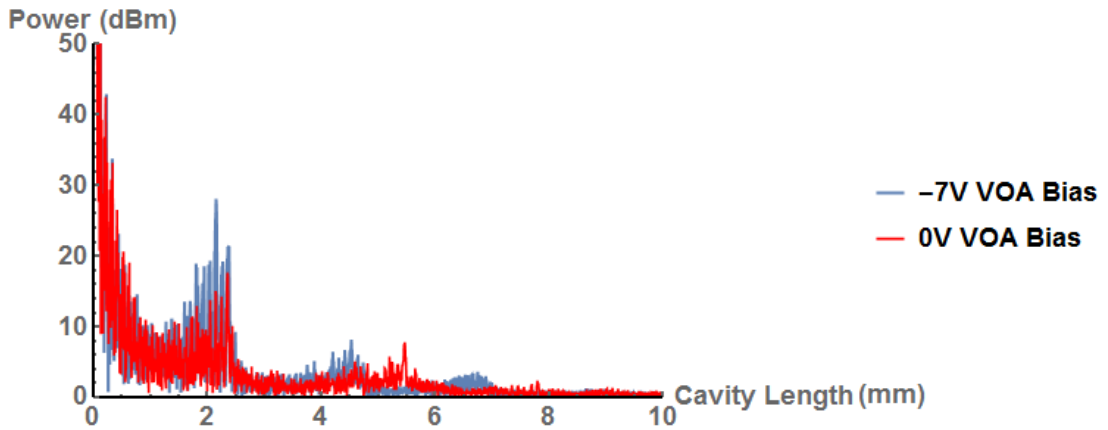


Figure 3.22: Fourier transform of OSA traces for a laser when there are  $-7V$  on the VOA (blue) and  $0V$  on the VOA (red) from the mutual coupling experiment results outlined in figure 3.21.

The blue trace shows a strong peak at approximately 2.2 mm, which corresponds to the single laser length. Unlike in figure 3.18, the  $700\mu m$  VOA does not have a  $420\mu m$  long waveguide section at the end of the device, for it to become part of the lasing cavity like in the  $100\mu m$  VOA variant. There is a secondary peak at approximately 4.4 mm which is a harmonic of the main peak. The red trace in figure 3.22 is from during the coupling experiment, when there was zero bias on the VOA. This shows a secondary peak at 5.5 mm, which is close to the length of two 2.2 mm lasers and a  $700\mu m$  VOA along with the short AR bends and waveguides. Importantly this secondary peak is not a harmonic of the peak around 2.2 mm and comes from its own resonance, indicating the entire device has formed a resonating cavity, or CCL.

### 3.3.8 On Chip Master/Slave Injection

Testing done in sections 3.3.5 and 3.3.7 has shown a difficulty in getting the on-chip lasers to interact in an expected way. There should be a beat note between the lasers as the reverse bias on the VOA is increased from highly negative. It was decided to try and re-create work done previously with on chip master slave injection [38]. Using the  $100\mu m$  VOA, one laser was biased strongly above threshold and the other was biased just at threshold. The VOA



was then given a small forward bias (10 mA) to make it transparent. The same circuit diagram as in figure 3.9 was used, but this time the current in the gain section of the master laser was varied.

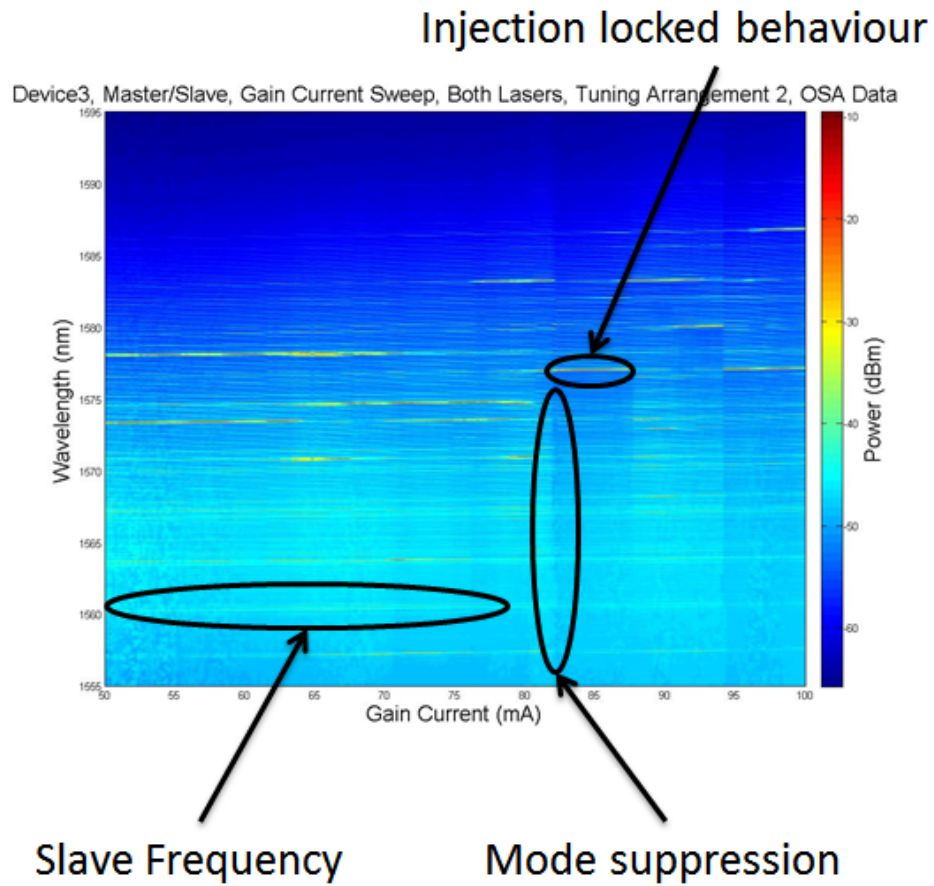


Figure 3.23: Coupled OSA intensity graph for on chip master/slave on the 100  $\mu\text{m}$  VOA device.

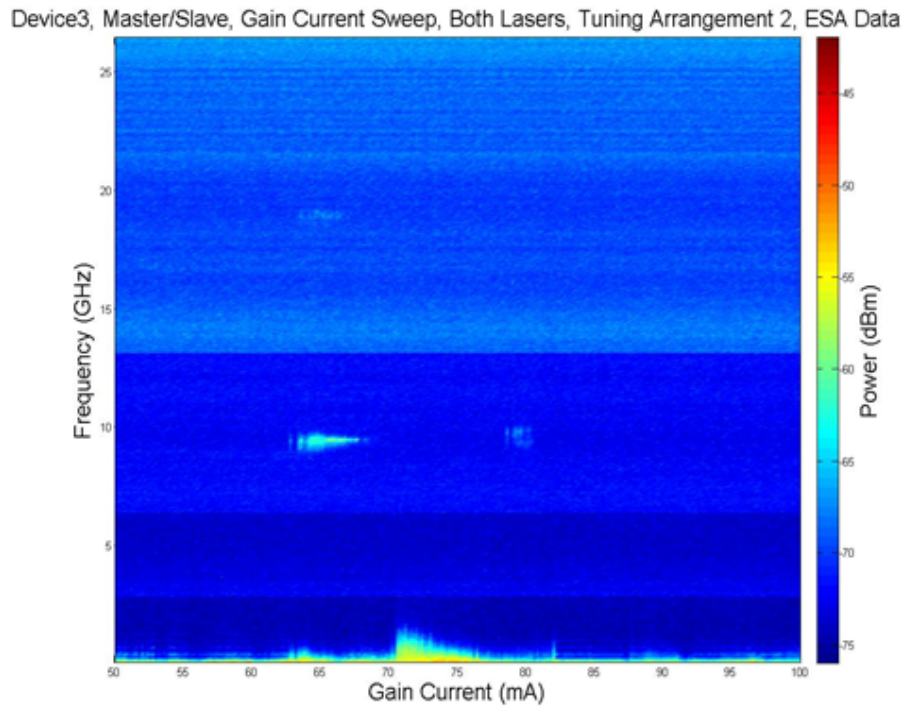


Figure 3.24: Coupled ESA intensity graph for on chip master/slave on the 100  $\mu\text{m}$  VOA device.

In figure 3.23 the main mode of the slave laser is indicated, then at approximately 82 mA master gain current, all modes become suppressed and the slave laser becomes injection locked. However just as in previous tests, there is nothing on the ESA intensity graph in figure 3.24. All tests to this point show that the lasers are not interacting as expected.

### 3.3.9 External Injection Locking of On Chip Lasers

To make sure the lasers behave as expected under injection, external injection locking was done on the lasers with a TLS. The circuit diagram for this test is in figure 3.25

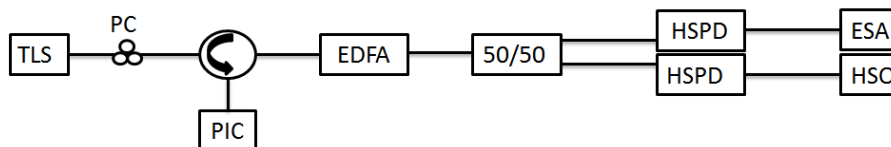


Figure 3.25: External injection locking test circuit. TLS - tunable laser source, PC - Polarisation Controller, EDFA - Erbium doped fibre amplifier, HSPD - High speed photodiode, ESA- Electrical spectrum analyser, HSO - High speed oscilloscope.

For this test the OSA was replaced with a HSO, as this will show the time trace of the signal, and allow the interesting dynamics to be observed.

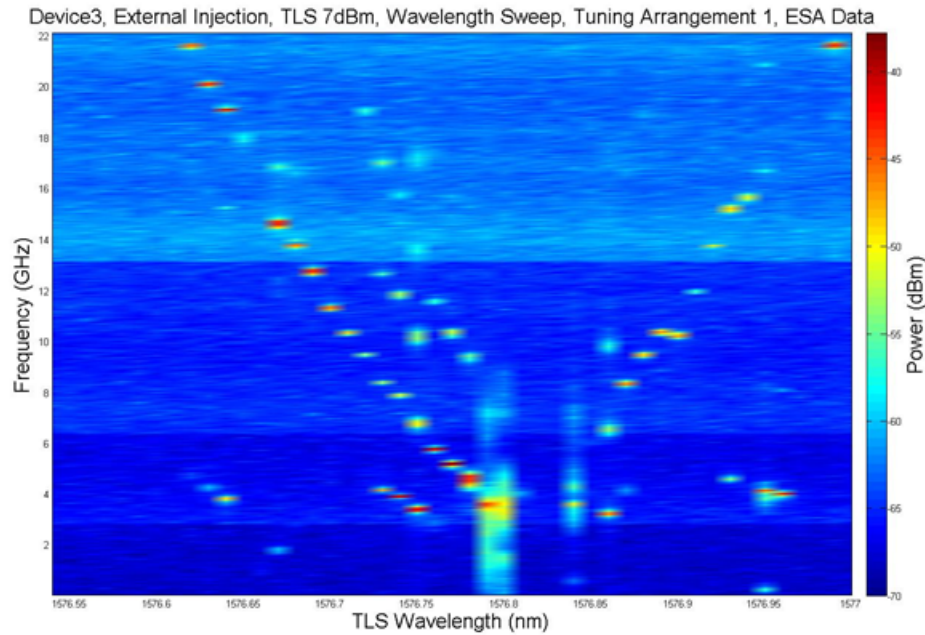
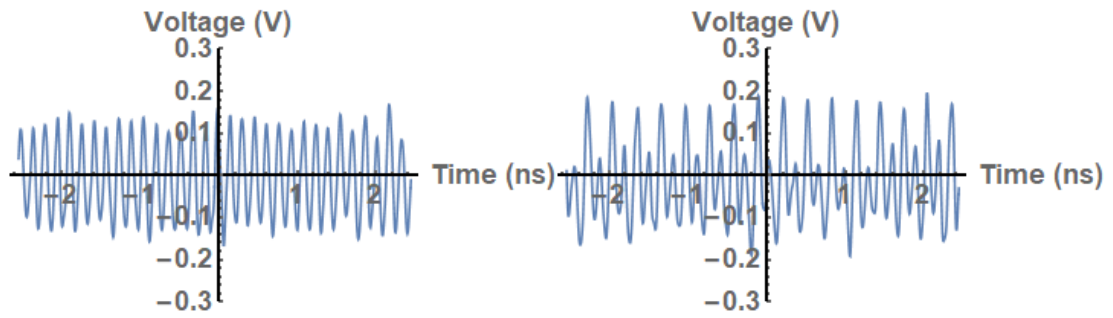


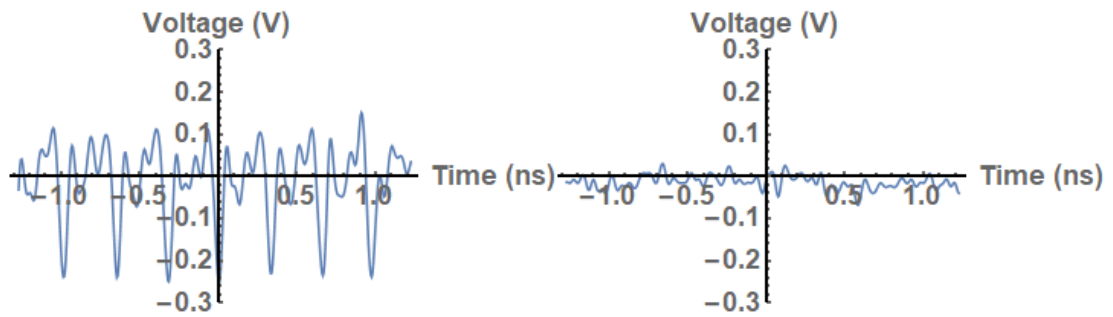
Figure 3.26: ESA intensity plot for external injection of the on chip laser with a TLS. The TLS power was fixed at 7 dBm, and the wavelength was swept across the peak of the slave laser.

The ESA intensity plot in figure 3.26 agrees with theoretical work and experimental work done on injection locked lasers. When the TLS is below the peak wavelength of the slave, there is a beat note whose frequency decreases as the wavelength get closer to the slave. At a certain point the system undergoes a period-doubling bifurcation, which is signified by the generation of a sub-harmonic at exactly half the main frequency. This turns into a complex area of chaos before the beat note disappears, and the lasers become locked. As the wavelength was increased the lasers becomes unlocked and the beat note re-appears. Examples of the HSO outputs of each of these dynamical regimes can be seen in figure 3.27.

These results show that these lasers can be injection locked and the issue with the mutual coupling testing is not because of the injection locking properties of the on chip lasers.



(a) An example of the beat note on the left of the locked area in figure 3.26. (b) At TLS wavelength 1576.75nm, in figure 3.26, below the beat note, a sub harmonic exists. This causes a period two oscillation seen above.



(c) This time trace corresponds to the complex area around 1576.8nm in figure 3.26. (d) This time trace corresponds to the injection locked region around 1576.25nm in figure 3.26.

Figure 3.27: High Speed Oscilloscope (HSO) plots of different dynamic regimes in figure 3.26.

### 3.3.10 Future Device Design

From the results shown, it was clear that improvements to the design had to be made. The first generation devices shown previously had poor electrical isolation between the sections on the chip, and the VOA lengths were too short to optically isolate the lasers from each other.

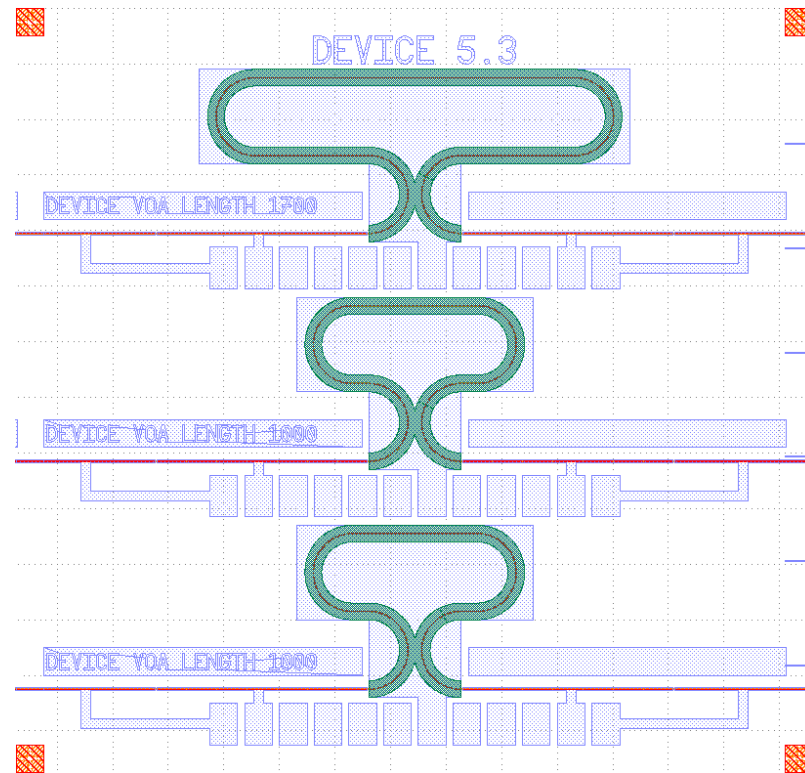


Figure 3.28: An improved design of MCL devices schematic.

The improved MCL devices in figure 3.28, were designed to have longer VOA lengths than previous devices. These lengths are 1 mm, 1.7 mm and 2.1 mm. The VOAs were designed to be in a curved pattern to make the device space efficient. To realise the small bend radius of the curves, a deep etched area (green area) was included around the ridge. This deep etch reduces the loss in the high curvature bends. An illustration of different etch depths can be seen in figure 3.29. A deep etch can be seen in the bottom figure. By etching through the quantum wells the effective index difference of the ridge/air interface is greatly increased compared the standard shallow etched waveguide. This improves the confinement of the mode within the ridge, allowing the tight bend radius needed. The deep etch should also improve the electrical isolation between sections, if the slots between them are deeply etched. Measurements showed an increase in the isolation resistance from  $k\Omega$  to  $M\Omega$ , thus achieving the improved electrical isolation desired.



Figure 3.29: Diagram illustrating different etch depths of ridges on a PIC. The bottom picture shows the deep etch used, which goes through the quantum wells<sup>1</sup>.

At this point the experimental work was handed over to new PhD student who's focus has been on the experiments associated with MCLs. This work provided a baseline for her work and set some rules for future device designs. From this work it was adjudged that longer VOA lengths were needed to optically isolate one laser from another and that further steps would be needed to improve the electrical isolation between sections of the devices. Her further testing discovered another flaw in the previous design used in preliminary experiments. It was discovered that longer VOA lengths did not optically isolate one laser from the other as planned. This was due to substrate coupling, where light was coupling into the substrate of the chip and reaching the other laser. This necessitated the design feature that the lasers not be on

<sup>1</sup>Image courtesy of Mohomad Derneika

the same lateral plane (when the device is viewed from above), to minimise this effect. As the laser is orientated laterally across the top of the chip, any light that has leaked into the substrate would also travel in this plane (with some spreading do to lack of confinement). Moving the second laser to a part of the chip not directly opposite the other laser, this should minimise the "substrate light" reaching each laser from the other. Two more modern designs of MCLs on a PIC can be seen in figure 3.30. Here curved VOA sections were used to keep lasers of the same device on different lateral planes. Certain devices used a U-shaped VOA to ensure this effect was negligible. The areas highlighted in dark green are the deep etched sections. There is a deep etch along the length of the chip to ensure high resistance between adjacent sections. In figure 3.30a the VOA lengths vary from 1 – 1.7 mm, while in figure 3.30b, they vary from 385  $\mu\text{m}$  - 1735  $\mu\text{m}$ .

My colleague's work has provided experimental results which will be compared with theoretical results in Chapter 4.

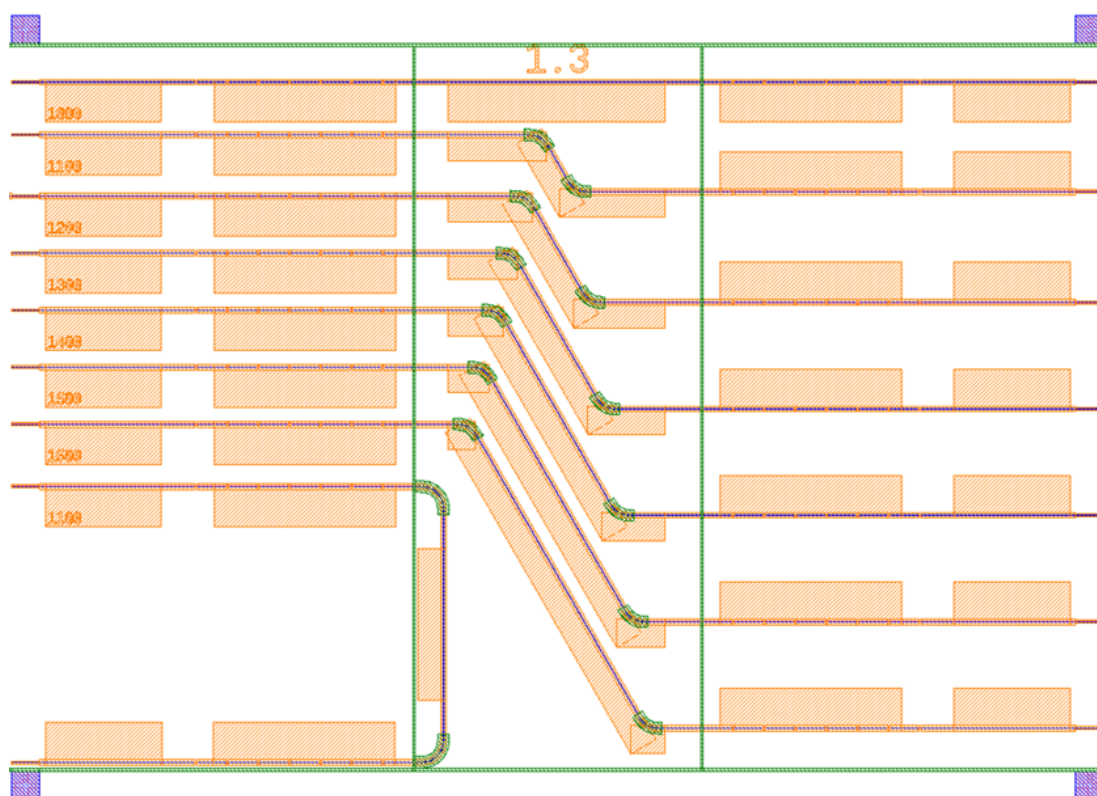
### 3.4 Experimental conclusion

Though experimental work carried out did not yield viable results for comparison with theory, it did provide design guidelines for future testing and provided a good starting point for my colleague, Alison Perrott, whose work has been invaluable in providing excellent results for comparison with modelling results. While no direct publication arose from this work, it did however earn best postgraduate poster award at the Photonics Ireland conference 2015. The work presented was an important first attempt at understanding MCLs on a PIC experimentally.

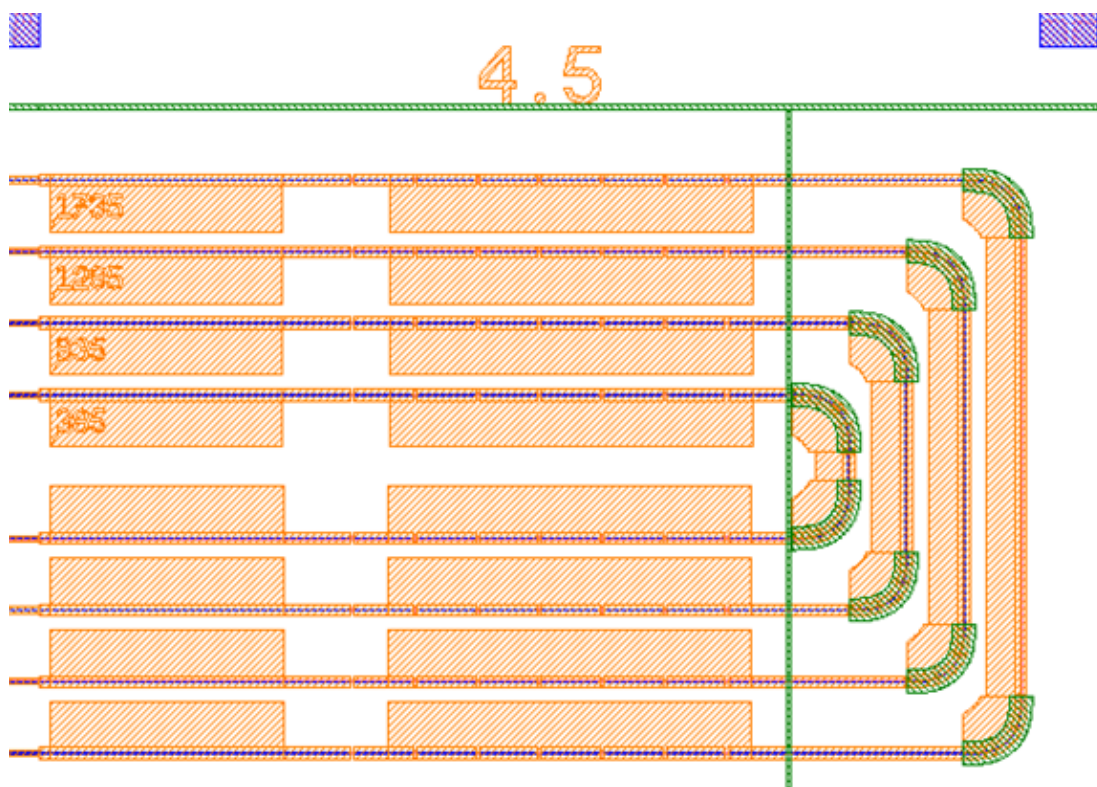
---

<sup>2</sup>Images courtesy of Alison Perrott





(a) H



(b) H

Figure 3.30: Later generation MCL chips tested by my colleague<sup>2</sup>.



## **Chapter 4**

# **Single mode model for identical lasers**

### **4.1 Model introduction**

### 4.1.1 Introduction

In this section the model for a system of two single mode lasers, optically coupled will be introduced, along with a breakdown of the variables used in the model. Methods for analytically finding bifurcations of the system without detuning (with and without time delay) will be shown. This work is an expanded version of the method outlined in [25]. Detailed descriptions of the derivations not highlighted in this publication, along with how certain mathematical problems not mentioned were overcome have been included. Bifurcations are key for comparing theory and experiment as the model presented here is a qualitative model, i.e. it predicts different types of behaviours. By analysing the different behavioural regimes present in the model this will allow for a direct comparison with the behavioural regimes that are observed experimentally. After presenting these different regimes it will be shown how these analytical methods breakdown when detuning is included. A study of the behaviours present in the model will be presented, followed by an attractor diagram study of the system. These results will then be compared with experiments done by my colleague, using the newer devices with design improvements suggested by work in Chapter 3.

### 4.1.2 The model

The model used is presented in Eqn. 4.1-4.5. It is a modified version of the Lang-Kobayashi equations, [34], which models a laser with feedback from a mirror. Here self-feedback is neglected, i.e. light from laser 1, reflecting back into laser 1. In this arrangement it is considered negligible.

$$\frac{d\bar{E}_1}{dt} = i\delta\bar{E}_1 + \frac{1}{2}(G_1(\bar{N}_1, |\bar{E}_1|^2) - \frac{1}{\tau_p})\bar{E}_1 + \kappa e^{-i\phi}\bar{E}_2(t - \bar{\tau}) \quad (4.1)$$

$$\frac{d\bar{N}_1}{dt} = I_1 - \frac{\bar{N}_1}{\tau_{c1}} - Re[G_1(\bar{N}_1, |\bar{E}_1|^2)]|\bar{E}_1|^2 \quad (4.2)$$

$$\frac{d\bar{E}_2}{dt} = \frac{1}{2}(G_2(\bar{N}_2, |\bar{E}_2|^2) - \frac{1}{\tau_p})\bar{E}_2 + \kappa e^{-i\phi}\bar{E}_1(t - \bar{\tau}) \quad (4.3)$$

$$\frac{d\bar{N}_2}{dt} = I_2 - \frac{\bar{N}_2}{\tau_{c2}} - Re[G_2(\bar{N}_2, |\bar{E}_2|^2)]|\bar{E}_2|^2 \quad (4.4)$$

$$G_1(\bar{N}_1, |\bar{E}_1|^2) - \frac{1}{\tau_p} = G_N(1 + i\alpha)(\bar{N} - N_0) \quad (4.5)$$

Here  $\bar{E}_{1,2}$  are the complex electric fields,  $\bar{N}_{1,2}$  are the carrier densities,  $G_{1,2}$  are the gain profiles of the lasers,  $\tau_p$  is the photon lifetime,  $\tau_{c1,2}$  are the carrier lifetimes,  $\kappa$  is the injection parameter,  $\phi$  is the phase difference between the lasers,  $\bar{\tau}$  is the delay between the laser,  $I_{1,2}$  are the injected currents into the lasers,  $G_N$  is the gain constant of the laser,  $\alpha$  is a parameter called the linewidth enhancement factor ( $\alpha = 2.6$ ) and  $N_0$  is the transparency carrier density. Firstly the variables were re-scaled using  $E = \sqrt{G_N \tau_c} \bar{E}$ ,  $N = \frac{1}{2} \tau_p G_N (\bar{N} - N_0)$  and  $t_{new} = \frac{t}{\tau_p}$ . This gives equations 4.6-4.9.

$$E'_1(t) = i\delta E_1 + (i + i\alpha)E_1 N_1 + \eta e^{-i\phi} E_2(t - \tau) \quad (4.6)$$

$$E'_2(t) = (i + i\alpha)E_2 N_2 + \eta e^{-i\phi} E_1(t - \tau) \quad (4.7)$$

$$N'_1(t) = \epsilon[J - N_1 - (N_1 + \nu)|E_1|^2] \quad (4.8)$$

$$N'_2(t) = \epsilon[J - N_2 - (N_2 + \nu)|E_2|^2] \quad (4.9)$$

Where  $E'_{new1,2}$  is the derivative with respect to  $t_{new}$  and

$$\epsilon = \frac{\tau_p}{\tau_c}, J = \frac{\tau_p G_N (I \tau_c - N_0)}{2}, \tau = \frac{\bar{\tau}}{\tau_p}, \eta = \tau_p \kappa, \delta = \tau_p \bar{\delta}, \nu = 0.5$$

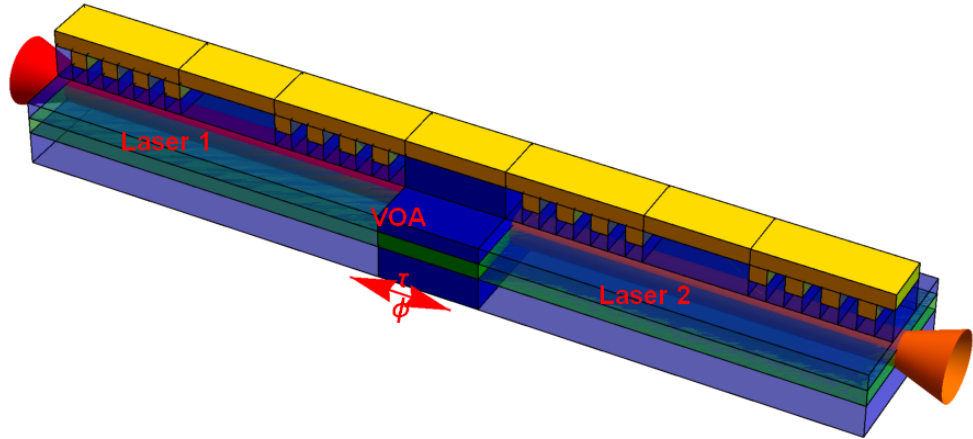


Figure 4.1: Example of a pair of mutually coupled lasers on a PIC. Here the intermediate section's (VOA) transparency is a measure of  $\eta$  and can be controlled by applying a voltage to the gold contact pad connected to this section. The time of flight between the lasers ( $\tau$ ) is the VOA length. This propagation induces a phase change of  $\phi$ . The difference in the frequencies emitted is  $\delta$  and the current injected,  $J$ , is through the gold contact pads on the top of the device.

Figure 4.1 shows a schematic of the theoretical arrangement being considered highlighting the parameters of the model where possible.  $J$  is the injection parameter and describes how strongly pumped the lasers are ( $J = 0.23$ ).  $\epsilon$  is the ratio of carrier and photon lifetimes ( $\epsilon = 0.0025$ ) (parameter values used from [32]).  $\alpha$ ,  $J$  and  $\epsilon$  are all fixed parameters being either a material property or a non-varying experimental parameter in the case of the injection parameter.  $\eta$  is the coupling coefficient, which describes the fraction of light

reaching one laser from the other and vice versa. The material used in fabricating the device is a PIN diode structure, and by reverse biasing this junction the material becomes absorbing, decreasing the fraction of light reaching one laser from the other. Therefore we can control  $\eta$  experimentally ( $\eta$  is a dynamical variable, with values between 0-0.5 considered).  $\phi$  is the coupling phase, described by the phase difference caused by the intermediate section ( $\phi$  ranges from  $0 - 2\pi$ ).  $\delta$  is frequency detuning of the lasers ( $\delta$  is a dynamical variable, values up to approximately 0.8 or 80 GHz were considered).  $\tau$  is the delay time between the lasers ( $\tau = nD/c$ , where  $D$  is the separation of the lasers,  $n$  is the refractive index of the material and  $c$  is the speed of light. Values from 0.5 to 4 mm were considered, corresponding to typical lengths associated with PICs).  $\eta$ ,  $\phi$  and  $\delta$  are the variable bifurcation parameters in this study.

The variables  $\delta$  and  $\tau$  are scaled by the photon lifetime,  $\tau_p$ , of the laser. To calculate this parameter the total rate of change of photon number in an optical cavity is considered.

$$\frac{dN_p}{dt} = (\Gamma v_g G - \frac{1}{\tau_p}) N_p \quad (4.10)$$

Here the rate of photon loss is  $N_p/\tau_p$  and  $\Gamma v_g G N_p$  is the rate of generation of photons by gain. For stable lasing to occur photon loss must equal photons generated. So for a laser at threshold:

$$\Gamma v_g G_t h = \frac{1}{\tau_p} \quad (4.11)$$

An expression for threshold gain is required. If the cavity is a simple Fabry-Pérot, the change in optical power after one round trip is:

$$R_1 R_2 e^{(\Gamma G - \tilde{\alpha}) 2L} \quad (4.12)$$

Where  $R_{1,2}$  are the reflectivities of the facets,  $\Gamma G$  represents the power gain and  $\tilde{\alpha}$  are the losses. At threshold this expression equals one, meaning:

$$\Gamma G_{th} = \frac{1}{L} \ln \frac{1}{\sqrt{R_1 R_2}} + \tilde{\alpha} \quad (4.13)$$

Therefore from Eqn. 4.11:

$$\frac{1}{\tau_p} = \frac{v_g}{L} \ln \frac{1}{\sqrt{R_1 R_2}} + v_g \tilde{\alpha} \quad (4.14)$$

If a loss-less system is assumed this can be re-arranged to give:

$$\tau_p = \frac{-2nL}{c \ln R_1 R_2} \quad (4.15)$$

Here,  $L$  is the cavity length of the laser (1.6 mm),  $c$  is the speed of light,  $R_{1,2}$  are the mirror reflectivities ( $R_1 = 0.3$  for a cleaved facet and  $R_2 = 0.1$  for the SFP mirrors used) and  $n$  is the refractive index (assumed to be 3.5 for the material used). For the semiconductor lasers used:  $\tau_p \approx 10$  ps, meaning for a detuning of 1GHz,  $\delta = 0.01$ , and  $\tau = 1$ , this translates to a separation  $\approx 3$  mm.

### 4.1.3 Analytical bifurcations of the no delay, no detuning system

#### 4.1.3.1 Model simplifications and CW solutions

Now that the model has been introduced and parameters defined, a bifurcation study of the most basic arrangement will be presented, where detuning and laser separation are assumed to be zero. After this a small delay time shall be included (on the order of 1 – 2 photon lifetimes). Bifurcations can be found using one of a number of numerical softwares, based on a principle called numerical continuation, or can be found analytically. The different softwares are based on whether the system is an ordinary differential equation (ODE) or delay differential equation (DDE). Here the analytic method shall be for no detuning and delay ( $\tau = 0$  and  $\delta = 0$ ). Then delay will be introduced to improve the experimental relevance of the model.

Here a version of the method presented in a previous work will be shown, [25], to confirm methods used in the future based upon this analysis are correct and understood. First it was assumed both lasers were identical ( $E_1 = E_2 = E$  and  $N_1 = N_2 = N$ ). This gave a simplified model to begin analysis, equations 4.16 - 4.17

$$E' = (1 + i\alpha)NE + \eta e^{-i\phi} E \quad (4.16)$$

$$N' = \epsilon[J - N - (N + \nu)|E|^2] \quad (4.17)$$

The CW solutions to these equations were of the form  $E = E_0 e^{j\omega_0 t}$  and  $N = N_0$ . Inserting these into equations 4.16 and 4.17 gave two solutions. The first solution was the off state of the laser  $E = 0$  and  $N = J$ . The second solution was:

$$N_0 = -\eta \cos(\phi)$$

$$\omega_0 = -\eta(\alpha \cos(\phi) + \sin(\phi))$$

$$E_0 = \sqrt{\frac{J + \eta \cos(\phi)}{\nu - \eta \cos(\phi)}}$$

Where  $-J < \eta \cos(\phi) < \nu$  for a solution to exist.

#### 4.1.3.2 Linearization of the equations

To analyse the stability of this CW solution a transformation of co-ordinates was done to make the solution a stationary point, i.e.  $f'(x) = 0$  and delay time,  $\tau$  will be re-introduced temporarily, before being set to zero again. The solution became  $E_1 = E_2 = E_s e^{j\omega_s t}$  and  $N_1 = N_2 = N_s$ . This co-ordinate system was defined by:

$$F_1 = \frac{E_1 + E_2}{2} e^{-j\omega_s t}$$

$$F_2 = \frac{E_1 - E_2}{2} e^{-j\omega_s t}$$

$$M_1 = \frac{N_1 + N_2}{2}$$

$$M_2 = \frac{N_1 - N_2}{2}$$

The model becomes:

$$\dot{F}_{1,2}(t) = (1 + i\alpha)[M_1 F_{1,2} + M_2 F_{2,1}(t)] - i\omega_s F_{1,2}(t) \pm \eta e^{-i(\phi + \omega_s t)} F_{1,2}(t - \tau) \quad (4.18)$$

$$\dot{M}_1 = \epsilon[J - M_1 - (M_1 + \nu)(|F_1|^2 + |F_2|^2) - M_2(F_1 \bar{F}_2 + \bar{F}_1 F_2)] \quad (4.19)$$

$$\dot{M}_2 = \epsilon[-M_2 - (M_1 + \nu)(F_1 \bar{F}_2 + \bar{F}_1 F_2) - M_2(|F_1|^2 + |F_2|^2)] \quad (4.20)$$

#### 4.1.3.3 Deriving the Characteristic Equation of the CW System

To derive an analytic expression for bifurcations a characteristic equation is required, which comes from solving the eigenvalues of the system. To find the characteristic equation, delay was re-introduced, but will be set to zero again later. After the system was linearised around the CW solution, which translates as follows to this linearised system,  $F_1 = E_s$ ,  $F_2 = 0$ ,  $M_1 = N_0$ ,  $M_2 = 0$ . The new variables were then split into real and complex parts using  $F_{1,2} = x_{1,2} + iy_{1,2}$ , making the system of variables  $\vec{v} = (x_1, y_1, M_1, x_2, y_2, M_2)$  and  $\frac{d}{dt} \vec{v} = A \vec{v}(t) + B \vec{v}(t - \tau)$ , where  $A$  and  $B$  are Jacobian matrices. To find these Jacobians,  $F_{1,2} = x_{1,2} + iy_{1,2}$  was entered into equations 4.18 - 4.20, and the real and imaginary parts were separated to get expressions for  $x_{1,2}$  and  $y_{1,2}$ . The equations were split into delayed and non-delayed parts and were then differentiated with respect to delayed and non-delayed variables to get the delayed and non-delayed Jacobians. The Jacobians were found to be of the form:

$$A = \begin{pmatrix} A_1 & 0 \\ 0 & A_1 \end{pmatrix}$$

$$B = \begin{pmatrix} B_1 & 0 \\ 0 & -B_1 \end{pmatrix}$$

where

$$A_1 = \begin{bmatrix} N & \omega_s - \alpha N & x_1 - \alpha y_1 \\ -(\omega_s - \alpha N) & N & \alpha x_1 + y_1 \\ -2\epsilon x_1(N + \nu) & -2\epsilon y_1(N + \nu) & -\epsilon(1 + x_1^2 + y_1^2) \end{bmatrix}$$

$$B = \begin{bmatrix} \eta \cos(\phi + \omega_s \tau) & \eta \sin(\phi + \omega_s \tau) & 0 \\ -\eta \sin(\phi + \omega_s \tau) & \eta \cos(\phi + \omega_s \tau) & 0 \\ 0 & 0 & 0 \end{bmatrix}$$



The characteristic function gives the bifurcations of the system of equations, and is of the form  $\chi^\tau(\Lambda) = \chi_L^\tau(\Lambda) \cdot \chi_T^\tau(\Lambda)$ .  $\chi_T^\tau(\Lambda)$ . This is used to generate the bifurcation diagrams and is given by equation 4.21

$$\chi_T^\tau(\Lambda) = \det(\Lambda I - A_1 + e^{-\Lambda\tau} B_1) \quad (4.21)$$

Inserting the calculated values for  $A$  and  $B$  into the following determinant yields:

$$\chi_T^\tau = \begin{vmatrix} \Lambda - N + e^{\Lambda\tau}\eta \cos \theta & -(\omega_s - \alpha N) + e^{-\Lambda\tau}\eta \sin \theta & x_1 \\ (\omega_s - \alpha N) - e^{-\Lambda\tau}\eta \sin \theta & \Lambda - N + e^{\Lambda\tau}\eta \cos \theta & a\alpha x_1 \\ 2\epsilon x_1(N + \nu) & 0 & \Lambda + \epsilon(1 + x_1^2) \end{vmatrix}$$

The determinant of this matrix was calculated at the fixed point,  $N_0 = -\eta \cos \theta$ ,  $\omega_s = -\eta(\alpha \cos \theta + \sin \theta)$ ,  $x_1^2 = \frac{J + \eta \cos \theta}{\nu - \eta \cos \theta}$  where  $\theta = \phi + \omega_s \tau$ . Finally the characteristic equation was found, shown here in equation 4.22.

$$\begin{aligned} \chi_T^\tau &= (\Lambda + \epsilon(1 + S))[\Lambda^2 \eta \cos(\theta)(1 + e^{-\Lambda\tau})\Lambda + \eta^2(1 + e^{-\Lambda\tau})^2] \\ &+ 2\eta S(\nu - \eta \cos(\theta))[\Lambda + \eta(\cos(\theta) - \alpha \sin(\theta))(1 + e^{-\Lambda\tau})] = 0 \end{aligned} \quad (4.22)$$

Where

$$S = \frac{J + \eta \cos(\phi)}{\nu - \eta \cos(\phi)}$$

It is the value of the eigenvalue  $\Lambda$  that determines what kind of bifurcation the characteristic equation represents.

#### 4.1.3.4 Zero Delay Pitchfork and Hopf Bifurcations

The two main bifurcations of the CW states that occur are Pitchfork and Hopf bifurcations and are defined in Sec. 1.7. Delay was set to zero again, and to find a pitchfork bifurcation  $\Lambda$  was set to zero,  $\Lambda = 0$ . Subbing this value for  $\Lambda$  into the characteristic equation 4.22, gave the pitchfork implicit function, equation 4.23.

$$\eta(1 + S) + S(\nu - \eta \cos(\phi))(\cos(\phi) - \alpha \sin(\phi)) = 0 \quad (4.23)$$

For a Hopf bifurcation the eigenvalue is pure imaginary,  $\Lambda = i\Omega$ . Subbing this into the characteristic equation and separating real and imaginary parts, gave

two expressions for  $\Omega^2$ . Equating these and re-arranging, the Hopf implicit function, equation 4.24, was found.

$$\begin{aligned} & [2\eta(\epsilon \cos(\phi)(2 + S) + 2\eta) + 2\epsilon S\nu][\epsilon(1 + S) + 4\eta \cos(\phi)] \\ & - 4\epsilon\eta(\eta(1 + S) + S(\nu \cos(\phi)))(\cos(\phi) - \alpha \sin(\phi)) = 0 \end{aligned} \quad (4.24)$$

These implicit functions needed to be solved graphically. To do this a number of steps were followed. Firstly the fixed parameters were set ( $\alpha$ ,  $J$ ,  $\epsilon$  and  $\nu$ ), and then meshes  $\phi$  and  $\eta$  were defined ( $\phi$  goes from 0 to  $2\pi$  and  $\eta$  from 0 to 0.5). After that for each  $\eta$  and  $\phi$  the associated  $S$  value was calculated. Finally each  $\phi$ ,  $\eta$  and associated  $S$  value were entered into the respective implicit function and a 3D surface was plotted. The bifurcation diagram was found by finding the intersection of this 3D surface with the  $Z=0$  plane, as highlighted in figure 4.2 and 4.3.

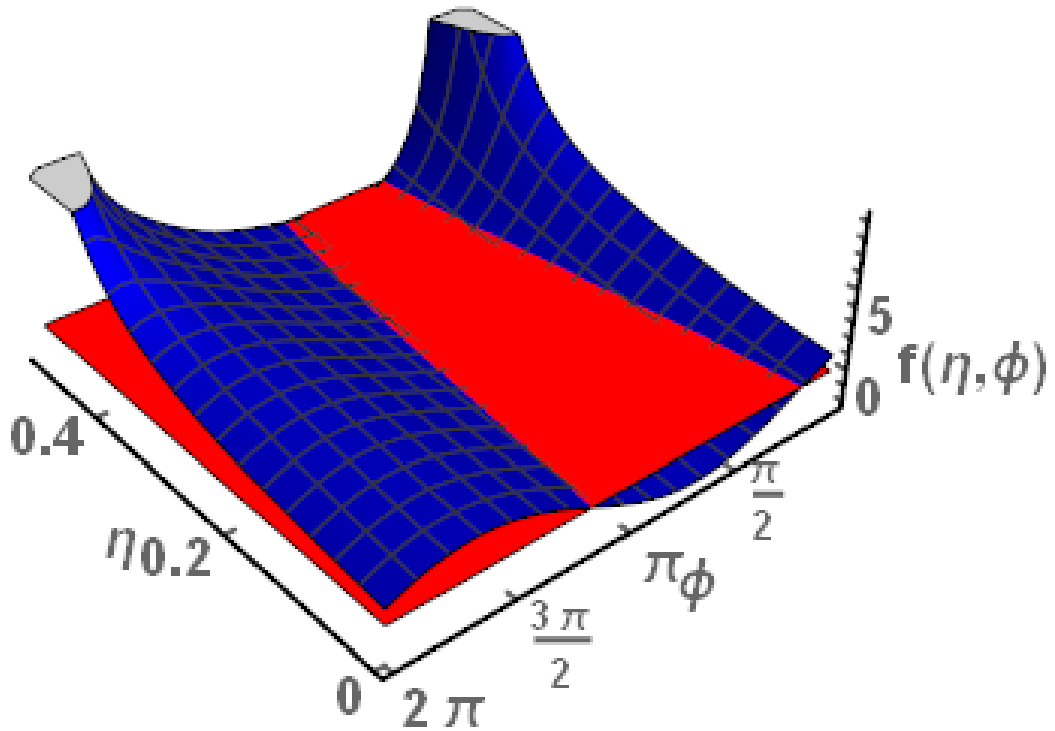


Figure 4.2: 3D plot of Eqn. 4.23, for varying  $(\phi, \eta)$  (blue) along with  $f(\eta, \phi) = 0$  plane (red).

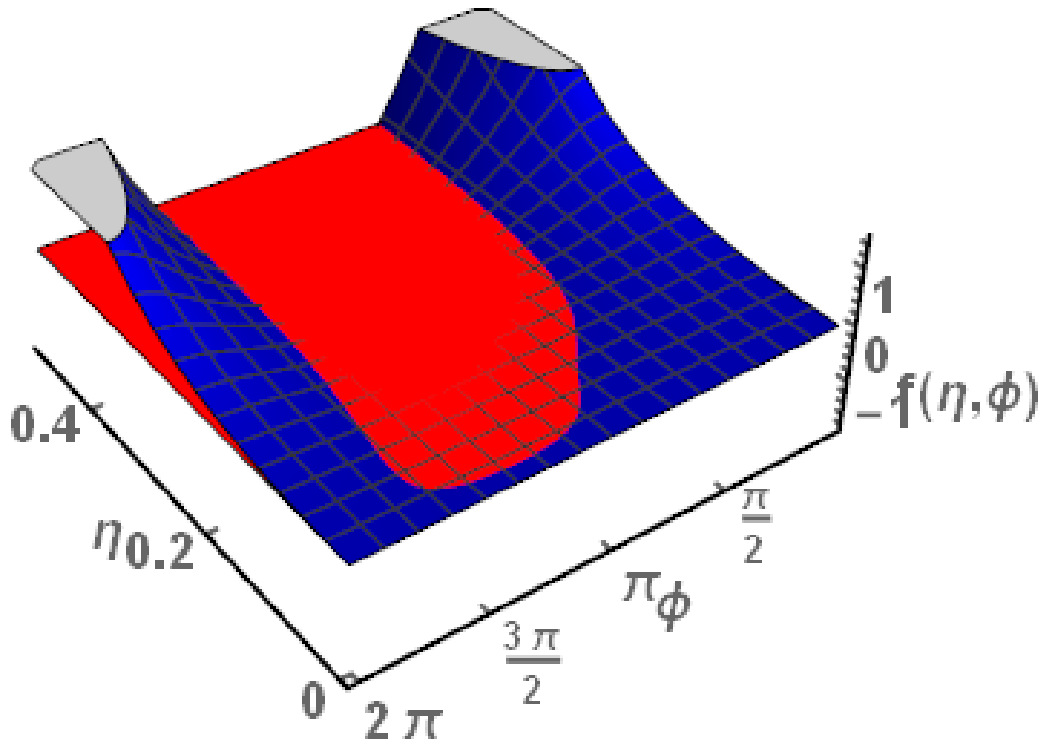


Figure 4.3: 3D plot of Eqn. 4.24, for varying  $(\phi, \eta)$  (blue) along with  $f(\eta, \phi) = 0$  plane (red).

The bifurcation diagrams can be seen in figure 4.4.  $\phi$  is a phase angle, so the range  $0 - 2\pi$  will be considered.  $\eta$  will be considered over the range of  $0 - 0.5$ , as this is the fraction of light reaching one laser from the other, it can go from  $0 - 1$ .

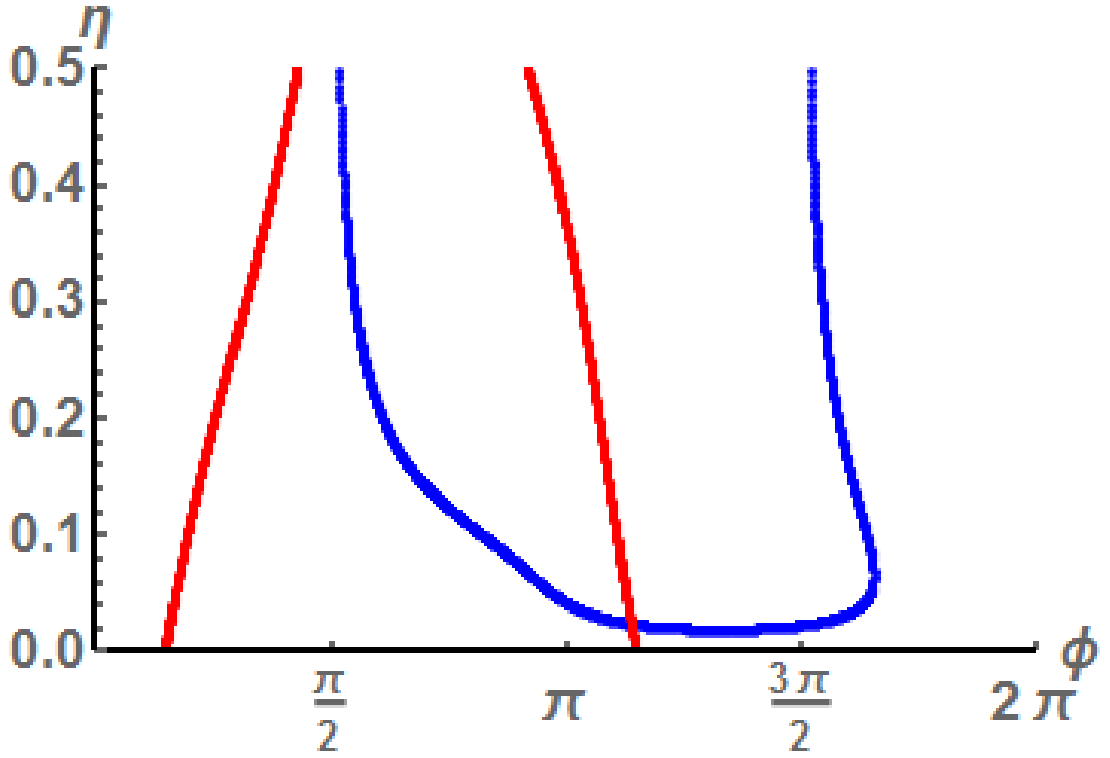


Figure 4.4: Diagrams of the Hopf (blue) and Pitchfork (red) bifurcations for zero delay.

#### 4.1.4 Analytical bifurcations of the delayed, no detuning system

Now that the basic case of no delay time between the lasers has been considered, a short delay time will now be introduced to improve how well the model recreates the experiment. When delay is re-introduced to the calculations the solving process must also be re-evaluated. Since  $\omega_s$  is no longer a constant, it must now be solved for each  $\eta$  and  $\phi$ .

$$\omega_s = -\eta(\alpha \cos(\theta) + \sin(\theta)) \quad (4.25)$$

where

$$\theta = \phi + \omega_s \tau$$

The expression for  $\omega_s$ , equation 4.25 was re-written as an implicit function using the trigonometric identity  $A \cos(\theta) + B \sin(\theta) = C \sin(\theta + \delta)$ .

$$y = \omega_s + \eta \sqrt{1 + \alpha^2} \sin(\phi + \omega_s \tau + \arctan(\alpha)) \quad (4.26)$$

Finding the roots of this equation gave the values of  $\omega_s$ . The issue encountered here was how to handle the multiple roots. An example of these multiple roots can be seen in figure 4.5.

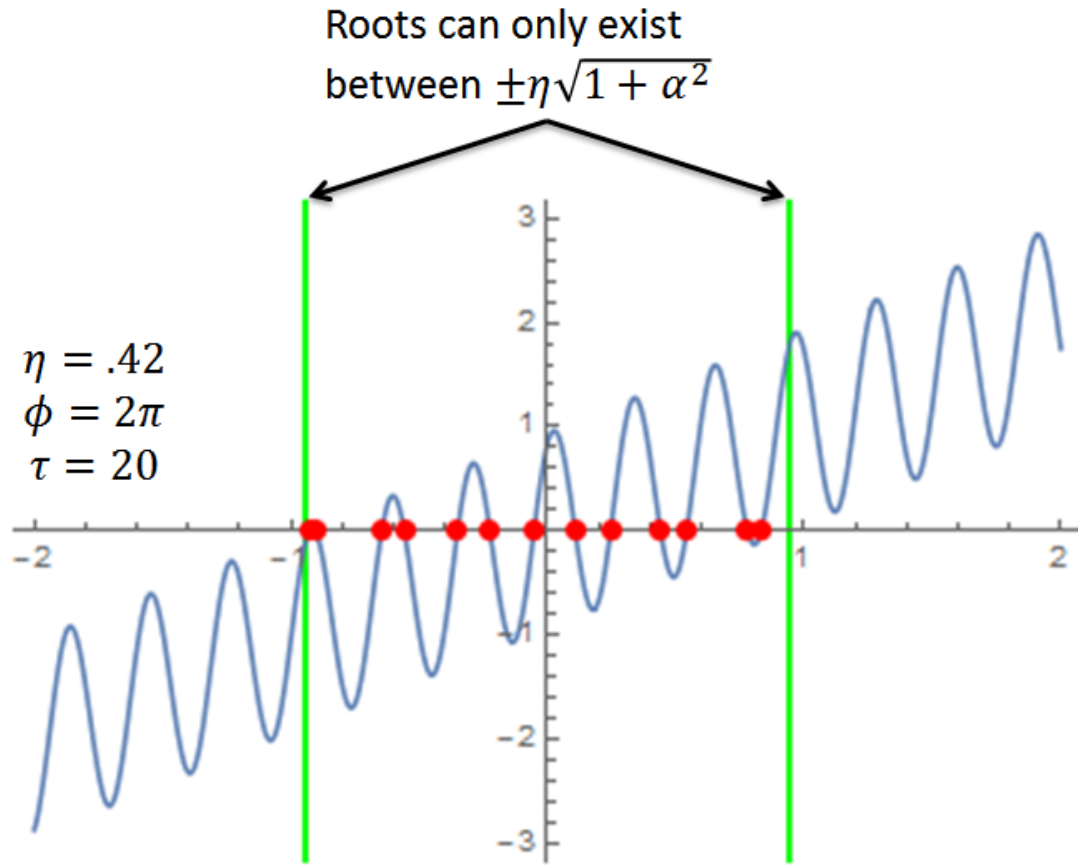


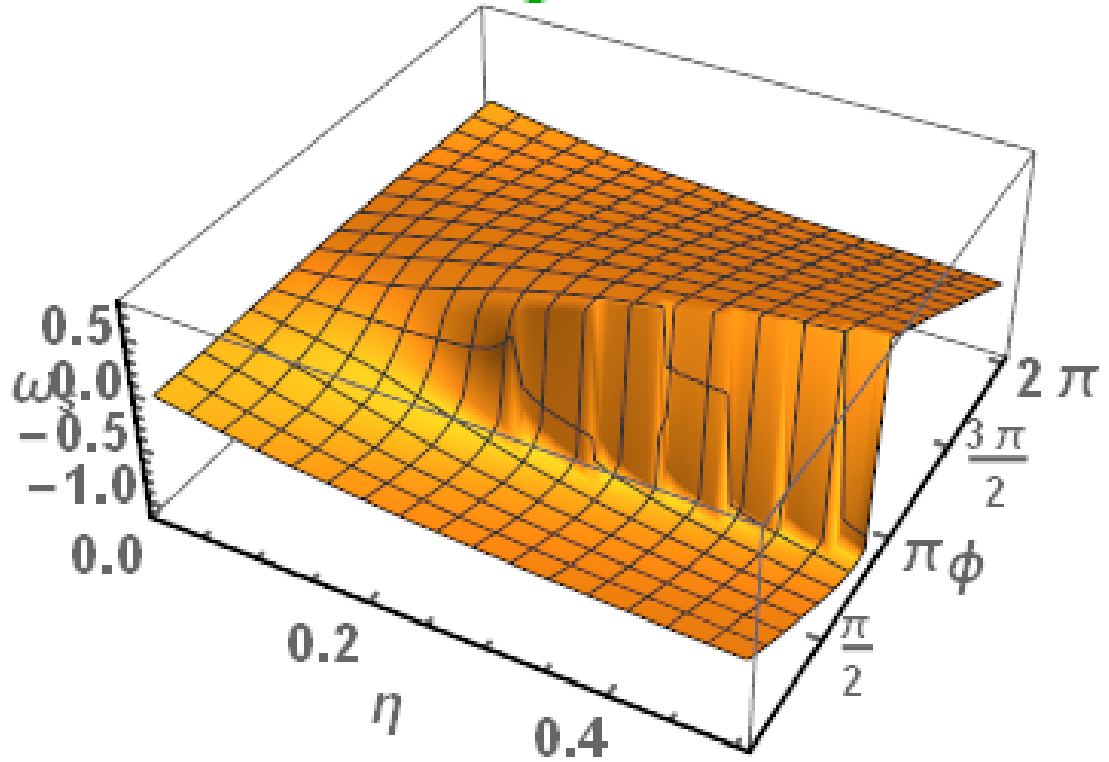
Figure 4.5: Example of multiple roots of  $\omega_s$  from solving Eqn. 4.26, with  $\eta = 0.42$ ,  $\phi = 2\pi$  and  $\tau = 20$ .

In the zero delay case,  $\omega_s$  was always single valued and when it became multi-valued a way of handling this had to be developed.

Unsure of how to handle the generation of these new roots to methods were tried: main root following and middle root following. For the main root following, if  $\omega_s$  was multivalued the first value was used. In contrast, the middle root following method took the middle root (e.g. if there were five roots, the third value was taken) if  $\omega_s$  was multi-valued, noting that there was always an odd number of roots. A 2-D variable sweep ( $\eta$  and  $\phi$ ) of equation 4.5 is shown in figure 4.6.

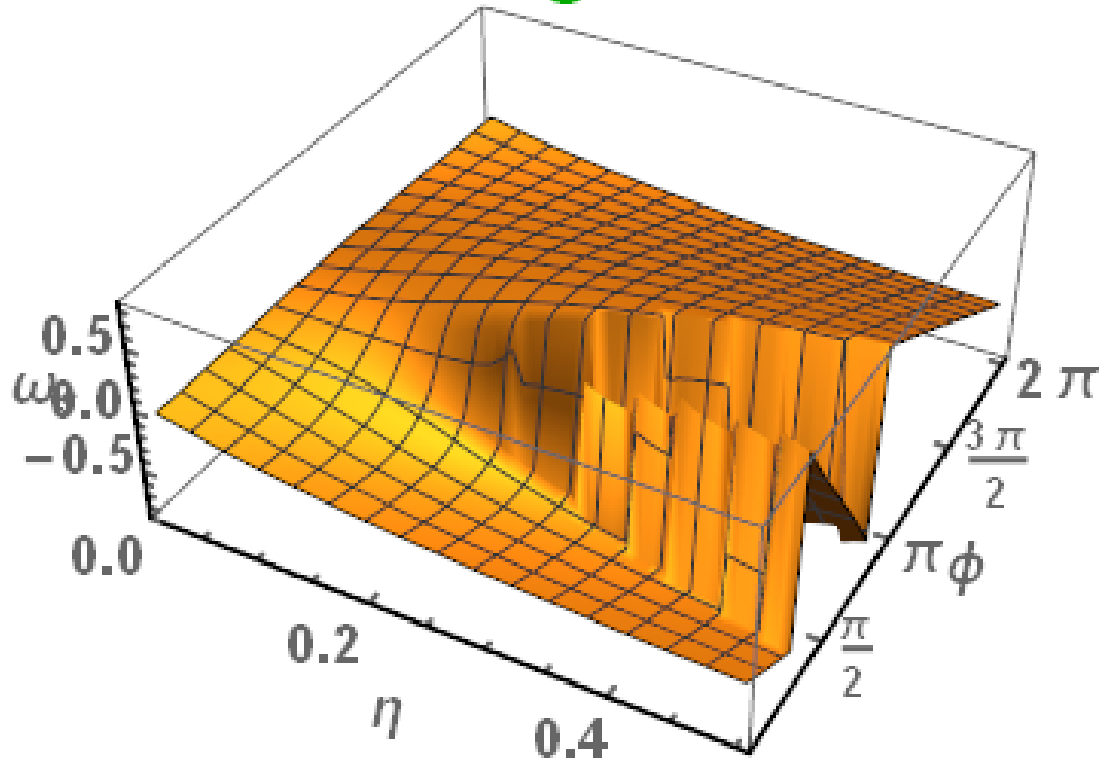
It was discovered that to find the bifurcation line, the original root must be followed. Using the full characteristic equation 4.22, the same process for

## First Root algorithm for $\tau=2$



(a) First root algorithm applied to equation 4.5 for a 2D mesh of  $\eta$  and  $\phi$ .

## Middle Root algorithm for $\tau=2$



(b) First root algorithm applied to equation 4.5 for a 2D mesh of  $\eta$  and  $\phi$ .

Figure 4.6: Examples of main and middle root algorithms.

finding the Pitchfork bifurcation was followed, i.e. setting  $\Lambda = 0$ , gave equation 4.27.

$$\epsilon(1+S)4\eta^2 + 2\eta S(\nu - \eta \cos(\phi + \omega_s \tau))(2\eta(\cos(\phi + \omega_s \tau) - \alpha \sin(\phi + \omega_s \tau))) = 0 \quad (4.27)$$

To solve this equation, a similar process to the non-delayed version was followed, except this time for each  $\eta$  and  $\phi$  the value of  $\omega_s$  had to be calculated. The result for different values of  $\tau$  can be seen in figure 4.7.

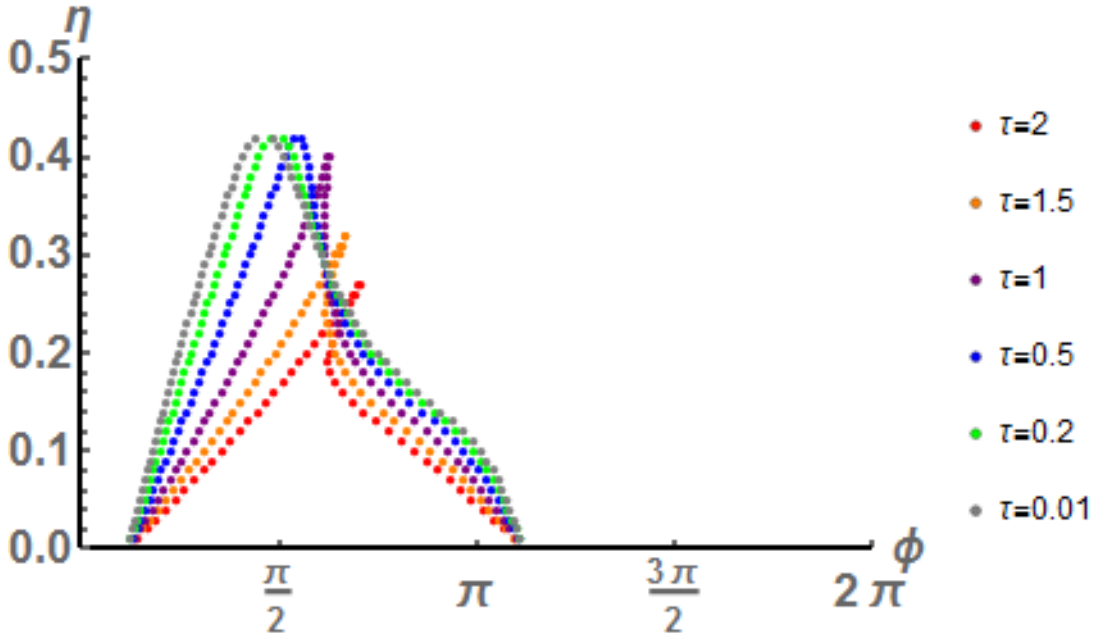


Figure 4.7: Delayed pitchfork bifurcations for varying  $\tau$  values.

Next the delayed Hopf bifurcation was investigated. As in the non-delay case, a value of  $\Lambda = i\Omega$  was subbed into the characteristic equation 4.22. This gave real and imaginary expressions, which are seen in equations 4.28 and 4.29 respectively.

$$\begin{aligned} -\Omega^2 + 2\eta\Omega \cos(\theta) \sin(\Omega\tau) + (1 + \cos(\Omega\tau))(2\eta^2\Omega \sin(\Omega\tau) + 2\eta^2\epsilon(1 + S) \cos(\Omega\tau) \\ + 2\epsilon\eta S(\nu - \eta \cos(\theta))(\cos(\theta) - \alpha \sin(\theta))) = 0 \end{aligned} \quad (4.28)$$

$$(1 + \cos(\Omega\tau))[2\eta\Omega(\cos(\theta) + \eta \cos(\Omega\tau)) - 2\eta^2\epsilon(1 + S)\sin(\Omega\tau)] + 2\epsilon S(\nu - \eta \cos(\theta))$$

$$[\Omega - \eta(\cos(\theta) - \alpha \sin(\theta))\sin(\Omega\tau)] = 0$$

(4.29)

There was no explicit way of solving these equations for  $(\phi, \eta)$ , and previous works neglect how to solve this problem, [25], therefore another solution method was required. The Hopf bifurcation occurs when the eigenvalue of the characteristic equation is purely imaginary (hence why  $\Lambda = i\Omega$  was subbed into 4.22). By entering the full characteristic equation, Eqn. 4.22, into a numerical root finder, and specifically looking for the complex root, at any  $(\phi, \eta)$  values where the complex root is purely complex ( $Re(\Lambda) = 0$ ) a Hopf bifurcation occurs. The parameter space was broken down into a series of  $\phi$  values for a fixed  $\eta$ , and for each  $\phi$  the real part of the complex root was tracked, giving figure 4.8. Using this initial data, a bisection method was implemented to refine the answer and find exactly where the curve crosses the zero axis. The Hopf bifurcations for a range of  $\tau$  values is shown in 4.9.

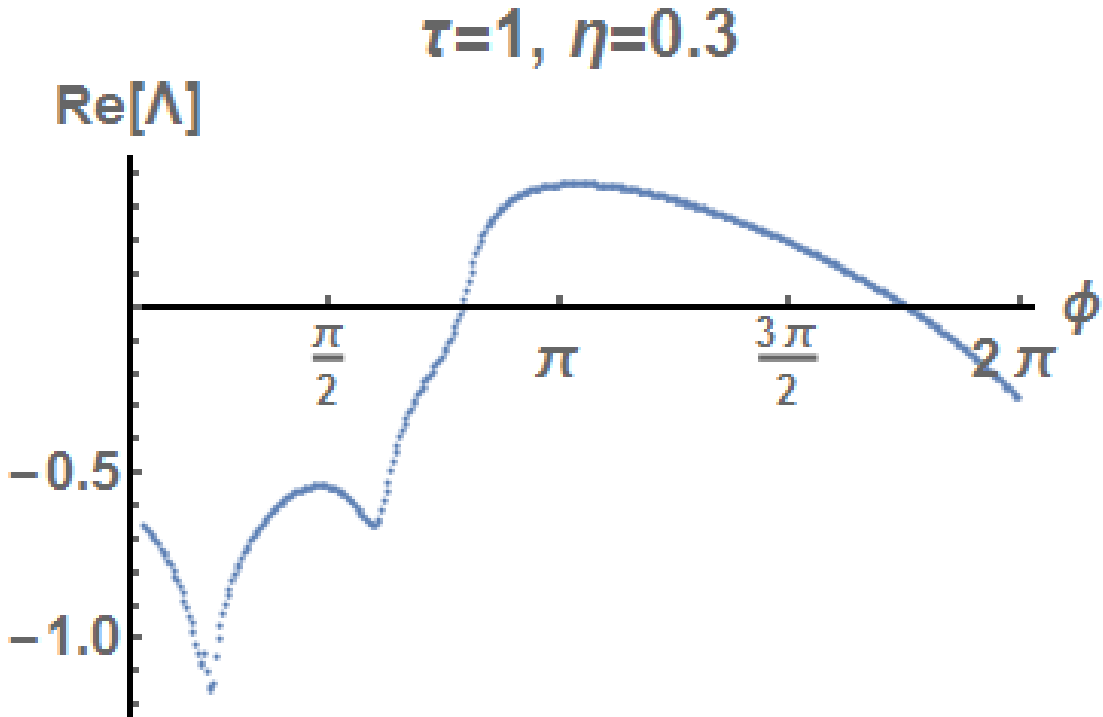


Figure 4.8: Plot of the real part of the eigenvalue of Eqn. 4.22 for varying  $\phi$  and  $\eta = 0.3$  and  $\tau = 1$ . Where this curve crosses the  $y = 0$  axis, a Hopf bifurcation occurs.



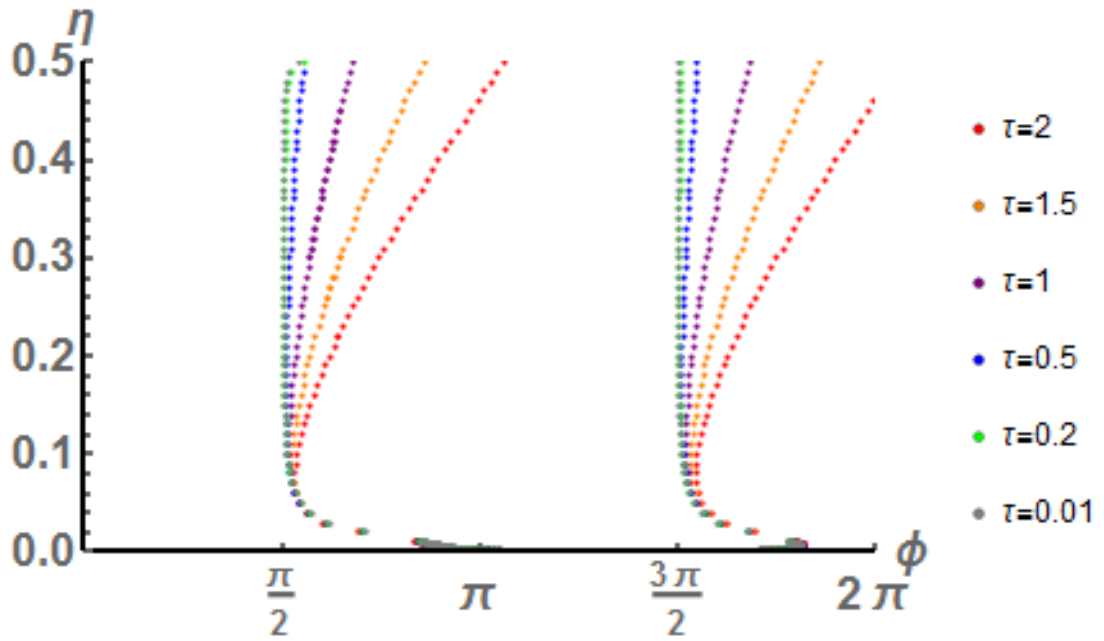


Figure 4.9: Delayed Hopf bifurcations for varying  $\tau$  values.

The characteristic equation, 4.22, can also be used to track the stability of the CW solutions ( $E_{1,2} = E_0 e^{i\omega_0 t}$ ). Performing root finding on this equation (real and complex roots), and analysing the sign of real root/real part of the complex root gives the stability. If any  $Re[\Lambda] \geq 0$  the solution is unstable. Breaking the parameter space into a 2D mesh, and analysing the stability compared to the bifurcations found previously yields figure 4.10 and 4.11. This shows how the bifurcations affect the stability of the CW states.

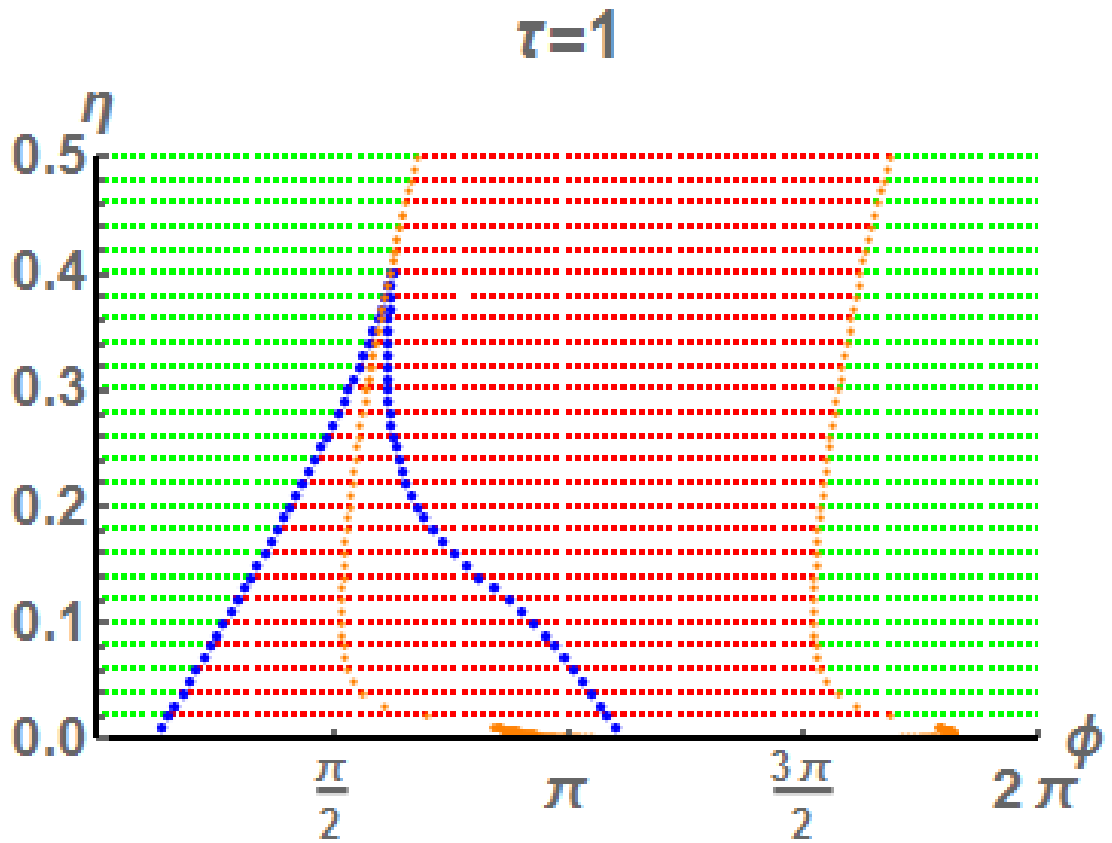


Figure 4.10: Diagram of the  $(\phi, \eta)$  space, showing stable CW states (green), unstable CW states (red), pitchfork bifurcation (blue), Hopf bifurcation (Orange), for  $\tau = 1$ .

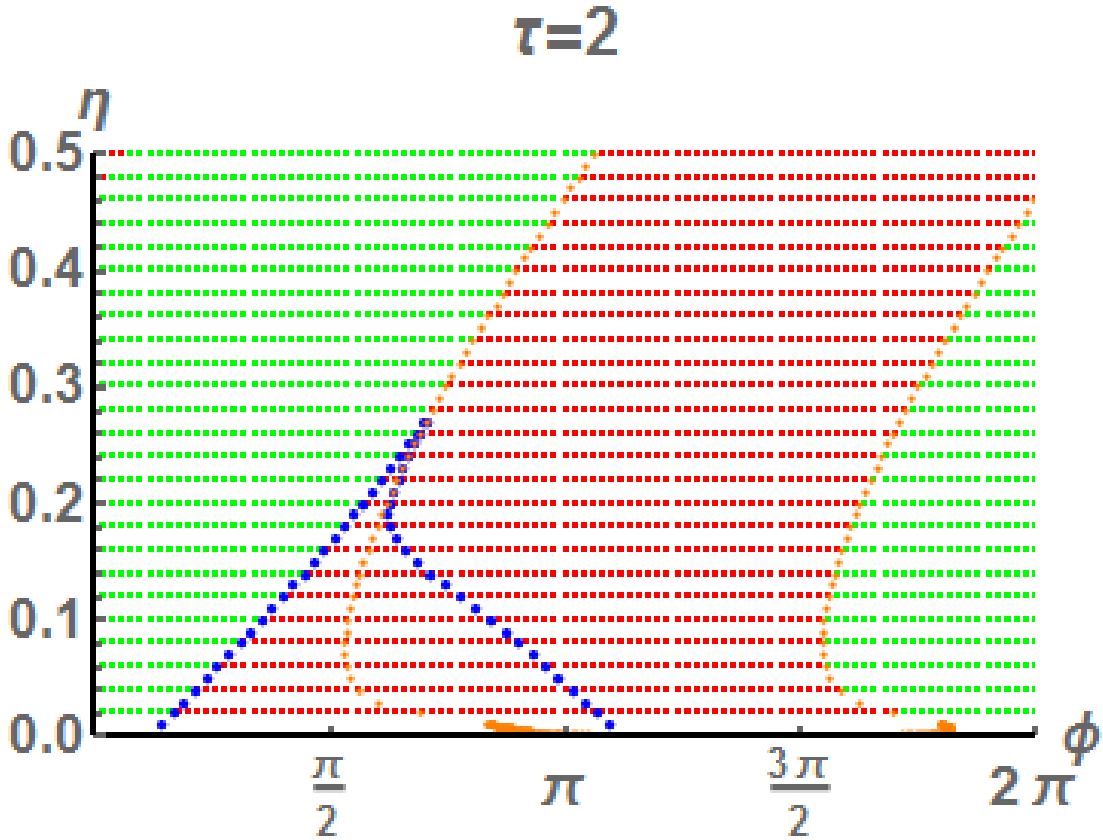


Figure 4.11: Diagram of the  $(\phi, \eta)$  space, showing stable CW states (green), unstable CW states (red), pitchfork bifurcation (blue), Hopf bifurcation (Orange), for  $\tau = 2$ .

#### 4.1.5 Saddle-node bifurcation

In Sec. 4.1.4 it was noted that there are multiple possible values of  $\omega_s$  based on the root finding result of Eqn. 4.26.

$$y = \omega_s + \eta \sqrt{1 + \alpha^2} \sin(\phi + \omega_s \tau + \arctan(\alpha))$$

Transitions between regions of different numbers of solutions for  $\omega_s$  is a bifurcation. It is the destruction/creation of possible solution branches. This typifies a saddle-node bifurcation. By using the same parameter grid created previously, and looking for the change from one solution of  $\omega_s$  to three solutions of  $\omega$ , and performing a bisection to narrow down the answer gives figure4.12.

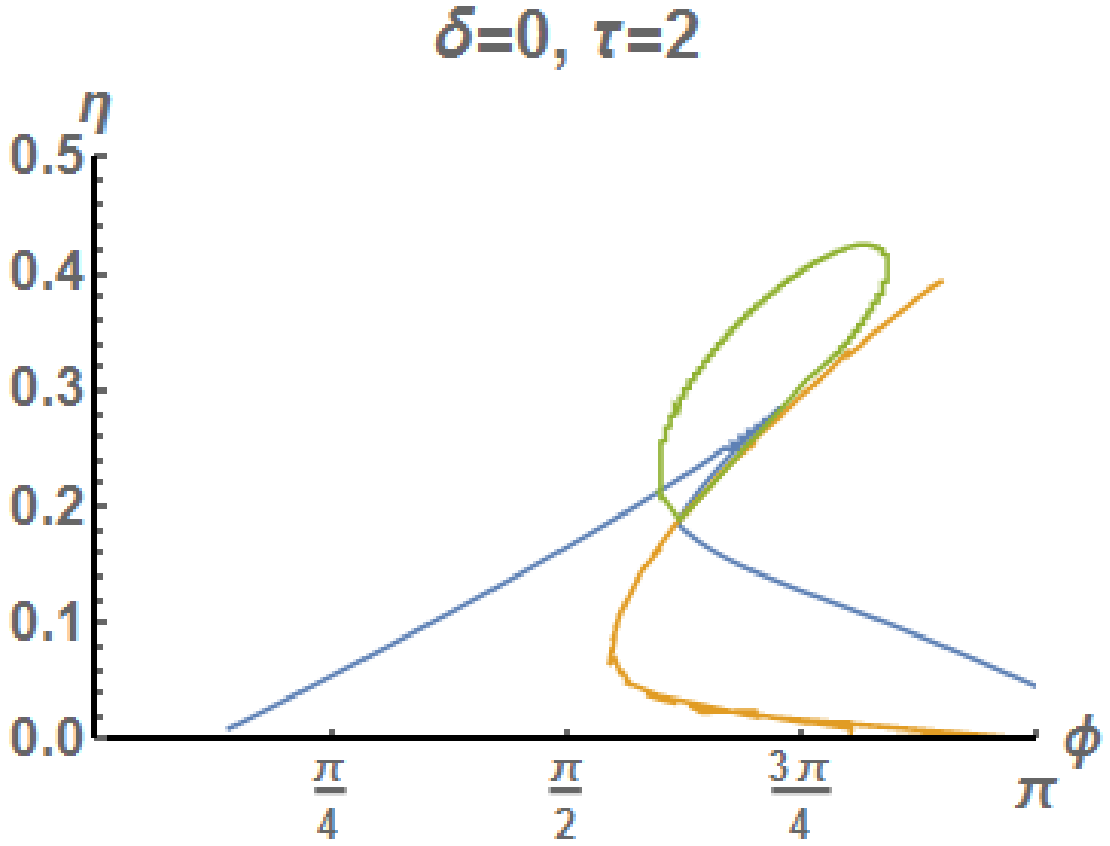


Figure 4.12: Plot of the pitchfork bifurcation (blue), Hopf bifurcation (orange) and the saddle-node bifurcation (green) for  $\tau = 2$  over the  $(\phi, \eta)$  space.

It is important to note, it does not change the type of dynamics, i.e. not a change of one colour to two colour state, merely generates more solutions of the same type, i.e. multiple values of  $\omega_s$ .

#### 4.1.6 Analytical solutions of one colour states in the zero detuning case

A bifurcation study establishes the boundaries between different solutions of the model, but it is also important to consider the forms of the solutions present in these regions. In this section an analytical breakdown of the behaviours associated with the bifurcations shown previously will be presented and compared with numerically solved solutions. In Sec. 4.1.3.2 the CW solution for the complex electric fields ( $E_{1,2}$ ) was introduced. This is a subset of what is called a one colour state. One colour states occur when the FFT of the complex fields,  $\tilde{E}_{1,2}$ , which shows the frequencies present in the rapidly oscillating physical field, has a single peak, or if the power output ( $|E_{1,2}|$ ) is

constant as can be seen in figure 4.13. Note that ideally this single peak would have no width, if an infinite length time trace could be considered. Due to this there is a width to the peak. The slowly varying field,  $E_{1,2}$ , can be recovered via  $\tilde{E}_{1,2} = E_{1,2}(t)e^{i\omega_0 t}$ , where  $\omega_0$  is the free running frequency of the laser. The mathematical definition of a one colour state is given by Eqn. 4.30-4.32.

$$\tilde{E}_1 = a_1 e^{i\omega_a t} \quad (4.30)$$

$$\tilde{E}_2 = a_2 e^{i\omega_a t} e^{i\delta_a} \quad (4.31)$$

$$N_{1,2} = N_S \quad (4.32)$$

$$(4.33)$$

Here  $a_{1,2}$  are the amplitudes (the state is called symmetric if  $a_1 = a_2$ ),  $\omega_A$  is the single frequency present, and  $\delta_a$  allows for a phase difference between the solutions ( $\delta_a = 0$  in phase,  $\delta_a = \pi$  anti-phase). It is important to note that this is an exact solution, as every variable has an assumed solution. Next an analytical prediction of the one colour state solutions shall be presented, these will then be compared with simulated results, obtained by solving time traces of  $E_{1,2}$  and taking the fast Fourier transform (FFT).

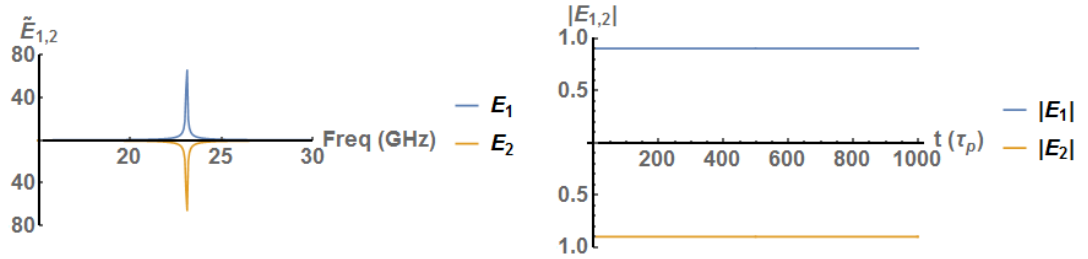


Figure 4.13: FFT of  $\tilde{E}_{1,2}$  (left) and time trace of  $|\tilde{E}_{1,2}|$  (right) for  $\eta = 0.1$ ,  $\phi = 0$ ,  $\tau = 0$  and  $\delta = 0$ .

#### 4.1.6.1 Symmetric in phase/anti-phase one colour solutions

By substituting the one colour ansatz (Eqn. 4.30 and 4.31) into Eqn. 4.6 and 4.7, one ends up with Eqn. 4.34, [32].

$$\frac{\omega_A^2}{\eta^2(1 + \alpha^2)} = \sin^2(\phi + \omega_a \tau + \arctan(\alpha)) - \sin^2(\delta_a) \quad (4.34)$$

This equation holds for the in-phase and anti-phase symmetric solutions.

Figure 4.14 shows the in-phase analytic solution of  $\omega_a$  from Eqn. 4.34 in blue,

along with the peak wavelength of FFT of  $E_1$  from solving Eqn. 4.6-4.9 (with  $\tau = 0$  and  $\delta = 0$ ) in orange, for  $\eta = 0.1$  and varying  $\phi$  from  $0 - 2\pi$ . The stability of the in-phase one colour solution is also included (stable in green, unstable in red) The stability is found by solving the characteristic equation Eqn. 4.21 for  $\lambda$  at each  $(\phi, \eta)$  value and if  $Re[\lambda] > 0$  the solution is unstable, otherwise it is stable.

On the left and right hand side of the diagram there is good overlap of the analytic and simulated results, and they line up well with the stability of the in phase one colour solution. The solution in the middle of diagram are the anti-phase solutions ( $\delta_a = \pi$ ), which Eqn. 4.21 does not track the stability of.

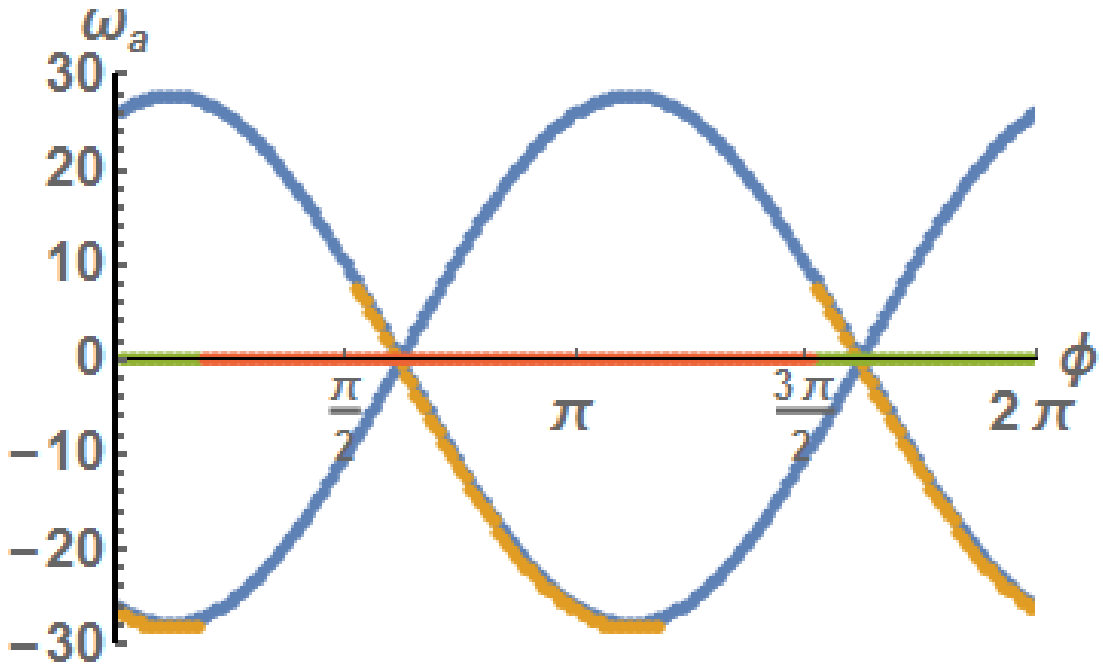


Figure 4.14: Plot of  $\omega_a$  from Eqn. 4.34 (blue), peak wavelength of FFT of  $E_1$  from solving Eqn. 4.6-4.9 (with  $\tau = 0$  and  $\delta = 0$ ) (orange)) along with the stability of the in-phase one colour solution (stable in green, unstable in red), for  $\eta = 0.1$  and varying  $\phi$  from  $0 - 2\pi$ .

Next  $\tau$  was re-introduced to Eqn. 4.34 and compared with simulation results and stability of the in-phase one-colour states. This is shown in figure 4.15 and 4.16 for  $\tau = 0.5$  and  $2$  respectively. Similar to the case without delay, there is good agreement between the simulated and analytical results, and the stability lines up with stability of the in-phase one colour states from Eqn. 4.21.

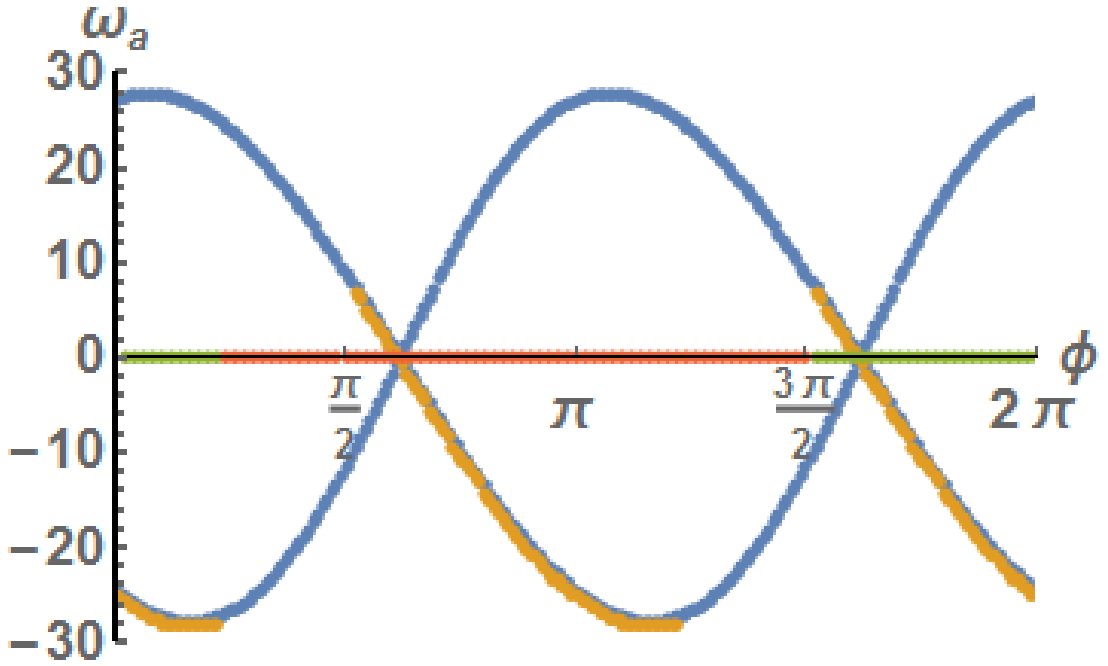


Figure 4.15: Plot of  $\omega_a$  from Eqn. 4.34 (blue), peak wavelength of FFT of  $E_1$  from solving Eqn. 4.6-4.9 ( $\delta = 0$ ) (orange)) along with the stability of the in-phase one colour solution (stable in green, unstable in red), for  $\tau = 0.5, \eta = 0.1$  and varying  $\phi$  from  $0 - 2\pi$ .

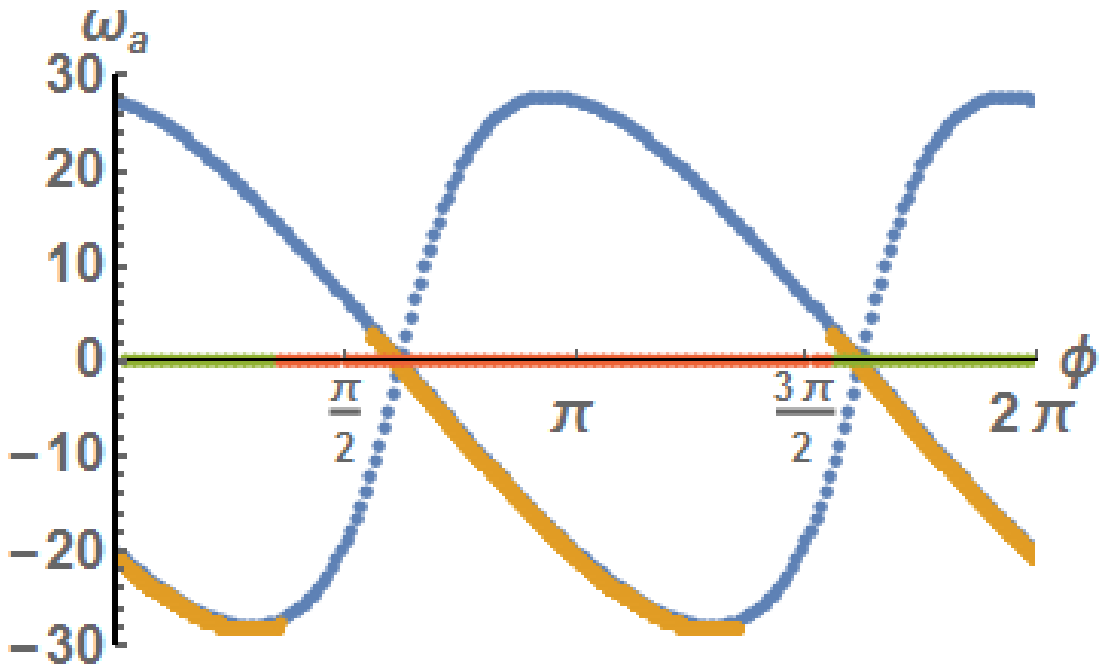


Figure 4.16: Plot of  $\omega_a$  from Eqn. 4.34 (blue), peak wavelength of FFT of  $E_1$  from solving Eqn. 4.6-4.9 ( $\delta = 0$ ) (orange)) along with the stability of the in-phase one colour solution (stable in green, unstable in red), for  $\tau = 2, \eta = 0.1$  and varying  $\phi$  from  $0 - 2\pi$ .

#### 4.1.6.2 Symmetry broken one colour states

From Eqn. 4.30 and 4.31 there also exists a solution where the amplitudes of the fields  $E_{1,2}$  do not match, i.e.  $a_1 \neq a_2$ , referred to as a symmetry broken one colour state. To analytically solve for these symmetry broken solutions a more rigorous approach is required. Outlined in [25] is a method for solving the no delay, no detuning case ( $\tau = 0, \delta = 0$ ). The one colour ansatz is substituted into Eqn. 4.6-4.9 giving the following set of equations.

$$a_1 i\omega_a = (1 + i\alpha)N_1 a_1 + \eta a_2 e^{-i(\delta_a + \phi)} \quad (4.35)$$

$$a_2 i\omega_a = (1 + i\alpha)N_2 a_2 + \eta a_1 e^{-i(\delta_a - \phi)} \quad (4.36)$$

$$J - N_1 - (N_1 + \nu)a_1^2 = 0 \quad (4.37)$$

$$J - N_2 - (N_2 + \nu)a_2^2 = 0 \quad (4.38)$$

Separating these into real and imaginary parts yields:

$$a_1 N_1 + a_2 \eta \cos(\phi + \delta_a) = 0 \quad (4.39)$$

$$a_1(\alpha N_1 - \omega_a) - a_2 \eta \sin(\phi + \delta_a) = 0 \quad (4.40)$$

$$a_2 N_2 + a_1 \eta \cos(\delta_a - \phi) = 0 \quad (4.41)$$

$$a_2(\alpha N_2 - \omega_a) + a_1 \eta \sin(\delta_a - \phi) = 0 \quad (4.42)$$

$$J - N_1 - (N_1 + \nu)a_1^2 \quad (4.43)$$

$$J - N_2 - (N_2 + \nu)a_2^2 \quad (4.44)$$

The ratio of the amplitudes is defined to be  $x = a_2/a_1$  and the system of unknowns then becomes  $x, \delta_a, \omega_a, N_1, N_2$ .

$$N_1 + x\eta \cos(\phi + \delta_a) = 0 \quad (4.45)$$

$$(\alpha N_1 - \omega_a) - x\eta \sin(\phi + \delta_a) = 0 \quad (4.46)$$

$$xN_2 + \eta \cos(\delta_a - \phi) = 0 \quad (4.47)$$

$$x(\alpha N_2 - \omega_a) + \eta \sin(\delta_a - \phi) = 0 \quad (4.48)$$

$$\frac{(J - N_2)(N_1 + \nu)}{(J - N_1)(N_2 + \nu)} = x^2 \quad (4.49)$$

The variable,  $x$  is then eliminated from the system using the following pairs of equations, (4.45,4.46), (4.47,4.48), (4.45,4.47), and (4.45,4.49). This leaves a system with unknowns  $\delta_a, \omega_a, N_1, N_2$ .



$$N_1 \sin(\phi + \delta_a) + (\alpha N_1 - \omega_a) \cos(\phi + \delta_a) = 0 \quad (4.50)$$

$$N_2 \sin(\delta_a - \phi) - (\alpha N_2 - \omega_a) \cos(\delta_a - \phi) = 0 \quad (4.51)$$

$$N_1 N_2 = \eta^2 \cos(\phi + \delta_a) \cos(\delta_a - \phi) \quad (4.52)$$

$$\frac{(J - N_2)(N_1 + \nu)}{(J - N_1)(N_2 + \nu)} = \frac{N_1^2}{\eta^2 \cos^2(\delta_a + \phi)} \quad (4.53)$$

$N_1$  and  $N_2$  can be determined from Eqn. 4.50 and 4.51.

$$N_1 = \omega_a / [\alpha + \tan(\phi + \delta_a)] \quad (4.54)$$

$$N_2 = \omega_a / [\alpha + \tan(\phi - \delta_a)] \quad (4.55)$$

Substituting these into Eqn. 4.52, an expression for  $\omega_a$  can be obtained as a function of  $\delta_a$ .

$$\omega_a^2 = \eta^2 \cos(\phi + \delta_a) \cos(\phi - \delta_a) [\tan(\phi + \delta_a) + \alpha] [\tan(\phi - \delta_a) + \alpha] \quad (4.56)$$

Eqn. 4.54 and 4.55 is then entered into Eqn. 4.53.

$$\frac{[J[\tan(\phi + \delta_a) + \alpha] - \omega_a][\nu[\tan(\phi - \delta_a) + \alpha] + \omega_a]}{J[\tan(\phi - \delta_a) + \alpha] - \omega_a[\nu[\tan(\phi + \delta_a) + \alpha] + \omega_a]} = \frac{\eta^2}{\omega_a^2} \cos^2(\phi + \delta_a) [\alpha + \tan(\phi + \delta_a)]^2 \quad (4.57)$$

Eqn. 4.56 can be substituted into Eqn 4.56, giving a transcendental equation for  $\delta_a$  that can be solved numerically. This is made easier as  $\delta_a$  is constrained to the interval  $(0, 2\pi)$ . Figure 4.17 shows the analytic symmetry broken one colour state solution,  $\omega_a$ , for  $\eta = 0.1$  and varying  $\phi$ . A small overlap is seen at approximately  $\frac{\pi}{2}$  and  $\frac{3\pi}{2}$ , this means that for the no delay/ detuning case, there are only small windows of stable symmetry broken one colour behaviour.

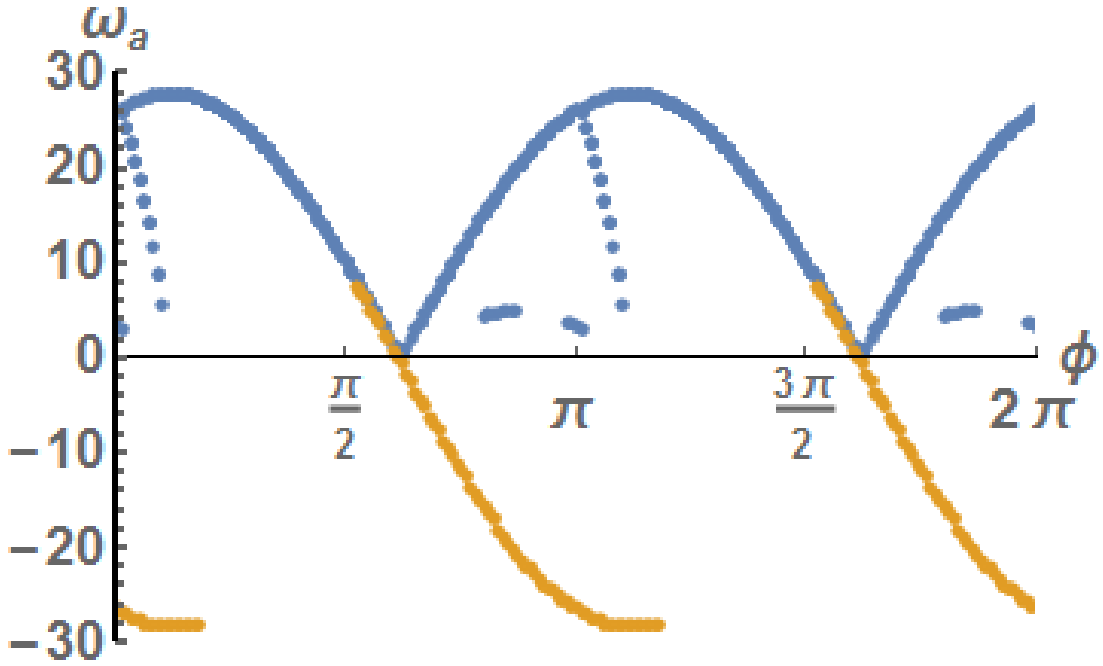


Figure 4.17: Plot of symmetry broken one colour solution,  $\omega_a$  from solving Eqn. 4.57 (blue), and peak wavelength of FFT of  $E_1$  from solving Eqn. 4.6-4.9 (with  $\tau = 0$  and  $\delta = 0$ ) (orange)), for  $\eta = 0.1$  and sweeping  $\phi$  from  $0 \rightarrow 2\pi$ .

Next, delay is included and Eqn. 4.35 and 4.36 become:

$$a_1 i \omega_a = (1 + i\alpha) N_1 a_1 + \eta a_2 e^{-i(\delta_a + \phi + \omega_a \tau)} \quad (4.58)$$

$$a_2 i \omega_a = (1 + i\alpha) N_2 a_2 + \eta a_1 e^{-i(\delta_a - \phi + \omega_a \tau)} \quad (4.59)$$

Now the complex exponential terms contain a  $\omega_a \tau$  term. Solving for  $\omega_a$  yields:

$$\omega_a^2 = \eta^2 \cos(\phi + \delta_a + \omega_a \tau) \cos(\phi - \delta_a + \omega_a \tau) [\tan(\phi + \delta_a + \omega_a \tau) + \alpha] [\tan(\phi - \delta_a + \omega_a \tau) + \alpha] \quad (4.60)$$

$$\begin{aligned} & \frac{J(\alpha + \tan(\phi + \omega_a \tau + \delta_a) - \omega_a) \nu(\alpha + \tan(\phi + \omega_a \tau - \delta_a) + \omega_a)}{J(\alpha + \tan(\phi + \omega_a \tau - \delta_a) - \omega_a) \nu(\alpha + \tan(\phi + \omega_a \tau + \delta_a) + \omega_a)} \\ &= \frac{\eta^2}{\omega_a^2} \cos(\phi + \omega_a \tau + \delta_a)^2 (\alpha + \tan(\phi + \omega_a \tau + \delta_a))^2 \quad (4.61) \end{aligned}$$

Though it is not possible to solve Eqn. 4.60 explicitly and substitute into Eqn. 4.61, they do form two equations with only two unknowns, so through root

finding a numerical solution can be found. An example of this is shown in figure 4.18 and 4.19, for  $\tau = 0.5$  and  $2$ ,  $\eta = 0.1$  and varying  $\phi$  from  $0 \rightarrow 2\pi$ .

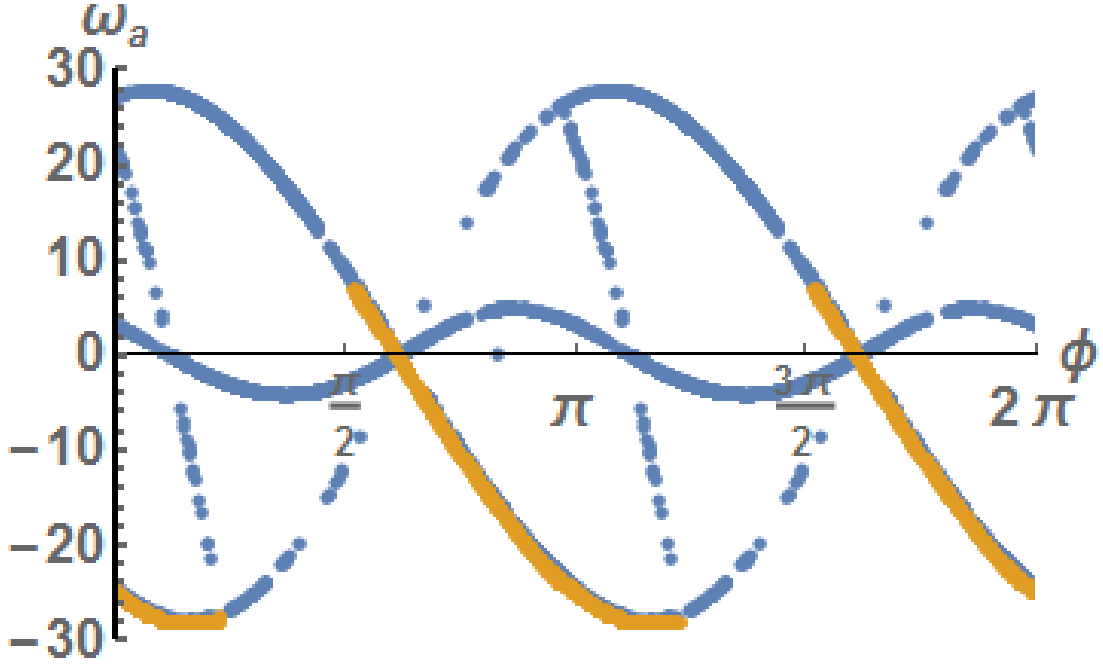


Figure 4.18: Plot of symmetry broken one colour solution,  $\omega_a$  from solving Eqn. 4.60 and 4.61 (blue), and peak wavelength of FFT of  $E_1$  from solving Eqn. 4.6-4.9 (with  $\delta = 0$ ) (orange)), for  $\tau = 0.5$ ,  $\eta = 0.1$  and sweeping  $\phi$  from  $0 \rightarrow 2\pi$ .

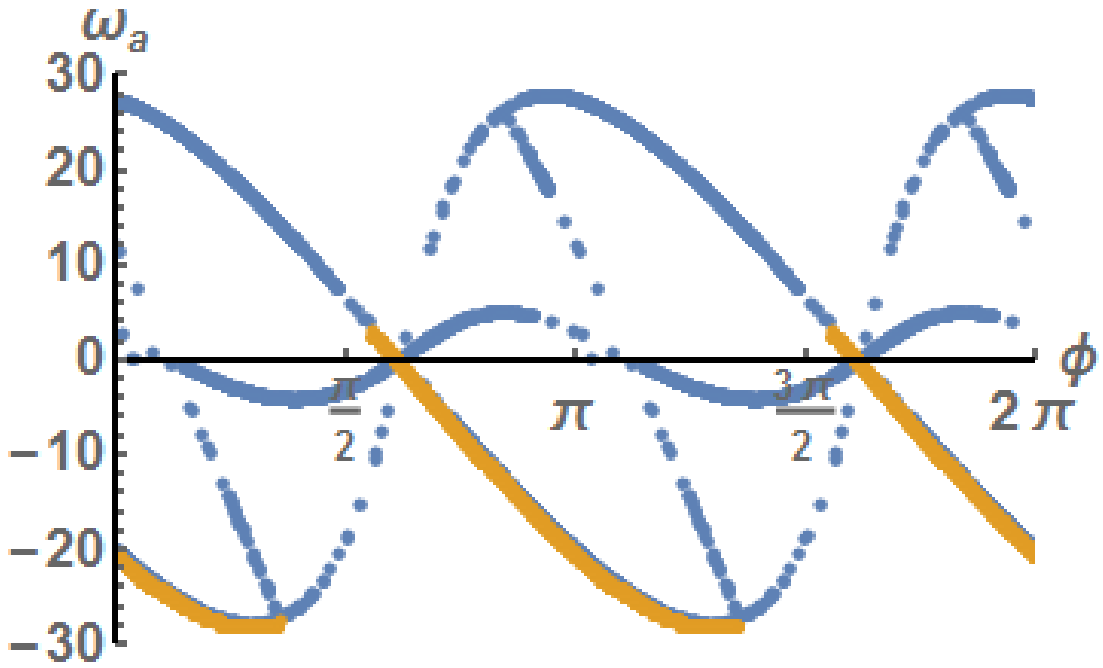


Figure 4.19: Plot of symmetry broken one colour solution,  $\omega_a$  from solving Eqn. 4.60 and 4.61 (blue), and peak wavelength of FFT of  $E_1$  from solving Eqn. 4.6-4.9 (with  $\delta = 0$ ) (orange)), for  $\tau = 2$ ,  $\eta = 0.1$  and sweeping  $\phi$  from  $0 \rightarrow 2\pi$ .

Compared to figure 4.17, there are more symmetry broken solution branches. However, when compared to simulated results, there are again only small windows where this behaviour is stable (around  $\phi = \frac{\pi}{2}$  and  $\frac{3\pi}{2}$ ). In this section a detailed breakdown of the derivation of the analytical approach to solving for the symmetric and symmetry broken states, in the cases of zero and non-zero delay was shown. These analytical methods were then compared with simulated results to test their accuracy. In this case it was shown these methods agreed very well with simulations.

#### 4.1.7 Analytical solutions of two colour states in the zero detuning case

Following the one colour state, another common dynamical regime encountered was the two colour state. Here there are two frequencies present in  $\tilde{E}_{1,2}$ , as is shown in figure 4.20.

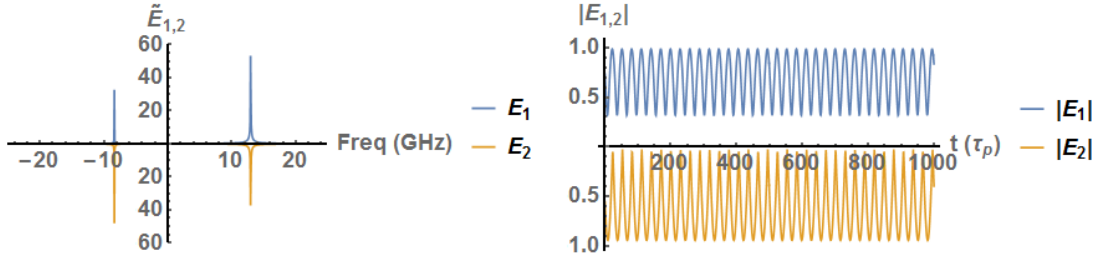


Figure 4.20: FFT of  $\tilde{E}_{1,2}$  (left) and time trace of  $|\tilde{E}_{1,2}|$  (right) for  $\eta = 0.1$ ,  $\phi = 0.5\pi$ ,  $\tau = 0$  and  $\delta = 0$ .

The two colour state is mathematically defined by Eqn. 4.62 and 4.63. As an extension of the one colour state there are now four amplitudes ( $a_{1,2}$  and  $b_{1,2}$ ), two frequencies ( $\omega_{a,b}$ ) and two phase differences ( $\delta_{a,b}$ ). In this instance no assumption is made for the form of the carrier densities ( $N_{1,2}$ ). Therefore this is only an approximate solution, as compared to the one colour state, which is an exact solution.

$$\tilde{E}_1 = a_1 e^{i\omega_a t} + b_1 e^{i\omega_b t} \quad (4.62)$$

$$\tilde{E}_2 = a_2 e^{i\omega_a t} e^{i\delta_a} + b_2 e^{i\omega_b t} e^{i\delta_b} \quad (4.63)$$

$$(4.64)$$

Taking the absolute value of Eqn. 4.62 yields Eqn. 4.65.

$$|\tilde{E}_1(t)|^2 = a_1^2 + b_1^2 + 2a_1 b_1 \cos((\omega_a - \omega_b)t) \quad (4.65)$$

This corresponds to the right panel of figure 4.20 which shows an example  $|\tilde{E}|$  for a two colour state. It is a Cosine term, determined by the frequency difference of the two peaks in the FFT of  $\tilde{E}$  ( $\omega_a - \omega_b$ ). A method to analytically find the symmetry broken two colour solutions has been outlined in previous work [32]. The method presented here, is similar but differs in execution. By substituting the two colour ansatz Eqn. 4.62 and 4.63 in the Eqn. 4.6 and 4.7 one can write the matrix formulae.

$$\begin{pmatrix} (1 + i\alpha)N_1 - i\omega_a & \eta e^{-i(\phi + \omega_a \tau)} \\ \eta e^{-i(\phi + \omega_a \tau)} & (1 + i\alpha)N_2 - i\omega_a \end{pmatrix} \begin{pmatrix} a_1 \\ a_2 e^{i\delta_a} \end{pmatrix} = 0.$$

$$\begin{pmatrix} (1 + i\alpha)N_1 - i\omega_b & \eta e^{-i(\phi + \omega_b\tau)} \\ \eta e^{-i(\phi + \omega_b\tau)} & (1 + i\alpha)N_2 - i\omega_b \end{pmatrix} \begin{pmatrix} b_1 \\ b_2 e^{i\delta_b} \end{pmatrix} = 0.$$

For a solution to exist, the determinants of the left hand side matrices must equal zero. Taking the determinant, and separating the real and imaginary parts gives Eqn. 4.66-4.67.

$$(1 - \alpha^2)N_1N_2 + \alpha\omega_a(N_1 + N_2) = \eta^2 \cos(2(\phi + \omega_a\tau)) + \omega_a^2 \quad (4.66)$$

$$2\alpha N_1N_2 - \omega_a(N_1 + N_2) = -\eta^2 \sin(2(\phi + \omega_a\tau)) \quad (4.67)$$

These equations were solved for  $N_1(\omega_a)$  and  $N_2(\omega_a)$ . Repeating the process for the  $\omega_b$  equations gives similar results. Then solving  $N_1(\omega_a) = N_2(\omega_b)$  and  $N_2(\omega_a) = N_1(\omega_b)$  should give two solutions for  $\omega$ . figure 4.21 shows a parametric plot of  $N_1(\omega_a)$ ,  $N_2(\omega_a)$  and  $N_1(\omega_b)$ ,  $N_2(\omega_b)$ . The intersection of the curves gives the frequencies  $\omega_{a,b}$ .

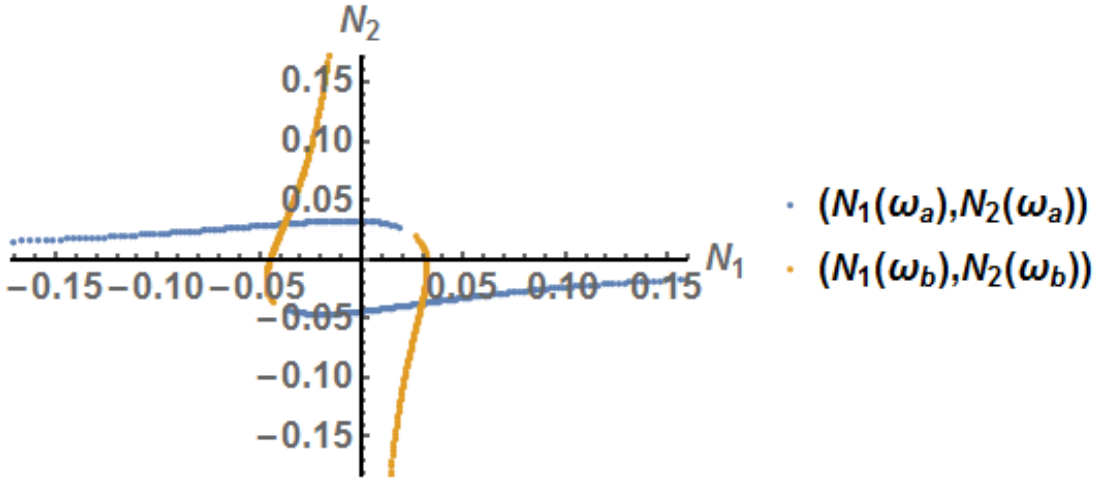
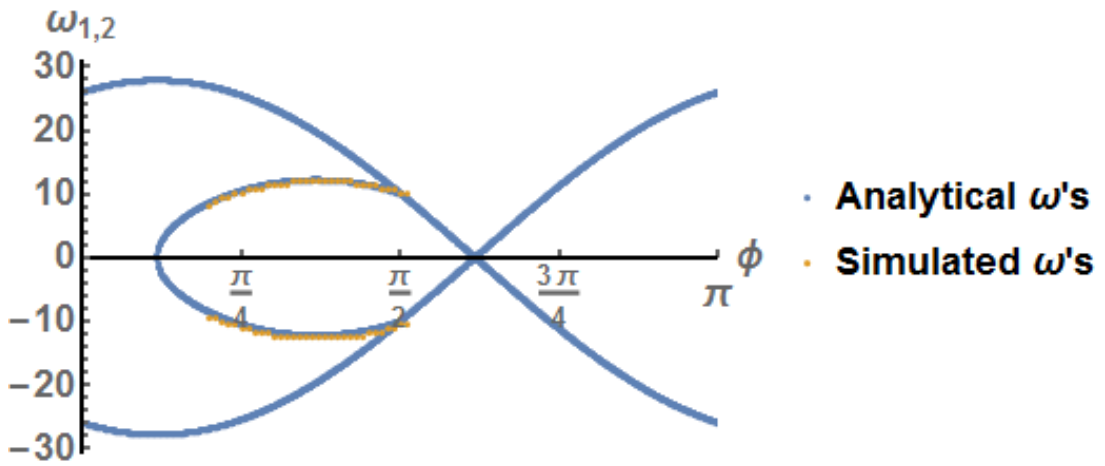


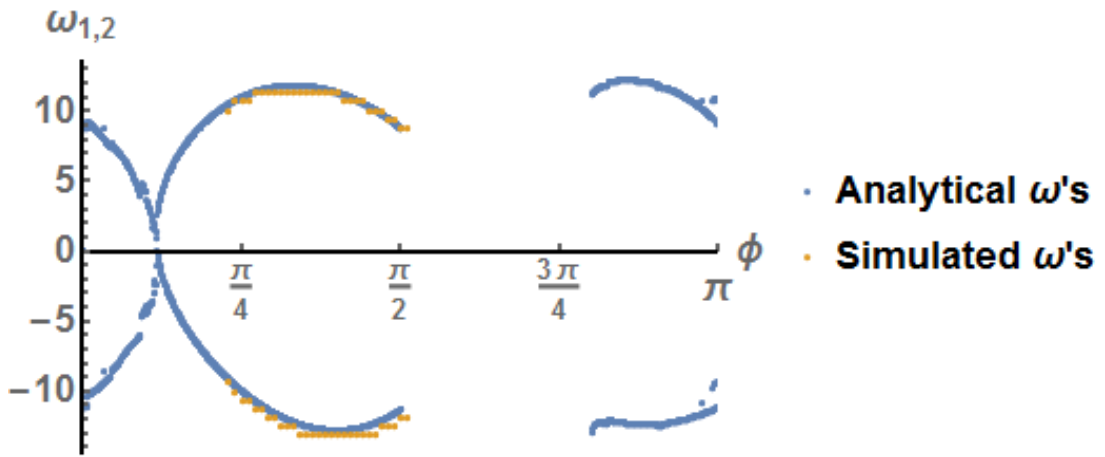
Figure 4.21: Parametric plot of  $N_1(\omega_a)$ ,  $N_2(\omega_a)$  and  $N_1(\omega_b)$ ,  $N_2(\omega_b)$ , from Eqn. 4.66 and 4.67, for  $\eta = 0.1$ ,  $\phi = 1.26$  and  $\tau = 0.5$ .

Figure 4.22 shows the result of finding  $\omega_{a,b}$  using the analytical method outlined, compared with the simulated peak location of the FFT of  $E_1$  from Eqn. 4.6-4.9 while varying  $\phi$ . Excellent agreement is seen.

In this chapter, analytical work on finding the bifurcations of the delayed and non-delayed system was re-created and expanded upon from previous works. After this an analytical study of the main behavioural regimes was re-created



(a)  $\tau = 0$ .



(b)  $\tau = 0.5$ .

Figure 4.22: Analytical solutions for  $\omega_{a,b}$  (blue) compared with simulated results (orange), for  $\eta = 0.1$ , a)  $\tau = 0$ , b)  $\tau = 0.5$ , while varying  $\phi$  from  $0 - \pi$ .

and expanded upon, again from previous work. This chapter showed that the two main behavioural regimes for identical lasers are one and two colour states. These correspond to a locked behaviour of the lasers in the case of one colour states, and periodic power fluctuation of the lasers in the case of two colour states. It is interesting to note that even at high injection strength ( $\eta > 0.4$ ), there exist windows of periodic behaviour. This is in contrast to the injection locked case, where for zero detuning the lasers always lock (however it is important to note that it is possible for injection locked lasers to not oscillate in the coupling regime, for a high value of  $\alpha$ ). This further shows the added complexity of this system when the optical isolator is removed. A good agreement between numerical simulation and analytical results was observed. In the next chapter detuning will be included. With  $\delta \neq 0$  the model loses

many of its symmetries and some of the mathematical techniques used in this section will not be valid. This will make an analytical bifurcation analysis impossible. But, an analytical representation of one and two colour states is still possible and will be outlined and compared with simulated values. Detuning is a key parameter to this study as it makes the model more experimentally realistic.



# **Chapter 5**

## **Including detuning**

### **5.1 Analytical approach to the single mode model with detuning**

### 5.1.1 Introduction

In this chapter the work will be focused on the unexplored parameter region of short, but non zero, delay times associated with two lasers coupled on a single PIC, while also including a frequency difference between said lasers. Also, as in the experimental arrangement where the lasers were coupled on a single chip, a higher percentage of light reached the other laser than would typically be associated with free space coupling. The standard way to study this model would be to perform a bifurcation study, be it analytical or numerical.

However, there are mathematical difficulties in finding these bifurcations analytically, which shall be shown, meaning a numerical method was needed. A numerical method based around attractor diagrams will be introduced, developed and implemented, before simulations that can be compared directly to experimental results will be performed, and this chapter will conclude with this comparison to experimental results.

Firstly, in this section the analytical methods for solving the one and two colour states from Section 4.1 shall be adapted and re-derived for cases that include detuning. Then it will be shown how the analytical methods for finding the bifurcations from Section 4.1 breakdown in this  $\delta \neq 0$  regime.

### 5.1.2 Analytical solutions of one colour states in the detuned case

When  $\delta \neq 0$ , the broken symmetries mean that symmetric one colour solutions are not possible, hence the symmetry broken solutions will be the only form of the one colour ansatz considered. This is due to the breaking of what is called the  $\mathbb{Z}_2$  symmetry  $(E_1, N_1, E_2, N_2) \rightarrow (E_1, N_2, E_2, N_1)$  and the symmetry  $(E_1, N_1, E_2, N_2) \rightarrow (-E_2, N_2, -E_1, N_1)$ , which held when  $\delta = 0$ . A modified version of the method outlined in Sec. 4.1.6 to analytically solve for the symmetry broken states in the case with detuning was developed. Once again the one colour ansatz (Eqn. 4.30 and 4.31) is substituted in the full model Eqn. 4.6-4.7.

$$a_1 i \omega_a = i \delta a_1 + (1 + i \alpha) N_1 a_1 + \eta a_2 e^{-i(\phi + \omega_a \tau - \delta_a)} \quad (5.1)$$

$$a_2 i \omega_a = (1 + i \alpha) N_2 a_2 + \eta a_1 e^{-i(\phi + \omega_a \tau + \delta_a)} \quad (5.2)$$

$$J - N_1 - (N_1 + \nu) a_1^2 = 0 \quad (5.3)$$

$$J - N_2 - (N_2 + \nu) a_2^2 = 0 \quad (5.4)$$

These equations are then separated into real and imaginary parts.

$$a_1 N_1 + a_2 \eta \cos(\phi + \omega_a \tau - \delta_a) = 0 \quad (5.5)$$

$$a_1(\delta + \alpha N_1 - \omega_a) - a_2 \eta \sin(\phi + \omega_a \tau - \delta_a) = 0 \quad (5.6)$$

$$a_2 N_2 + a_1 \eta \cos(\phi + \omega_a \tau + \delta_a) = 0 \quad (5.7)$$

$$a_2(\alpha N_2 - \omega_a) - a_1 \eta \sin(\phi + \omega_a \tau + \delta_a) = 0 \quad (5.8)$$

$$J - N_1 - (N_1 + \nu) a_1^2 = 0 \quad (5.9)$$

$$J - N_2 - (N_2 + \nu) a_2^2 = 0 \quad (5.10)$$

Again the ratio of the amplitudes is defined as  $x = a_2/a_1$ , this yields:

$$N_1 + x \eta \cos(\phi + \omega_a \tau - \delta_a) = 0 \quad (5.11)$$

$$(\delta + \alpha N_1 - \omega_a) - x \eta \sin(\phi + \omega_a \tau - \delta_a) = 0 \quad (5.12)$$

$$x N_2 + \eta \cos(\phi + \omega_a \tau + \delta_a) = 0 \quad (5.13)$$

$$x(\alpha N_2 - \omega) - \eta \sin(\phi + \omega_a \tau + \delta_a) = 0 \quad (5.14)$$

$$\frac{(J - N_2)(N_1 + \nu)}{(J - N_1)(N_2 + \nu)} = x^2 \quad (5.15)$$

Then using these equations in pairs,  $x$  was eliminated. The pairs are (5.11,5.12), (5.13,5.14), (5.11,5.13) and (5.11,5.15).

$$N_1 \sin(\phi + \omega_a \tau + \delta_a) + (\alpha N_1 + \delta - \omega_a) \cos(\phi + \omega_a \tau + \delta_a) = 0 \quad (5.16)$$

$$N_2 \sin(\phi + \omega_a \tau - \delta_a) + (\alpha N_2 - \omega_a) \cos(\phi + \omega_a \tau - \delta_a) = 0 \quad (5.17)$$

$$N_1 N_2 = \eta^2 \cos(\phi + \omega_a \tau + \delta_a) \cos(\phi + \omega_a \tau - \delta_a) \quad (5.18)$$

$$\frac{(J - N_2)(N_1 + \nu)}{(J - N_1)(N_2 + \nu)} = \frac{N_1^2}{\eta^2 \cos^2(\phi + \omega_a \tau + \delta_a)} \quad (5.19)$$

From Eqn. 5.16 and 5.17, expressions for the carrier densities ( $N_{1,2}$ ) was

found:

$$N_1 = \frac{\omega_a - \delta}{\alpha + \tan(\phi + \omega_a \tau + \delta_a)} \quad (5.20)$$

$$N_2 = \frac{\omega_a}{\alpha + \tan(\phi + \omega_a \tau - \delta_a)} \quad (5.21)$$

These were then substituted into Eqn. 5.18 and 5.19.

$$\begin{aligned} \omega_a(\omega_a - \delta) = \\ \eta^2 \cos(\phi + \delta_a + \omega_a \tau) \cos(\phi - \delta_a + \omega_a \tau) [\tan(\phi + \delta_a + \omega_a \tau) + \alpha] \\ [\tan(\phi - \delta_a + \omega_a \tau) + \alpha] \end{aligned} \quad (5.22)$$

$$\begin{aligned} & \frac{(J(\alpha + \tan(\phi + \omega_a \tau + \delta_a)) - (\omega_a - \delta))(\nu(\alpha + \tan(\phi + \omega_a \tau - \delta_a)) + \omega)}{(J(\alpha + \tan(\phi + \omega_a \tau - \delta_a)) - \omega_a)(\nu(\alpha + \tan(\phi + \omega_a \tau + \delta_a)) + (\omega - \delta))} \\ &= \frac{N_1^2}{\eta^2 \cos^2(\phi + \omega_a \tau + \delta_a)} \end{aligned} \quad (5.23)$$

These equations can be solved using numerical root finding, examples of which can be seen in figure 5.1 and 5.2. figure 5.1 is for a small time delay and detuning values ( $\tau = 0.5$  and  $\delta = 0.05$ ), while figure 5.2 is for higher values ( $\tau = 2$  and  $\delta = 0.2$  which correspond to a separation of 6 mm and a detuning of 20 GHz).

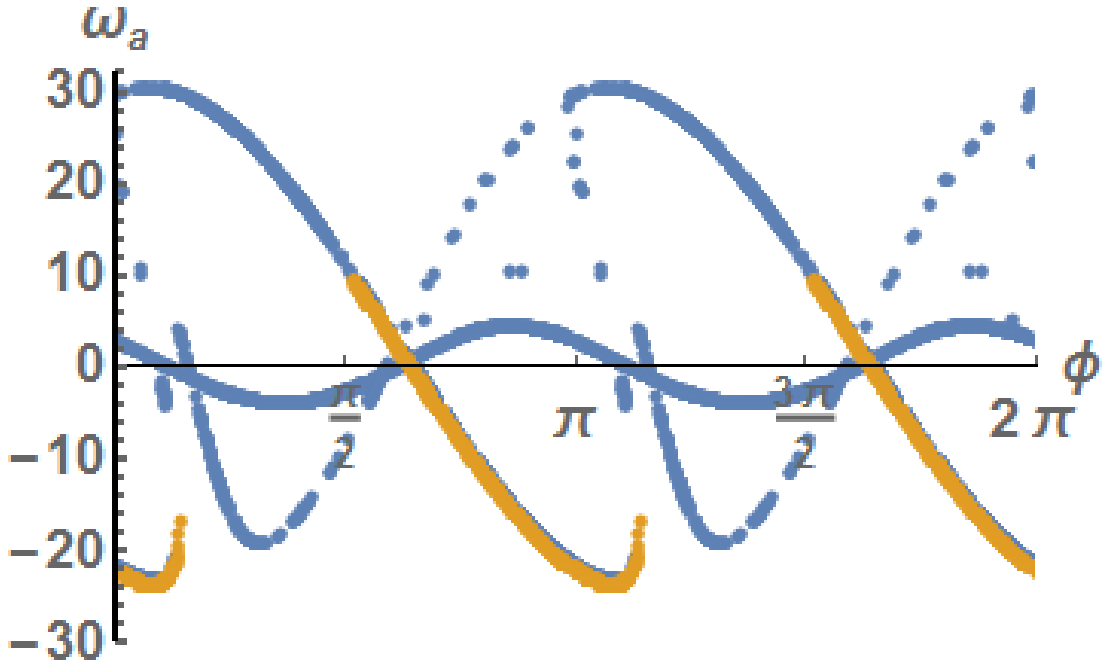


Figure 5.1: Plot of symmetry broken one colour solution,  $\omega_a$  from solving Eqn. 5.22 and 5.23 (blue), and peak wavelength of FFT of  $E_1$  from solving Eqn. 4.6-4.9 (orange), for  $\delta = 0.05$ ,  $\tau = 0.5$  and  $\eta = 0.1$  and sweeping  $\phi$  from  $0 \rightarrow 2\pi$ .

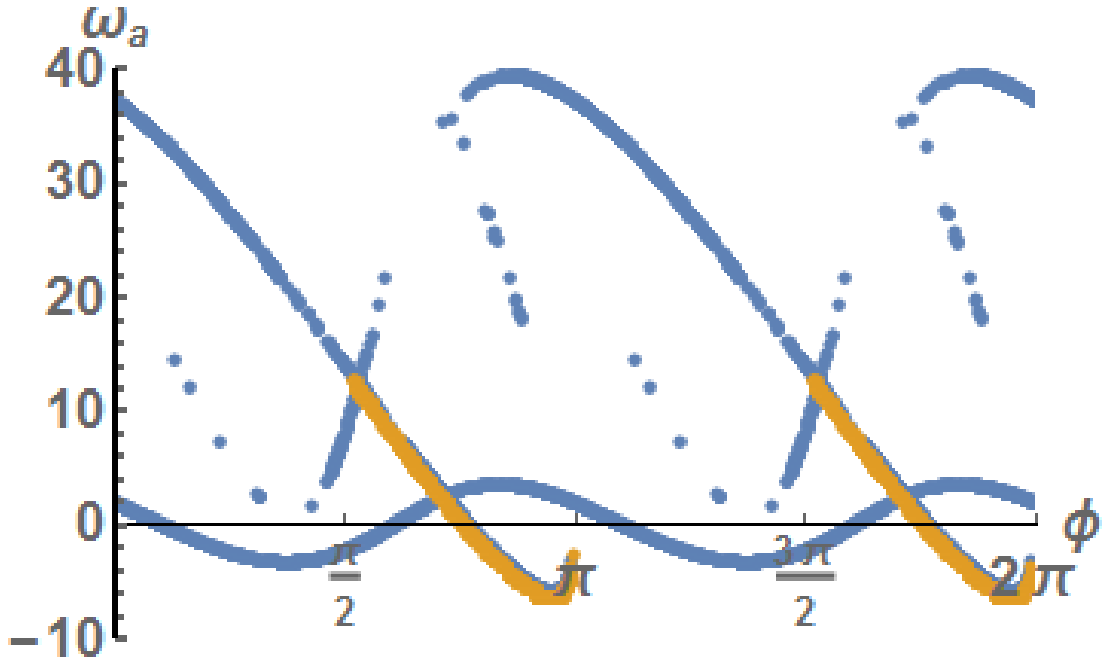


Figure 5.2: Plot of symmetry broken one colour solution,  $\omega_a$  from solving Eqn. 5.22 and 5.23 (blue), and peak wavelength of FFT of  $E_1$  from solving Eqn. 4.6-4.9 (orange), for  $\delta = 0.2$ ,  $\tau = 2$  and  $\eta = 0.1$  and sweeping  $\phi$  from  $0 \rightarrow 2\pi$ .

Excellent agreement is seen in the overlap of the analytical results and

simulated results, and in contrast to Sec. 4.1.6.2, the symmetry broken solution is the predominant solution that exists. This is due to the breaking of the symmetries introducing detuning caused by including the detuning parameter.

### 5.1.3 Analytical solutions of two colour states in the detuned case

Next the two colour states of the system with  $\delta \neq 0$  was considered. The method developed was a modified version of that used in Sec. 4.1.7. Again the two colour ansatz is substituted into the full detuned model, Eqn. 4.6-4.7. This can be written in the matrix formulation:

$$\begin{pmatrix} (1 + i\alpha)N_1 - i\omega_a + i\delta & \eta e^{-i(\phi + \omega_a \tau)} \\ \eta e^{-i(\phi + \omega_a \tau)} & (1 + i\alpha)N_2 - i\omega_a \end{pmatrix} \begin{pmatrix} a_1 \\ a_2 e^{i\delta_a} \end{pmatrix} = 0.$$

$$\begin{pmatrix} (1 + i\alpha)N_1 - i\omega_b + i\delta & \eta e^{-i(\phi + \omega_b \tau)} \\ \eta e^{-i(\phi + \omega_b \tau)} & (1 + i\alpha)N_2 - i\omega_b \end{pmatrix} \begin{pmatrix} b_1 \\ b_2 e^{i\delta_b} \end{pmatrix} = 0.$$

For a solution to exist, the determinants of the left hand side matrices must equal zero. Taking the determinant, and separating the Real and Imaginary parts gives Eqn. 4.66-4.67.

$$\begin{aligned} (1 - \alpha^2)N_1 N_2 + \alpha\omega_a(N_1 + N_2) - \alpha\delta N_2 \\ = \eta^2 \cos(2(\phi + \omega_a \tau)) + \omega_a^2 - \delta\omega_a \end{aligned} \quad (5.24)$$

$$2\alpha N_1 N_2 - \omega_a(N_1 + N_2) + \delta N_2 = -\eta^2 \sin(2(\phi + \omega_a \tau)) \quad (5.25)$$

Following the same method as in Sec. 4.1.7 of parametrically plotting  $N_1(\omega_a)$ ,  $N_2(\omega_a)$  and  $N_1(\omega_b)$ ,  $N_2(\omega_b)$  and finding their intersect, allows for the numerical approximation of  $\omega_{a,b}$ . figure 5.3 shows a comparison of analytical and simulated values of  $\omega_{a,b}$ .

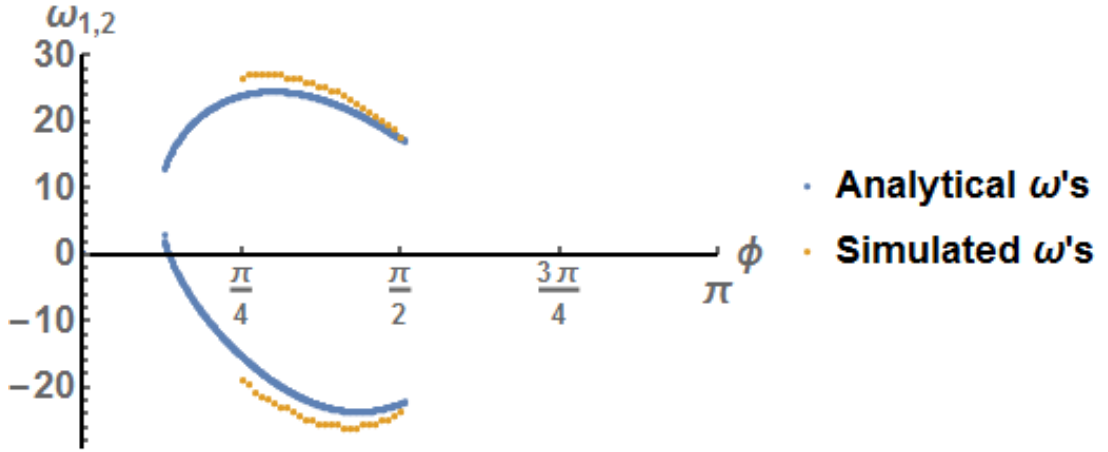


Figure 5.3: Analytical solutions for  $\omega_{a,b}$  (blue) compared with simulated results (orange), for  $\eta = 0.1$ ,  $\tau = 0.5$  and  $\delta = 0.05$ , while varying  $\phi$  from  $0 - \pi$ .

As can be seen the agreement is not as good as in the case with no detuning, from Sec. 4.1.7, however it is important to remember that since the equations for  $N_{1,2}$  were not used in the derivation of this analytical method these are only approximate solutions.

#### 5.1.4 Analytical attempts to study bifurcations of the detuned, delayed model

Re-introducing frequency detuning ( $\delta$ ) complicates the mathematics previously done. One cannot simply re-use the same methods, while including the  $\delta$  parameter. When  $\delta = 0$  the model contains a number of symmetries; the most important of which is the phase shift invariance

$(E_1, N_1, E_2, N_2) \rightarrow (E_1 e^{i\psi}, N_1, E_2 e^{i\psi}, N_2)$ . This phase shift invariance allowed the introduction of new coordinates  $F_{1,2} = (E_1 \pm E_2)/2e^{-i\omega_s t}$  and  $M_{1,2} = (N_1 \pm N_2)/2$ , which was integral to finding the analytical expression for the characteristic equation. However a non-zero  $\delta$  breaks the phase shift invariance, meaning the change of coordinates previously employed is no longer valid. Thus, an alternative method was required. Unfortunately no similar change in coordinates was found to work, and an analytical approach had to be abandoned.

The failure of the analytical methods meant a numerical method was needed. The most common software for performing a bifurcation study is the MATLAB developed package DDE-Biftool[39]. This package employs a technique known as numerical continuation to track steady state solutions and find bifurcations.

Alternatively the attractor diagrams of the system can be studied. Attractor diagrams are similar to bifurcation diagrams, but are simpler and focus only on bifurcations that cause an experimentally visible change in behaviour.

There is a subtle difference between a bifurcation diagram and an attractor diagram, which figure 5.4 outlines. This plot shows the stable and unstable steady states that exist in the model with detuning but no delay ( $\tau = 0$ ) and was found using the package XPPAut [40] (a numerical solver for differential equations that can perform bifurcation studies on systems of ODEs, but not DDEs). Performing a bifurcation study on these solutions gives the Saddle-Node and Hopf bifurcations highlighted. Starting at  $\phi = 0$ , there is a stable steady state, which continues to the first saddle-node bifurcation around  $\phi = 1$ . There is a small window of unstable steady states, between the two saddle-node bifurcation points close together, with another stable branch extending out from the bottom, which continues until approximately  $\phi = 1.25$ , where a Hopf bifurcation generates a stable periodic solution, as the steady state solution becomes unstable. The stable periodic solution continues to  $\phi = 1.5$ , where another Hopf bifurcation results in the destruction of the periodic solution, and the creation of a stable steady state. This behaviour continues to  $\phi = \pi$ . Performing an attractor diagram study on this, one finds the boundaries between steady and periodic behaviour caused by the two Hopf bifurcations. Note there are other unstable steady state solutions in the periodic window; however the attractor diagram study only focuses on stable behaviours. In short an attractor diagram will only show the boundaries on a type of solution, and is not concerned with the unstable solutions generated by bifurcations. This makes attractor diagrams highly applicable to studying a system, with the intention of confirming the result experimentally, as unstable solutions will not manifest themselves experimentally.

In the next section the bifurcation diagrams for the detuned system with no delay will be studied using XPPAut. This package does not handle DDE systems ,i.e. systems with a delay time, but will provide a baseline for the form of bifurcations when there is no delay time. These results will also hold for short enough delays where the separation between the lasers is less than or equal to the photon lifetime,  $\tau_p$ .



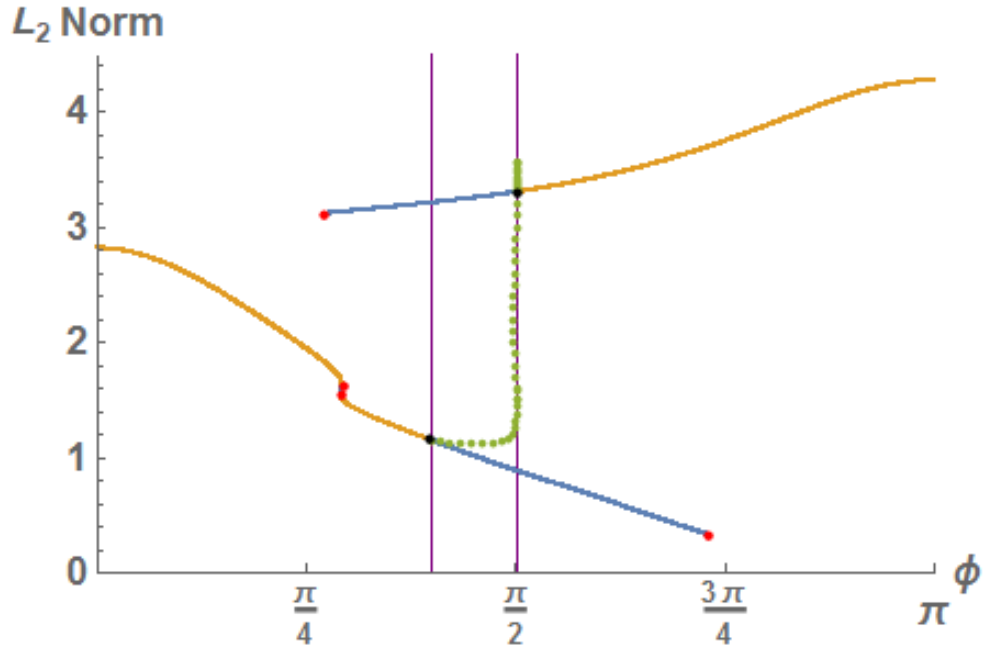


Figure 5.4: Plot of  $L_2$  Norm from Eqn. 4.6-4.9 for  $\eta = 0.2$ ,  $\delta = 0.05$  and  $\tau = 0$ , versus coupling phase ( $\phi$ ). Showing stable steady states (orange), unstable steady states (blue), stable periodic orbits (green), saddle node bifurcation (red dot), Hopf bifurcation (black dot), and change in system detected by attractor diagram (purple).

### 5.1.5 Bifurcations of the no delay detuned system

In terms of model formulation the best way to write the complex fields in this instance is a formulation used in [32], where a Poincare sphere representation is used, as shown below.

$$q_x + iq_y = 2E_1 * E_2 \quad (5.26)$$

$$q_z = |E_1|^2 - |E_2|^2 \quad (5.27)$$

Using this representation the total output power of both lasers can be found using  $R = (q_x^2 + q_y^2 + q_z^2)^{\frac{1}{2}} = |E_1|^2 + |E_2|^2$ , and the power of each individual laser can be found using  $|E_{1,2}|^2 = r \pm q_z$ . Subbing Eqn. 5.26 and 5.27 into the detuned model Eqn. 4.6-4.9 gives:

$$q'_x = q_x(N_1 + N_2) + \alpha q_y(N_1 - N_2) + 2\eta \cos(\phi)R + 2\delta q_y \quad (5.28)$$

$$q'_y = q_y(N_1 + N_2) - \alpha q_x(N_1 - N_2) - 2\eta \sin(\phi)q_z - 2\delta q_x \quad (5.29)$$

$$q'_z = q_z(N_1 + N_2) + R(N_1 - N_2) + 2\eta q_y \sin(\phi) \quad (5.30)$$

$$N'_1 = \epsilon[J - N_1 - (N_1 + \nu)\frac{(R + q_z)}{2}] \quad (5.31)$$

$$N'_2 = \epsilon[J - N_2 - (N_2 + \nu)\frac{(R - q_z)}{2}] \quad (5.32)$$

The bifurcation diagrams in the  $(\phi, \eta)$  space for various detunings can be seen in figure 5.5 and were found using XPPAut.

Next a sampling of behaviours from across these diagrams will be shown. If  $\eta$  is fixed at the two values highlighted by the dashed lines in figure 5.6a ( $\eta = 0.0275$  and  $\eta = 0.3$ ), the behaviours can be seen in figure 5.6b and 5.6c. These are one-dimensional bifurcation diagrams where one parameter is varied and bifurcations occur as a point is crossed rather than a line in the two-dimensional bifurcation diagram.

Figure 5.6b shows three different types of periodic behaviours, each having stable and unstable branches. Examples of the forms of the periodic solutions can be seen in figure 5.7. Branch A and C are different forms of pulsed behaviour and branch B is a simple sinusoid (two colour state). For low  $\phi$  there is a bistability of solution branch A and B. A period-doubling bifurcation brackets the stable part of branch A (blue) on the left, with the unstable part being shown in orange. On the right side a saddle node bifurcation then switches the behaviour to branch B as  $\phi$  is increased. The basic sinusoidal behaviour (two colour state) associated with branch B is stable for a large part of the  $0 - \pi$  window, given by the green line, with two small unstable windows in red. In the center of the graph the unstable part of this solution doubles back on the stable part, through two saddle-node bifurcations. While on the right side of the graph the two colour state changes stability through a torus bifurcation. Finally solution C has a large unstable branch in brown, as  $\phi$  is increased, a small stable window, in purple, is bracketed by two torus bifurcations, before entering a larger stable area between  $\phi = 2.2$  and  $\phi = 2.8$ .

Figure 5.6c follows the same process of fixing  $\eta$  and varying  $\phi$ , tracking the

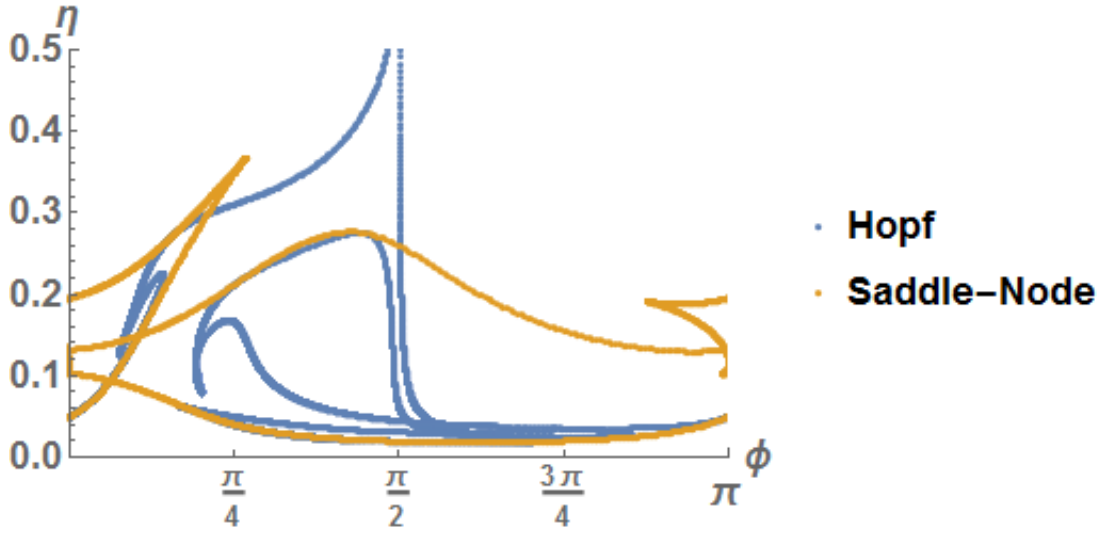
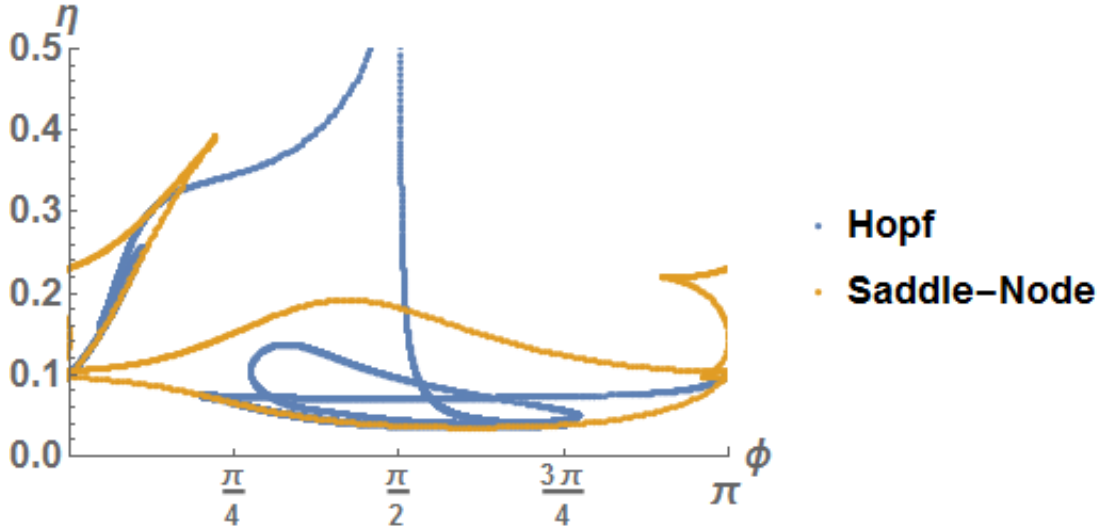
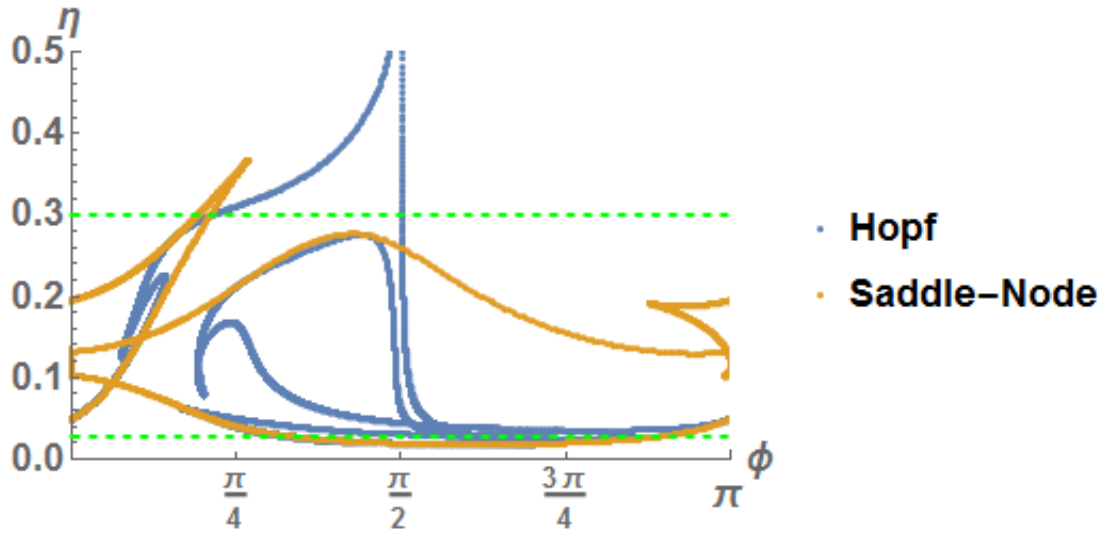
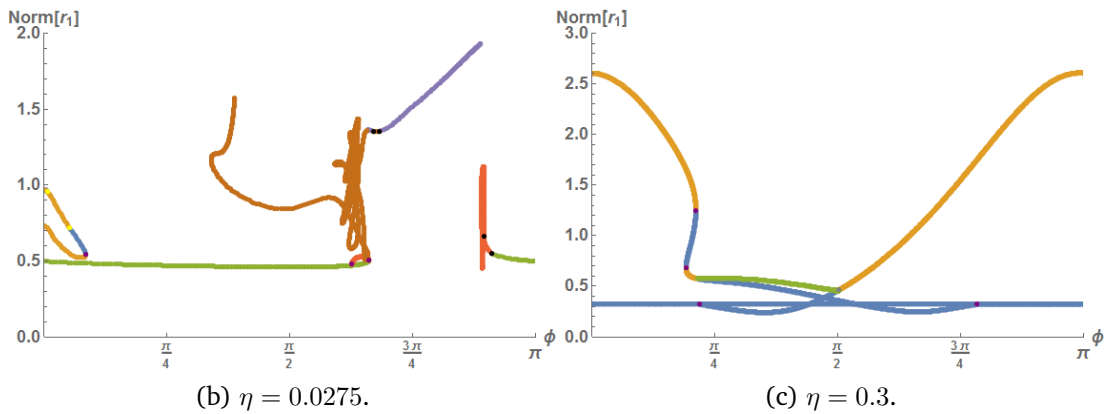
(a)  $\delta = 0.05$ .(b)  $\delta = 0.1$ .

Figure 5.5: Hopf (blue) and saddle-node (orange) bifurcation lines in the  $(\phi, \eta)$  space for a)  $\delta = 0.05$  and b)  $\delta = 0.1$ .

forms of the solutions and the bifurcations, this time for  $\eta = 0.3$ . Unlike figure 5.6b there are windows of steady state behaviour, the stable branches are in orange and unstable in blue. These transition to a stable periodic behaviour (shown in green), through two Hopf-fold bifurcations. At the Hopf-fold, a periodic solution is generated and the steady state behaviour changes stability but continues on. On the two dimensional bifurcation diagram, in figure 5.6a where the Hopf and saddle-node lines overlap, this forms a Hopf-fold bifurcation. In this case the Periodic behaviour exhibited is a simple sinusoid (two-colour state). In the next section the numerical methods for finding these



(a) Bifurcation diagram for  $\delta = 0.05$ , with the green lines highlighting the two  $\eta$  values of interest.



(b)  $\eta = 0.0275$ .

(c)  $\eta = 0.3$ .

Figure 5.6: a) shows the bifurcation diagram for  $\delta = 0.05$  with the  $\eta$  values of interest highlighted by the dashed green lines, b) The L2 Norm for varying  $\phi$  with the stable and unstable parts of the three types of periodic solutions that exist (labelled A, B and C), with the bifurcations between them being as follows: saddle node in purple, period-doubling in yellow and torus in black for  $\eta = 0.0275$  c) The L2 Norm for varying  $\phi$  with the stable steady state in blue, unstable steady state in orange, and the stable periodic solution in green. The saddle node bifurcation is given by the purple dots and the Hopf-fold bifurcation given by the grey dots.

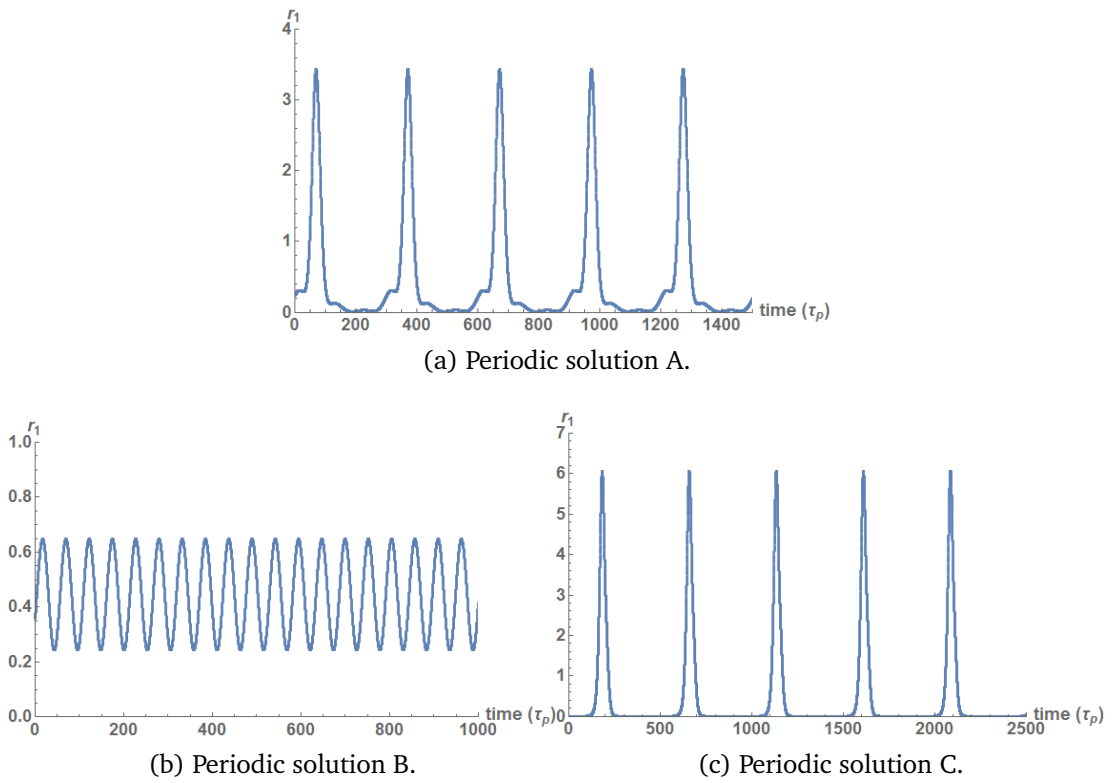


Figure 5.7: Time traces of the different periodic behaviours shown in figure 5.6b.

attractor diagrams will be introduced. Various methods were tried, tested and compared against previously analytically found bifurcation lines to test their accuracy. Then the most successful method will be applied to the unexplored parameter space we are interested in.

## 5.2 Attractor diagram study of the detuned model

### 5.2.1 Attractor diagram methodology introduction

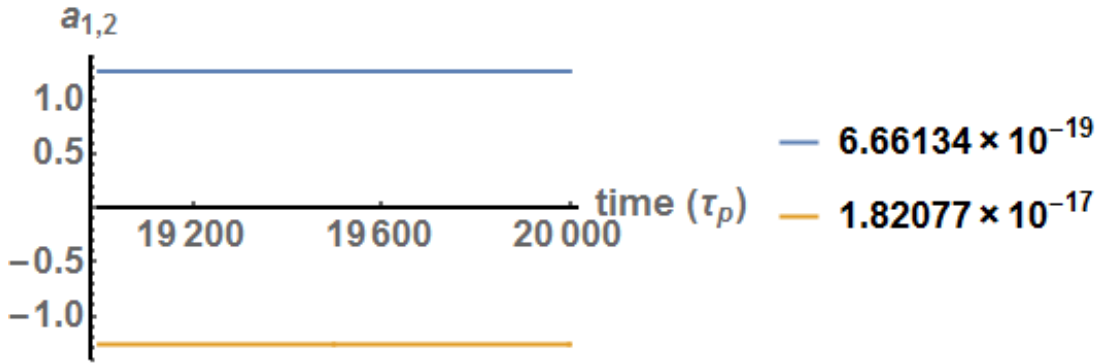
In this section attractor diagrams will be described and compared to bifurcations, then the numerical methods for finding these diagrams will be described and their accuracy will be discussed. All these numerical methods will be based upon breaking the parameter space of interest into a 2D grid of points, then numerically solving the full system of equations, Eqn. 4.6-4.9 at these parameter values and analysing the output graphically. The first method tried was based on analysing the time traces and having functions characterise the different behavioural regimes present. This was ultimately dropped in favour of analysing the FFT of the output, which proved successful. Each of these methods shall now be outlined, tested and their merits discussed.

### 5.2.2 Time series analysis method

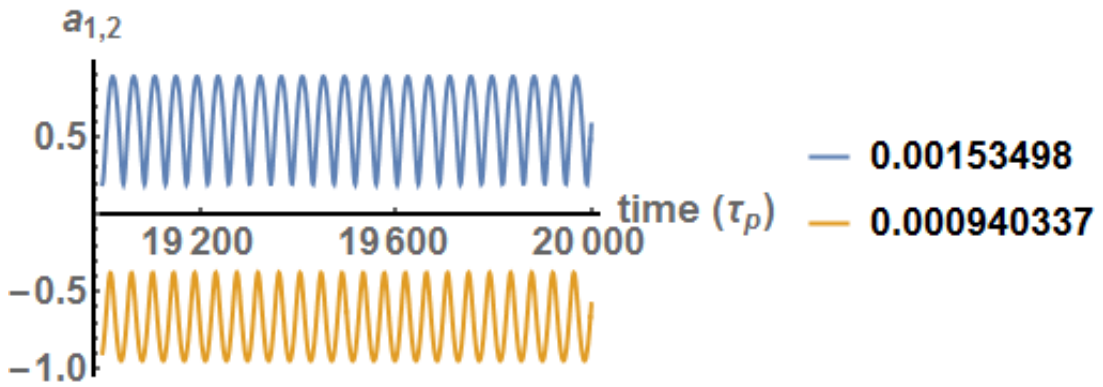
This method breaks the parameter space of interest, in this case the injection strength and phase difference, into a two dimensional grid, following this the time series solutions of the model at each 2D grid point is analysed. A function was written that takes the slope between the first maximum peak and the last minimum peak of these simulated time traces, and sees if it is below a certain threshold value. If it is below this value the system is at a stable steady state, i.e. low slope value corresponds to a flat line. An example of the detection functions applied to the model can be seen in figure 5.8. The difference in the slope of the interpolated line between the max and min can be seen in the case of steady state in 5.8a, and a limit cycle behaviour 5.8b.

Now with the ability to differentiate between a steady state and an unstable state, a comparison can be drawn with previous bifurcation diagrams. Each point in the  $(\phi, \eta)$  grid was evaluated and if the slope was below a threshold value of  $10^{-6}$ , it was stored as a steady state. The result can be seen in figure 5.9, for two different  $\tau$  values, 5.9a  $\tau = 0.5$  and 5.9b  $\tau = 2$ .

A good agreement was seen where the bifurcation lines form a boundary of the steady state solutions, as expected (the pitchfork bifurcation after meeting the Hopf bifurcation changes the symmetry of the one colour state, as discussed in Section 4.1.3.4, but does not cause an experimentally visible change in behaviour). This method works very well for steady state detection, however analysing the oscillatory behaviour of a limit cycle would be difficult, as it would require curve fitting. To diagnose a basic limit cycle a Cosine fitting



(a)  $\eta = 0.22, \phi = 0.31, \tau = 0.5$  and  $\delta = 0$ .



(b)  $\eta = 0.06, \phi = 1.41, \tau = 0.5$  and  $\delta = 0$ .

Figure 5.8: Plot of  $a_{1,2}(=|E_{1,2}|)$  vs time, showing the slope of the line between the max and min value of the time trace, for a steady state (a), and a limit cycle (b).

would be required, however more complicated oscillations would require more advanced function fitting. It was decided that analysing the FFTs of the full complex field would be more efficient. Steady states (one colour states) have a single peak, and limit cycles (two colour states) have two peaks, so by performing peak counting on the FFTs of the complex field, functions to classify these behaviours would be very efficient.

### 5.2.3 FFT analysis methods

The time series based analysis method proved to ultimately be ineffective for analysing oscillatory behaviour, so another approach was needed. Here we shall introduce the methods for characterising different behavioural regimes based on the FFT of the complex electric fields,  $\tilde{E}_{1,2}$ . It was found that the total time the model was integrated over was important, especially as the solution got close to a bifurcation line, where it can take a long time for a solution to



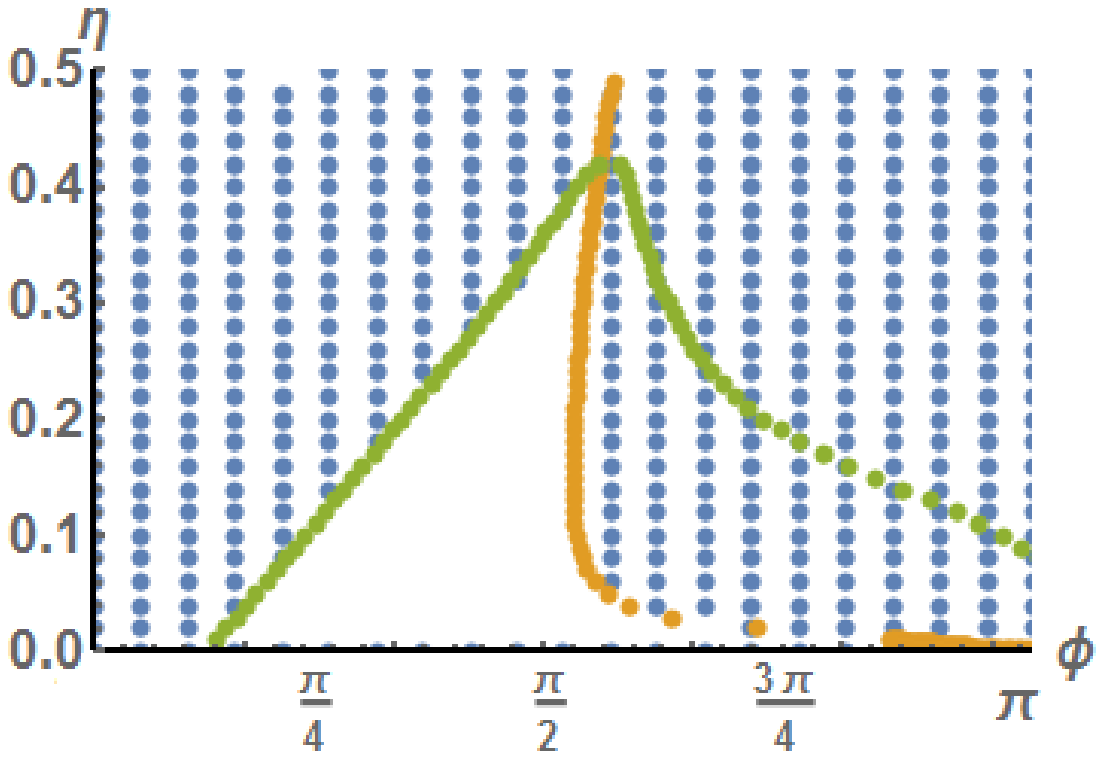
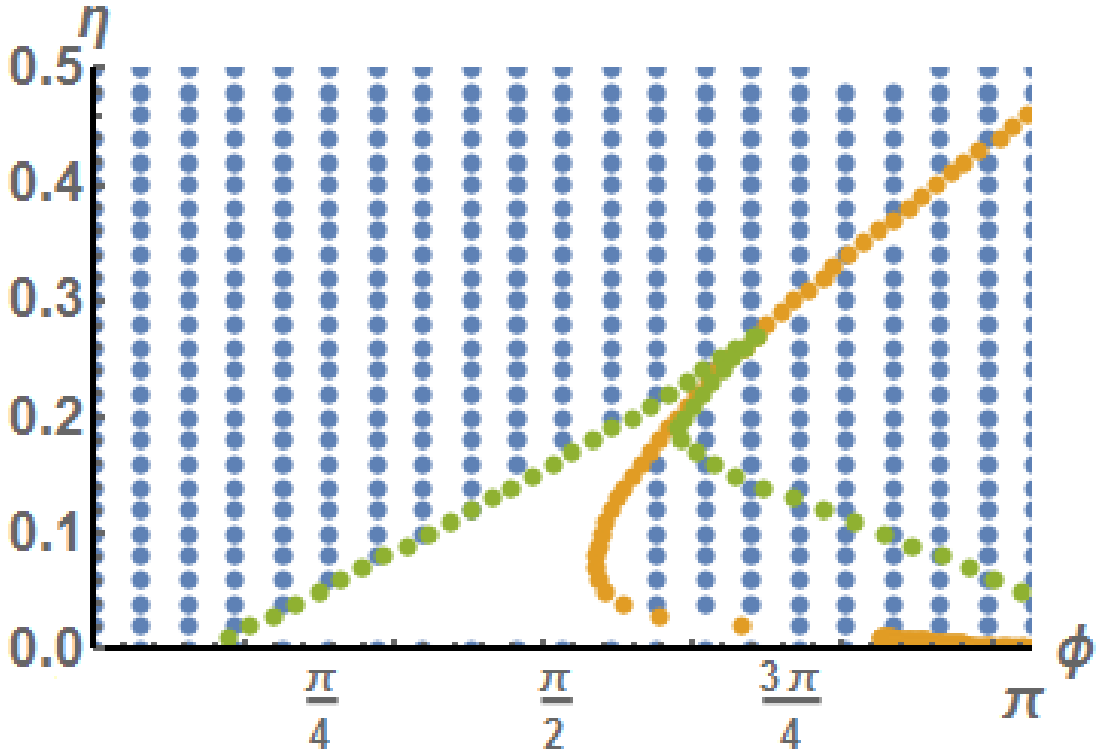
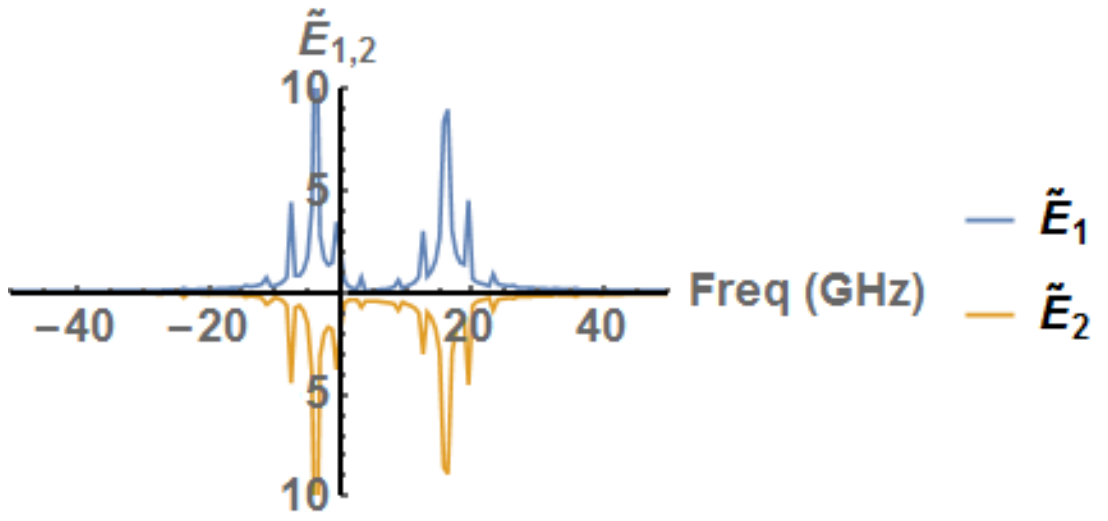
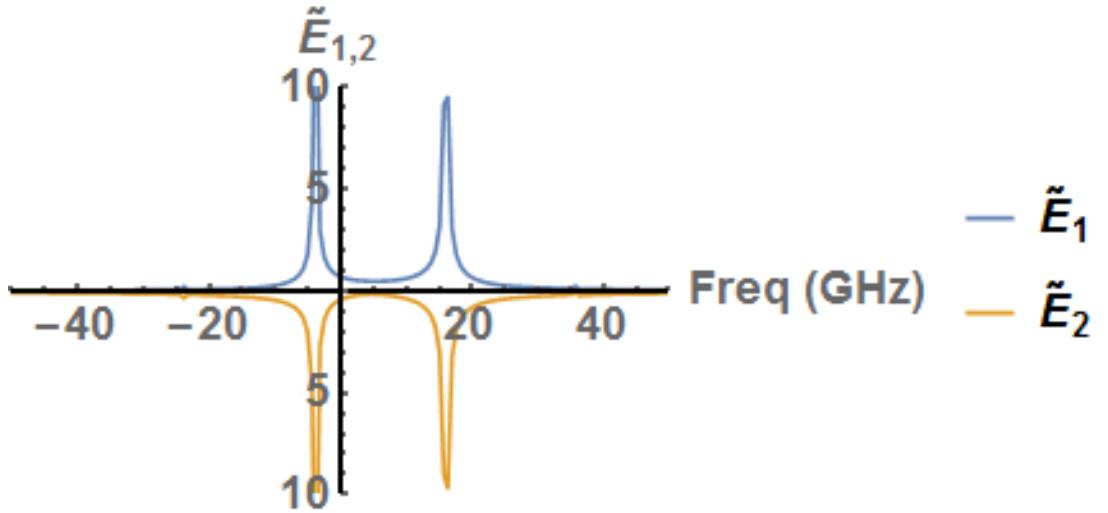
(a)  $\tau = 0.5$ .(b)  $\tau = 2$ .

Figure 5.9: Plot of the  $(\phi, \eta)$  space, where the steady states are in blue, the analytically found Hopf bifurcation line is in orange, and the pitchfork bifurcation is in green.

settle into a stable behaviour. Initially the model was integrated to 20000 time steps; however this broke down in certain areas. For example figure 5.10 shows  $\tilde{E}_{1,2}$  close to the Hopf bifurcation for  $\tau = 2$ ,  $\delta = 0$  (figure 4.11), for two different integration times, 20000 and 100000. With the longer integration time (figure 5.10b) the system clearly looks like a two colour state. However for the shorter time (figure 5.10a) the system has not yet settled into its stable behaviour and there are extra frequencies present. This can be seen from the short and long time traces of  $|E_{1,2}|$  corresponding to the results of figure 5.10, as shown in figure 5.11.



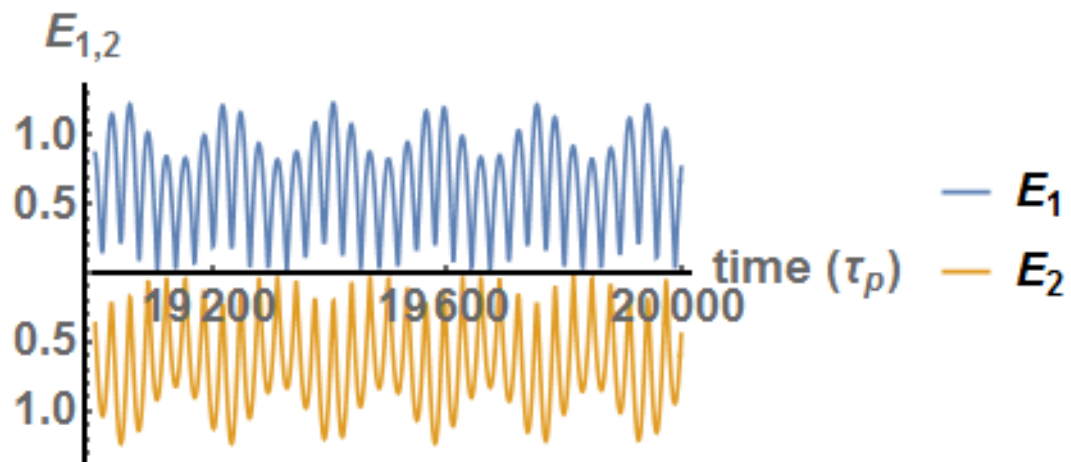
(a) 20000 integration time.



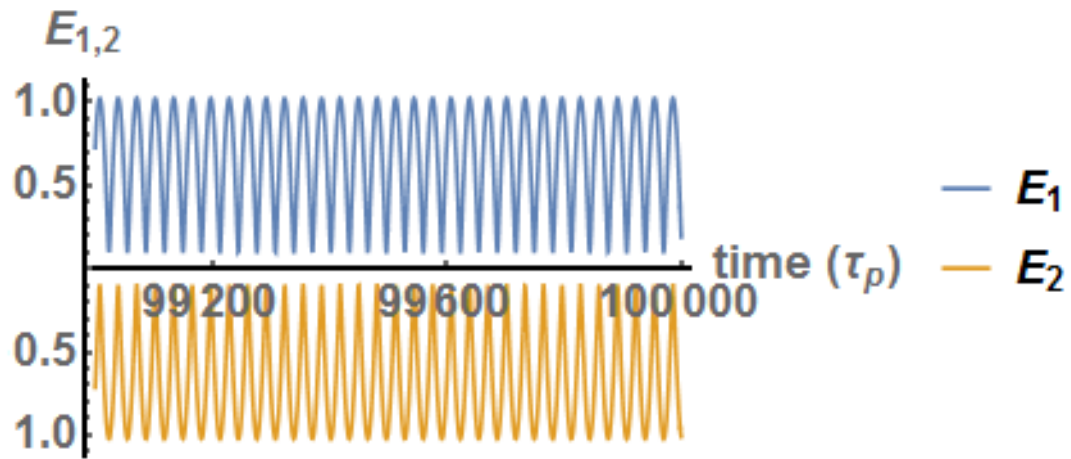
(b) 100000 integration time.

Figure 5.10:  $\tilde{E}_{1,2}$  for  $\eta = 0.1$ ,  $\phi = 1.721$ ,  $\tau = 2$  and  $\delta = 0$  for two different integration times. a) 20000 and b) 100000.

To analyse the FFTs, Mathematica's peak detection capability was employed,



(a) time trace from 19000 – 20000.



(b) time trace from 99000 – 100000.

Figure 5.11: Time trace of  $|E_{1,2}|$  for  $\eta = 0.1$ ,  $\phi = 1.721$ ,  $\tau = 2$  and  $\delta = 0$  for two different time periods. a) between 19000 and 20000 and b) between 99000 and 100000.

and by counting the peaks detected one and two colour states can be identified. In this peak detection function a couple of parameters can be defined to help with slightly noisy data. First by defining a  $\sigma$  all peaks must survive a Gaussian blurring up to scale  $\sigma$ . Secondly a minimum sharpness of peaks detected can be defined. Based on the transitions between these states different bifurcations can be classified. Figure 5.12 shows an example of a one colour and two colour state after being run through peak detection, with the black dots showing the aforementioned peaks.

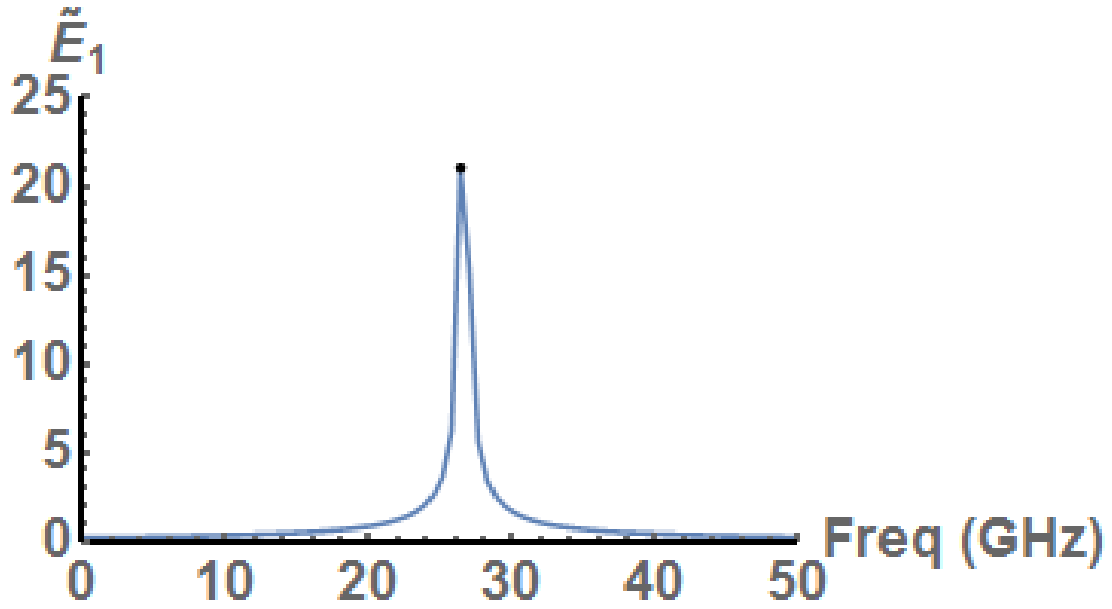
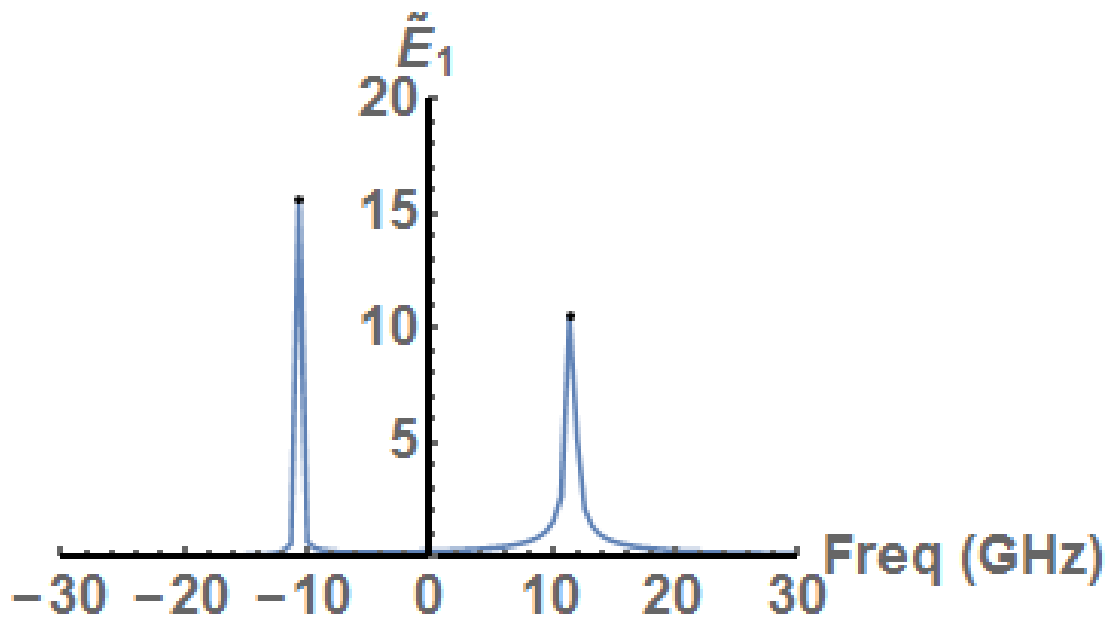
(a) One colour state ( $\eta = 0.1, \phi = 0$  and  $\tau = 0$ ).(b) Two colour state ( $\eta = 0.1, \phi = 1.5$  and  $\tau = 0$ ).

Figure 5.12: Plot of  $\tilde{E}_1$ , for a) one colour and b) two colour states, with the result of peak detection on the solution (black dots).

### 5.2.4 Nine point grid comparison method

Now that different behavioural regimes can be characterised and identified, the boundaries between these regions will be found. An algorithm was developed, which was referred to as the nine point grid comparison method, which is outlined in figure 5.13. The two-dimensional parameter space is broken into a grid of points, and at each grid point the algorithm checks the eight points directly surrounding the point of interest for the desired change in behaviour. Each time a change in behaviour is detected a bisection is performed until a solution with the desired accuracy is achieved. Compared to the time series analysis method, this method focuses on the boundary between behavioural regimes. Just as in the previous section, the parameters of interest are the coupling coefficient,  $\eta$ , and the coupling phase,  $\phi$ , as these are the experimentally relevant variables ( $\tau$  is fixed for a given device, as lasers will have a fixed separation on a PIC, and  $\delta$  is fixed for a given experiment). The method was written in Mathematica, this was not the fastest platform in terms

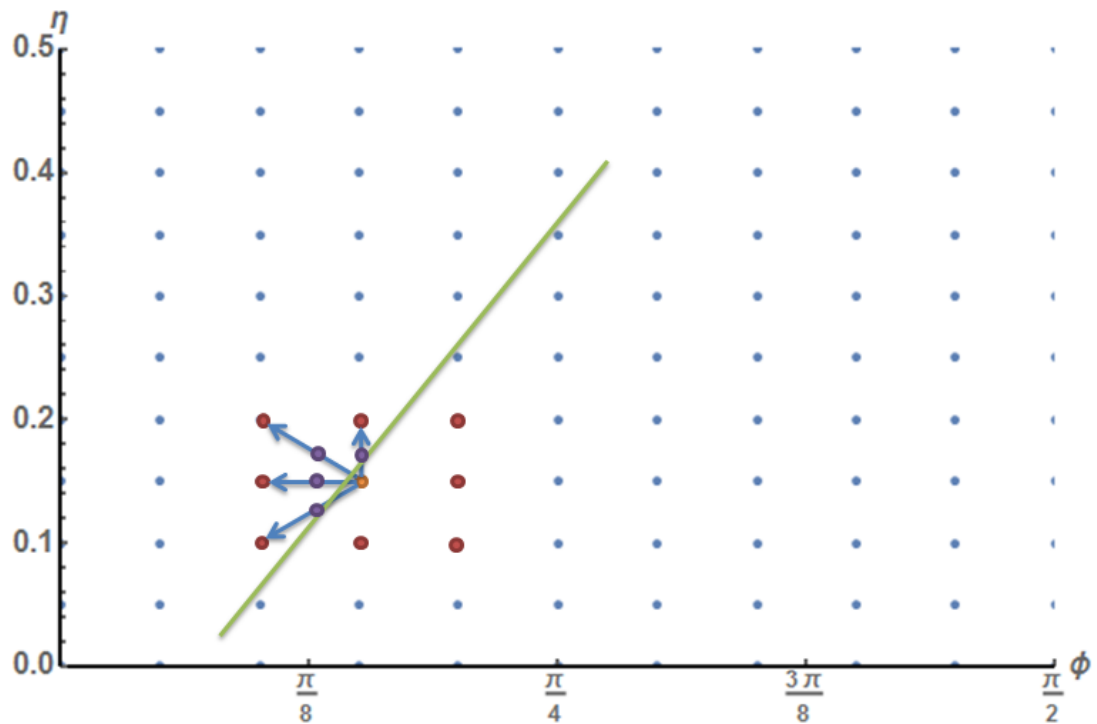


Figure 5.13: Graphical representation of 9 point grid comparison method. Here the example bifurcation line is in green, the point of interest is in orange, and it is being compared with the 8 points directly around it (red) for a change in behaviour. The blue arrows represent the algorithm detecting a change in behaviour as the bifurcation line is crossed, and the purple dots are the mid-points saved for further bisection.

of computation time but it was easy to implement. This method was benchmarked by comparing the output with the analytical results found in section 4.1.3.4. These bifurcations are the experimentally important ones, as they cause a measurable change in behaviour. This comparison can be seen in figure 5.14 and 5.15.

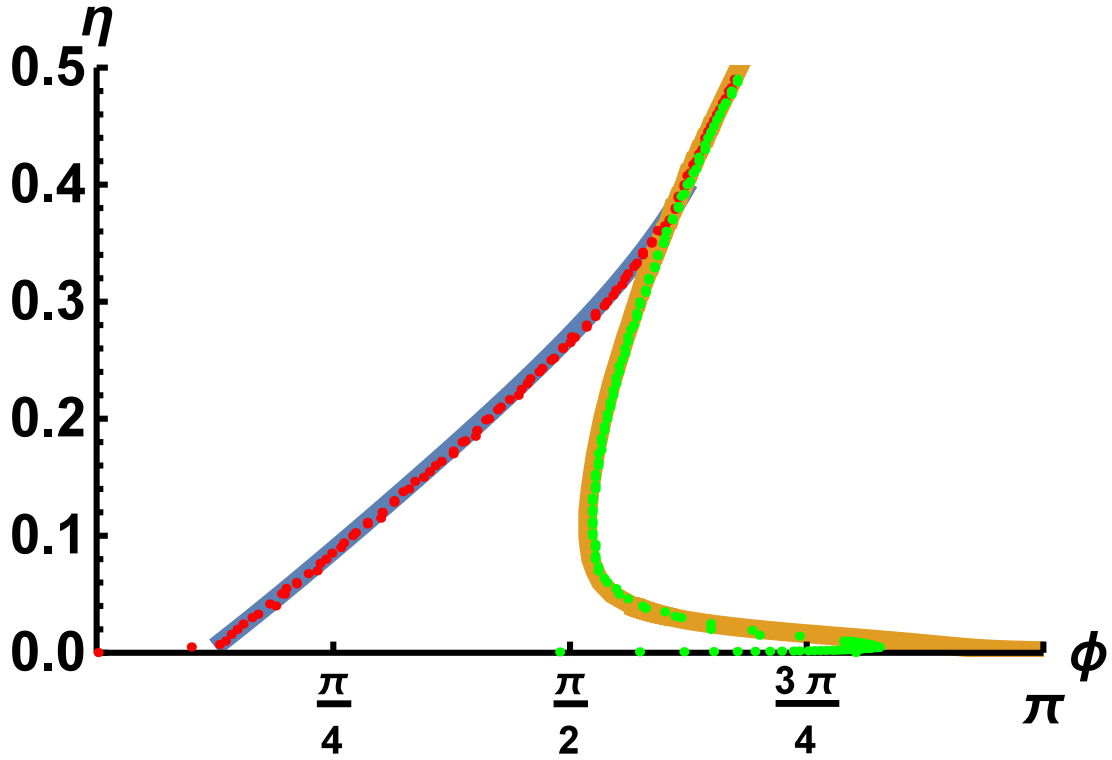


Figure 5.14: Output of the nine point grid comparison method, for finding the pitchfork (green dots) and hopf (red dots) bifurcations, for the model with  $\delta = 0$  and  $\tau = 1$ . The result is compared with previously calculated bifurcations for this system (pitchfork (blue line) and hopf (orange line)).

Figure 5.14 shows excellent agreement. The pitchfork bifurcation line is found by setting the algorithm to look for the change from an in phase one colour state ( $\delta_a = 0$  in Eqn. 4.31) and the Hopf line is found by setting the algorithm to detect a change from a  $\pi$  out of phase one colour state ( $\delta_a = \pi$  in Eqn. 4.31). The pitchfork detection algorithm continued above the pitchfork and overlapped with the Hopf line. From [33] it is known that there actually two Hopf lines very close together in this case, with a small window of symmetric two colour states between them. Because in the high  $\eta$  regime it is one of these Hopf bifurcations that causes a change in the symmetric one colour states, this is why the algorithm picked up one of these Hopf lines. The divergence in the Hopf lines can be seen at low  $\eta$  values, where in [33] they split around

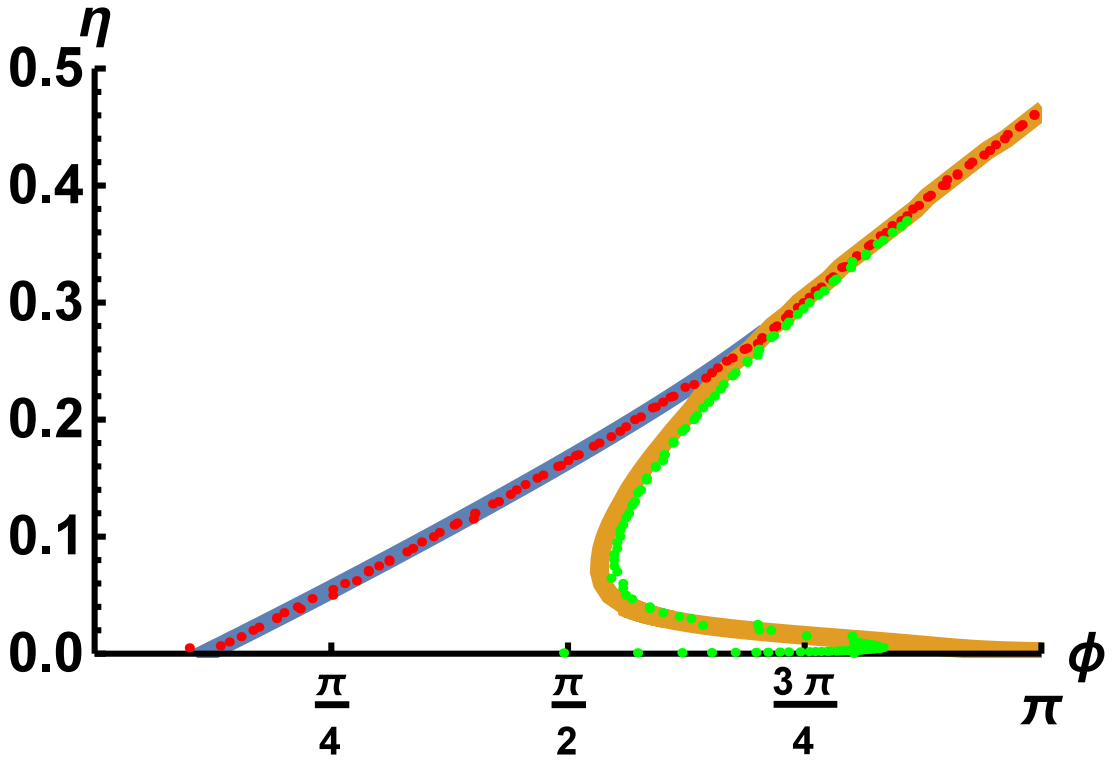
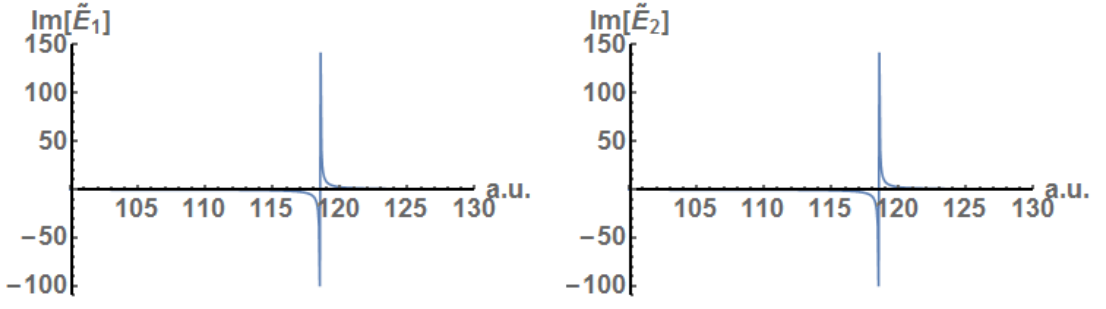


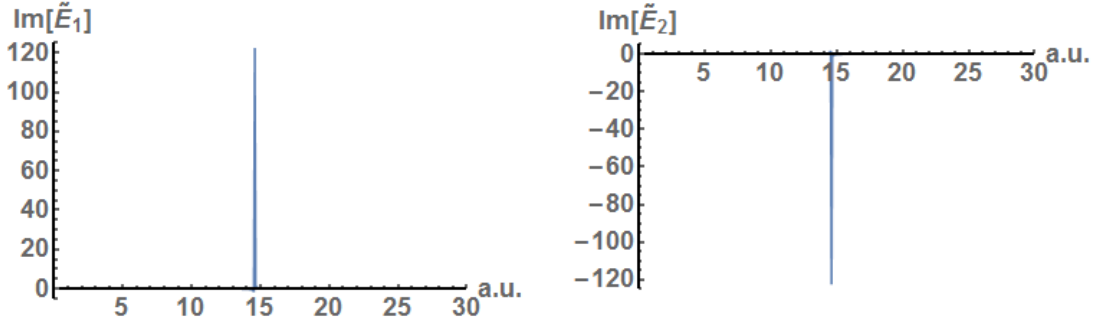
Figure 5.15: Output of the nine point grid comparison method, for finding the pitchfork (green dots) and hopf (red dots) bifurcations, for the model with  $\delta = 0$  and  $\tau = 2$ . The result is compared with previously calculated bifurcations for this system (pitchfork (blue line) and hopf (orange line)).

$\phi = 2.6$ . One Hopf lines curls back, while the other continues on. It is the Hopf that curls back that controls the stability of the anti-phase one colour states, hence why the algorithm followed this Hopf line rather than the other. As detection of whether the fields were anti-phase or in phase was needed, a method was developed to detect this. After taking the FFT, the absolute value of the output is taken, which gives plots like in figure 5.12. Taking this absolute value removes phase data. To detect a  $\pi$  phase shift the real and imaginary part of the FFT must be considered. The real and imaginary parts of the FFT were studied on either side of this Hopf bifurcation line to observe the impact of the  $\pi$  phase shift, resulting in figure 5.16.

It can be seen in figure 5.16a that  $\tilde{E}_1$  and  $\tilde{E}_2$  have the same peak values in their imaginary parts of FFTs, however in figure 5.16b, after crossing the Hopf bifurcation it is observed that the peak values of  $\tilde{E}_1$  are inverted in  $\tilde{E}_2$ . Considering the polar definition employed in Eqn. 4.30, using Euler's formula



(a) Left side of hopf bifurcation ( $\phi = 1.88$ , and  $\eta = 0.45$ ) ( $\tilde{E}$  fields in phase) for  $\tau = 1$ .



(b) Right side of hopf bifurcation ( $\phi = 2.2$ , and  $\eta = 0.45$ ) ( $\tilde{E}$  fields  $\pi$  out of phase) for  $\tau = 1$ .

Figure 5.16: Plots of the Imaginary parts of  $\tilde{E}_{1,2}$  on either side of the Hopf bifurcation in figure 5.14.

this can be re-written:

$$E_1 = a_1 e^{i\omega_a t} = a_1 (\cos(\omega_a t) + i \sin(\omega_a t)) \quad (5.33)$$

$$E_2 = a_2 e^{i\omega_a t} e^{i\delta_a} = a_2 (\cos(\omega_a t + \delta_a) + i \sin(\omega_a t + \delta_a)) \quad (5.34)$$

If  $\delta_a = 0$  (in-phase), the real and imaginary parts are equal. However if  $\delta_a = \pi$  (anti-phase) then the Cosine term remains positive, however the Sine term becomes negative, hence the inversion seen in figure 5.16 A detection algorithm was written that detects this inversion and can classify a one colour state as being in phase or out of phase.

### 5.2.5 Interpolation Expansion Method

The basic 9 point grid comparison method gave a good initial insight into the location of bifurcations but had some draw-backs. Depending on the initial grid size, the method could miss areas of high curvature or small details. An alternative method was needed to overcome this issue. The interpolation



expansion method used the raw data of the previous method (before bisection), which was then divided into the different bifurcation lines. From this data an interpolating function was created, points were generated along this function with a small step size, for better accuracy. Then each interpolated point was taken and expanded around in steps of  $\epsilon$ , with each new step being compared to the previous value, until the desired change in behaviour is encountered. Once this change occurs, the algorithm stepped back  $\frac{\epsilon}{2}$  and saved that point. The method is outlined in figure 5.17. This method ended up

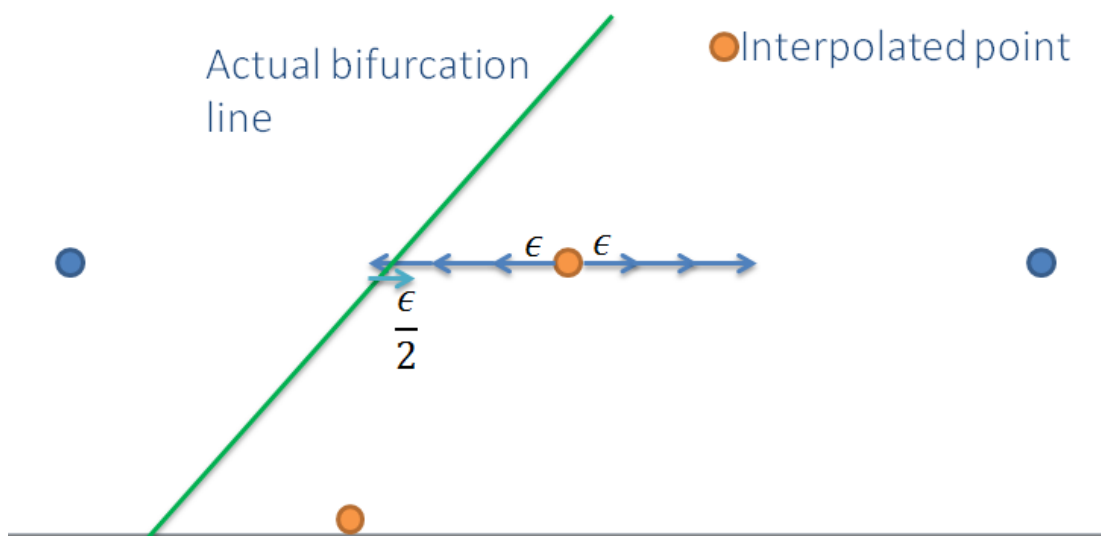


Figure 5.17: Graphical representation of Interpolation Expansion method. Here the example bifurcation line is in green, the interpolated point is in orange. The blue arrows represent expanding left and right around the interpolated point in steps of  $\epsilon$ .

not being used; instead a higher precision localised version of the nine point grid comparison method was employed. However this method was an important tool in studying regions where multiple behavioural regimes are close together and are missed by the mesh size of the nine point grid comparison method. After the algorithms for finding attractor diagrams have been established and tested in the next section they shall be used to investigate a new regime and study the dynamics present in the system.

### 5.2.6 Attractor Diagram Study of the Model with Detuning

After the attractor diagram method was refined and confirmed, it was then applied to an unknown system. The detuning,  $\delta$ , was re-introduced, where no bifurcation study had been performed for this range of delay times and

coupling strengths. Previous work ([9, 28, 31, 30] studied the bifurcations of this system for larger laser separations, 20 – 50 mm, and low coupling, 2%).

### 5.2.6.1 $(\phi, \eta)$ Parameter Space Study

The nine point grid comparison method was implemented to detect changes from one colour  $\rightarrow$  not one colour and two colour  $\rightarrow$  not two colour. For each detuning value, selected delay times of  $\tau = 0.5, 1, 1.5$  and  $2$  were chosen as these are the values of  $\tau$  that correspond to experimental devices being tested within the research group. The results can be seen in figure 5.18.

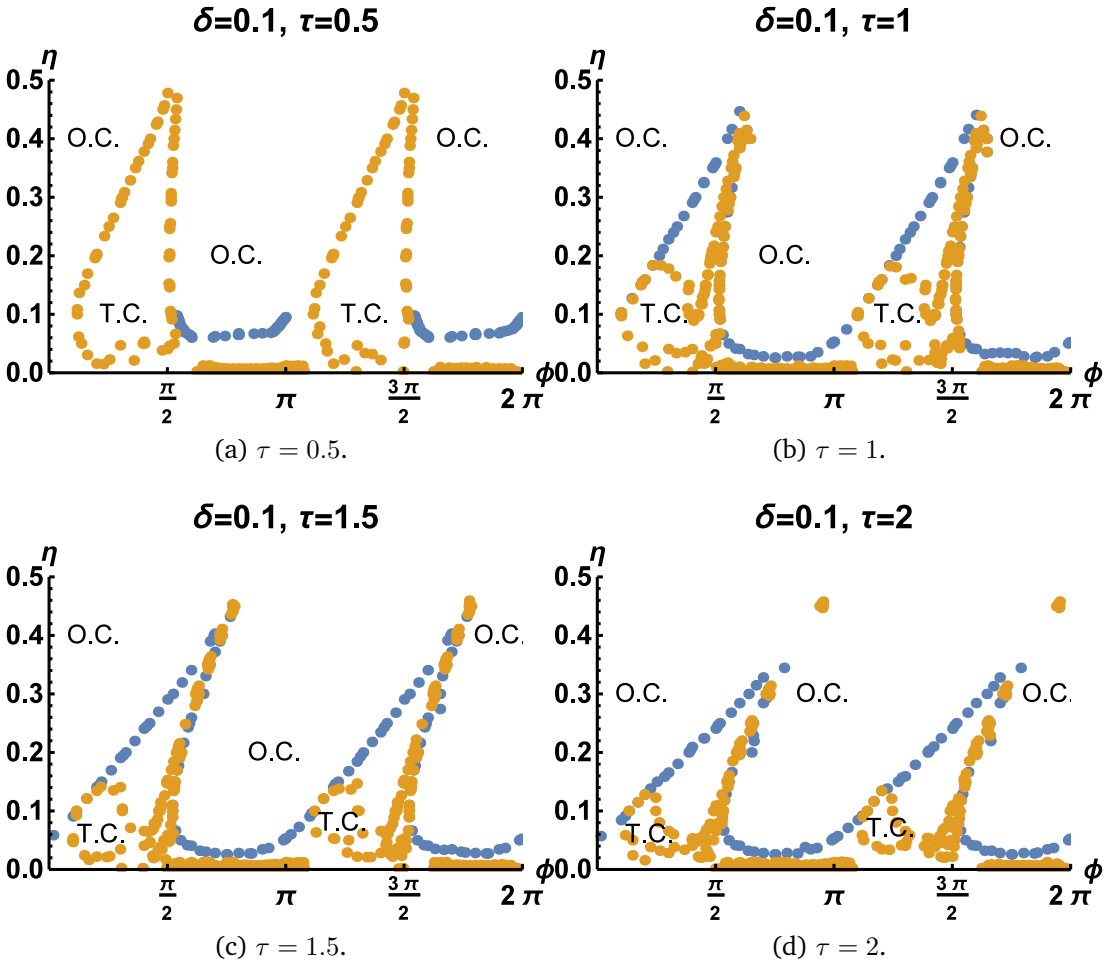


Figure 5.18: Results of nine point grid comparison method for defining the boundaries of the one colour region, O.C., (blue) and two colour, T.C., (orange) for  $\delta = 0.1$  and varying  $\tau$ .

For  $\tau = 0.5$  (figure 5.18a) a clear change from one colour  $\rightarrow$  two colour, thus forming a Hopf bifurcation. When the delay time was increased to  $\tau = 1$  a large shift in the two colour behaviour was observed compared to  $\tau = 0.5$ .

These two "triangular areas" in figure 5.18a, that were purely two colour, now contained two behavioural regimes, a two colour regime (indicated by T.C.) and another regime unidentified by the algorithm. An example of this behaviour can be seen in figure 5.19. One can also see in figure 5.18 the Hopf line on the right of the "triangular" region tilts further to the right with increasing delay time,  $\tau$ .

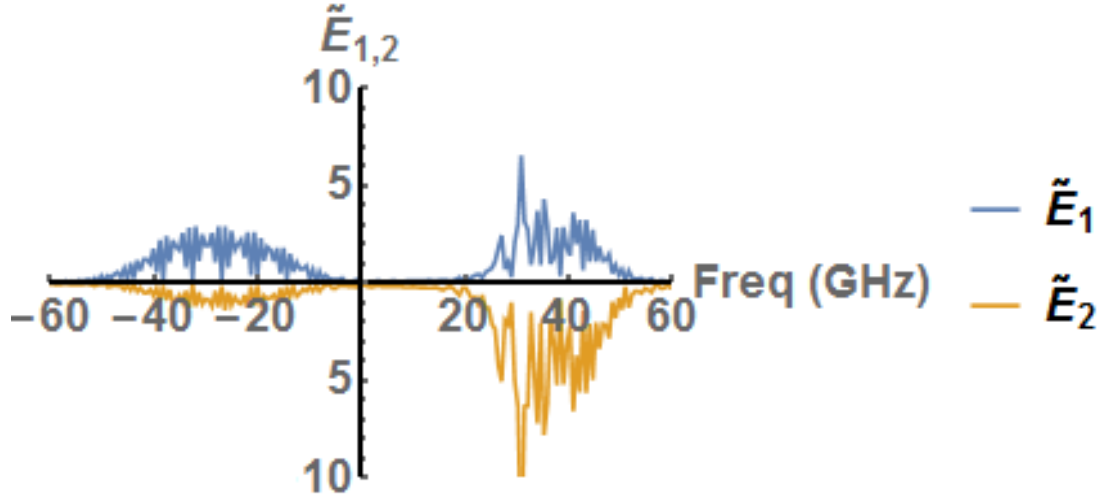
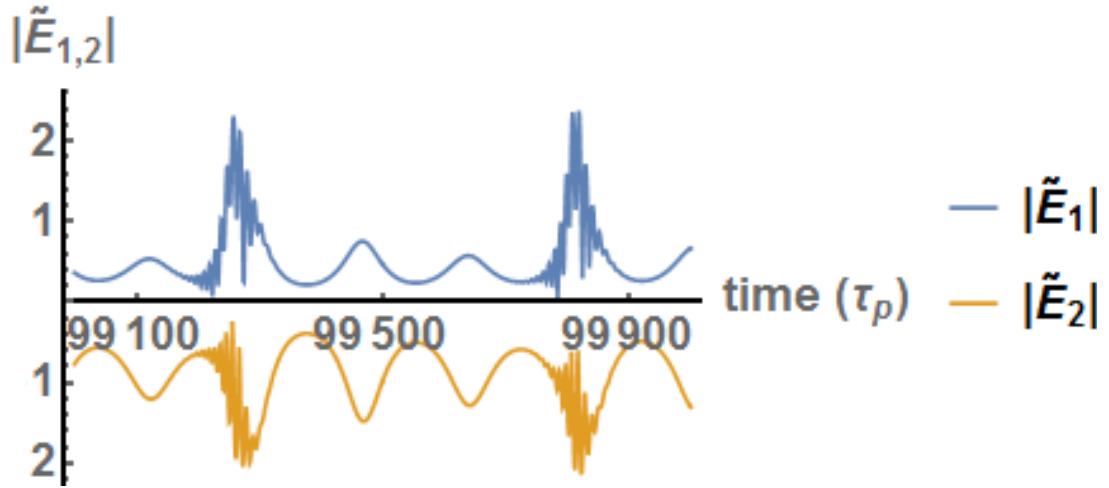
(a)  $\tilde{E}_{1,2}$ .(b) Time trace of  $|E_{1,2}|$ .

Figure 5.19:  $\tilde{E}_{1,2}$  and time traces of  $|E_{1,2}|$  for  $\eta = 0.25, \phi = 1.26, \tau = 1$  and  $\delta = 0.1$  ( $\tilde{E}_2$  is inverted for clarity).

From 5.19b the time trace of  $|E|$  looks as if it has the envelope of a sinusoid, but this sinusoid has its own modulation upon it. This can also be identified by the clustering of the peaks around two broad frequencies in  $\tilde{E}$  in figure 5.19a.

These methods were then applied to higher detuning values ( $\delta = 0.2$  and  $0.3$ ) providing the results shown in figure 5.20.

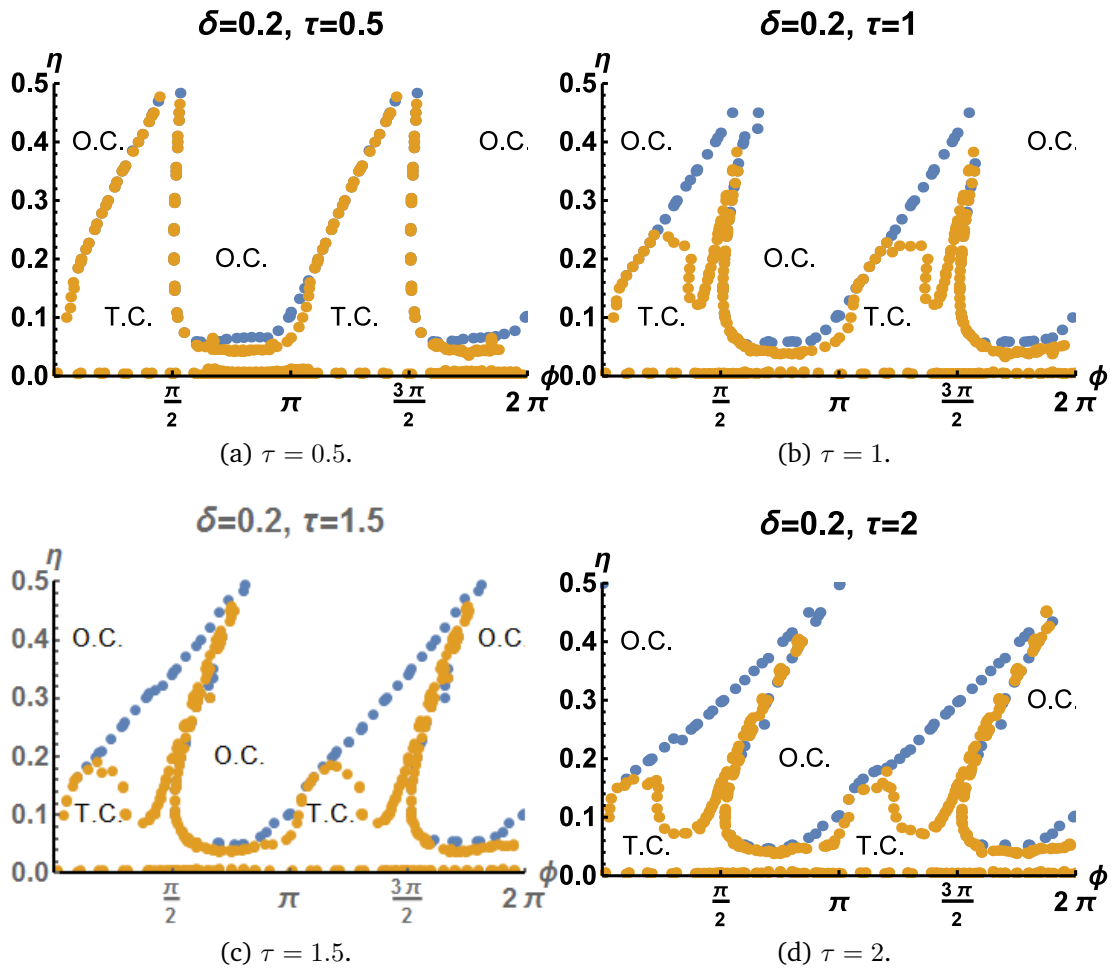


Figure 5.20: Results of nine point grid comparison method for defining the boundaries of the one colour region, O.C., (blue) and two colour, T.C., (orange) for  $\delta = 0.2$  and varying  $\tau$ .

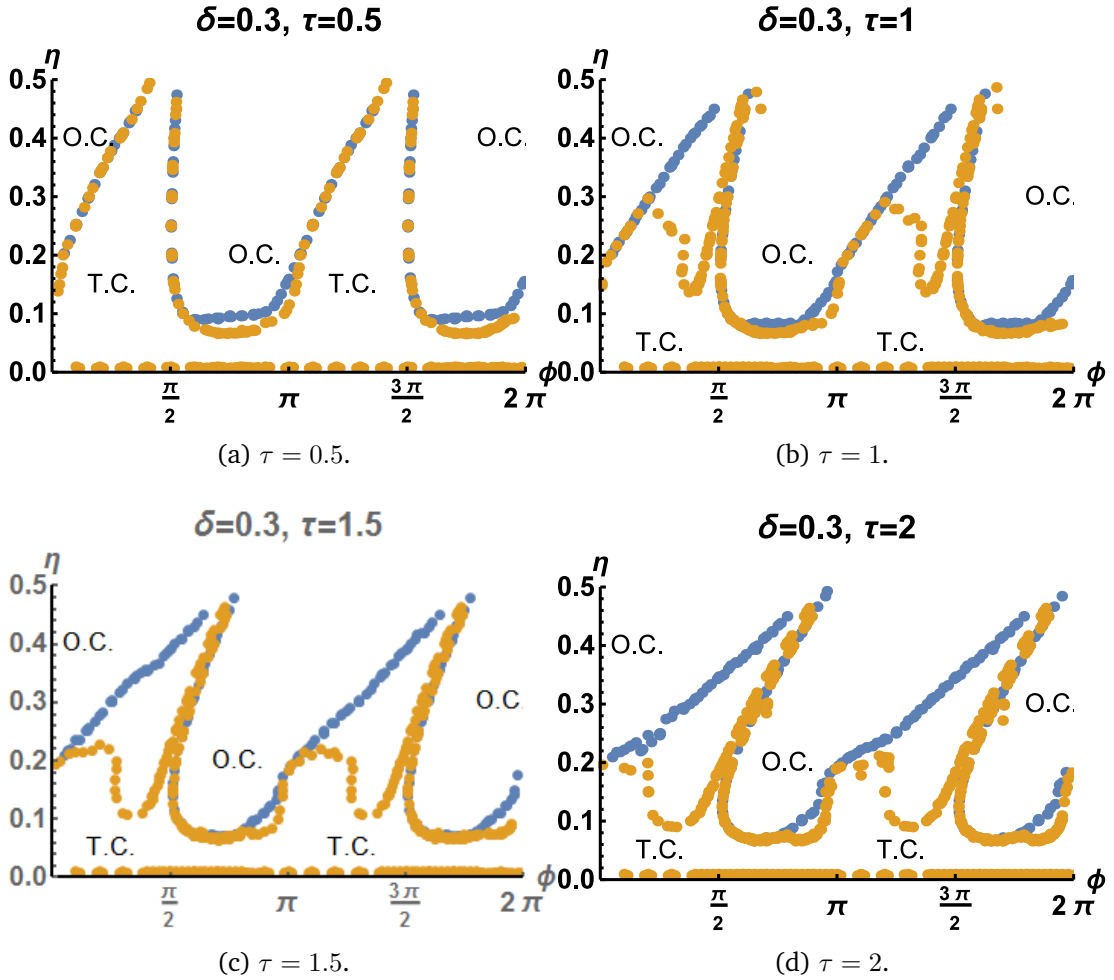


Figure 5.21: Results of nine point grid comparison method for defining the boundaries of the one colour region, O.C., (blue) and two colour, T.C., (orange) for  $\delta = 0.3$  and varying  $\tau$ .

From the results in figure 5.20 one can deduce that for a moderate detuning of 20 GHz (a high speed photodiode can detect up to  $\sim 50$  GHz), and low coupling ( $\eta < 0.05$ ) that the lasers are in a two colour state. This is in contrast to results from [33] where for low coupling with no detuning the result is mostly chaotic across the span of  $\phi$ . Around the value of  $\eta = 0.05$  between  $\phi = 2$  and 3 (repeats between 5 and 6), there is a window of behaviour between the one colour regime above and two colour window below. Investigating this parameter space yields figure 5.22. From figure 5.22b the system has a pulse train behaviour. One can see that the period of these pulses is approximately  $400\tau_p$  (or 4 ns). This is close to the carrier lifetime  $\tau_n$ , so this oscillation could be a carrier induced feature.

In figure 5.21b, 5.21c and 5.21d, there is a pocket of behaviour that is not one

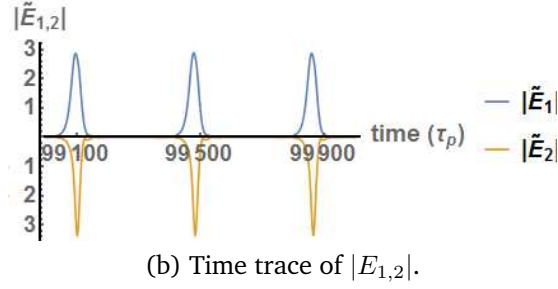
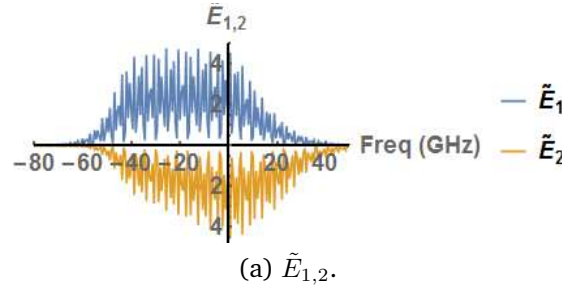


Figure 5.22:  $\tilde{E}_{1,2}$  and time traces of  $|E_{1,2}|$  for  $\eta = 0.07, \phi = 2.2, \tau = 0.5$  and  $\delta = 0.3$  ( $\tilde{E}_2$  is inverted for clarity).

colour or two colour located at the left hand base of the "triangular" region (around approximately  $\eta = 0.1$  and  $\phi = 3$ ). This area was investigated yielding figure 5.23. Here one observes a high order pulsation; the order of a pulsation is the number different peaks observable in one period of the time trace. This oscillation again has a period close to  $400\tau_p$ , and could be carrier induced.

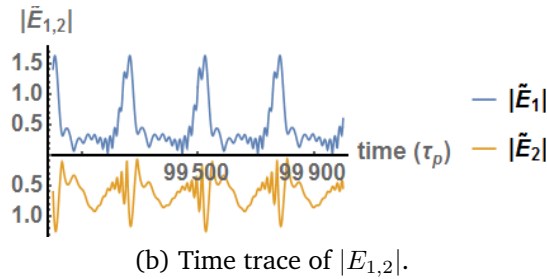
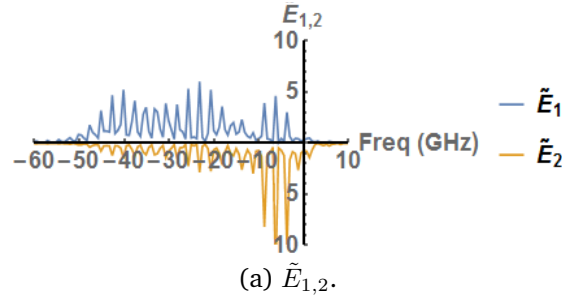


Figure 5.23:  $\tilde{E}_{1,2}$  and time traces of  $|E_{1,2}|$  for  $\eta = 0.1, \phi = 2.83, \tau = 2$  and  $\delta = 0.3$  ( $\tilde{E}_2$  is inverted for clarity).

### 5.2.7 $(\phi, \delta)$ Parameter Space Study

The inclusion of frequency detuning,  $\delta$ , is a key parameter in this study. It was decided that rather than sampling a few values (in Sec. 5.2.6.1),  $\delta$  would be considered as a bifurcation parameter. To do this the injection parameter,  $\eta$ , was made a fixed parameter, with a set of values sampled from low ( $\eta = 0.025$ ), moderate ( $\eta = 0.1$ ) and high ( $\eta = 0.3$ ) coupling. This also allowed for the study of negative detuning, i.e. where  $\omega_2 > \omega_1$ . The same procedure as Sec. 5.2.6.1 was followed except the parameter space being sampled was now the  $(\phi, \delta)$  space. This produced the results shown in figure 5.24.

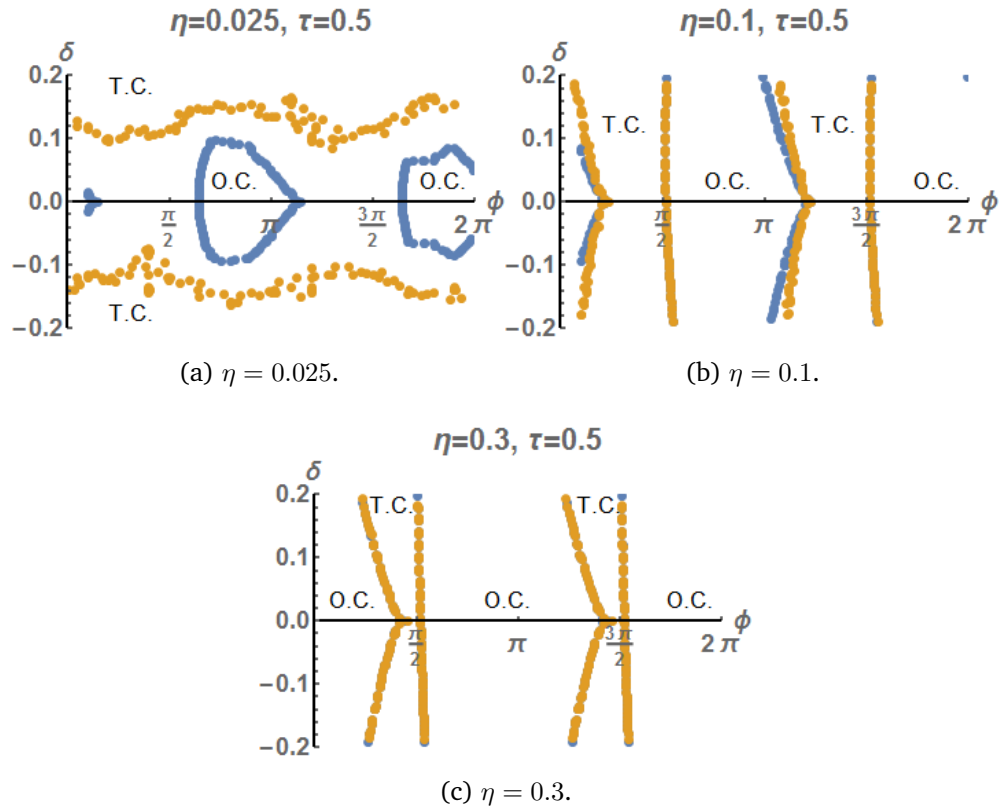


Figure 5.24: Results of nine point grid comparison method for detecting change from one colour  $\rightarrow$  not one colour (Orange) and two colour  $\rightarrow$  not two colour (Blue), in the  $(\phi, \delta)$  parameter space, for  $\tau = 0.5$  and varying  $\eta$ . The areas of one colour states are highlighted by O.C. and the two colour regions are denoted by T.C.

From figure 5.24, one can see that the system is symmetric around the  $\delta$  parameter, i.e. the bifurcation diagrams are the same for  $\delta$  and  $-\delta$ . Figure 5.24a shows the bifurcations for low coupling ( $\eta = 0.025$ ). One can see small regions of one colour behaviour, below  $\delta \approx 0.1$ . This region is surrounded by a

region of chaotic behaviour, as can be seen from figure 5.25. This is identified as chaotic behaviour, by observing the unequally spaced, unequal height value peaks in  $\tilde{E}_{1,2}$ .

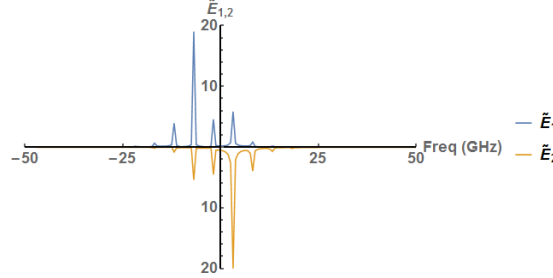


Figure 5.25:  $\tilde{E}_{1,2}$  for  $\tau = 0.5, \eta = 0.025, \delta = 0.05$  and  $\phi = 1$  ( $\tilde{E}_2$  is inverted for clarity).

Interestingly, for high enough detuning ( $\delta > 0.15$ ) there is only two colour behaviour. Considering the low injection strength, the high frequency separation is most likely resulting in a beating between the lasers, which would correspond to a two-colour state. The frequency of this beat note was investigated by investigating a series of delta values above this bifurcation line.

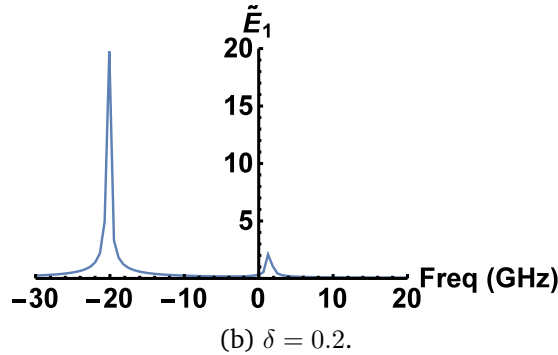
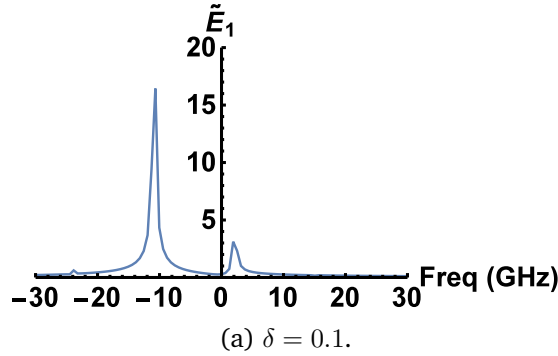


Figure 5.26:  $\tilde{E}_1$  for  $\eta = 0.025, \phi = 0.94, \tau = 0.5$  and (a)  $\delta = 0.1$ , (b)  $\delta = 0.2$ .

In figure 5.26a, the separation of the peaks (which would correspond to the beat note in the case of the  $|E|$ ) is  $12\text{GHz}$ , when the lasers were set to be 10



GHz apart. This separation was then increased to 20 GHz ( $\delta = 0.2$ , figure 5.26b), and the peak separation became 20.7 GHz. This shows that the frequency of the two colour beat note has a strong correlation to the frequency separation of the lasers, further supporting the conclusion that this two colour state corresponds to the beating of two lasers, due to the low injection strength.

Increasing the coupling to  $\eta = 0.1$  gave figure 5.24b. Here it can be seen that there is a much smaller multi-periodic regime as the bifurcation diagram is dominated by one colour and two colour states. One can see regions of different behaviour in the divergence of the two algorithms (at approximately,  $\phi = 3.3$  and  $\delta = 0.2$ ). An example of this chaotic region can be seen in figure 5.27.

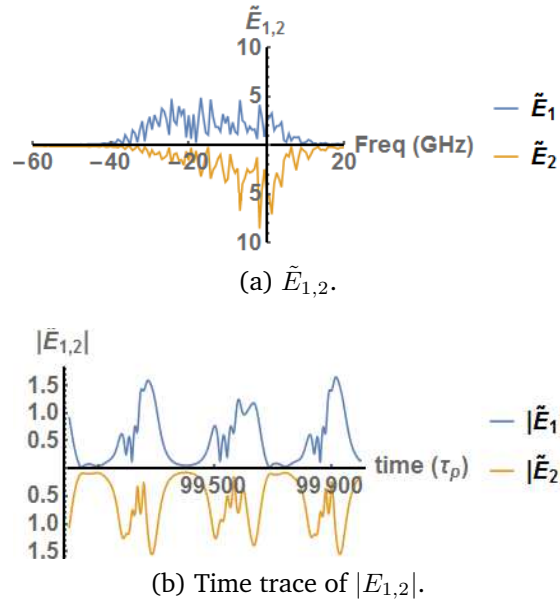


Figure 5.27:  $\tilde{E}_{1,2}$  and time traces of  $|E_{1,2}|$  for  $\eta = 0.1$ ,  $\phi = 3.3$ ,  $\tau = 0.5$  and  $\delta = 0.2$  ( $\tilde{E}_2$  is inverted for clarity).

Further increasing  $\eta = 0.3$ , in figure 5.24c one can see the detection algorithms perfectly overlap, and all windows of chaotic behaviour have disappeared. For this high injection, the lasers can only lock together (one colour state) or beat (two colour state). Increasing  $\tau$  to 1 results in figure 5.28. For  $\eta = 0.025$  (figure 5.28a) one can see identical behaviour to figure 5.24a. However one can see a drastic change between figure 5.28b and 5.24b, where an extra region has appeared within the two colour regions. This corresponds to the regions described in Sec. 5.2.6.1, where a new behavioural regime unidentified by the algorithm appeared when  $\tau = 1$ .

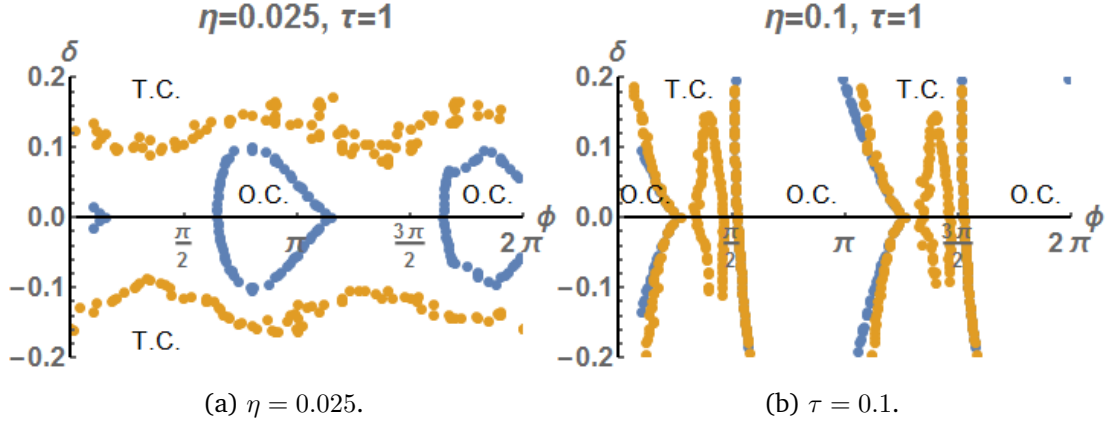


Figure 5.28: Results of nine point grid comparison method for detecting change from one colour  $\rightarrow$  not one colour (Orange) and two colour  $\rightarrow$  not two colour (Blue), in the  $(\phi, \delta)$  parameter space, for  $\tau = 1$  and varying  $\eta$ . The areas of one colour states are highlighted by O.C. and the two colour regions are denoted by T.C.

In the next section these attractor diagrams will be translated to experimental results. The methodology of the procedures undertaken in the lab will be re-created theoretically. This will correspond to taking vertical slices across the  $(\phi, \eta)$  attractor diagrams and then these will be compared directly with experimental results.

## 5.3 Recreation of experimental methods

### 5.3.1 Dependence on the injection parameter

To correspond with the experiment, the  $\delta$ ,  $\tau$  and  $\phi$  values were fixed and the results were obtained as a function of the  $\eta$  parameter. At each  $\eta$  value the FFT of the complex field,  $\tilde{E}_1$ , was taken. These were then stacked into a contour plot, as seen in figure 5.29a. This translates to taking a vertical line across the attractor diagrams from Section 5.2.6.1. The two-colour states can be seen on the left hand side of the diagram, where there are two diverging lines. At approximately  $\eta = 0.3$  the system changes to a one-colour state. This change in dynamics corresponds to a pitchfork bifurcation in the system without detuning ( $\delta = 0$ ) [33], however when  $\delta$  is included it breaks symmetries within the model and this becomes a saddle-node bifurcation. Previous studies give insight into the stability of the solutions observed. One such study showed that for zero detuning and non-zero delay, one colour states are stable for low

values of  $\phi$  and values close to  $\phi = \pi$ , for all cases of  $\eta \in (0, 0.5)$  [25]. Another study showed stable symmetry broken two colour states for a window of values around  $\phi = \frac{\pi}{2}$ , in the case of  $\tau = 0$  [32]. A work by another member of the research group confirmed the stability of these symmetry broken states for  $\tau \neq 0$  [33]. Initial investigations into the bifurcation diagrams of this non-zero detuning and delay system confirms similar results for the stability of the solutions, as seen in these works. In the following section, results from solving the DDE system Eqn.4.6-4.9 are shown for varying parameters that can be controlled in the experiment; enabling direct comparison with the experiment.

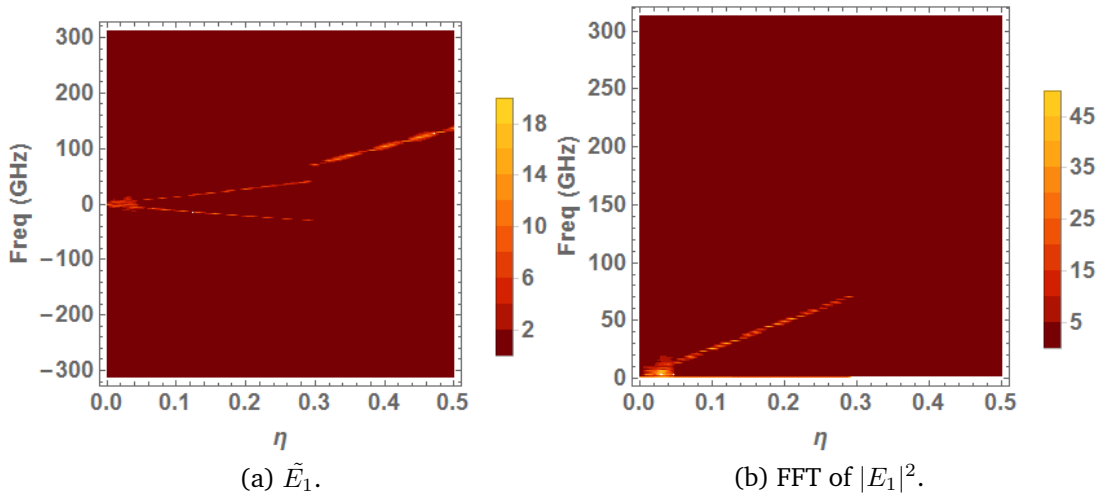


Figure 5.29: Logarithmic contour plots of  $\tilde{E}_1$  and the FFT of  $|E_1|^2$  for varying coupling coefficient, for  $\delta=0.01$ ,  $\tau = 0.5$ , and  $\phi = 0.4\pi$ .

To observe these dynamics experimentally, an electronic spectrum analyser (ESA) would be used. This shows the Fourier transform of the voltage signal received by a photodiode. The photodiode measures  $|E|^2$ , therefore the ESA displays the Fourier transform of  $|E|^2$ . Repeating the process used to generate figure 5.29a, but this time showing the FFT of  $|E_1|^2$  yields figure 5.29b. In figure 5.29, while the result was shown for  $\tilde{E}_1$ , it should be noted that behaviourally  $\tilde{E}_1$  and  $\tilde{E}_2$  are the same, so only  $\tilde{E}_1$  is shown in the results.

Now the two-colour state manifests as a single peak, whose frequency increases as the peaks of the two-colour states diverge in figure 5.29a. Recall Eqn. 4.65, where the absolute value squared of the definition of a two-colour state, Eqn. 4.62, gives:

$$|E_1(t)|^2 = a_1^2 + b_1^2 + 2a_1b_1 \cos((\omega_a - \omega_b)t)$$

A Fourier transform of this would give a single beat note, between the frequencies  $\omega_{a,b}$ , as observed. Similarly for the one colour states  $|E_1|^2 = a_1^2$ , a constant, yielding an FFT with no distinct frequencies, as seen in figure 5.29b.

From the study by my colleague it is known that in the case with  $\delta = 0$ , more complex dynamics (i.e. not a one or two colour state) only exist for low coupling ( $\eta < 0.1$  approx.) [33]. However having included detuning, more complex behaviours can be achieved by increasing the detuning and delay time. For example figure 5.30, 5.31 and 5.32 show results of sweeping  $\eta$  for higher detuning ( $\delta = 0.2$ ) and higher delay time ( $\tau = 2$ ), for various coupling phases ( $\phi$ ).

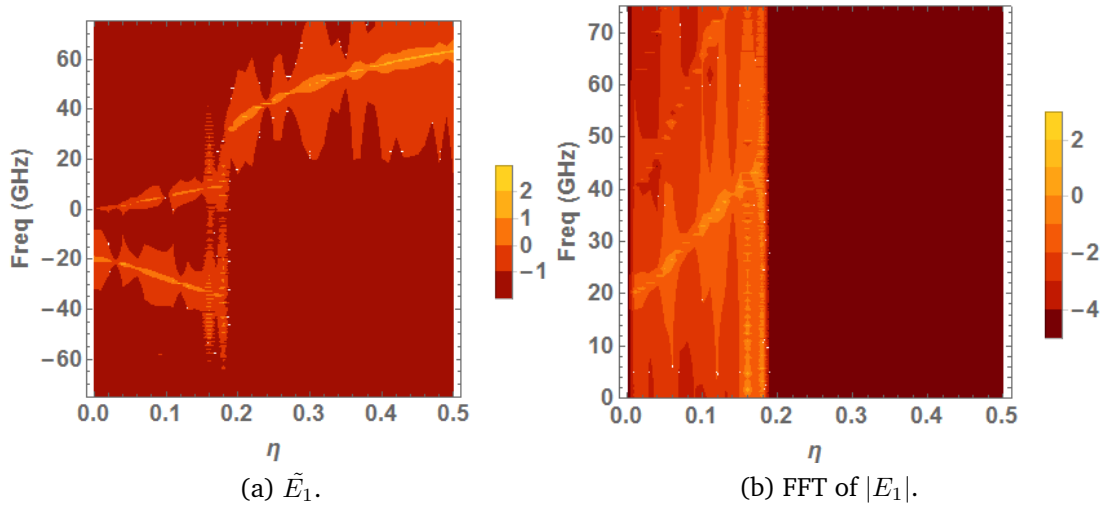


Figure 5.30: Logarithmic contour plots of  $\tilde{E}_1$  and  $|E_1|$  for varying coupling coefficient, for  $\delta=0.2$ ,  $\tau = 2$ , and  $\phi = 0.2\pi$ .

In all of these one can see complex dynamics for coupling strength above  $\eta = 0.1$ , unlike the case for  $\delta = 0$ . For example in figure 5.30 for low coupling a two colour state exists, whose frequency difference ( $\omega_a - \omega_b$  in equation 4.65) for very low coupling matches the detuning of the lasers (20 GHz corresponds to  $\delta = 0.2$ ). As  $\eta$  increases the frequency of this beat note increases, before undergoing a torus bifurcation to a window of highly periodic behaviour ( $\eta = 0.16$ ), then goes through a saddle-node bifurcation to form a one colour state ( $\eta = 0.2$ ). The highly periodic behaviour can be identified by looking at the time trace of  $|E_1|$ , in figure 5.33a, where 11 peaks in the time trace can be seen.

For  $\phi = 0.4\pi$ , figure 5.31, the chaotic region becomes wider. For  $\phi = 0.7\pi$ , figure 5.32, the system goes from the two colour, to a one colour state

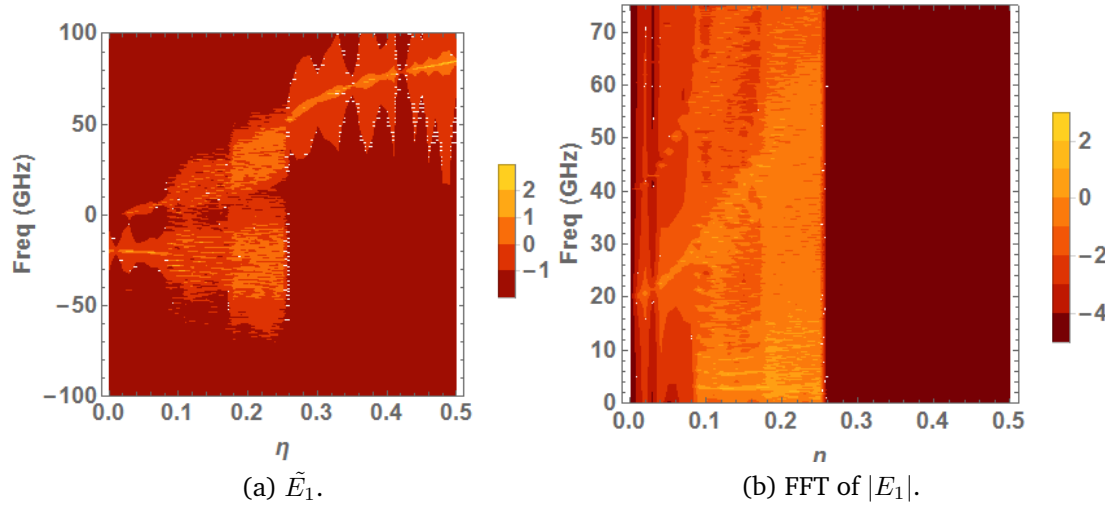


Figure 5.31: Logarithmic contour plots of  $\tilde{E}_1$  and  $|E_1|$  for varying coupling coefficient, for  $\delta=0.2$ ,  $\tau = 2$ , and  $\phi = 0.4\pi$ .

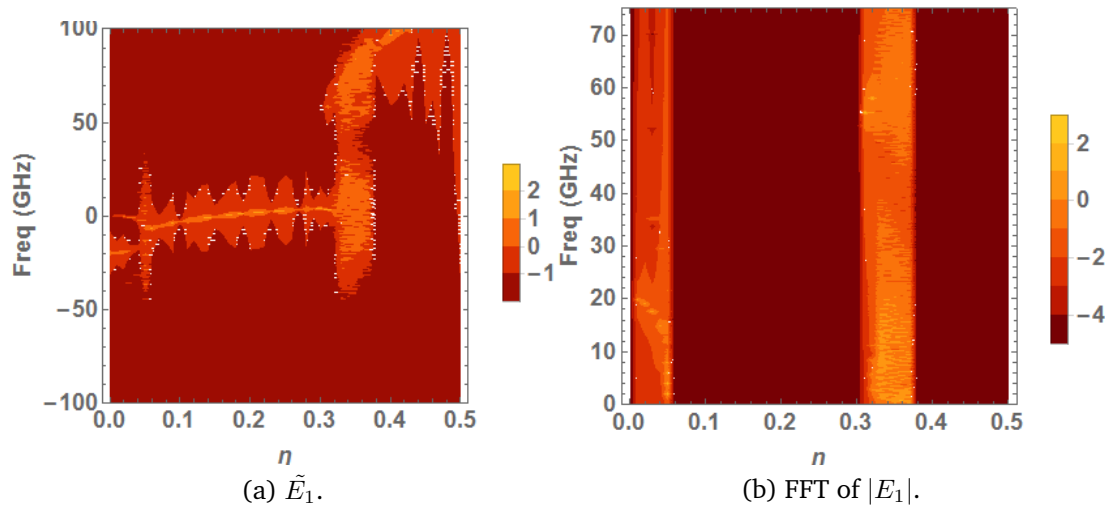


Figure 5.32: Logarithmic contour plots of  $\tilde{E}_1$  and  $|E_1|$  for varying coupling coefficient, for  $\delta=0.2$ ,  $\tau = 2$ , and  $\phi = 0.7\pi$ .

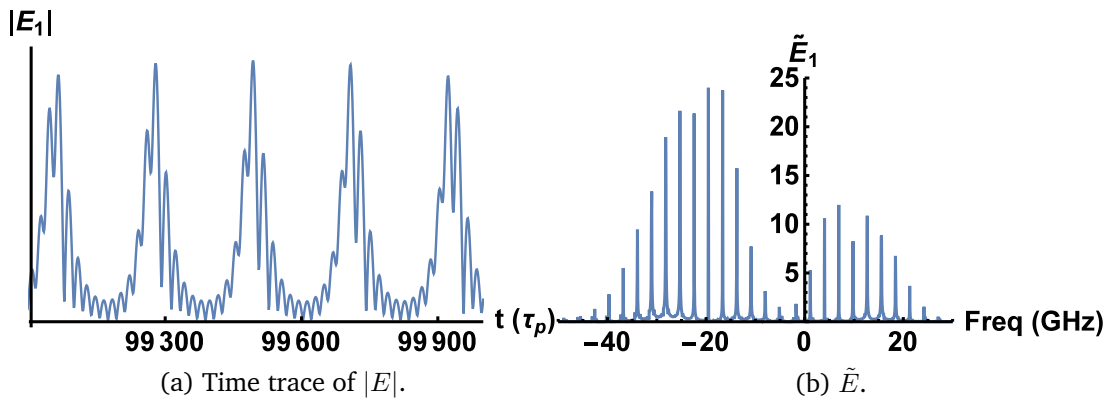


Figure 5.33: Time trace of  $|E|$  and  $\tilde{E}$  for  $\eta = 0.1$ ,  $\phi = 0.4\pi$ ,  $\tau = 2$  and  $\delta = 0.2$ .

( $\eta = 0.05$ ) via a Hopf bifurcation, before entering a chaotic regime ( $\eta = 0.33$ ) through a torus bifurcation and then transitioning into another one colour state at  $\eta = 0.37$  via a saddle-node bifurcation. In the next section we shall repeat this procedure for the  $(\phi, \delta)$  parameter space, so directly observe the effect of varying the detuning in a continuous manner.

### 5.3.2 Dependence on detuning

Using parameters closely matching experimental values, figure 5.34a shows the contour plot of the FFT of  $|E_1|^2$  for moderate injection strength ( $\eta = 0.2$ ), a delay time of  $\tau = 0.5$  and a coupling phase of  $\phi = 0.2\pi$ , while varying the detuning from  $-0.2$  to  $0.2$  (corresponds to  $-20$  -  $20$  GHz). To the left of the graph a beat note corresponding to a two colour state of decreasing frequency can be seen. At approximately  $\delta = -0.12$  the system changes to a one colour state. As the detuning crosses zero and becomes positive the system changes back to a two colour state at approximately  $\delta = 0.1$ .

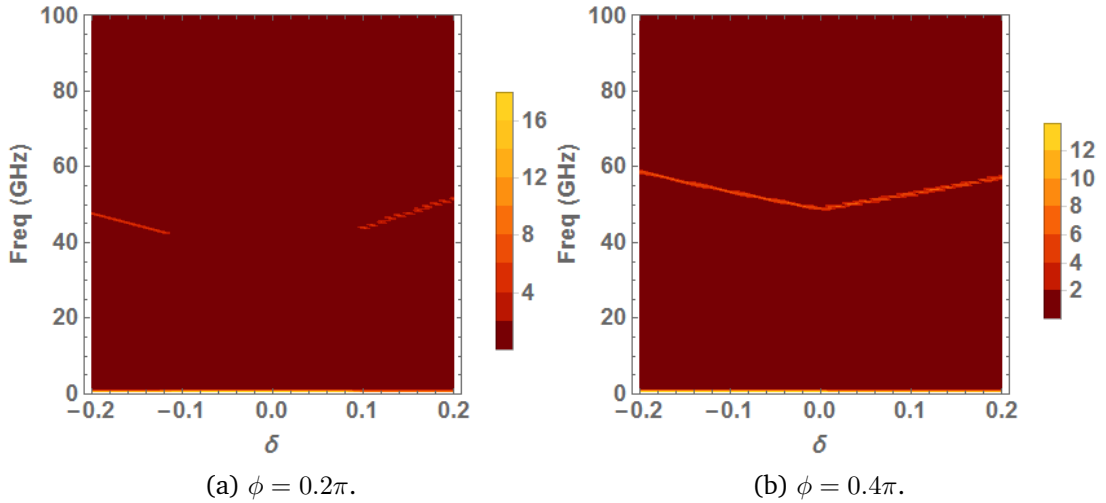


Figure 5.34: Logarithmic contour plots of  $|E_1|^2$  for varying detuning ( $\delta = -0.2$  to  $0.2$ ), for  $\eta = 0.2$ ,  $\tau = 0.5$ , and a)  $\phi = 0.2\pi$ , b)  $\phi = 0.4\pi$ .

The width of this one colour state is affected by phase. For example if the coupling phase was changed to  $\phi = 0.4\pi$ , one can see the one colour state has disappeared, as seen in figure 5.34b. Here the beat note of the two colour state decreases as the detuning approaches zero from negative values and then increases in frequency as the detuning becomes more positive. This beat frequency linearly changes with  $\delta$ .

It is known from studies ([32, 33]), that at low coupling there is chaotic

behaviour for the system without detuning. Figure 5.35 shows the behaviour of the system for  $\eta = 0.025$ . For high values of  $|\delta|$  (the far left and right of the graph), there exists the beat notes of two colour states, however as  $\delta$  approaches zero the system goes through windows of highly harmonic behaviour (e.g. at  $\delta = 0.1$ ), before entering chaotic behaviour, identified by a high power regime, with no clear dominant frequency or harmonics. The generation of sub-harmonics in these windows could either be a period-doubling or torus bifurcation. However period-doubling bifurcations are characterised by the fact that the sub harmonics are exactly half the original frequency. Hence here it is most likely a torus bifurcation as the sub harmonics are not exactly at half frequencies.

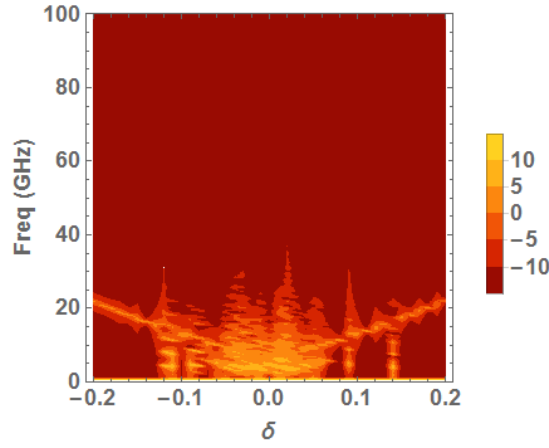


Figure 5.35: Logarithmic contour plots of  $|E_1|^2$  for varying detuning ( $\delta = -0.2$  to  $0.2$ ), for  $\eta = 0.025$ ,  $\tau = 0.5$ , and  $\phi = 0.2\pi$ .

Next a behavioural regime referred to as self-pulsations in previous literature will be studied in a parameter space that was not considered. That being the delayed system ( $\tau \neq 0$ ).

## 5.4 Self-Pulsations

Simplifications can be made to Eqn. 4.6-4.9, based on making assumptions for  $\phi$ . By setting  $\phi$  to 0 or  $\frac{\pi}{2}$ , the complex exponential terms become simpler. This was also done when  $\tau = 0$  and  $\delta \neq 0$  [25]. Firstly the model is re-written with the complex fields represented in polar form,  $E_{1,2} = a_{1,2}e^{i\Psi_{1,2}}$ . A new variable is also defined,  $\delta\Psi = \Psi_1 - \Psi_2$ .

$$a_1' = N_1 a_1 + \eta a_2(t - \tau) \cos(\phi + \Psi_1 - \Psi_2(t - \tau)) \quad (5.35)$$

$$N'_1 = \epsilon[J - N_1 - (N_1 + \nu)a_1^2] \quad (5.36)$$

$$a'_2 = N_2 a_2 + \eta a_1(t - \tau) \cos(\phi + \Psi_2 - \Psi_1(t - \tau)) \quad (5.37)$$

$$N'_2 = \epsilon[J - N_2 - (N_2 + \nu)a_2^2] \quad (5.38)$$

$$\delta\Psi = \delta + (N_1 - N_2)\alpha - \frac{\eta a_2(t - \tau)}{a_1} \sin(\phi + \Psi_1 - \Psi_2(t - \tau)) + \frac{\eta a_1(t - \tau)}{a_2} \sin(\phi + \Psi_2 - \Psi_1(t - \tau)) \quad (5.39)$$

Firstly it will be assumed  $\phi = \frac{\pi}{2}$ . This gives Eqn. 5.40-5.45.

$$a'_1 = N_1 a_1 - \eta a_2(t - \tau) \sin(\Psi_1 - \Psi_2(t - \tau)) \quad (5.40)$$

$$\Psi'_1 = \delta + \alpha N_1 - \frac{\eta a_2(t - \tau)}{a_1} \cos(\Psi_1 - \Psi_2(t - \tau)) \quad (5.41)$$

$$a'_2 = N_2 a_2 - \eta a_1(t - \tau) \sin(\Psi_2 - \Psi_1(t - \tau)) \quad (5.42)$$

$$\Psi'_2 = \alpha N_2 - \frac{\eta a_1(t - \tau)}{a_2} \cos(\Psi_2 - \Psi_1(t - \tau)) \quad (5.43)$$

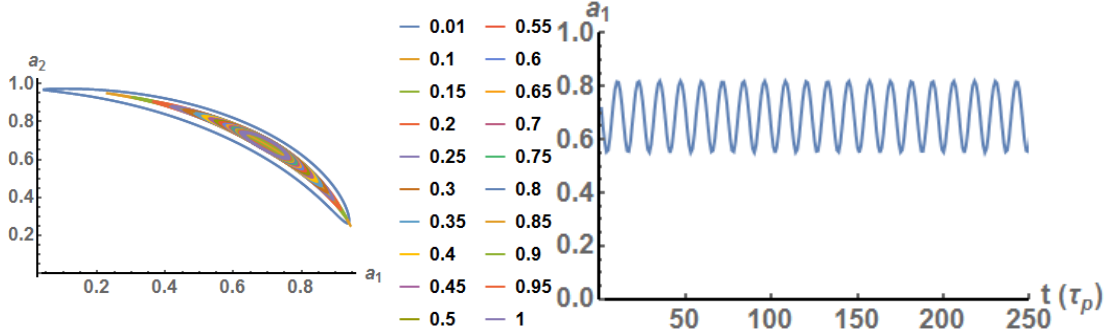
$$N'_1 = \epsilon[J - N_1 - (N_1 + \nu)a_1^2] \quad (5.44)$$

$$N'_2 = \epsilon[J - N_2 - (N_2 + \nu)a_2^2] \quad (5.45)$$

This model was studied over a large parameter space. In each case  $\delta$  was varied from 0.01 – 1. Figure 5.36 shows this  $\delta$  variation for  $\eta\tau a = 0.1$  and  $\tau = 0.5$ . By observing the parametric plots in figure 5.36a, the closed loops indicate a limit cycle behaviour, and the single closed loops indicate a period one oscillation. This is confirmed in figure 5.36b, where the time trace of the field amplitude  $a_1$  is plotted. This fits the definition of a two colour state from Eqn. 4.65 (repeated below for reader's convenience). This means that a first order self-pulsation (SP) is a two colour state.



$$|E_1(t)|^2 = a_1^2 + b_1^2 + 2a_1b_1 \cos((\omega_a - \omega_b)t)$$

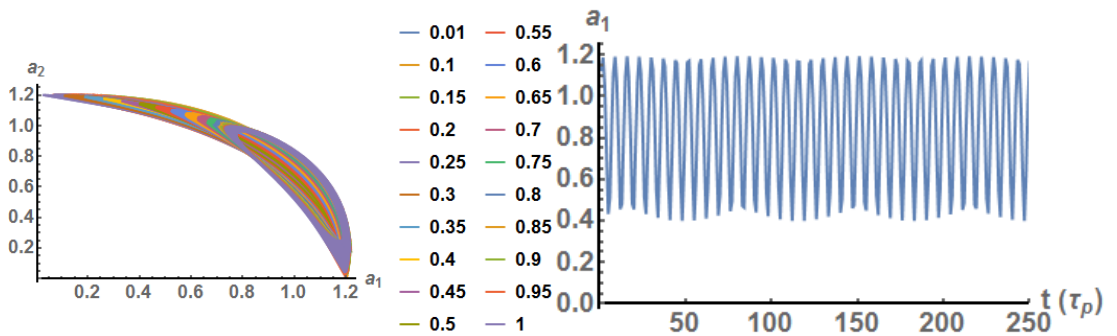


(a) Parametric plots of  $a_1$  vs  $a_2$  for varying  $\delta$ , (b) Time trace of  $a_1$  for  $\delta = 0.5$ , with  $\eta = 0.1$  and  $\tau = 0.5$ .

Figure 5.36: Solving the model with  $\phi = \frac{\pi}{2}$  simplification for  $\eta = 0.1$  and  $\tau = 0.5$ . a) Shows parametric plots of  $a_1$  vs  $a_2$ , while b) shows the time trace of  $a_1$  for  $\delta = 0.5$ .

However this simplified model can achieve higher than first order SPs.

Increasing the injection strength to  $\eta = 0.4$ , gives figure 5.37. The parametric plot in figure 5.37a shows the closed loops associated with a limit cycle behaviour, are now thicker, meaning the system is oscillating between two closed loops, i.e. a second order SP. This is confirmed in the time trace in figure 5.37b, where there is a sinusoidal modulation upon the basic sinusoidal behaviour.



(a) Parametric plots of  $a_1$  vs  $a_2$  for varying  $\delta$ , (b) Time trace of  $a_1$  for  $\delta = 0.5$ , with  $\eta = 0.4$  and  $\tau = 0.5$ .

Figure 5.37: Solving the model with  $\phi = \frac{\pi}{2}$  simplification for  $\eta = 0.4$  and  $\tau = 0.5$ . a) Shows parametric plots of  $a_1$  vs  $a_2$ , while b) shows the time trace of  $a_1$  for  $\delta = 0.5$ .

This simplified model can be pushed even further, increasing the delay time to

$\tau = 2$ , and setting  $\eta = 0.4$  and sweeping the  $\delta$  parameter to give the results as displayed in figure 5.38. For low values of detuning the system is in a locked state (flat power output in figure 5.38a), when  $\delta$  reached a value of 0.6 the behaviour changed to chaotic pulsation (figure 5.38b), before switching to a highly periodic solution (figure 5.38c) when  $\delta = 0.7$ . The period of figure 5.38b is close to the 4 ns observed previously, indicating again this could be a carrier induced oscillation. Looking at the period of the long period envelope of figure 5.38c (rather than the short period of the individual peaks), it is in the range of  $250 \tau_p$  (or 2.5 ns). Which is also close to the carrier lifetime,  $\tau_n$ .

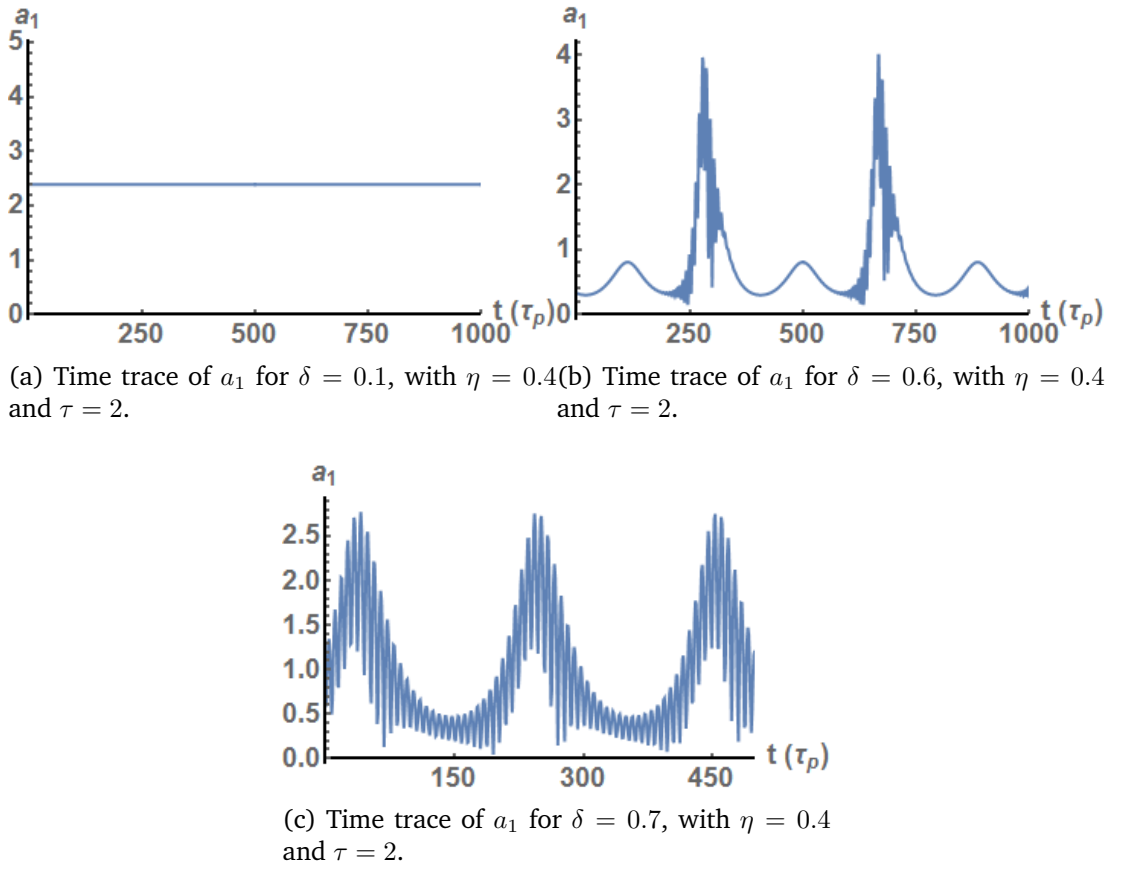


Figure 5.38: Solving the model with  $\phi = \frac{\pi}{2}$  simplification for  $\eta = 0.4$  and  $\tau = 2$ , for various  $\delta$  values. a)  $\delta = 0.1$ , b)  $\delta = 0.6$ , c)  $\delta = 0.7$ .

The highest  $\tau$  value considered in the study was  $8\tau_p$ , this translates to a distance of approximately  $27\tau_p$  between the lasers and could only be achieved through the use a spiral waveguide or through external coupling of the lasers using a fiber arrangement, if it were to be experimentally verified. Firstly low injection strength was looked at,  $\eta = 0.1$ , for varying detuning. This produced the behaviours in figure 5.39. For low detuning, up to  $\delta = 0.15$ , the system was

in a high order periodic behaviour, figure 5.39a. After this point up to  $\delta = 0.5$ , the system is in a basic first order SP, figure 5.39b, before returning a high order SP again until  $\delta = 0.7$ , figure 5.39c. Finally at  $\delta = 1$  the system produces a second order SP, figure 5.39d. Considering the period of these solutions, figure 5.39a has a period of approximately  $350 \tau_p$  which is close to the  $400 \tau_p$  period observed earlier, which is possibly linked to the carrier lifetime. Figure 5.39d has a period of approximately  $250 \tau_p$  (or  $2.5 \text{ ns}$ ), which was also observed in figure 5.38c. Figures 5.39b and 5.39d have a very short period of  $10 \tau_p$  and  $5 \tau_p$ . These are much faster than the carrier lifetime, so the dynamics are coming from somewhere else.

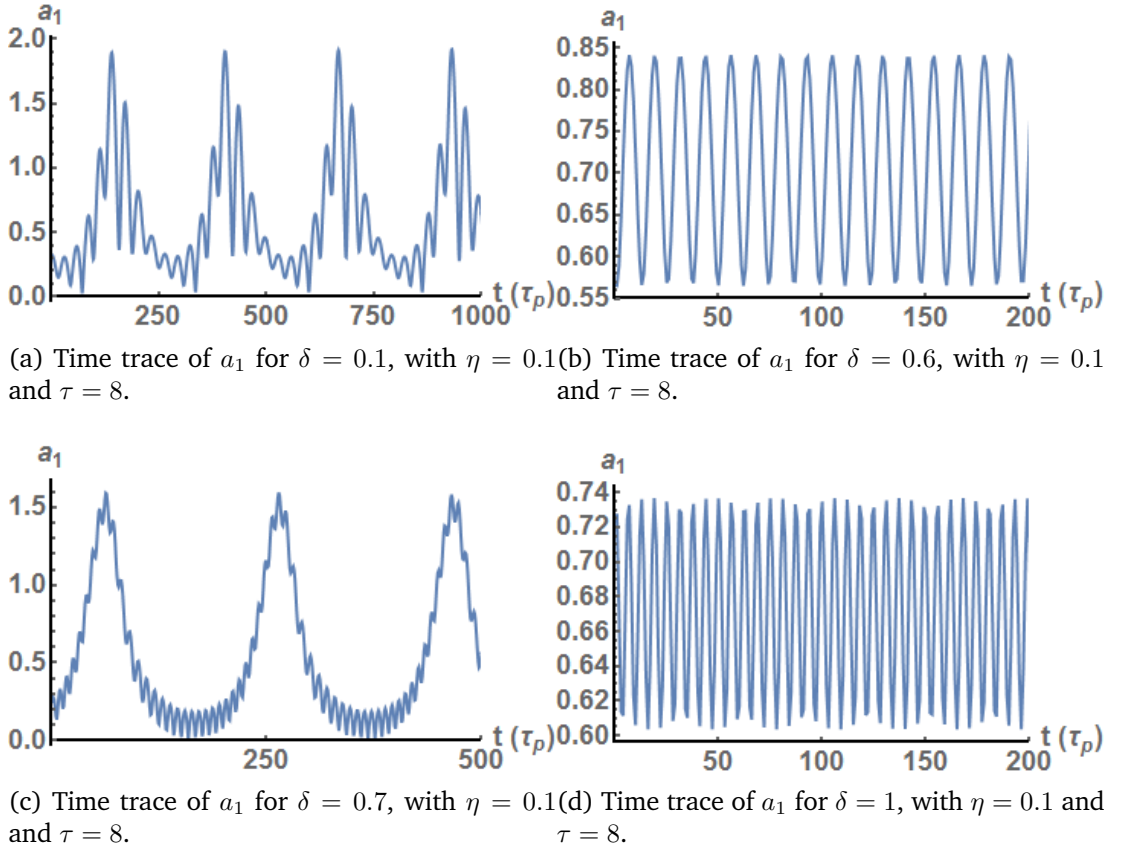


Figure 5.39: Solving the model with  $\phi = \frac{\pi}{2}$  simplification for  $\eta = 0.1$  and  $\tau = 8$ , for various  $\delta$  values. a)  $\delta = 0.15$ , b)  $\delta = 0.5$ , c)  $\delta = 0.7$  d)  $\delta = 1$ .

Finally for this  $\tau$  value a high injection strength was looked at, of  $\eta = 0.4$ , for varying detuning. This yielded figure 5.40. Up to  $\delta = 0.45$ , this system is in a locked state, as seen in figure 5.40a, after this and up to  $\delta = 0.6$ , a high order SP is achieved, seen in figure 5.40b. At  $\delta = 0.8$  the system returns to a second order SP, as seen in figure 5.40c.

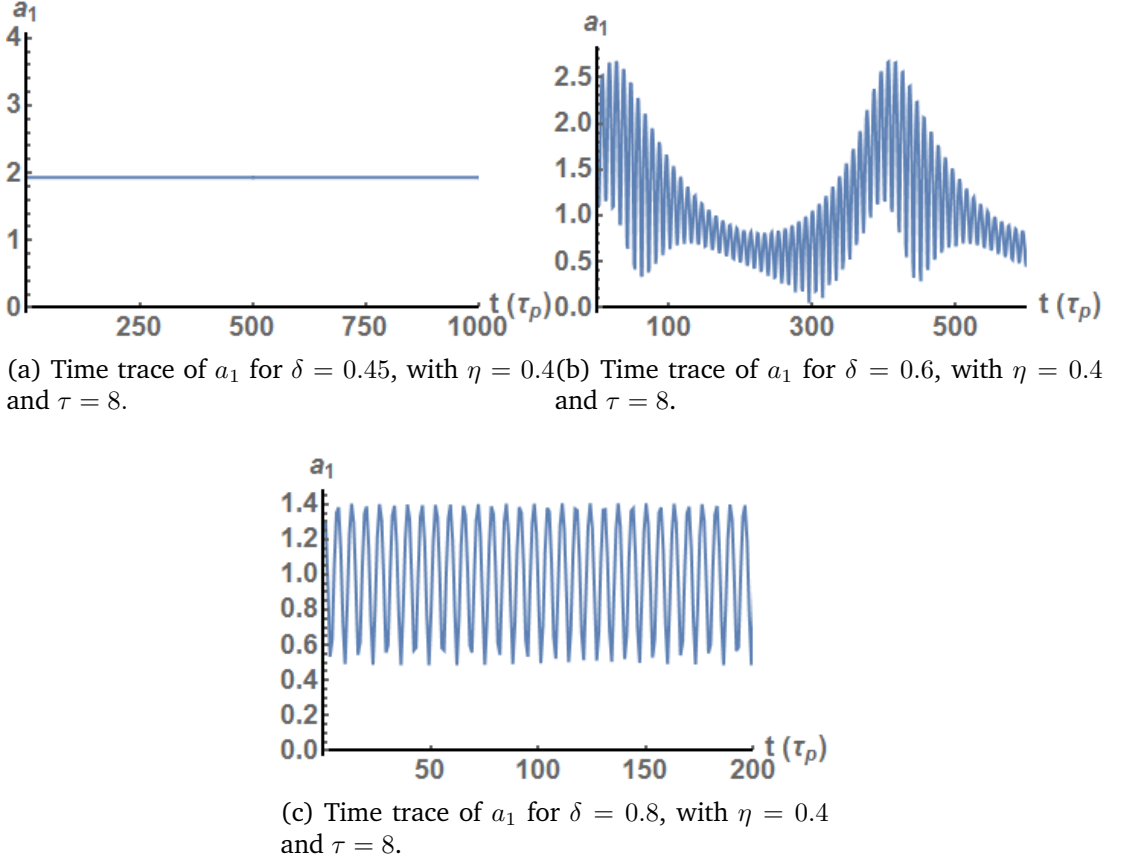


Figure 5.40: Solving the model with  $\phi = \frac{\pi}{2}$  simplification for  $\eta = 0.4$  and  $\tau = 8$ , for various  $\delta$  values. a)  $\delta = 0.45$ , b)  $\delta = 0.6$ , c)  $\delta = 0.8$ .

In summary from this simplified model various behavioural regimes have been shown to exist through study of the time traces of the field amplitudes. There exist locked states, first order SPs (two colour state), second order SPs and high order SPs. To consider how these behaviours would manifest experimentally, figure 5.41 shows contour plots of the FFT of  $a_1$  for varying  $\eta$ .

Figure 5.41a shows multi periodic behaviour, before transition into locking after  $\eta \approx 0.43$ , for  $\tau = 0.5$  and  $\delta = 0.05$ . Figure 5.41b shows this multi periodic behaviour for a lower range of  $\eta$ , transitioning to locked behaviour at  $\eta \approx 0.21$ . Figure 5.41c shows harmonic behaviour for across all  $\eta$  values, when  $\tau = 0.5$  and  $\delta = 0.8$ . Figure 5.41d shows this harmonic behaviour, until  $\eta \approx 0.23$ , before entering a chaotic regime. In the next section a detailed breakdown will be given on the experimental results of MCL devices found in the group. These will be compared with the results of this section to see if any improvements could be made to the modelling approach.

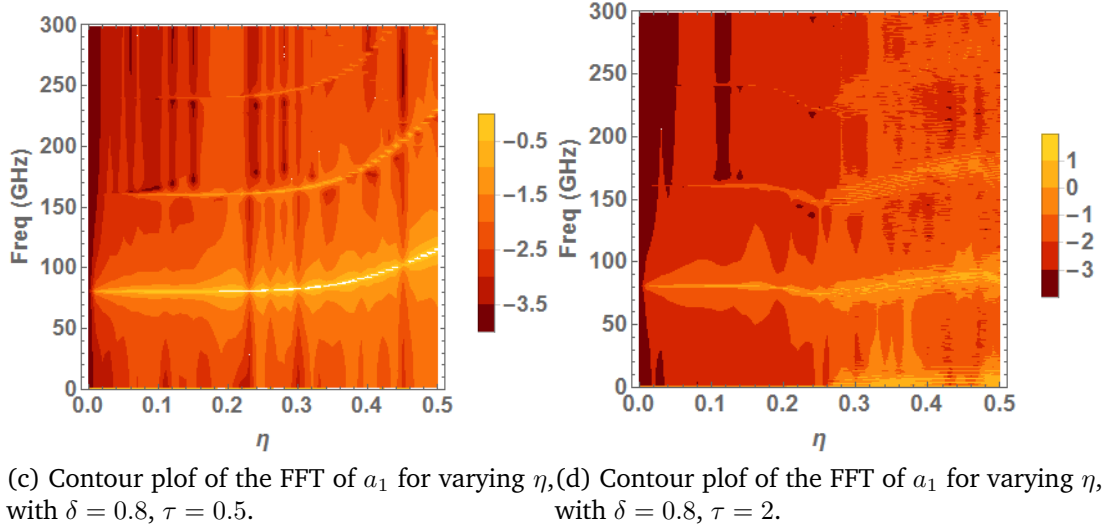
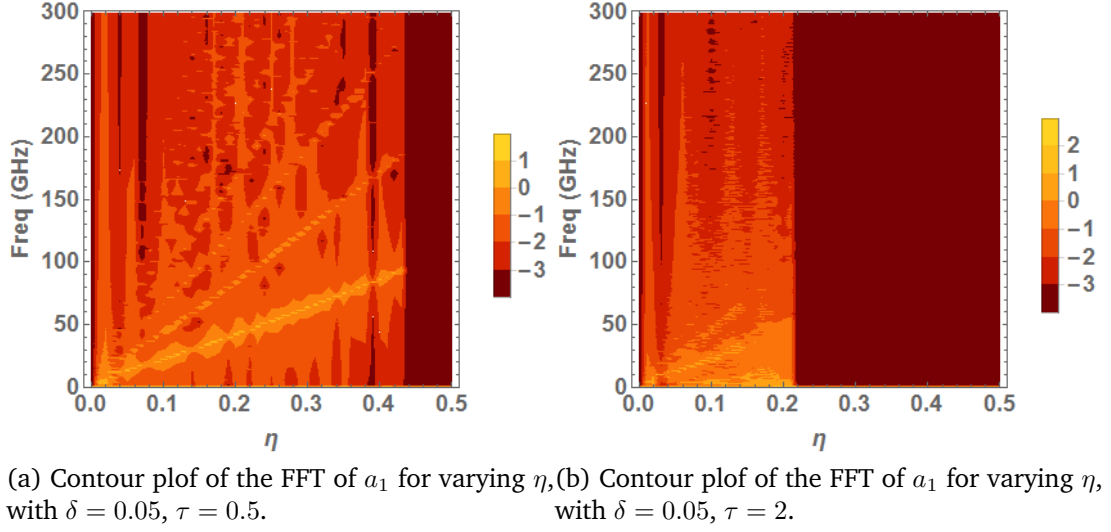


Figure 5.41: Contour plots of  $a_1$  from the model with  $\phi = \frac{\pi}{2}$  simplification for varying  $\eta$  and a)  $\delta = 0.05$ ,  $\tau = 0.5$ , b)  $\delta = 0.05$ ,  $\tau = 2$ , c)  $\delta = 0.8$ ,  $\tau = 0.5$  d)  $\delta = 0.8$ ,  $\tau = 2$ .

### 5.4.1 Experimental results

#### 5.4.1.1 Results from 2<sup>nd</sup> generation MCL devices

An in depth study of the theoretical behaviours has been performed; now these shall be compared with a range of experimental results. As stated in Section 3.3.10 the experimental work started by this thesis was continued by another PhD student, using devices with design improvements made from Chapter 3. The first set of results that were compared with theoretical results come from figure 3.30a (the schematic is shown below for the readers convenience). The PIC consists of a series of devices; each containing two,

two-section Slotted Fabry-Perot (SFP) lasers (each approximately 1.6 mm in length) separated by a curved VOA section of lengths varying from 1.2 mm - 2 mm. The chip was fabricated from the same commercially available epitaxial structure used in Chapter 3, and is outlined in Appendix A. Between the lasers and the VOAs, there is a deep etched section to improve electrical isolation between the sections.

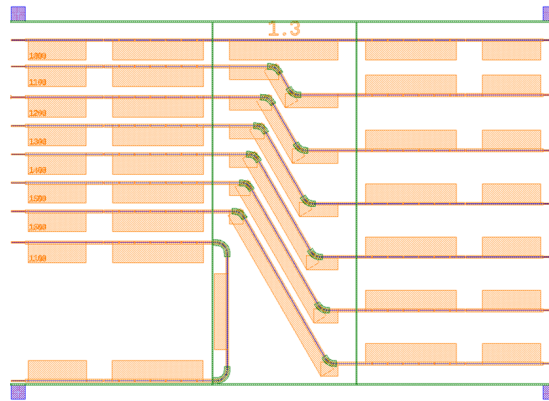


Figure 5.42: Second generation of MCL on chip devices.

In the experiment the lasers were individually tuned to have a specific frequency difference ( $\delta$ ), 0, 5 and 10 GHz, and the VOA section's bias is varied to adjust the coupling of light between the lasers. The device chosen for this test was the U-shaped device on the bottom left of the chip in Fig 5.42, which has a VOA length of 1mm (corresponding to  $\tau \approx 0.3$ ). The VOA bias was swept from 0.8 – 2 V (analogous to sweeping the injection strength  $\eta$ , an example of measured  $\eta$  versus the varying VOA voltage can be seen in figure 5.43) and the output of the lasers were analysed using an ESA to observe the dynamics of the system.

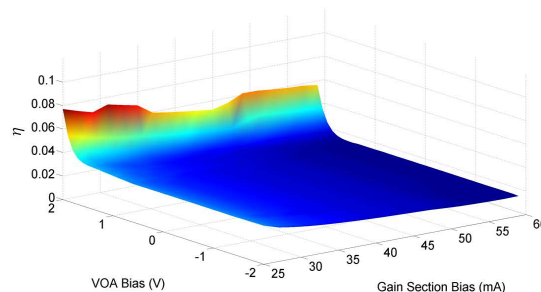


Figure 5.43: Measurement of injection parameter  $\eta$  vs. VOA bias for various mirror section biases of the SFP laser.

Figure 5.44 shows contour plots of these ESA traces for varying VOA bias, for a number of detuning arrangements. On the left of figure 5.44b and 5.44c a

single peak can be seen, corresponding to the laser detuning values of 5 and 10 GHz respectively. Here the VOA is strongly absorbing, eliminating any interaction between lasers. Thus, the laser signals are beating together rather than being allowed to interact; this explains the lack of a peak in figure 5.44a as the laser frequencies are matched. As the VOA becomes more transparent a series of complicated dynamics can be seen. At 1.8 V in figure 5.44b, one can see a region of many frequencies with varying power. Just after this a series of equally spaced peaks of increasing frequency with VOA bias exists. This is at least a fourth order oscillation, as higher frequency peaks are beyond the bandwidth of the ESA. Similar behaviour can be seen in figure 5.44a and 5.44c, where there are a series of equally spaced peaks at several locations. For comparison with theoretical results a direct link between VOA bias and  $\eta$  was required. As mentioned previously, tests were done to find the amount of power absorbed by the VOA compared to the power of the lasers, to find the fraction of light that makes it through the VOA to the other laser, 5.43. For this VOA length a maximum of 8% of the light makes it through the VOA ( $\eta = 0.08$ ). So for comparison with experiment one must look at the  $\eta < 0.1$  regions of the results in Sec. 5.3.1.

The beat note at low voltage, which is equal to the set detuning between the lasers corresponds to theoretical results from Sec. 5.3.1, where the two colour states outlined have a frequency difference equal to the set detuning for low  $\eta$ . The chaotic region around 1.7 V in figure 5.44a and 1.8 V in figure 5.44b can be compared to the manifestation of the chaotic behaviour in the FFT of  $|E|$  in figure 5.30b at  $\eta = 0.16$ ,  $\eta = 0.18$ . 3rd, 4th and 5th order oscillations can be seen across the experimental results in figure 5.44a, 5.44b and 5.44c. However from Section. 5.4 theoretically achieving higher order SPs requires much higher delay time, ( $\tau$ ), and frequency detuning, ( $\delta$ ) then used in this experiment. The expectation is that these pulsations are caused by Q-switching of the absorber, which is not accounted for in the model. However it is important to note again that this chip could not achieve high  $\eta$  values, and when  $\delta = 0$ , the low coupling regime is mostly chaotic behaviour [33]. This makes comparison with theoretical results difficult.

The low value attained for maximum coupling was due to various fabrication issues such as metal adhesion, and for a better comparison with theoretical results, a higher coupling was desired. So another generation of devices was designed and the process was improved to fix the metal adhesion issues. In the next section results from this third generation of devices will be shown.



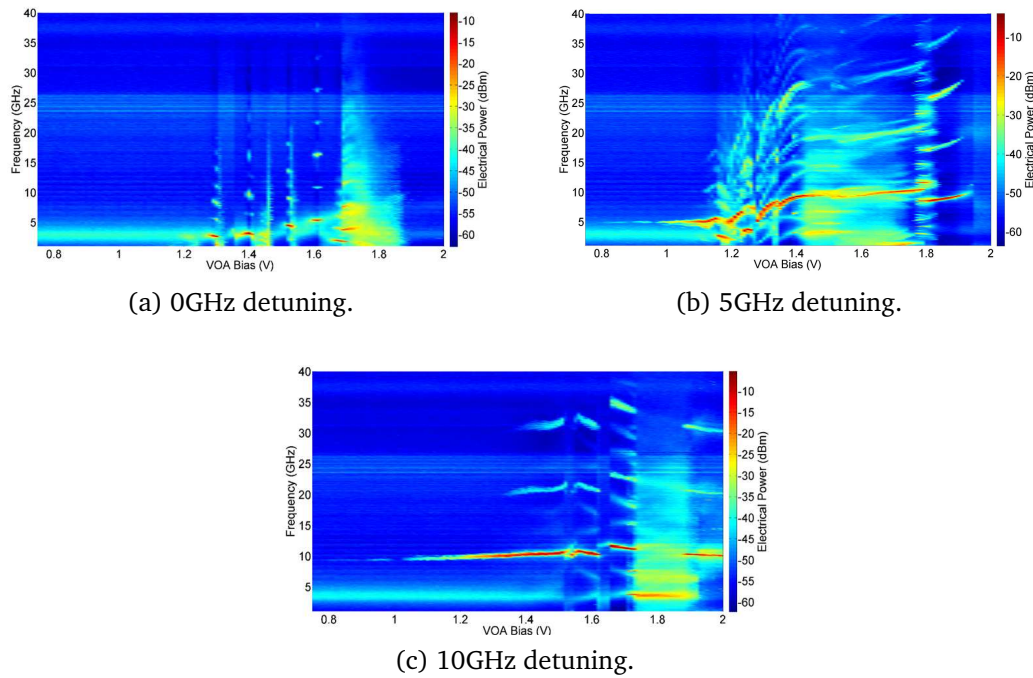


Figure 5.44: Experimental result for varying VOA bias, for a device separation of 1 mm and various detunings.

#### 5.4.1.2 Results from 3<sup>rd</sup> generation MCL devices

After improvements were made to the processing of fabrication a further generation of devices was made. A schematic of these 3rd generations MCL devices can be seen in figure 3.30b. The PIC consists of a series of devices; each containing two, two-section Slotted Fabry-Pérot (SFP) lasers (each approximately 1.4 mm in length), similar to the second generation, however as the most successful design from the previous design was the U-shape VOA, only U-shaped VOA devices were on this chip. These VOAs ranged in length from 385  $\mu\text{m}$  - 1735  $\mu\text{m}$  (corresponding to  $\tau$  values of 0.1 – 1.5).

The experimental procedure was identical to the previous case where the lasers were individually tuned to have a specific frequency difference ( $\delta$ ), and the VOA section's bias is varied to adjust the coupling of light between the lasers. The coupled devices chosen for this test included the shortest VOA device on the chip in Fig 5.45, which has a VOA length of 385  $\mu\text{m}$  (corresponding to  $\tau \approx 0.1$ ). The VOA bias was swept from 0.5 – 2 V (analogous to sweeping the injection strength  $\eta$ ) and the lasers were tuned to have a 15 GHz frequency difference ( $\delta = 0.15$ ). The output of the lasers were analysed using an Electronic Spectrum Analyser (ESA) to observe the dynamics of the



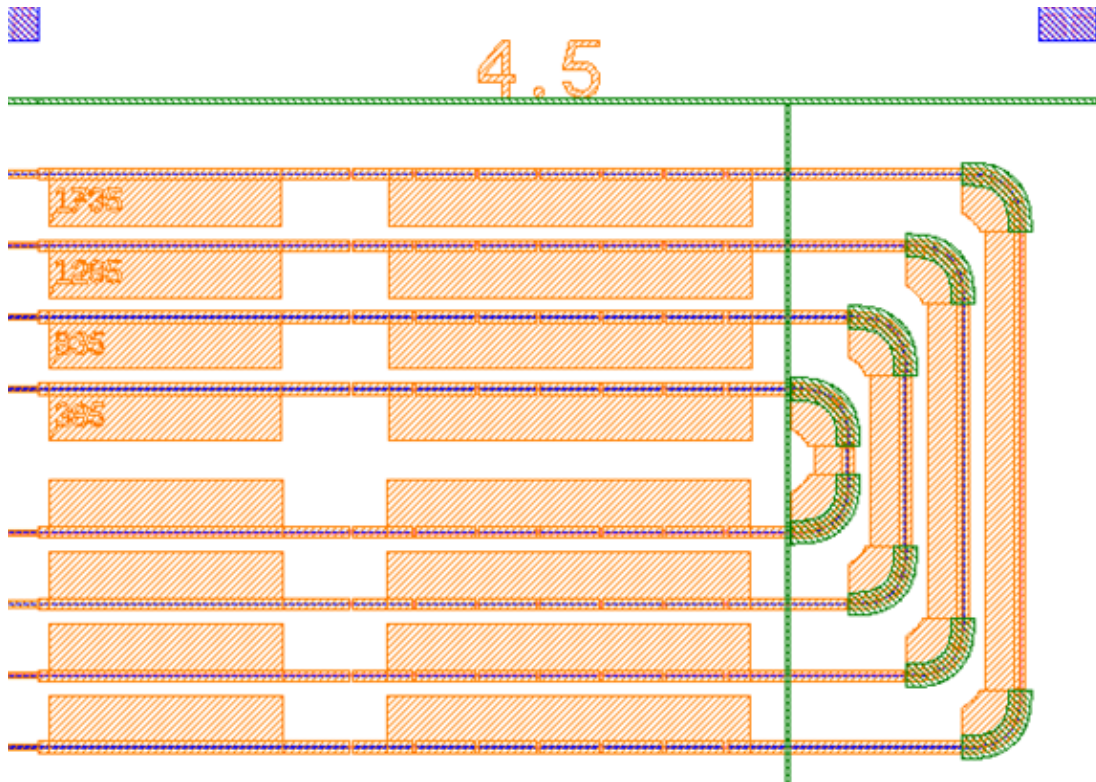


Figure 5.45: Third generation of MCL on chip devices.

system. This experiment can be visualised in the density plot in figure 5.46.

One can see a beat note at low voltage corresponding to the frequency difference of the lasers ( $\sim 15$  GHz). This matches the two-colour state regions at low coupling in figure 5.20 and 5.21. Figure 5.47 shows how the VOA voltage corresponds to the fraction of light reaching the other laser for this device, i.e. measurement of  $\eta$ . It shows that this system reaches a maximum value of  $\eta \approx 0.32$ , which is a big improvement over the second generation devices.

The system then transitions into a strong multi-harmonic signal of decreasing frequency (between 1.4 – 1.5 V). figure 5.48 shows a time trace from a High Speed Oscilloscope (HSO), for the laser output in one of these regions of harmonics. The behaviour observed is a sinusoid, with a slowly varying sinusoidal envelope. The first line of this harmonic behaviour is similar to the two colour states observed theoretically, however these states lack the sinusoidal envelope.

There is a small window of locked behaviour (one colour state) at approximately 1.55 V. The multi-harmonic behaviour is repeated between approx. 1.6 – 1.8 V. This harmonic behaviour could be compared with some of

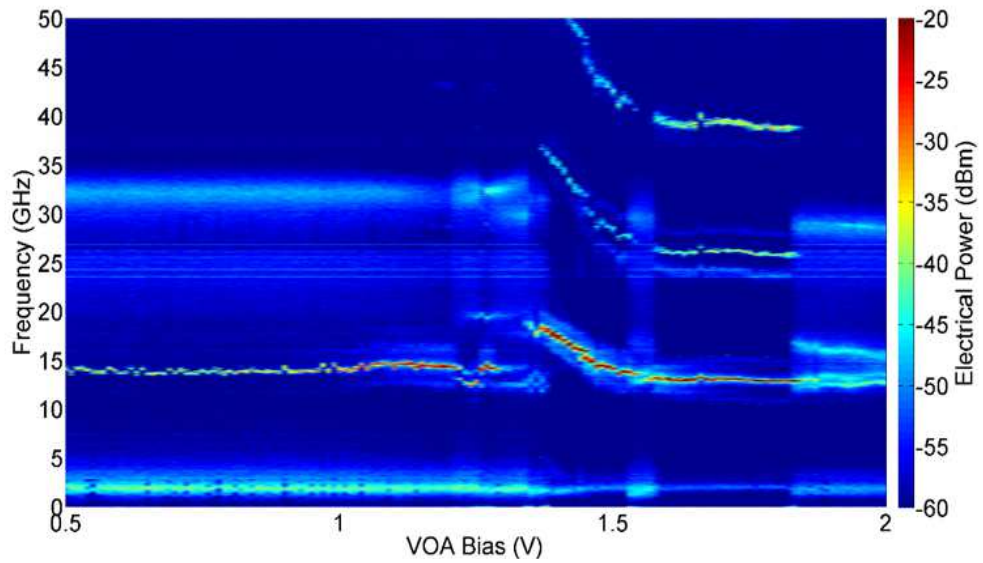


Figure 5.46: Density plot of ESA traces for varying VOA bias for 385  $\mu\text{m}$  VOA device in figure 5.45, with the lasers tuned to have a detuning of 15 GHz.

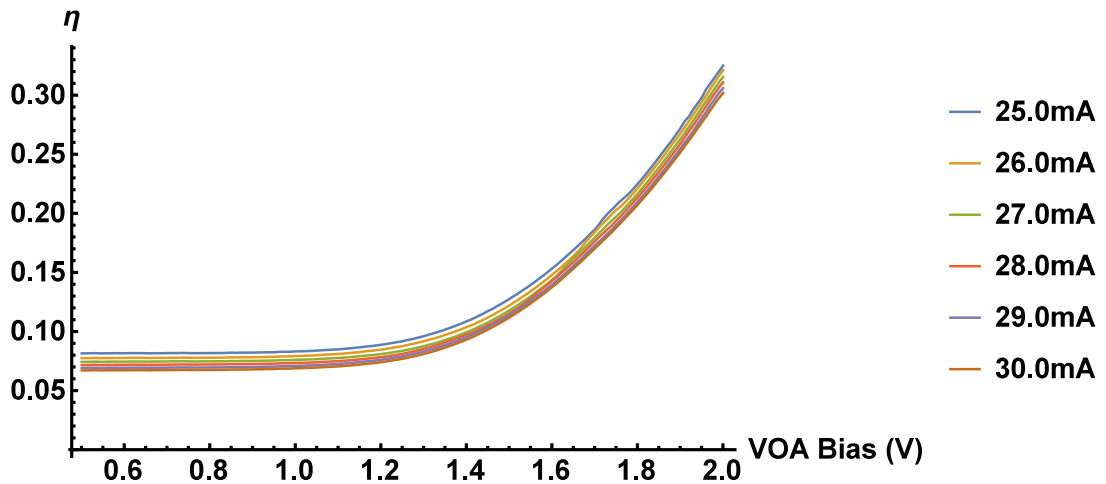


Figure 5.47: Measurement of the amount of light reaching one laser from the other ( $\eta$  parameter) for the 385  $\mu\text{m}$  device in figure 5.45 for different currents applied to the mirror section of the laser.

the dynamics seen in figure 5.41, however in Fig 5.41c and 5.41d, the detuning values were set to 80 GHz which is significantly higher than the 15 GHz set in the experiment. In figure 5.41b the delay time is too high to compare with this device ( $\tau = 2$  gives a physical separation of approximately 6 mm, device VOA length = 385  $\mu\text{m}$ ). Figure 5.41a shows harmonic behaviour, and its delay time and detuning are comparable to the experiment, however for this behaviour to occur experimentally,  $\phi$  would have to be fixed at  $\frac{\pi}{2}$ , while sweeping the VOA voltage. Varying the voltage of the VOA would affect the

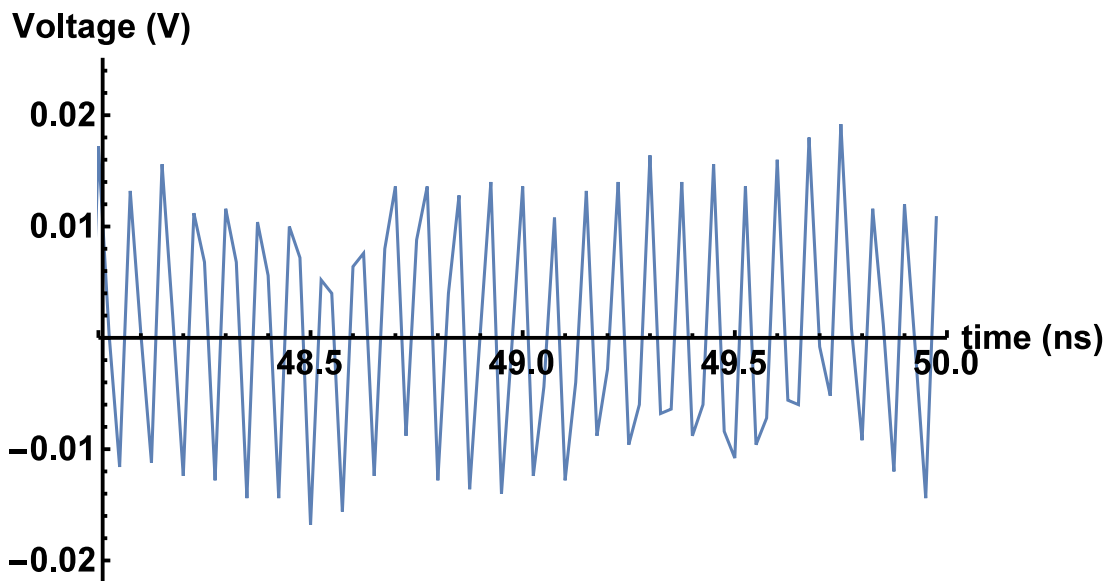


Figure 5.48: HSO trace of one of the MCL lasers in the harmonic region of figure 5.46, between 1.6V and 1.8V.

refractive index,  $n$ , of the material, altering the path length, and therefore adjusting the phase difference between the lasers. This would suggest rather than travelling vertically along a fixed  $\phi$  value when sweeping VOA voltage, a parametrised curve/line is being drawn across the attractor diagrams. The fact that the harmonic behaviour is similar to a two colour state with extra harmonics would suggest that a more complex model with additional frequencies, like a multi-mode model (or more accurate modelling of the VOA section, see Appendix B) is required to describe this system.

In summary of this experiment, for low coupling we transition from a two-colour state with frequency difference corresponding to the frequency difference of the lasers, transitioning to a two-colour state, with harmonics, transition to a small window of one colour state behaviour, then back to a two colour state with harmonics.

The lack of chaotic or pulsing behaviour agrees with theoretical results presented earlier. To achieve larger windows of chaotic behaviour or pulsed behaviour higher  $\tau$  values are required. For example figure 5.20a has small window of pulsed behaviour, but everywhere else on the  $(\phi, \eta)$  diagram is either one colour or two colour behaviour. Compare this to 5.20b where there is a large window of chaotic behaviour within the outlined "triangular" region.

Figure 5.49 further emphasises the need for a multi-mode model to recreate this experiment. For low VOA voltage it clear the laser was tuned to be single

moded, at a set frequency. However as coupling increases one can see side modes being excited leading to multi-mode behaviour (see behaviour after approximately 1.3V).

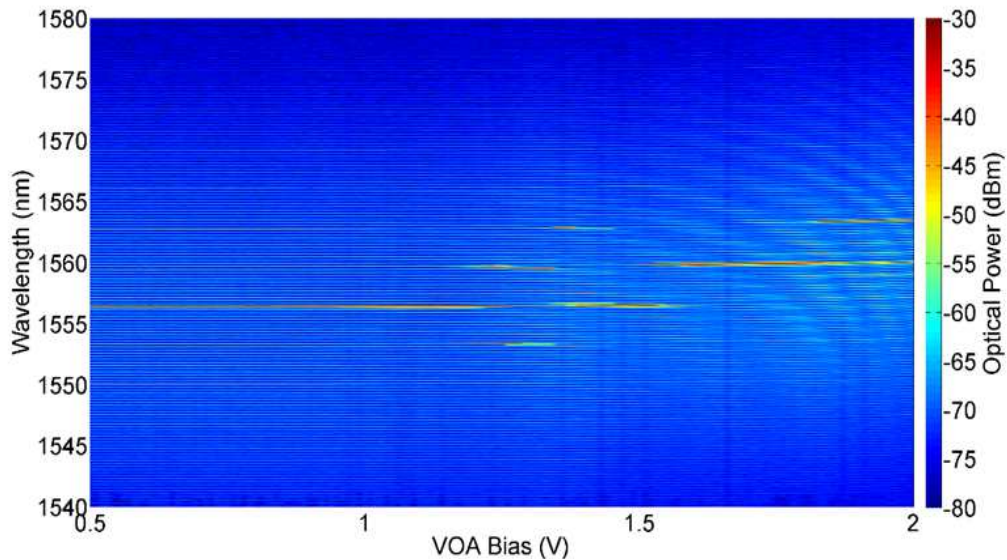


Figure 5.49: Density plot of optical spectrum analyser (OSA) traces for varying VOA bias for  $385\mu m$  VOA device in figure 5.45, with the lasers tuned to have a detuning of  $15GHz$ .

Figure 5.50 shows the cavity lengths present in the lasing spectrum of the experiment as coupling,  $\eta$ , is increased. This is done calculated by taking the Fourier transform of the optical spectra. The strong peak at  $1400\mu m$  corresponds to length of each individual laser, with it's harmonic present above it at  $2800\mu m$ . At approx. 1.7 V a strong peak at approx.  $3200\mu m$  appears, this corresponds to the total length of the two lasers, plus the  $385\mu m$  VOA section. This means at this voltage the whole device is lasing, forming a coupled cavity device. Thus the results for a VOA bias  $> 1.7$  V in figure 5.46 are irrelevant to this study.

## 5.5 Conclusion

In this chapter an extensive study of the single mode model for mutually coupled lasers was presented. Initially, an analytic study of the model was presented, for both finding solutions of the model and finding bifurcations of the system. It was shown how these analytical bifurcation methods break down when the detuning parameter was included. Given this breakdown an alternate method of study was required. An algorithm was developed for

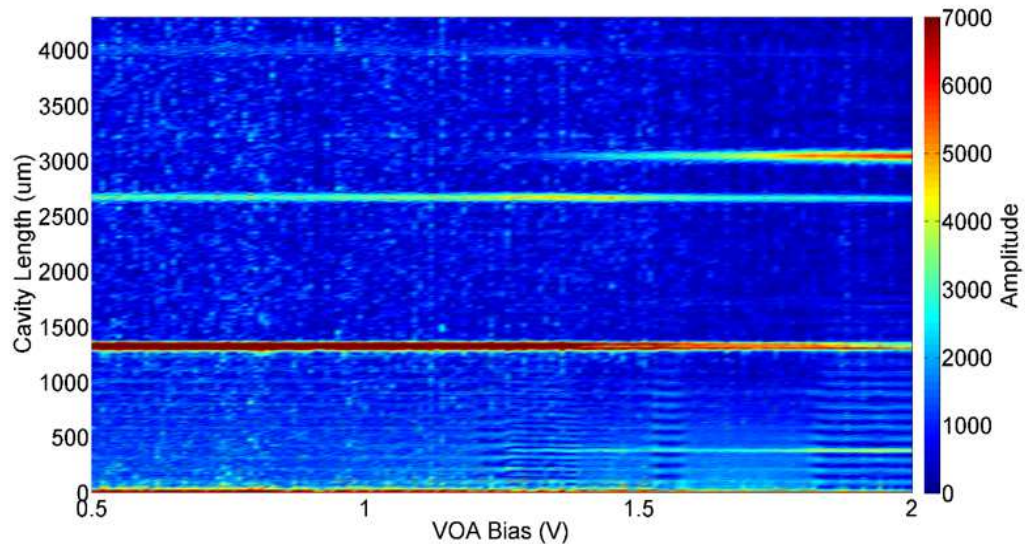


Figure 5.50: Cavity lengths present in the optical spectra, for varying VOA bias, for  $385\ \mu\text{m}$  VOA device in figure 5.45, with the lasers tuned to have a detuning of 15 GHz.

finding attractor diagrams of the system, which were then compared with bifurcation diagrams. This algorithm was then used to study the system in the unexplored regime of short delay and non-zero detuning. Experimental procedure was then re-created to allow for direct comparison with experiments. Finally experimental results were presented and compared to the theoretical results. This comparison showed that a more complex model was required to model the experiment more accurately. Specifically the experimental results showed that a multi-mode model was needed. Therefore in the next chapter a multi-mode model will be developed and studied.

## **Chapter 6**

### **Multimode approach to modelling mutually coupled lasers**



## 6.1 Introduction

Following an extensive study of the single mode model, it was established that a more advanced model was required to successfully recreate the experimental results obtained. This was due to the unforeseen behaviour from the experiment, where despite being tuned to be single moded, a side mode of the laser was excited during coupling with a second single moded laser. This prompted the development of a multi-mode model to try and re-create this process. In this chapter the creation of this model will be outlined, and then a study of coupling two, two-moded lasers will be presented. In this model the delay time between the lasers was neglected for simplicity. This is a reasonable assumption for any physical device where the separation is approximately equal to the photon lifetime,  $\tau_p$ . In the derivation of these rate equation based models the change in the variables are noted for one cavity round trip (i.e. the gain and losses during one cycle of the cavity), giving  $\frac{\Delta E}{\Delta t}$ . By taking the limit of  $t$  going to zero, this turns these  $\Delta$ s into differentials. So the minimum time-scale that can be resolved from these equations is anything in the order of the cavity round-trip time. As long as the separations considered on this timescale,  $\tau = 0$  is a valid assumption. This allowed the use of the numerical continuation software XXPaut to be used to perform a bifurcation study. Following this, to make the model more experimentally realistic, the modes of the lasers will be made non-symmetric, i.e. one with significantly more power than the other, and it will be investigated whether the weaker mode can be excited during coupling as was observed experimentally. Then this model will be compared with experiment once again to see if the more advanced model was successful.

## 6.2 Model introduction

The multi-mode model used was derived starting with the model presented in [41], where a two mode laser under injection was studied. The equations used can be seen in Eqn. 6.1-6.3.

$$\dot{E}_1 = \frac{1}{2}(1 + i\alpha)[g_1(2n + 1) - 1]E_1 \quad (6.1)$$

$$\dot{E}_2 = \frac{1}{2}(1 + i\alpha)[g_2(2n + 1) - 1] - i\Delta\omega E_2 + K \quad (6.2)$$

$$T\dot{n} = P - n - (1 + 2n)\Sigma_n g_m |E_n|^2 \quad (6.3)$$

Where the non-linear modal gain has the following form:

$$g_m = g_m^{(0)} (1 + \epsilon \Sigma_n \beta_{mn} |E_n|^2)^{-1} \quad (6.4)$$

These equations represent the temporal evolution of the complex electric fields of the two modes ( $E_{1,2}$ ), and the carriers of the laser  $n$ . The second mode is injected with a source of strength  $K$ , offset in frequency by  $\Delta\omega$ . The reason the injection term only appears in one equation is that the model assumes the modes are far enough apart that the injection will have no effect on the first mode (minimum separation of modes for model to be valid  $\approx 200GHz$  and from the experimental results in section 5.4.1, it is seen that the second mode being excited is approximately 5 nm from the main mode, satisfying this criterion).  $T$  is the ratio of the carrier lifetime and the photon lifetime (equivalent to  $\epsilon^{-1}$  from single mode case, which was the ratio of the carrier lifetime to the photon lifetime),  $P$  is the pump parameter (equivalent to  $J$  in single mode case),  $\alpha$  is the linewidth enhancement factor,  $\epsilon\beta_{mn}$  are the cross and self-saturation terms between modes and  $g_m^{(0)}$  is the linear model gain term. The parameter values  $\alpha = 2.6$ ,  $P = 0.25$ ,  $1/T = 0.00125$ ,  $g_m^{(0)}$ , and  $\epsilon = 0.01$ . For stable two mode lasing the  $\beta$  terms were set to  $\beta_{11} = \beta_{22} = 1$  and  $\beta_{12} = \beta_{21} = 0.667$  ( $\beta_{mn} \neq \beta_{nm}$  in all cases as will be shown). Eqn. 6.1-6.3 were then adapted to the case of two MCLs, where the  $\eta e^{-i\phi} E_{2,1}$  terms account for the mutual coupling. This results in Eqn. 6.5-6.10.

$$E'_{L1} = [\frac{1}{2}(1 + i\alpha)(g_{L1}(2n_L + 1) - 1) - \Delta\omega_1]E_{L1} + \eta e^{-i\phi} E_{R1} \quad (6.5)$$

$$E'_{L2} = [\frac{1}{2}(1 + i\alpha)(g_{L2}(2n_L + 1) - 1) - \Delta\omega_2]E_{L2} + \eta e^{-i\phi} E_{R2} \quad (6.6)$$

$$Tn'_L = P - n_L - (1 + 2n_L)\Sigma_{Lm} g_{Lm} |E_{Lm}|^2 \quad (6.7)$$

$$E'_{R1} = [\frac{1}{2}(1 + i\alpha)(g_{R1}(2n_R + 1) - 1) + \Delta\omega_1]E_{R1} + \eta e^{-i\phi} E_{L1} \quad (6.8)$$



$$E'_{R2} = \left[ \frac{1}{2}(1 + i\alpha)(g_{R2}(2n_R + 1) - 1) + \Delta\omega_2 \right] E_{R2} + \eta e^{-i\phi} E_{L2} \quad (6.9)$$

$$Tn'_R = P - n_R - (1 + 2n_R)\Sigma_{Rm}g_{Rm}|E_{Rm}|^2 \quad (6.10)$$

Where

$$g_{L,Rm} = g_{L,Rm}^{(0)}(1 + \epsilon\Sigma_n\beta_{mn}|E_{L,Rn}|^2)^{-1} \quad (6.11)$$

These equations describe the temporal evolution of the complex electric fields of the two modes of the left laser ( $E_{L1,2}$ ) and right laser ( $E_{R1,2}$ ) along with the carrier densities of left and right lasers ( $n_{L,R}$ ). Similarly to the single mode model, each complex field can be written in a polar form ( $E_{L,R1,2} = a_{L,R1,2}e^{i\psi_{1,2}}$ ) or complex number form ( $E_{L,R1,2} = E_{x_{L,R1,2}} + iE_{y_{L,R1,2}}$ ), however this causes an issue when trying to use XPPaut to calculate bifurcations of the system. This is due to an issue of equivariance, when written in these forms; any fixed point found, was only a relative fixed point, not an absolute fixed point. This issue was also encountered in a previous study [32], where the author overcame this issue of equivariance by employing a new formulation for the complex fields. This transformation also acts to reduce the dimension (note this was for the single mode coupled case).

$$\begin{aligned} q_x + iq_y &= 2E_1 * E_2 \\ q_z &= |E_1|^2 - |E_2|^2 \end{aligned} \quad (6.12)$$

The total power of the two lasers can be expressed as

$R = (q_x^2 + q_y^2 + q_z^2)^{\frac{1}{2}} = |E_1|^2 + |E_2|^2$ . The single mode model in Eqn. 4.6-4.9 then takes the form:

$$\dot{q}_x = q_x(n_1 + n_2) + \alpha q_y(n_1 - n_2) + 2\eta R \cos \phi + 2\delta q_y \quad (6.13)$$

$$\dot{q}_y = q_y(n_1 + n_2) - \alpha q_x(n_1 - n_2) - 2\eta R \sin \phi - 2\delta q_x \quad (6.14)$$

$$\dot{q}_z = q_z(n_1 + n_2) + R(n_1 - n_2) + 2\eta q_y \sin \phi \quad (6.15)$$

$$T\dot{n}_1 = P - n_1 - (1 + 2n_1)(R + q_z)/2 \quad (6.16)$$

$$T\dot{n}_2 = P - n_2 - (1 + 2n_2)(R - q_z)/2 \quad (6.17)$$

This representation can be extended to the two mode case. By using two sets of  $q's$ ,  $(q_{x_1}, q_{y_1}, q_{z_1})$  and  $(q_{x_2}, q_{y_2}, q_{z_2})$ , where  $q_{x,y,z_1}$  describes the interaction of  $E_{L_1}$  and  $E_{R_1}$ , while  $q_{x,y,z_2}$  does the same for  $E_{L_2}$  and  $E_{R_2}$ . Using the  $q$  representation, the Eqn. 6.5-6.10 becomes:

$$\begin{aligned} \dot{q}_{x_1} = & q_{x_1}(g_{L_1}(2n_L + 1) + g_{R_1}(2n_R + 1) - 2) + \alpha q_{y_1}(g_{L_1}(2n_L + 1) - g_{R_1}(2n_R + 1)) \\ & + 2\eta R_1 \cos \phi + 2\Delta\omega_1 q_{y_1} \end{aligned} \quad (6.18)$$

$$\begin{aligned} \dot{q}_{y_1} = & q_{y_1}(g_{L_1}(2n_L + 1) + g_{R_1}(2n_R + 1) - 2) - \alpha q_{x_1}(g_{L_1}(2n_L + 1) - g_{R_1}(2n_R + 1)) \\ & - 2\eta q_{z_1} \sin \phi - 2\Delta\omega_1 q_{x_1} \end{aligned} \quad (6.19)$$

$$\begin{aligned} \dot{q}_{z_1} = & q_{z_1}(g_{L_1}(2n_L + 1) + g_{R_1}(2n_R + 1) - 2) + R_1(g_{L_1}(2n_L + 1) - g_{R_1}(2n_R + 1)) \\ & + 2\eta q_{y_1} \sin \phi \end{aligned} \quad (6.20)$$

$$Tn_L = P - n_L - (1 + 2n_L)[g_{L_1}(\frac{q_{z_1} + R_1}{2}) + g_{L_2}(\frac{q_{z_2} + R_2}{2})] \quad (6.21)$$

$$\begin{aligned} \dot{q}_{x_2} = & q_{x_2}(g_{L_2}(2n_L + 1) + g_{R_2}(2n_R + 1) - 2) + \alpha q_{y_2}(g_{L_2}(2n_L + 1) - g_{R_2}(2n_R + 1)) \\ & + 2\eta R_2 \cos \phi + 2\Delta\omega_2 q_{y_2} \end{aligned} \quad (6.22)$$

$$\begin{aligned}\dot{q}_{y_2} = & q_{y_2}(g_{L_2}(2n_L + 1) + g_{R_2}(2n_R + 1) - 2) - \alpha q_{x_2}(g_{L_2}(2n_L + 1) - g_{R_2}(2n_R + 1)) \\ & - 2\eta q_{z_2} \sin \phi - 2\Delta\omega_2 q_{x_2}\end{aligned}\quad (6.23)$$

$$\begin{aligned}\dot{q}_{z_2} = & q_{z_2}(g_{L_2}(2n_L + 1) + g_{R_2}(2n_R + 1) - 2) + R_2(g_{L_2}(2n_L + 1) - g_{R_2}(2n_R + 1)) \\ & + 2\eta q_{y_2} \sin \phi\end{aligned}\quad (6.24)$$

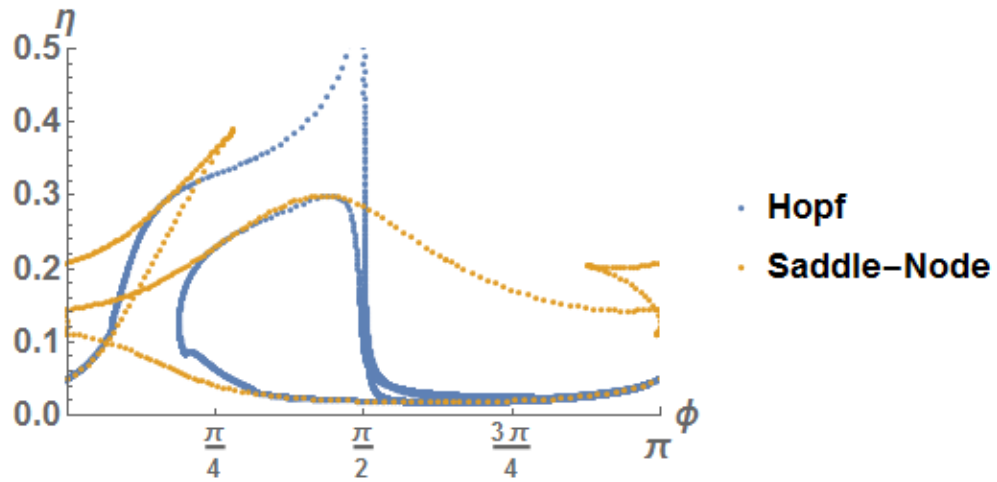
$$Tn_R = P - n_R - (1 + 2n_R)[g_{R_1}(R_1 - \frac{q_{z_1}}{2}) + g_{R_2}(R_2 - \frac{q_{z_2}}{2})] \quad (6.25)$$

Now that the model has been developed, a bifurcation study of the system will be presented. To allow for a comparison with experiment, it is important to understand how the behaviour changes by varying the experimentally changing parameters.

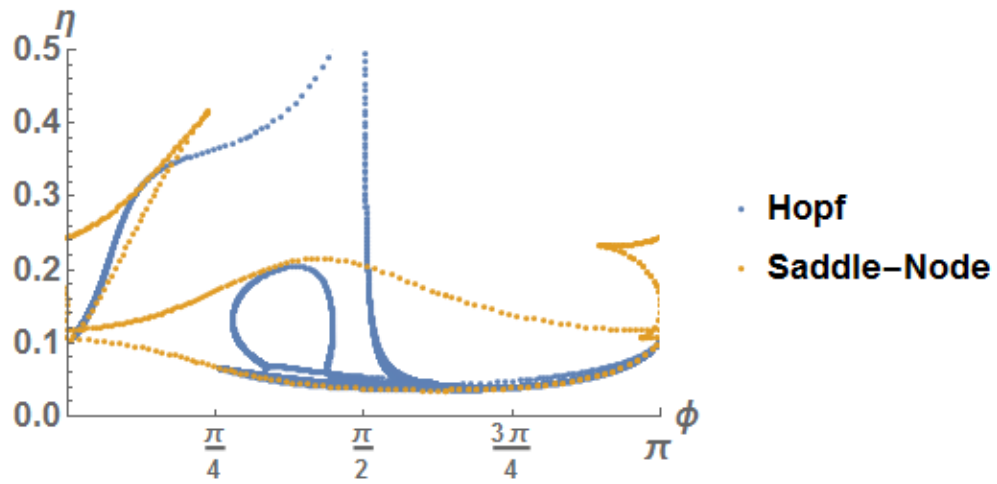
## 6.3 Bifurcation study of two mode coupled laser model

### 6.3.1 Study of the $(\phi, \eta)$ space bifurcations

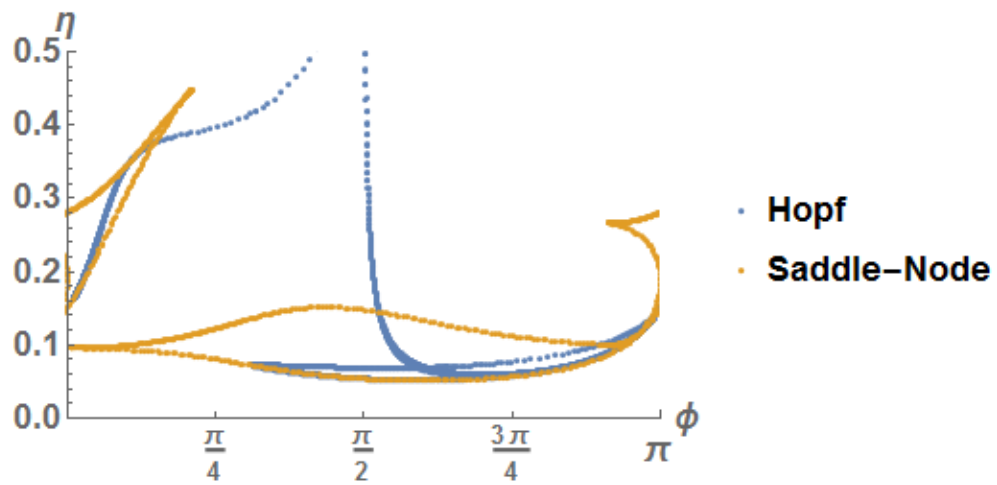
Just as in the attractor diagram study of the single mode case (Sec. 5.2.1), the parameters of interest to study were the injections strength,  $\eta$ , and the coupling phase,  $\phi$ . In this case though there now exists two detunings that can be set,  $\Delta\omega_{1,2}$ . These control the frequency differences between  $E_{L_1}$ ,  $E_{R_1}$  and  $E_{L_2}$ ,  $E_{R_2}$  respectively. Initially these values will be symmetric, but later an asymmetry in the detuning will be introduced and studied. Figure 6.1 shows bifurcation diagrams for different symmetric values of the detunings.



(a)  $\Delta\omega_1 = \Delta\omega_2 = 0.05$



(b)  $\Delta\omega_1 = \Delta\omega_2 = 0.1$



(c)  $\Delta\omega_1 = \Delta\omega_2 = 0.15$

Figure 6.1: Bifurcation diagrams, showing saddle-node bifurcations in orange and hopf in blue, for varying symmetric values of  $\Delta\omega_{1,2}$  for the multimode model.

Following this it was important to track the behavioural regimes across the parameter space. Figure 6.2 shows the L2 Norm (the square root of the sum of the squared vector values) for  $\Delta\omega_{1,2} = 0.05$ ,  $\eta = 0.3$  and  $0.1$  and varying  $\phi$  from  $0 - 2\pi$ . Figure 6.3 shows the bifurcations of these solutions. In figure 6.3a, the different behavioural regimes are outlined by the regions A, B, and C, with the lines between them occurring at the relevant bifurcations. In region A there exists a stable fixed point solution (orange) and an unstable one (blue). Here the two lasers lock together at the stable solution. Just before the line of changing behaviour a Hopf bifurcation (black) creates an unstable period one solution (red). The fixed points collide at the saddle-node bifurcation (purple dot) and the previously generated periodic solution becomes the stable behaviour (green). In this region of stable periodic behaviour, the lasers are unlocked and oscillating. This is the single stable solution in the region B. There exist unstable fixed points (blue) and a second unstable periodic branch (red) forms from the Hopf bifurcation (black) at  $\phi = 0.6$ . Finally the stable periodic solution (green) is destroyed at the Hopf bifurcation (black). After this Hopf bifurcation a stable fixed point behaviour (green) resumes in region C and the unstable periodic behaviour created in region B terminates at the Hopf point (black). Here the lasers return to the locked state. A higher injection strength is shown in figure 6.2b. Similar to the previous case the different behavioural regimes are highlighted by A, B, C, and D. In region A there is a stable fixed point (orange) and an unstable fixed point (blue). Then a Hopf bifurcation (black) at  $\phi = 0.55$  generates a stable period one solution, this generates a region of bi-stability, labelled B, between the previous stable fixed point (orange) and the newly generated stable periodic solution (green). In this area of bi-stability the lasers can exist in either a locked or periodic state, and if perturbed correctly the system can switch between these behaviours. This region ends when a saddle-node bifurcation (purple), annihilates the stable fixed point. This means in region C, there is one stable periodic solution (green) and some unstable fixed points (blue). Then at  $\phi = 1.6$  a Hopf-fold bifurcation (grey) ends the periodic solution (green) and changes the stability of the fixed point to make it stable (orange). In region D then multiple stable fixed points (orange) solutions exist meaning this is a region of multi stabilities.

If instead of fixing  $\eta$  and varying  $\phi$ , the process is swapped, i.e. fixing the phase difference between the lasers and varying the injection strength. A graph can be generate as seen in figure 6.4, where  $\phi = 0.7$ . For high  $\eta$  there

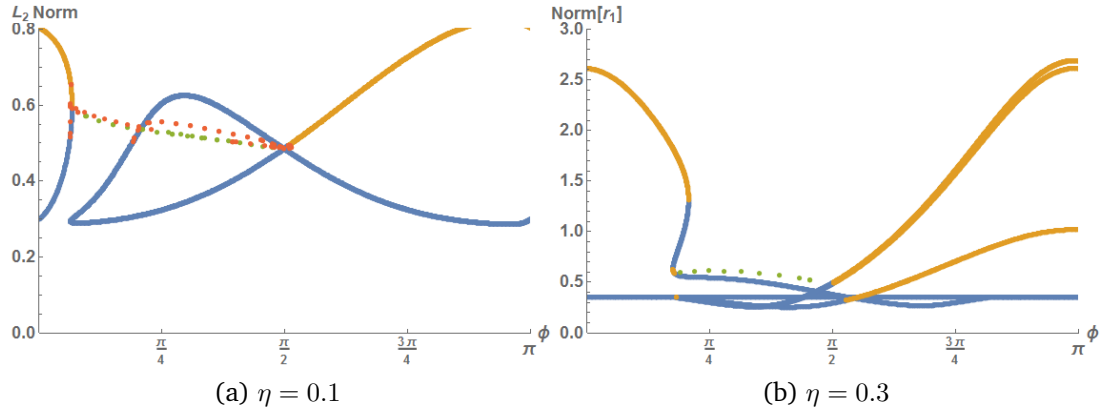


Figure 6.2: Plots of the  $L_2$  Norm from the multimode model, for varying  $\phi$  from  $0 - 2\pi$ , for  $\eta = 0.1$  and  $0.3$ . The stable steady states are in orange, unsteady stable states are blue, steady periodic solutions are green dots and unsteady periodic solutions are in red.

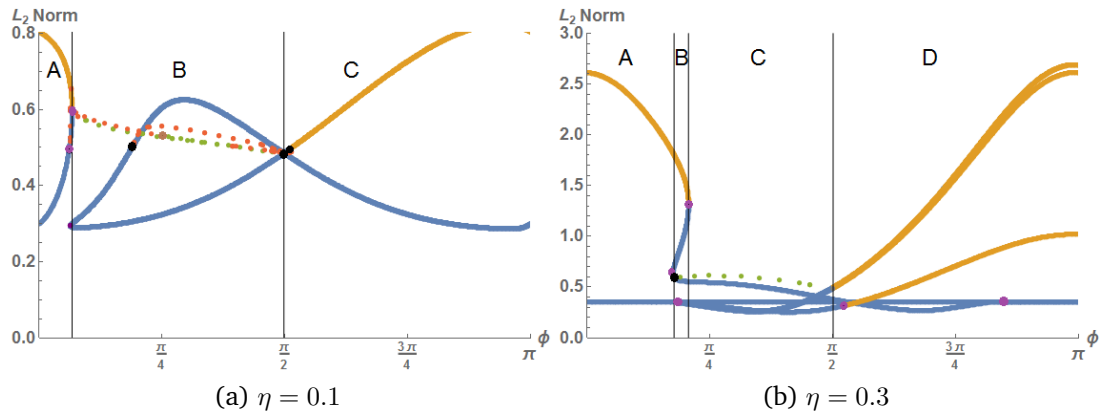


Figure 6.3: Plots of the  $L_2$  Norm from the multimode model, for varying  $\phi$  from  $0 - 2\pi$ , for  $\eta = 0.1$  and  $0.3$ . The stable steady states are in orange, unsteady stable states are blue, steady periodic solutions are green dots and unsteady periodic solutions are in red. Saddle-node bifurcations are shown by purple dots, Hopf given by black, and the Hopf-fold is highlighted in grey.

exists a stable steady state (orange) in region C, a saddle node bifurcation (purple), creates a second stable fixed point (orange), leading to a region of bi-stability, B. Next the behaviour transitions via the Hopf bifurcation to a stable periodic solution (green), labelled region A. As  $\eta$  is decreased, a torus bifurcation is encountered, producing an unstable periodic solution (not shown as it overlaps with the stable solution), before a second torus bifurcation ends this unstable branch.

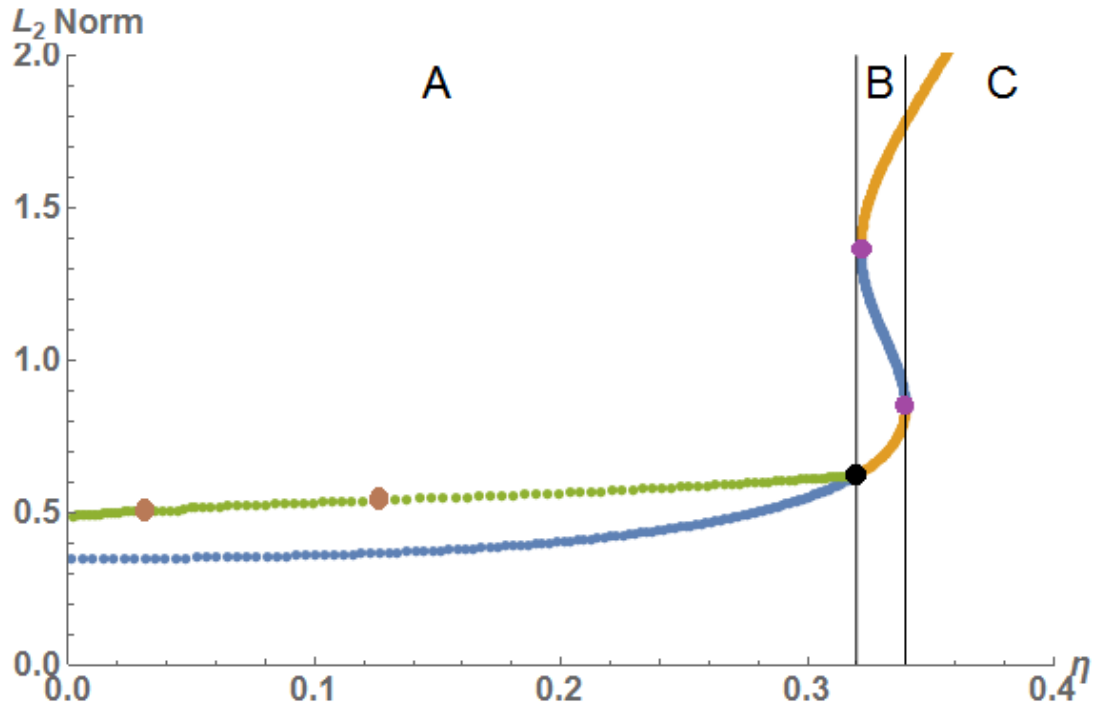


Figure 6.4:  $L_2$  Norm from the multimode model, for varying  $\eta$ , for  $\phi = 0.7$  and  $\Delta\omega_{1,2} = 0.05$ . The stable steady states are in blue, unsteady stable states are orange, steady periodic solutions are green dots and unsteady periodic solutions are in red. Saddle-node bifurcations are shown by purple dots, Hopf given by black, and the torus bifurcations is highlighted in brown.

Following the study of symmetric detunings, an asymmetry is introduced in these parameters. Figure 6.5 shows a bifurcation diagram for  $\Delta\omega_1 = 0.05$  and  $\Delta\omega_2 = 0.07$ . Comparing this to figure 6.1a, where the detunings were symmetric and equal to 0.05, one can see that there is almost no change in the shape of the saddle-node bifurcation, but there exists more Hopf bifurcations. These Hopf bifurcations exist in the region that is already an oscillatory behaviour, meaning they will create more periodic solutions in this region. This means that a non-symmetric detunings, in this case, increases the number of possible periodic solutions. Intuitively this makes sense as there two different detunings to create more different states.

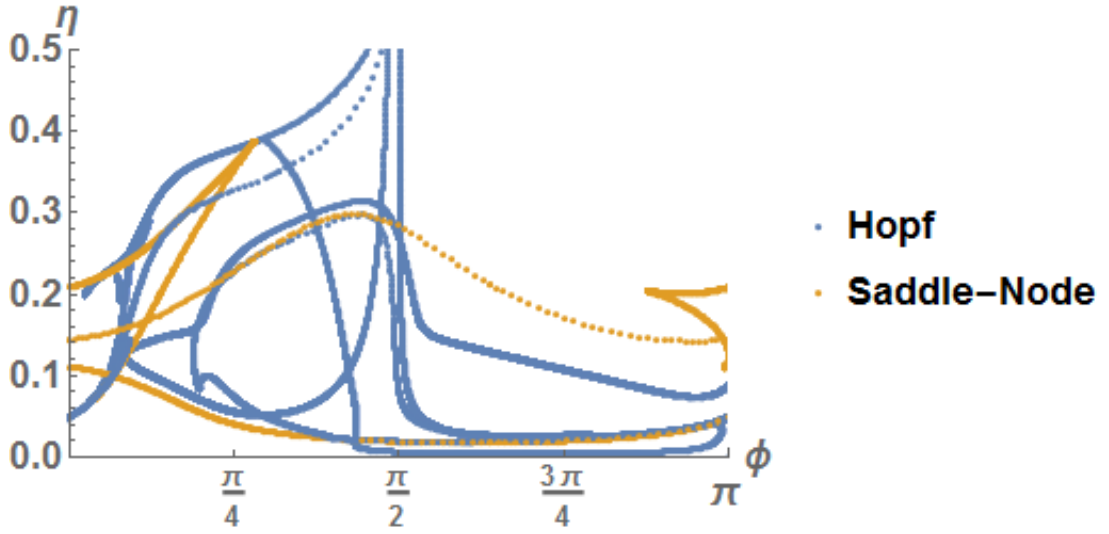


Figure 6.5: Bifurcation diagram over the  $(\phi, \eta)$  parameter space, showing saddle-node bifurcations in orange and hopf in blue, for non-symmetric values of  $\Delta\omega_1 = 0.05$  and  $\Delta\omega_2 = 0.07$  for the multimode model.

Next it will be shown how having non-symmetric detunings affects the solutions in comparison to the results from the symmetric detuning case.

Figure 6.6 shows the  $L_2$  Norm for varying  $\phi$ , for the two values of  $\eta$  used in figure 6.2 this time with  $\Delta\omega_1 = 0.05$  and  $\Delta\omega_2 = 0.07$ .

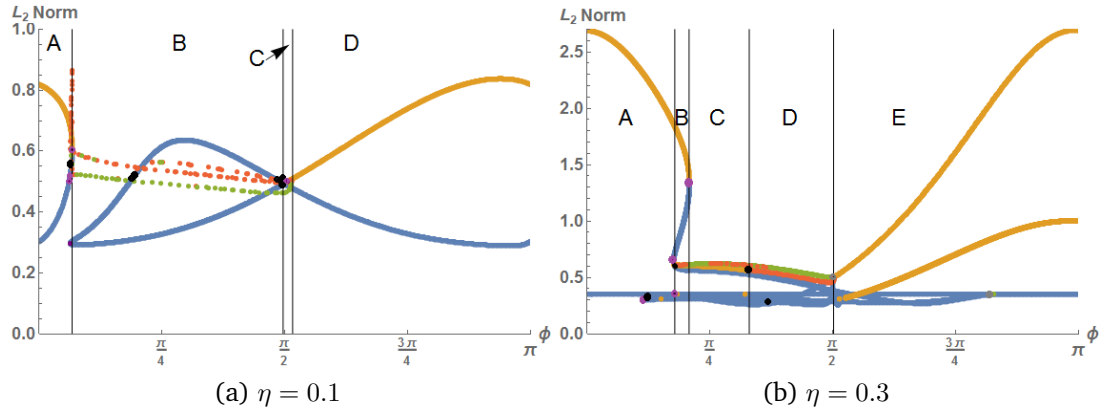


Figure 6.6: Plots of the  $L_2$  Norm from the multimode model, for varying  $\phi$ , with  $\Delta\omega_1 = 0.05$ ,  $\Delta\omega_2 = 0.07$  and a)  $\eta = 0.1$  b)  $\eta = 0.3$ . The stable steady states are in orange, unsteady stable states are blue, steady periodic solutions are green dots and unsteady periodic solutions are in red. Saddle-node bifurcations are shown by purple dots, Hopf given by black, and the Hopf-fold is highlighted in grey.

In figure 6.6a it shows, for  $\eta = 0.1$ , the steady states and their stability are identical to figure 6.2a, where the detunings were identical. However there is



now a periodic solution that forms a closed loop, which started at the Hopf bifurcation (black) at  $\phi = 0.4$ . In region B the lower part of the loop is stable (green) and the top part is unstable (red). Region C is a bi-stable region with the stable fixed point (orange) formed by the Hopf bifurcation (black) and the stable periodic solution which loops back and becomes unstable (red). Figure 6.6b shows the same  $\phi$  variation for  $\eta = 0.3$ . This again is similar to the case with symmetric detunings, however region B now has a bi-stability between two stable fixed points (orange) and the periodic solution generated by the Hopf bifurcation (black), which is unstable (red). This periodic solution then exchanges stability (red to green) in region C, creating another region of bi-stability. Then via a Hopf bifurcation (black) the extended fixed point (orange) disappears and forms an unstable periodic solution (red). Thus forming region D, where the other periodic solution returns to stable (green), becoming the lone stable solution. The two periodic solutions and an unstable fixed point then meet at a Hopf-fold bifurcation (grey) and generate a new stable fixed point (orange) in region E, which along with another stable fixed point solution forms a region of bi-stability. There are some Hopf bifurcations for low  $\phi$  values that produced solutions that did not converge and therefore could not be tracked.

In this section one and two parameter bifurcation diagrams were studied for this two mode system. This showed regions of locked and periodic behaviours, while also showing some regions of bi and multi-stability, where multiple different stable behaviours exist. Here the the lasers can display multiple different behaviours (both locked and periodic) depending on the experiment. Next the non-symmetric detunings were reversed so that  $\Delta\omega_1 = 0.07$  and  $\Delta\omega_2 = 0.05$ , the bifurcation diagram over the  $(\phi, \eta)$  space can be seen in figure 6.7. Again when compared to the symmetric case there is a no change in the saddle-node bifurcation, while there are more Hopf lines. However compared to figure 6.5 a clear difference in the structure of these Hopf lines is seen. Meaning there is a lack of symmetry in the effect of detunings  $\Delta\omega_{1,2}$  i.e. consider the parameter arrangement  $(\eta, \phi, \Delta\omega_1, \Delta\omega_2)$ , this is not equivalent to  $(\eta, \phi, \Delta\omega_2, \Delta\omega_1)$ .

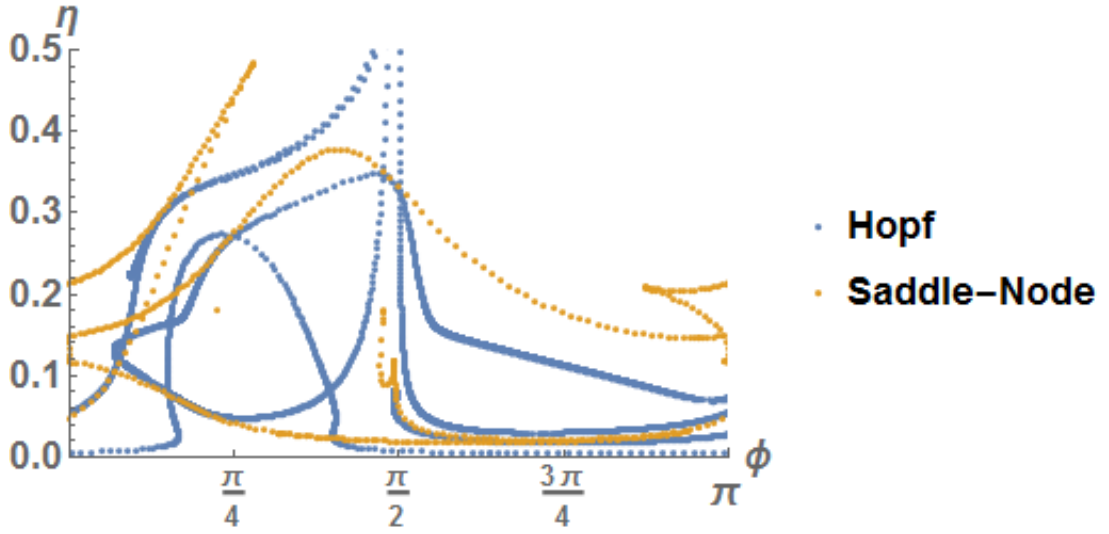


Figure 6.7: Bifurcation diagram over the  $(\phi, \eta)$  parameter space, showing saddle-node bifurcations in orange and hopf in blue, for non-symmetric values of  $\Delta\omega_1 = 0.07$  and  $\Delta\omega_2 = 0.05$  for the multimode model.

Figure 6.8 shows the  $L_2$  Norm for varying  $\phi$  at two different values of  $\eta$  (0.1 and 0.3), showing the solution structure of this non symmetric regime.

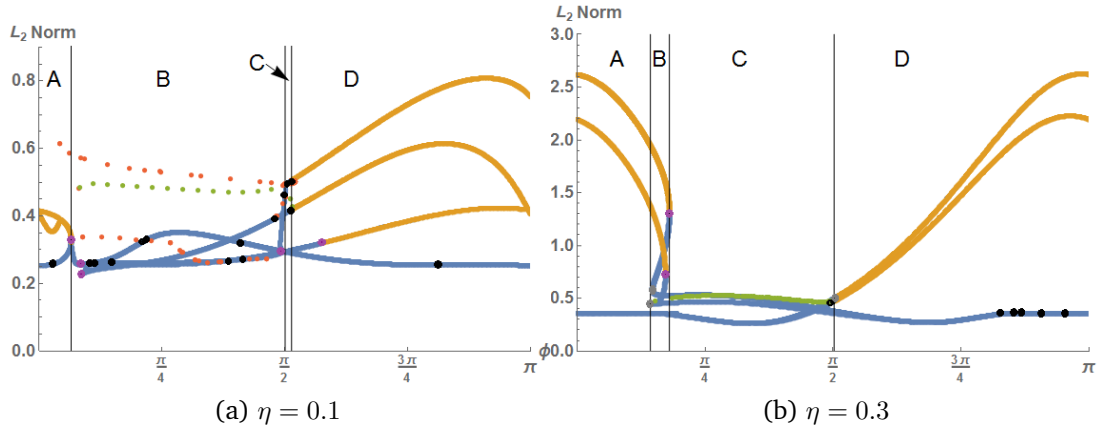


Figure 6.8: Plots of the  $L_2$  Norm from the multimode model, for varying  $\phi$ , with  $\Delta\omega_1 = 0.07$ ,  $\Delta\omega_2 = 0.05$  and a)  $\eta = 0.1$  b)  $\eta = 0.3$ . The stable steady states are in orange, unsteady stable states are blue, steady periodic solutions are green dots and unsteady periodic solutions are in red. Saddle-node bifurcations are shown by purple dots, Hopf given by black, and the Hopf-fold is highlighted in grey.

By comparing these figures with the case where the detunings were  $\Delta\omega_1 = 0.05$  and  $\Delta\omega_2 = 0.07$ , there is a drastic shift in the solution structure again exhibiting the lack of symmetry in the system for  $\Delta\omega_{1,2}$ . Fig 6.8a demonstrates a different solution layout to figure 6.6a. Region A displays

bi-stable behaviour between two stable fixed points (orange) along with an unstable fixed point (blue). These solutions converge and disappear via saddle node bifurcation (purple). The region B has various unstable fixed points (blue) and unstable periodic solutions (blue), which are created and destroyed via various Hopf bifurcations (black). There is however one stable periodic solution (green). Region C is a small bi-stable region, where a short periodic solution branch becomes stable and a stable fixed point is created via a Hopf bifurcation. Following this in region D, a multi-stable region of various stable fixed points exists. When  $\eta$  was increased to 0.3 and varying  $\phi$  produced figure 6.8b. Region A is bi-stable with two stable fixed points (orange), and then a Hopf bifurcation (black) produces a stable periodic solution (green), forming a small window of multi-stability. Both fixed points then disappear via saddle-node bifurcations (purple). In region C a single stable periodic solution (green) exists, until it reaches a Hopf-fold bifurcation (grey) and produces two stable fixed points in region D. Next a study of the effect of varying the detunings will be presented.

### 6.3.2 Study of the detuning space bifurcations

As mentioned in the previous section, the detunings seems to have an asymmetric effect on the behaviour of the system. In this section this will be investigated directly by making the detunings the bifurcation parameters of interest. To do so values for  $\phi$  and  $\eta$  need to be fixed. A value was needed where changing the detunings would have an effect. For example at high coupling changing detuning would have no effect, based on study of the bifurcation diagrams already found in the previous section. It was found that the results when  $\eta = 0.01$  and  $\phi = 2.5$  displayed appropriate sensitivity to the variation of  $\Delta\omega_{1,2}$ . Firstly  $\Delta\omega_2$  was set to zero while  $\Delta\omega_1$  was varied from  $-0.2$  to  $0.2$ , the result of this is show in figure 6.9.

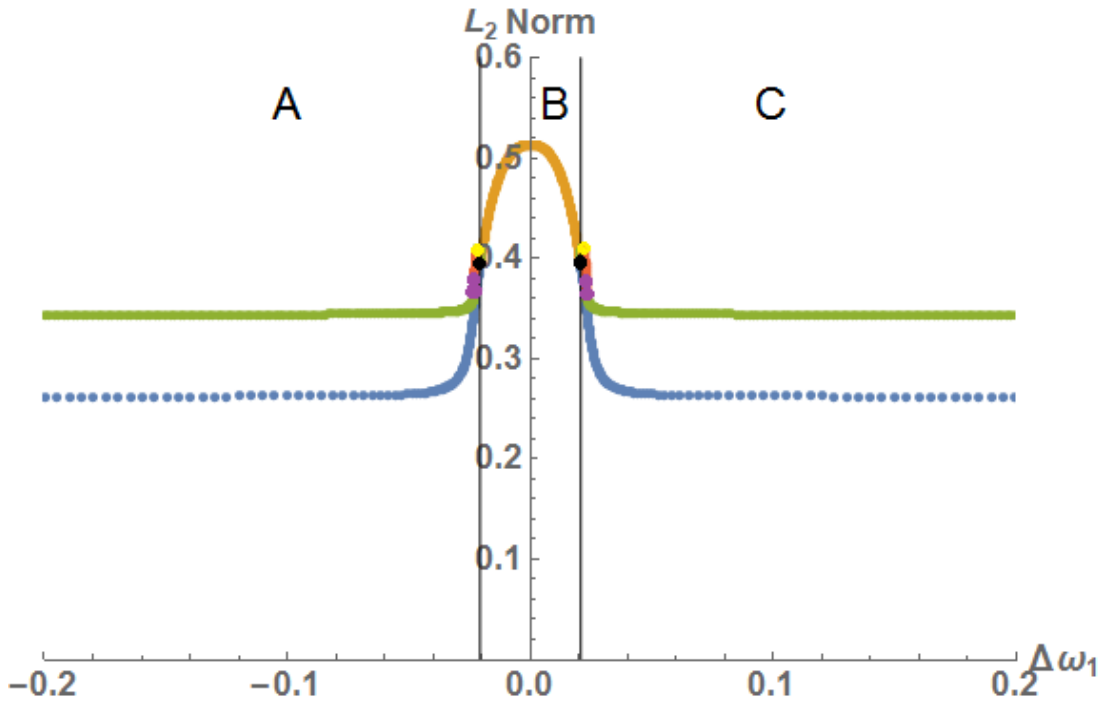


Figure 6.9: Plot of the  $L_2$  Norm from the multimode model, for varying  $\Delta\omega_1$ , with  $\Delta\omega_2 = 0$ ,  $\eta = 0.01$  and  $\phi = 2.5$ . The stable steady states are in orange, unsteady stable states are blue, steady periodic solutions are green dots and unsteady periodic solutions are in red. Saddle-node bifurcations are shown by purple dots, Hopf given by black and period doubling bifurcations are in yellow.

In regions A and C a stable period one solution exists (green), which is simply the beating between the lasers, considering the low coupling strength. These turn into a stable fixed point (orange) in region B via Hopf bifurcations (black). Two unstable periodic solutions (red) also exist close to these Hopf points, which undergo period doubling bifurcations (yellow) and saddle-node bifurcations (purple) but as this is an unstable solution will not affect the dynamics observed. Period doubling bifurcations take the periodic solution that existed and adds a second period to the solution, at exactly half the frequency, increasing the complexity of the oscillation. This diagram would be the equivalent of a sweeping of the detuning in the injection locked case, as seen in figure 3.26. In the injection locked case the locking width (the width in frequency of the stable region in the middle) is asymmetric, i.e. different width in positive and negative detuning. However in the case shown here, the locking width is symmetric. The asymmetry in injection locking is caused by the  $\alpha$  parameter of the slave laser. However in the mutual coupling case there are two  $\alpha$  parameters (one for each laser). This means for one laser, what is negative detuning, is positive for the other, this leads to the symmetry of the

locking width.

If instead of fixing  $\Delta\omega_2$ ,  $\Delta\omega_1$  was set to zero and  $\Delta\omega_2$  was varied from  $-0.2$  to  $0.2$  giving figure 6.10. As can be seen there is a stable fixed point solution across the parameter space chosen.

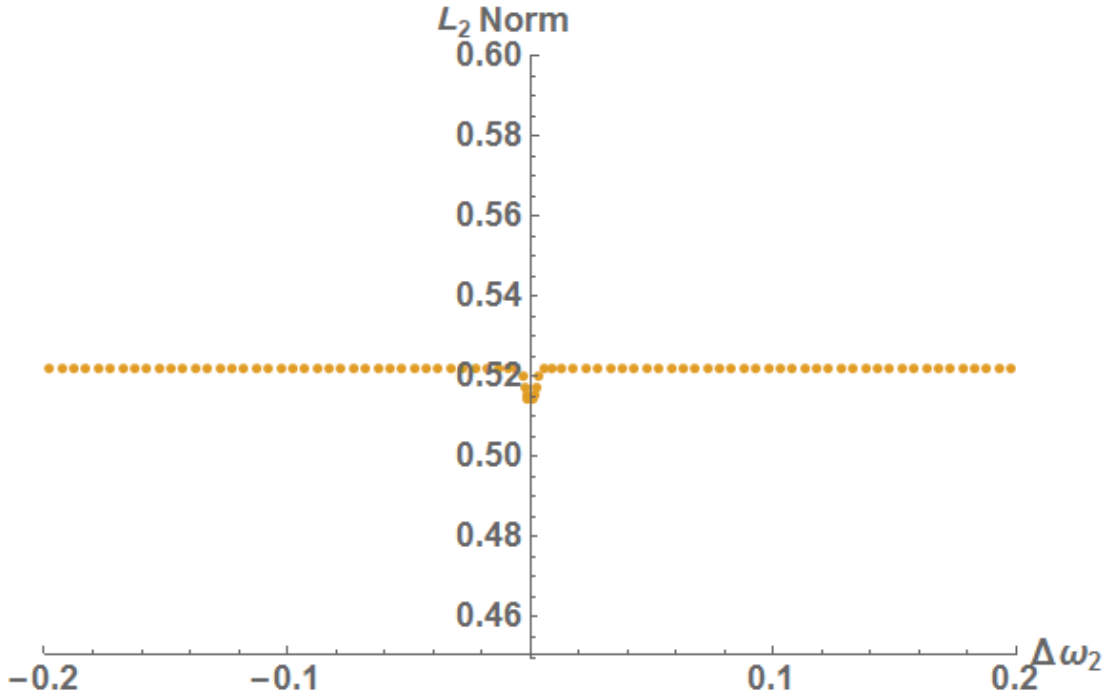


Figure 6.10: Plot of the  $L_2$  Norm from the multimode model, for varying  $\Delta\omega_2$ , with  $\Delta\omega_1 = 0$ ,  $\eta = 0.01$  and  $\phi = 2.5$ . The stable steady states are in orange.

Next  $\Delta\omega_2$  was set to 0.2 and  $\Delta\omega_1$  was varied. This gave figure 6.11.

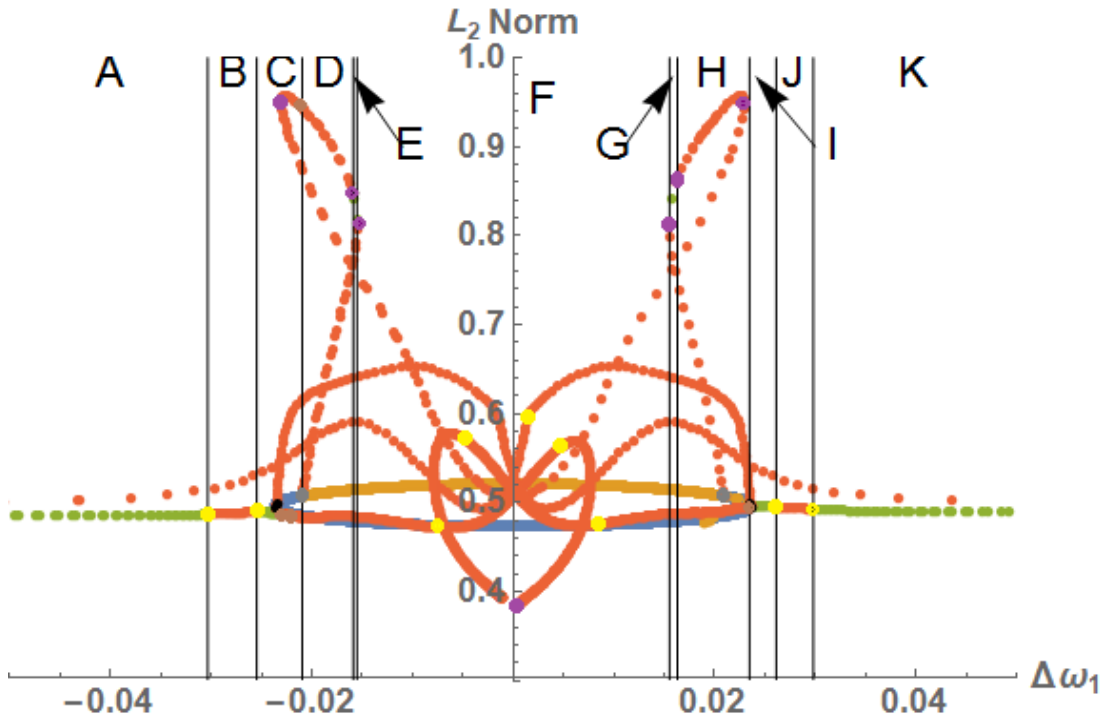


Figure 6.11: Plot of the  $L_2$  Norm from the multimode model, for varying  $\Delta\omega_1$ , with  $\Delta\omega_2 = 0.2$ ,  $\eta = 0.01$  and  $\phi = 2.5$ . The stable steady states are in orange, unsteady stable states are blue, steady periodic solutions are green dots and unsteady periodic solutions are in red. Saddle-node bifurcations are shown by purple dots, Hopf given by black, period doubling bifurcations are in yellow, Hopf-fold bifurcations in grey and taurus bifurcations are in brown.

A strong symmetry is seen in the behaviours, so these will be broken down from outer to inner. In regions A and K, a single period one solution exists (green), as  $|\Delta\omega_1|$  is decreased a period doubling bifurcation (yellow) transitions to a region of chaotic behaviour in regions B and J (an example time trace of  $R_1$  can be seen in figure 6.12), therefore, there must be a series of period doubling bifurcations, forming a period doubling route to chaos. This transitions to regions C and I where the system returns to a period one oscillation (green). These disappear via a Hopf bifurcation (black) for positive  $\Delta\omega_1$  and a Hopf-fold bifurcation (grey) for negative  $\Delta\omega_1$ . This gives rise to regions D and H, where there is a stable fixed point behaviour (green), while an unstable periodic solution also exists above it (red), which was generated via saddle-node bifurcation of orbits (purple). There also exists an unstable fixed point solution (blue) below the stable one. Regions E and G are small windows where this unstable periodic solution becomes stable (green) between two saddle-node bifurcations (purple). This means regions D and H display bi-stable behaviour. Finally at low  $|\Delta\omega_1|$  in region F, the behaviour

returns to the single stable fixed points solution.

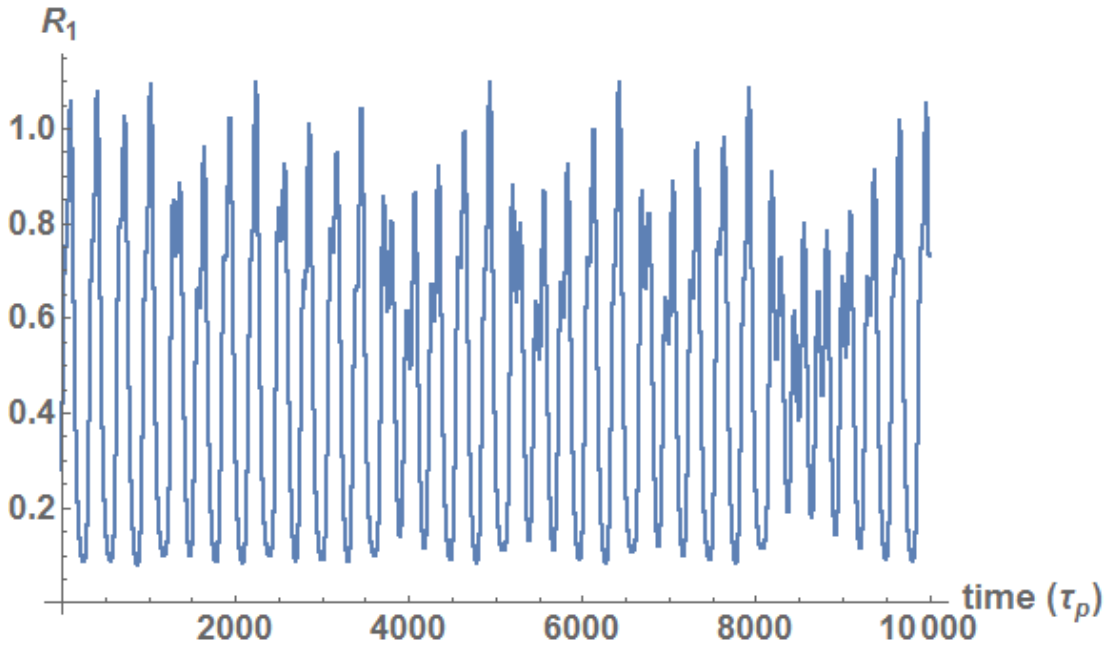


Figure 6.12: Time trace of  $R_1$  from the multimode model, with the parameter values equal to the regions B and J in figure 6.11.

Next  $\Delta\omega_2$  was fixed at 0.05, while  $\Delta\omega_1$  was varied, which yields figure 6.13.

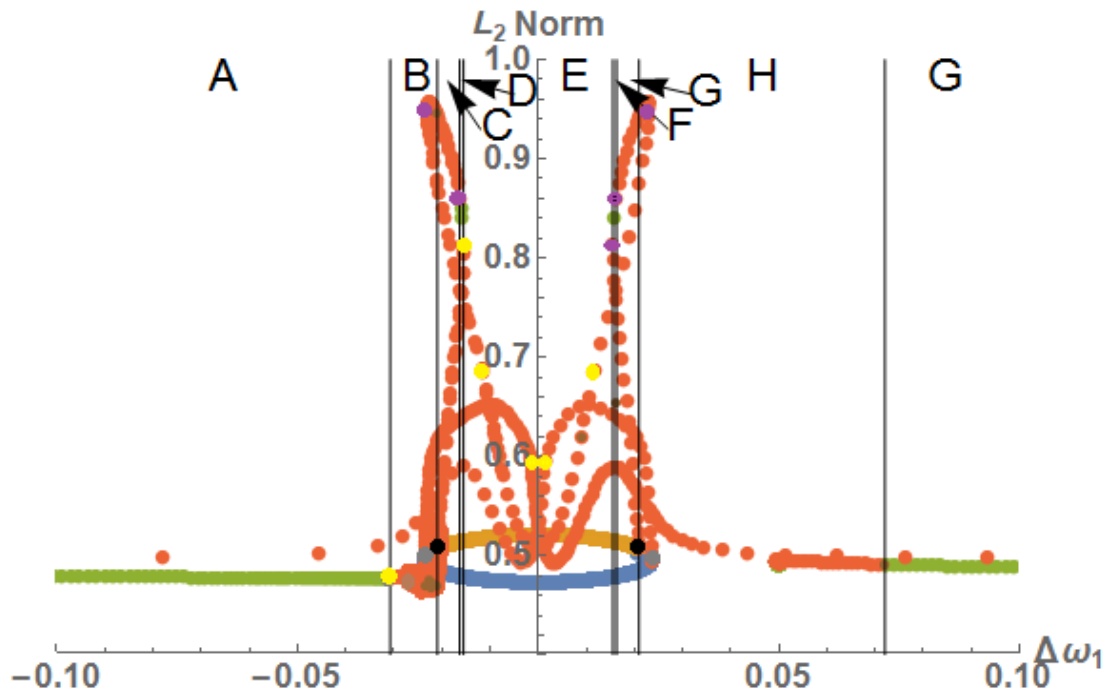


Figure 6.13: Plot of the L2 Norm from the multimode model, for varying  $\Delta\omega_1$ , with  $\Delta\omega_2 = 0.05$ ,  $\eta = 0.01$  and  $\phi = 2.5$ . The stable steady states are in orange, unsteady stable states are blue, steady periodic solutions are green dots and unsteady periodic solutions are in red. Saddle-node bifurcations are shown by purple dots, Hopf given by black, period doubling bifurcations are in yellow, Hopf-fold bifurcations are in grey and taurus bifurcations are in brown.

The overall shape is similar to that of the case of  $\Delta\omega_2 = 0.2$ , however the regions before the stable fixed point solution appear (regions B and H) are different. Region H is made up of a series of multi-periodic behaviours, and region B is a period doubling route to chaos window. Apart from these differences all regions are the same as in figure 6.11.

Figure 6.14 shows the results when  $\Delta\omega_2$  was set to  $-0.05$ , and an exact mirror of the behaviours observed in figure 6.13. The wider region of multi-period behaviours is on the left and the small window of period doubling route to chaos is on the left.



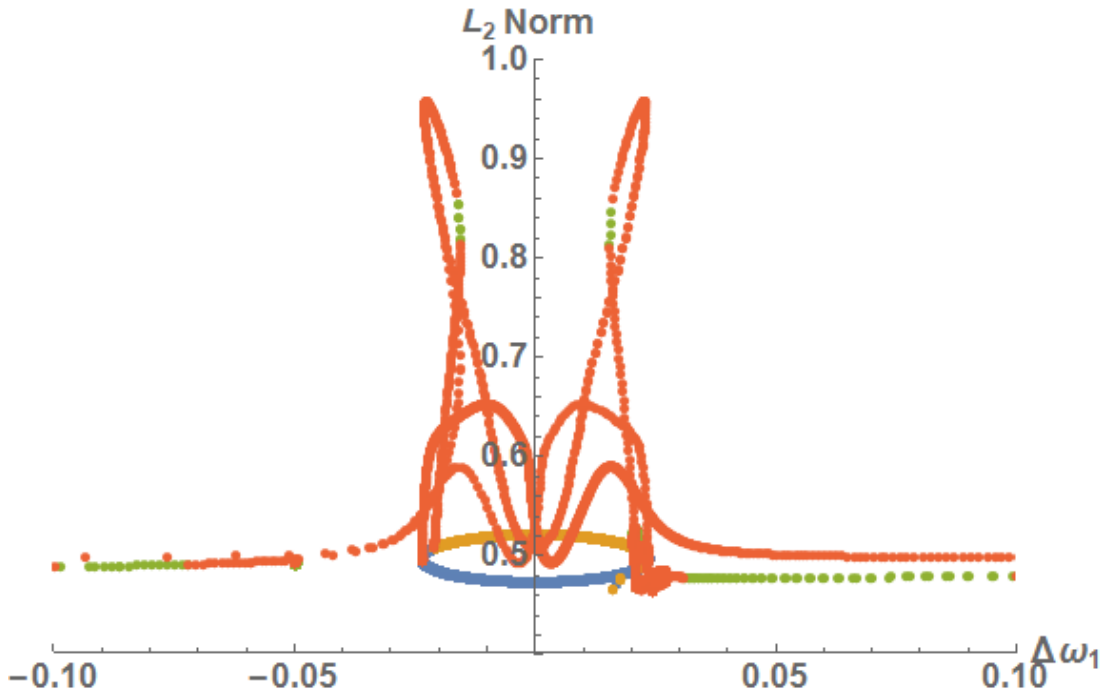


Figure 6.14: Plot of the  $L_2$  Norm from the multimode model, for varying  $\Delta\omega_1$ , with  $\Delta\omega_2 = -0.05$ ,  $\eta = 0.01$  and  $\phi = 2.5$ . The stable steady states are in orange, unsteady stable states are blue, steady periodic solutions are green dots and unsteady periodic solutions are in red. Saddle-node bifurcations are shown by purple dots, Hopf given by black, period doubling bifurcations are in yellow and Hopf-fold bifurcations are in grey.

Finally  $\Delta\omega_1$  was set to 0.05 while varying  $\Delta\omega_2$ , giving figure 6.15. In regions A and C a stable fixed point solution exists (green). Two torus bifurcations form a region of various multi-period solutions in region B. Torus bifurcations, similar to period doubling bifurcations add extra oscillation peaks to the time trace, but now they are not restricted to being at half the frequency. In this way they also add to the complexity of the oscillations seen.

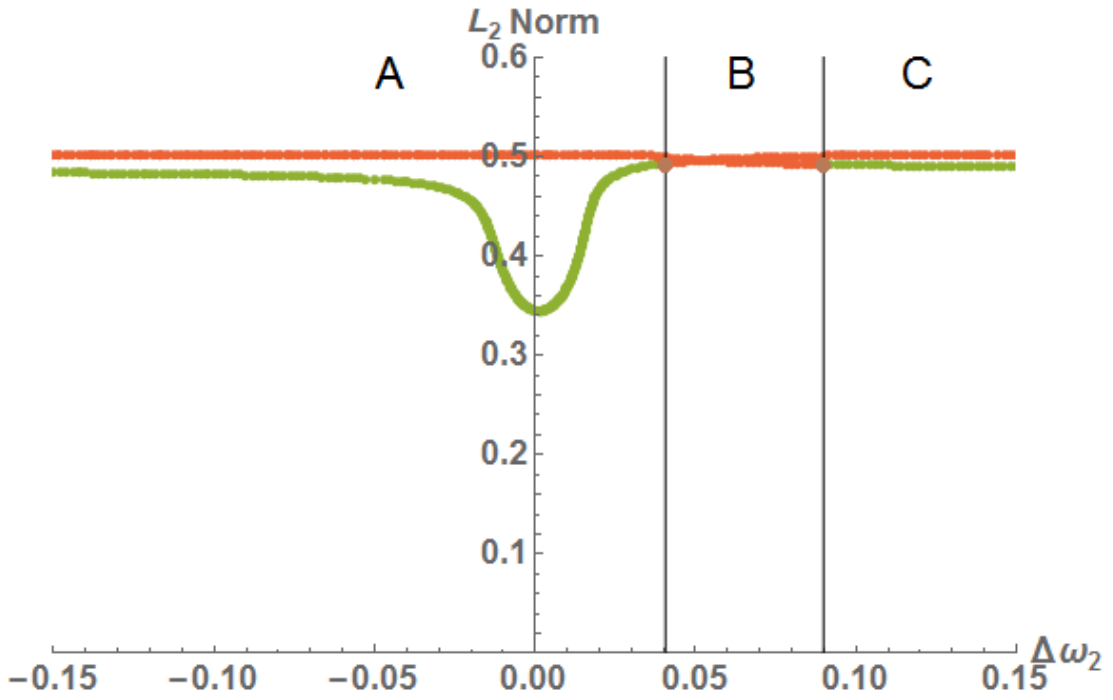


Figure 6.15: Plot of the L2 Norm from the multimode model, for varying  $\Delta\omega_2$ , with  $\Delta\omega_1 = 0.05$ ,  $\eta = 0.01$  and  $\phi = 2.5$ . The steady periodic solutions are green dots and unsteady periodic solutions are in red. Torus bifurcations are in brown

## 6.4 Introducing non symmetric modes

In the previous sections a system of two, two-mode lasers, where each mode is of equal power, were coupled. However in the experimental results that inspired the development of this multi-moded approach, before coupling the lasers were tuned to be single moded, with the side modes suppressed and during the experiment one of the side modes was excited. In this section different methods of unbalancing the power in the modes will be tested, with the intention of having one mode significantly more powerful than the other. To do this the multi-mode gain terms will be altered.

### 6.4.1 Alteration of multi-mode gain terms

In Eqn. 6.5-6.10 the multi-mode gain terms are of the form

$$g_{L,Rm} = g_{L,Rm}^{(0)} (1 + \epsilon \sum_n \beta_{mn} |E_{L,Rn}|^2)^{-1}$$

The important terms that can alter the relative power of the modes of the laser are the  $\beta_{mn}$  terms, which represent the cross and self-saturation between the

modes. For balanced lasing it was found that  $\beta_{11} = \beta_{22} = 1$  and  $\beta_{12} = \beta_{21} = 0.667$ . Initially it was decided to keep the self-saturation terms,  $\beta_{11}$  and  $\beta_{22} = 1$  and vary the cross terms. The optimal values were found to be  $\beta_{12} = 0.1$  and  $\beta_{21} = 0.9$  maximised the power in the first mode, while minimising the power of the second mode. In terms of cross saturation between modes, this creates a more powerful mode by favouring one over the other. The high  $\beta_{21}$  term, means a high fraction of power of the second mode is coupled into the first mode and the low  $\beta_{12}$  means a low fraction of power transfer from mode one to two. This can be seen in figure 6.16. A better difference in power was achieved for  $\beta_{12} = 0$  and  $\beta_{21} = 1$  (basically killing one mode) but this caused a similar problem to using a zero initial condition in the previous section where a bifurcation analysis was not possible.

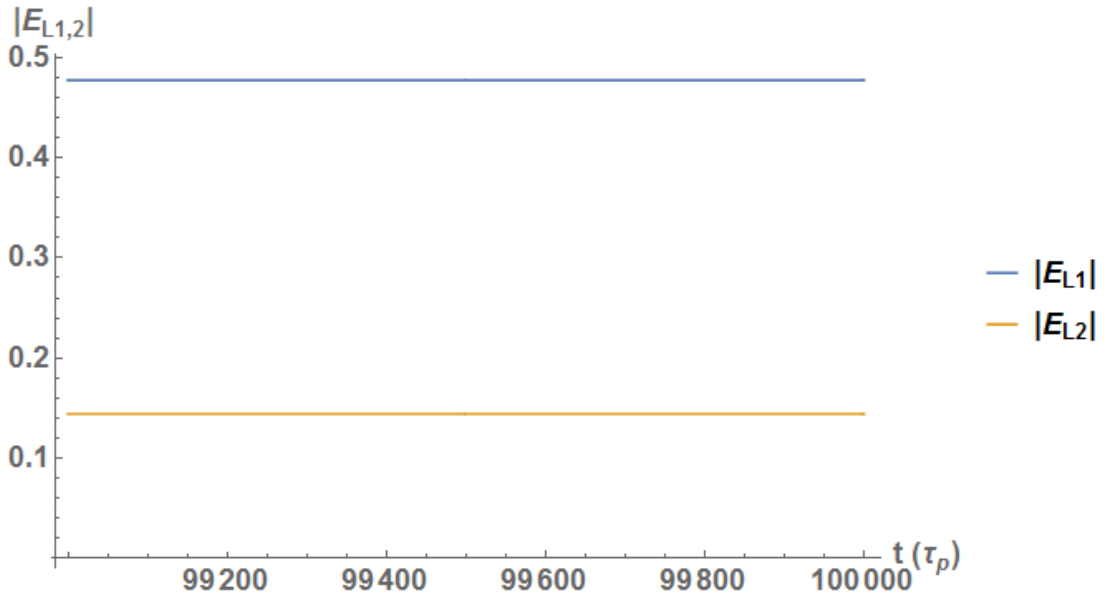


Figure 6.16: Time series of  $|E_{L1}|$  and  $|E_{L2}|$  from the multimode model, for  $\beta_{11} = \beta_{22} = 1$ ,  $\beta_{12} = 0.1$  and  $\beta_{21} = 0.9$

Now that the power of the modes has been unbalanced in each individual laser, the lasers will now be coupled and a bifurcation study will be performed on this system and the results will be compared with experiment.

## 6.5 Bifurcation study of the unbalanced mode arrangement

In this section the multi-mode gain terms will be set to those outlined in figure 6.16 to produce the desired unbalanced mode power arrangement and the bifurcations of this system will be highlighted for different detuning arrangements. This will provide insight into the behavioural regimes and how they change. In each case the bifurcation diagram will be compared to the same detuning arrangement with symmetrically powered modes. Figure 6.17-6.19 shows the bifurcations diagrams for symmetric detunings of  $\Delta\omega_{1,2} = 0.05, 0.1$  and  $0.15$ .

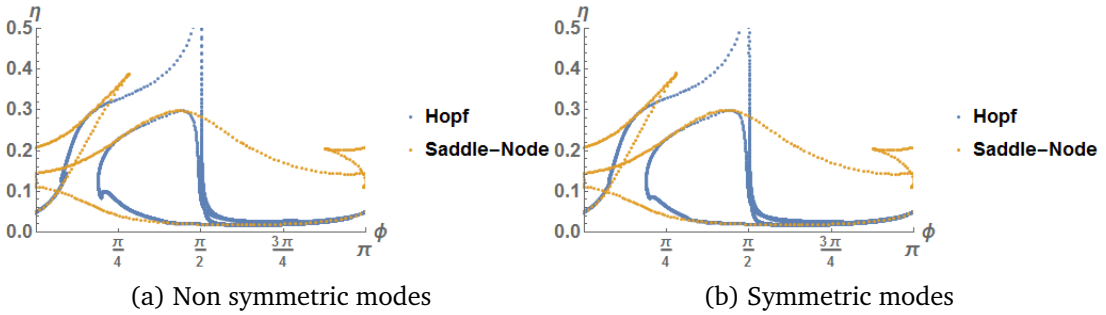


Figure 6.17: Bifurcation diagrams of the multimode model, showing saddle-node bifurcations in orange and hopf in blue,  $\Delta\omega_{1,2} = 0.05$ , for a) non symmetric modes b) symmetric modes.

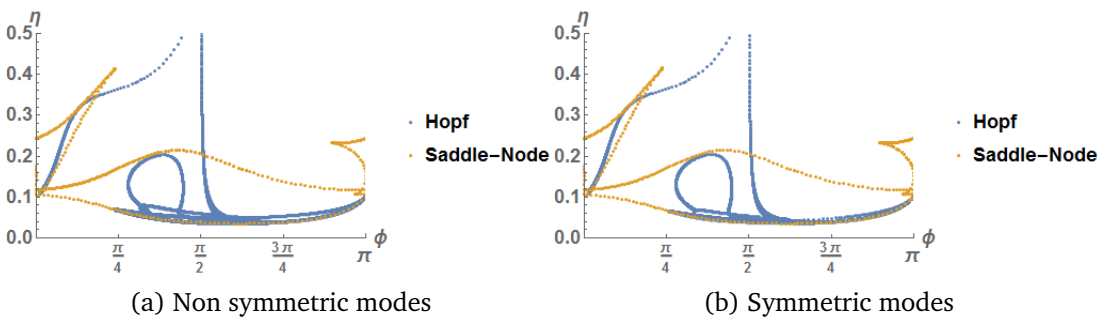


Figure 6.18: Bifurcation diagrams of the multimode model, showing saddle-node bifurcations in orange and hopf in blue, for  $\Delta\omega_{1,2} = 0.1$ , for a) non symmetric modes b) symmetric modes.

One can see there is only a minor difference in the bifurcation diagrams when the non-symmetric mode arrangement was introduced, specifically in the Hopf bifurcations. However a more dramatic shift is visible when a non-symmetric

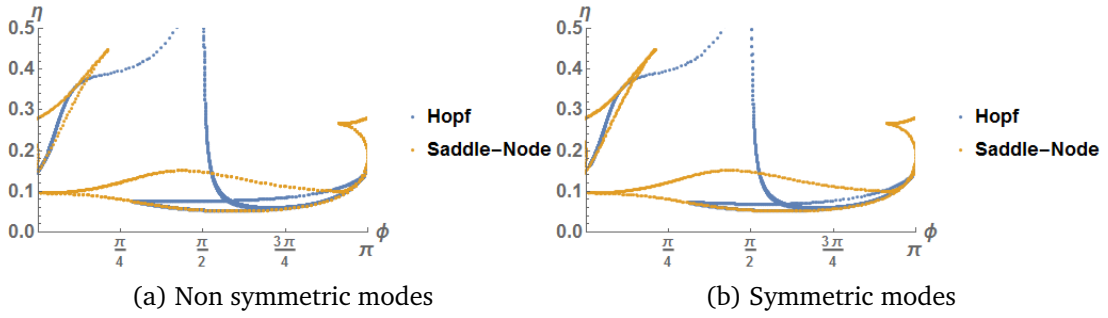


Figure 6.19: Bifurcation diagrams of the multimode model, showing saddle-node bifurcations in orange and hopf in blue, for  $\Delta\omega_{1,2} = 0.15$ , for a) non symmetric modes b) symmetric modes.

detuning is introduced to the non-symmetric mode arrangement, as seen in figure 6.20 and 6.21.

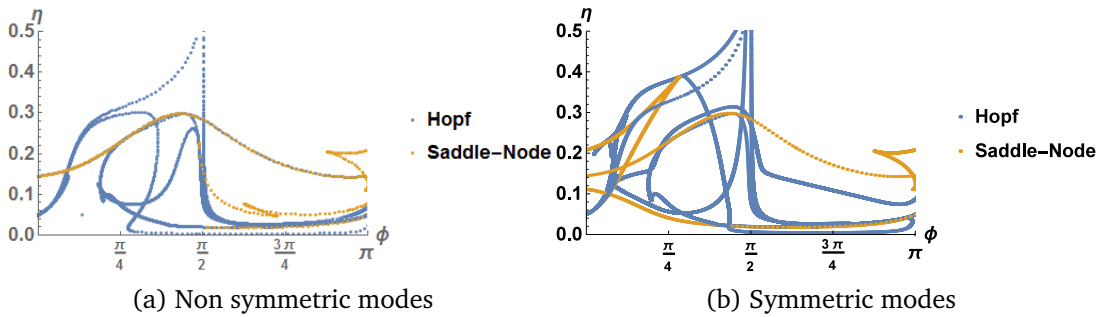


Figure 6.20: Bifurcation diagrams of the multimode model, showing saddle-node bifurcations in orange and hopf in blue,  $\Delta\omega_1 = 0.05$  and  $\Delta\omega_2 = 0.07$ , for a) non symmetric modes b) symmetric modes.

These show the first shift in the form of the saddle-node bifurcations, while also displaying a change in the Hopf bifurcation lines. Now that a bifurcation study has been performed on this multi-mode arrangement, with unbalanced power in the modes, in the next section an attempt shall be made to recreate experimental results.

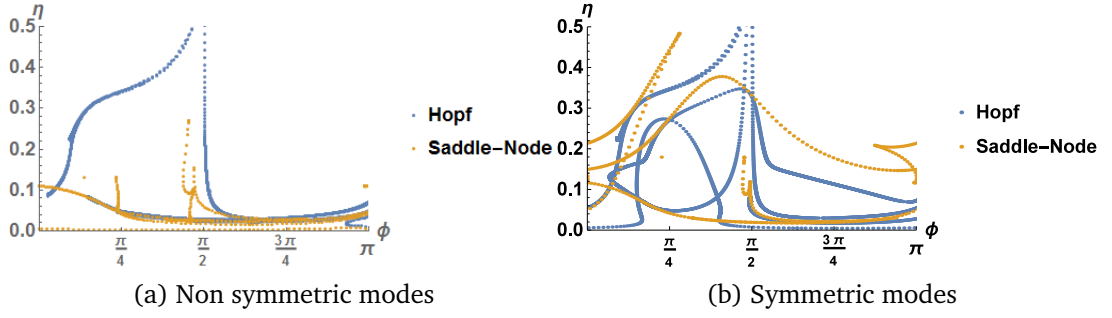


Figure 6.21: Bifurcation diagrams of the multimode model, showing saddle-node bifurcations in orange and hopf in blue,  $\Delta\omega_1 = 0.07$  and  $\Delta\omega_2 = 0.05$ , for a) non symmetric modes b) symmetric modes.

## 6.6 Recreation of experiment using multi-mode model

### 6.6.1 Individual VOA bias sweeps

To re-create experimental methods the same process was followed as was done in Sec. 5.3, where a  $\phi$  value will be fixed and  $\eta$  will be varied, while viewing the FFT of  $|E_{L,R_i}|$ . This re-creates how the dynamical regimes would be viewed on an ESA. This process is analogous to taking vertical slices of the bifurcation diagrams in the previous section. However unlike the previous simulations of this form, rather than linearly varying  $\eta$  from 0 – 0.5, a simulated sweep of the voltage applied to the VOA will be performed. In Sec. 5.4.1 5.47 (repeated below in figure 6.22 for reader's convenience) it was shown how the measured  $\eta$  varied with this voltage from the third generation MCL devices. The  $\eta$  values will be varied in the exponential manner displayed.

From figure 6.23b the FFT of  $\tilde{E}_{L_1}$  resembles a two colour state which was observed in Chapter 4, however there is an extra weaker frequency at 40 GHz. This would suggest that a higher harmonic oscillation also exists. This is also suggested in figure 6.23a, when the FFT of  $|E_{L_1}|$  was plotted. Rather than just a single beat note corresponding to a pure two colour state, higher harmonic oscillations also exist. To confirm the existence of the harmonics a time trace of  $E_{L_1}$  was plotted, figure 6.24. There also exists a small window of one colour behaviour at around VOA bias of 1.7 V, identifiable by the single frequency line in the FFT of  $\tilde{E}_{L_1}$  and the lack of features in the FFT of  $|E_{L_1}|$ .

At the highest VOA voltage in figure 6.28a there is a region that appears to

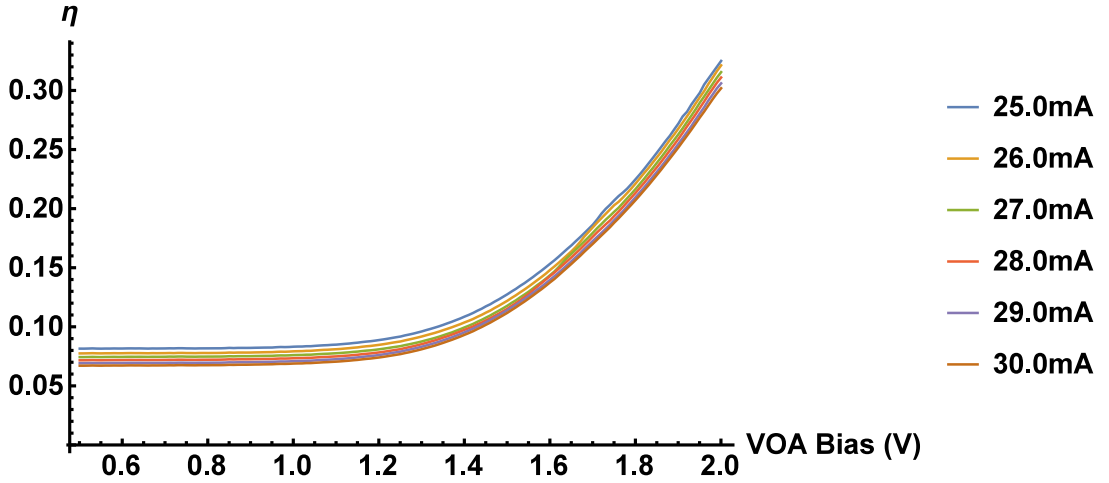


Figure 6.22: Measurement of  $\eta$  for the  $385\mu m$  device in figure 5.45, for various tuning arrangements.

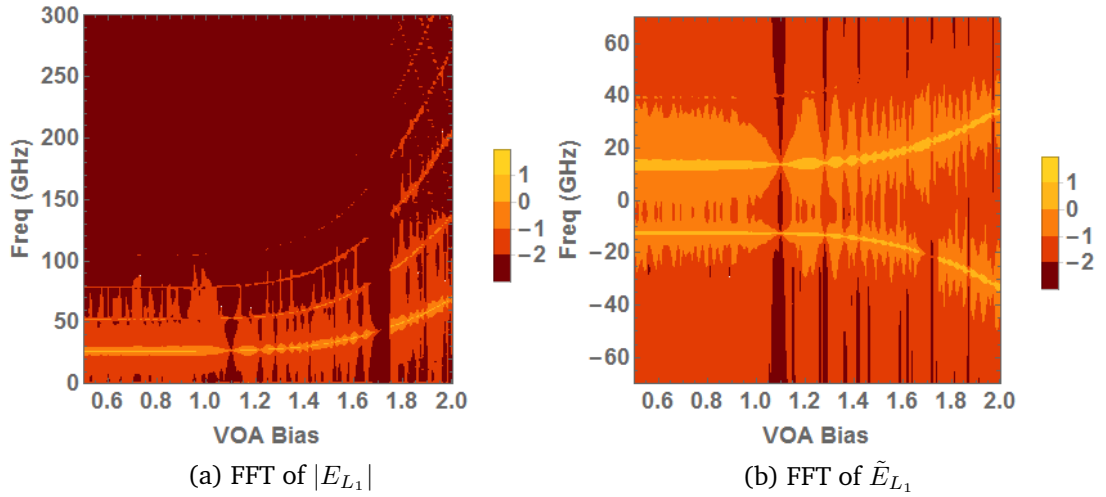


Figure 6.23: Logarithmic contour plot of a) FFT of  $|E_{L_1}|$ , b) FFT of  $\tilde{E}_{L_1}$  from the multimode model, for varying VOA bias (using associated  $\eta$  values in figure 5.43).  $\Delta\omega_{1,2} = 0.1$  and  $\phi = 1.57$

have subharmonics. Figure 6.25a shows the time trace and FFT of  $\log_{10}(|E_{L_1}|)$  at the associated  $\eta$  value.

As can be seen, there are a lot more frequencies present in the solution. However in figure 6.25 the solution was cut at a frequency of 70 GHz, as this was the fastest high speed photodiode available in our lab. Performing a similar cut on figure 6.25a yields figure 6.26, where there is a single strong peak at approximately 70 GHz, with a weaker subharmonic at 15 GHz. This is also evident in figure 6.27 where a linear sweep of  $\eta$  was performed, as opposed to the exponential one related to the VOA bias. Around 3 V there are

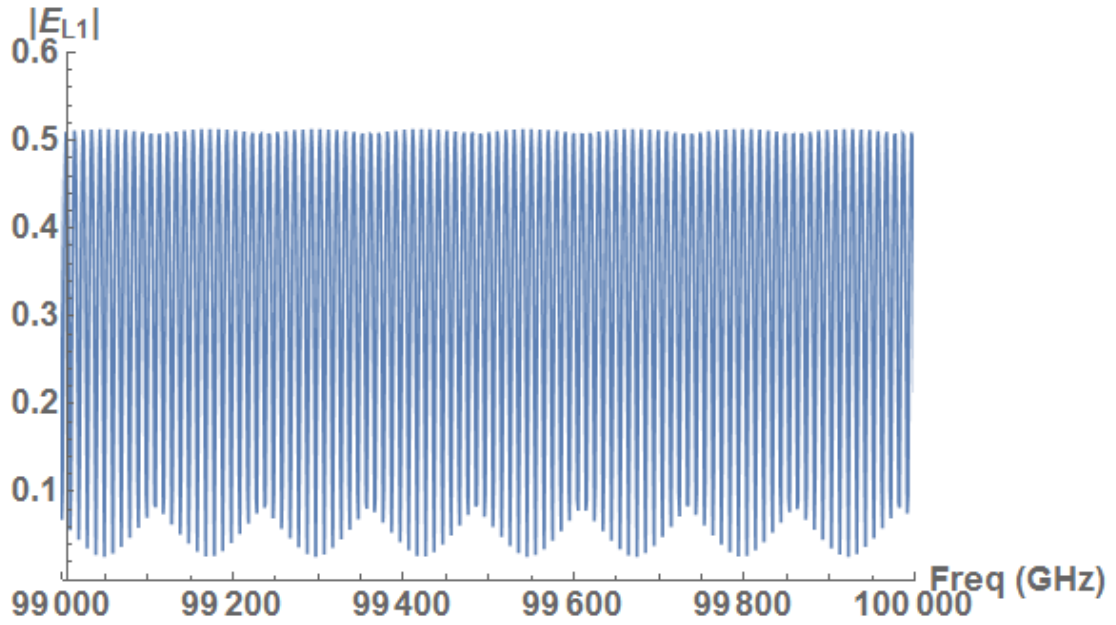


Figure 6.24: Time trace of  $|E_{L1}|$  from the multimode model, for  $\eta = 0.3$ ,  $\phi = 1.57$  and  $\Delta\omega_{1,2} = 0.1$

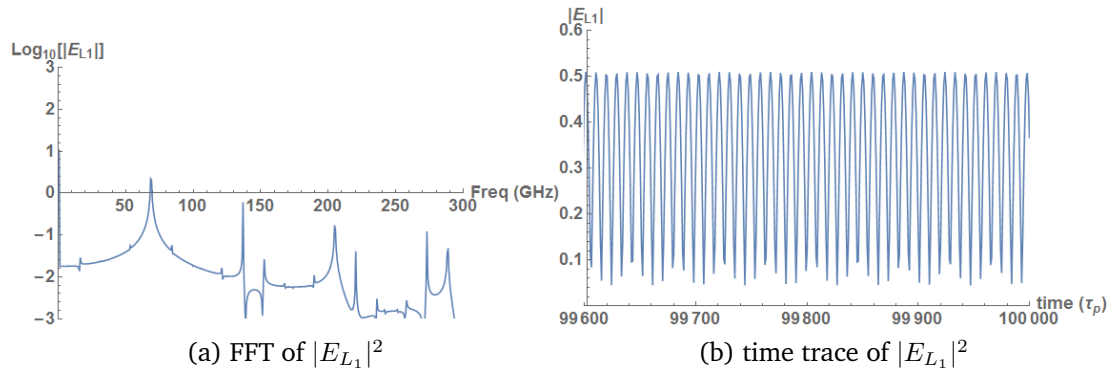


Figure 6.25: a)  $\text{Log}_{10}$  of the FFT and b) time trace of  $|E_{L1}|$  from the multimode model, for  $\eta = 0.32$ ,  $\phi = 2.51$  and  $\Delta\omega_{1,2} = 0.1$ .

what appear to be a series of subharmonics being generated.

Figure 5.43 shows the absorption of second generation of MCL devices had a much lower  $\eta$  parameter, never going above 10%. Repeating the process of exponentially varying the coupling strength and viewing the FFT of  $|E_{L,Ri}|^2$ , but for a lower max value of  $\eta$  can be seen in figure 6.28.

The harmonic two colour state again exists for low VOA bias, but transitions into a region of multiple closely spaced lines in the FFT of  $|E_{L1}|$ , through the observation of the time trace of  $|E_{L1}|$  in figure 6.29, this is a region of pulsing behaviour.



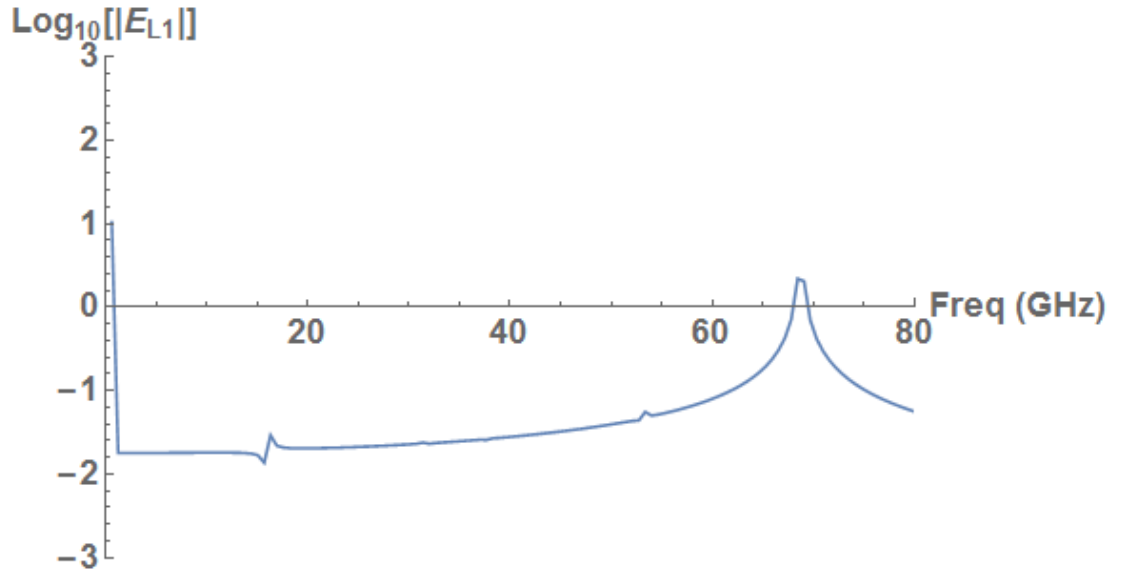


Figure 6.26:  $\log_{10}$  of the FFT of  $|E_{L1}|$  from the multimode model, for  $\eta = 0.32$ ,  $\phi = 2.51$  and  $\Delta\omega_{1,2} = 0.1$ , with the max frequency cut at  $80GHz$ .

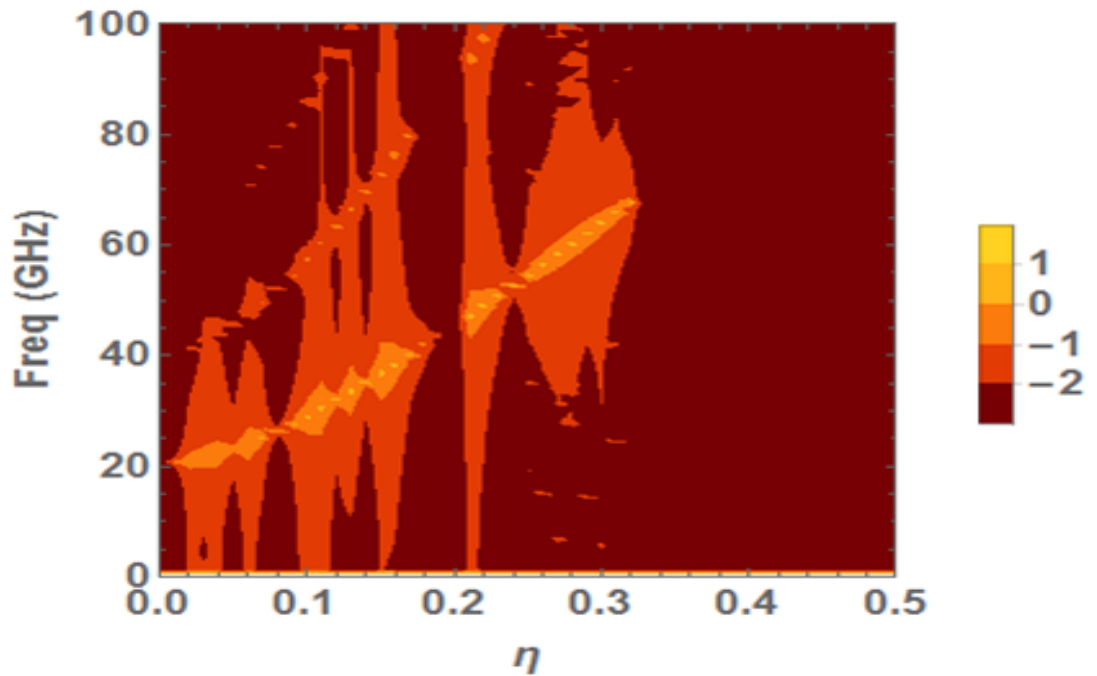


Figure 6.27: Logarithmic contour plot of FFT of  $|E_{L1}|$  from the multimode model, for linearly varying  $\eta$ .  $\Delta\omega_{1,2} = 0.1$  and  $\phi = 1.57$ .

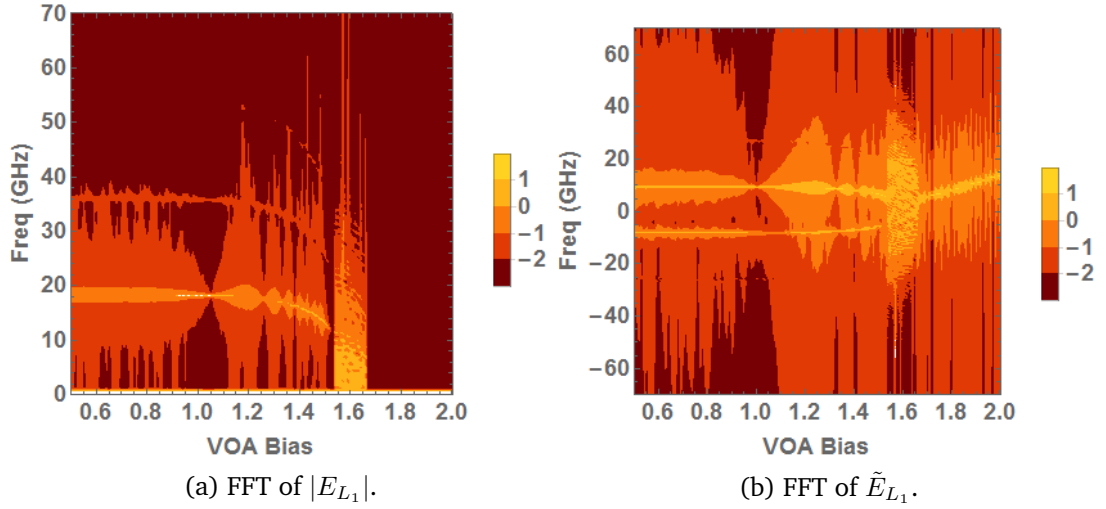


Figure 6.28: Logarithmic contour plot of a)FFT of  $|E_{L1}|^2$ , b) FFT of  $\tilde{E}_{L1}$  from the multimode model, for varying VOA bias (with  $\eta$  values associated with the lower  $\eta$  of the second generation MCL devices).  $\Delta\omega_{1,2} = 0.1$  and  $\phi = 2.51$ .

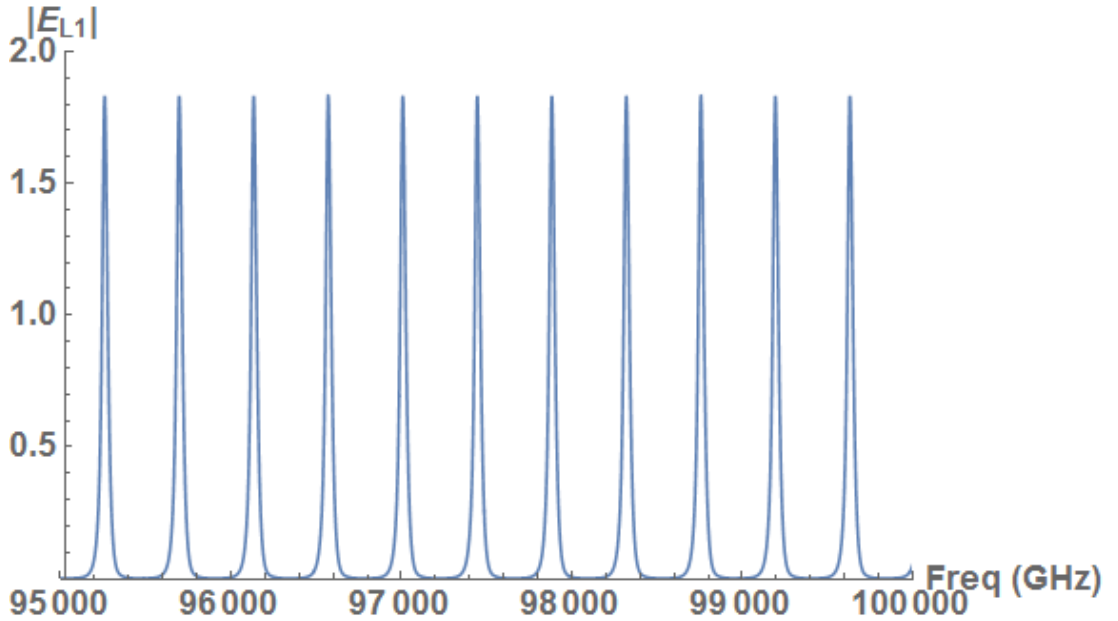


Figure 6.29: Time trace of  $|E_{L1}|$  from the multimode model, for  $\eta = 0.05$ ,  $\phi = 2.51$  and  $\Delta\omega_{1,2} = 0.1$ .

In Sec. 5.4.1 it was mentioned that when altering the VOA bias,  $\phi$  also changes, so doing fixed  $\phi$  values while sweeping  $\eta$  is not technically correct. Using a set of simple Fabry-Pérot (FP) devices the variation in optical path length per unit distance,  $\Delta L/d$ , where  $L$  is the optical path length,  $L = nd..$  Firstly an experiment was done where the optical spectra of an FP of length  $1050 \mu\text{m}$  was recorded for varying current. The density plot of this sweep can be seen in figure 6.30. As can be seen in the low current region, lasing has not

commenced so this data is ignored.

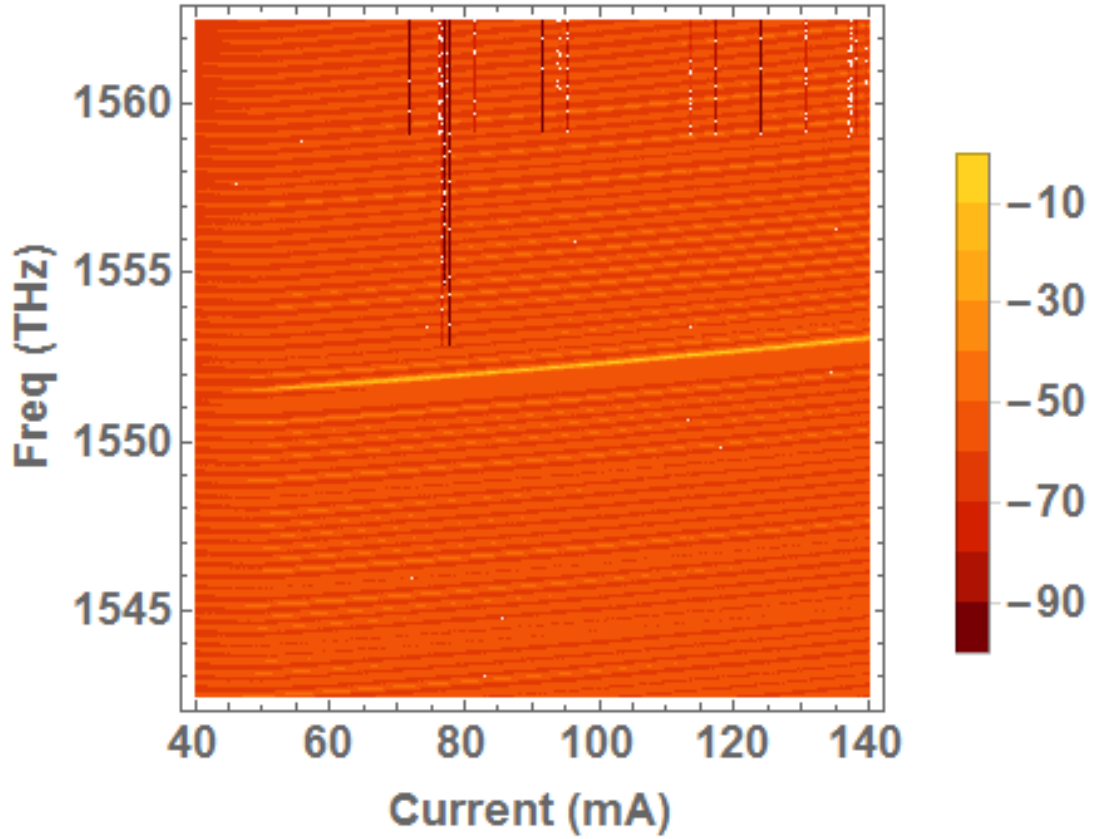


Figure 6.30: Experimental density plot of the wavelength versus the current applied for a simple FP laser.

Firstly the main mode of the laser was tracked, and a plot of  $\lambda$  vs  $I$  can be seen in figure 6.31. This was fit using a function of the form  $y = ax^2 + b$ .

Next a  $VI$  sweep of the laser was performed, where the voltage is varied and the current is measured. This gives figure 6.32. Note that for high current ( $I > 110$  mA) the equipment encountered an error and produced noisy data, this data will be ignored. This data was fit with a simple linear function of the form  $y = a + bx$ .

This was then converted to a plot of power vs current, by multiplying the current measured by the voltage applied, yielding figure 6.33. This data was fit using  $y = a + bx^2$ .

By applying the fitted function for  $\lambda(I)$ , a plot of power vs. wavelength was produced, as seen in figure 6.34.

This wavelength shift occurs due to the alteration of the optical path length,

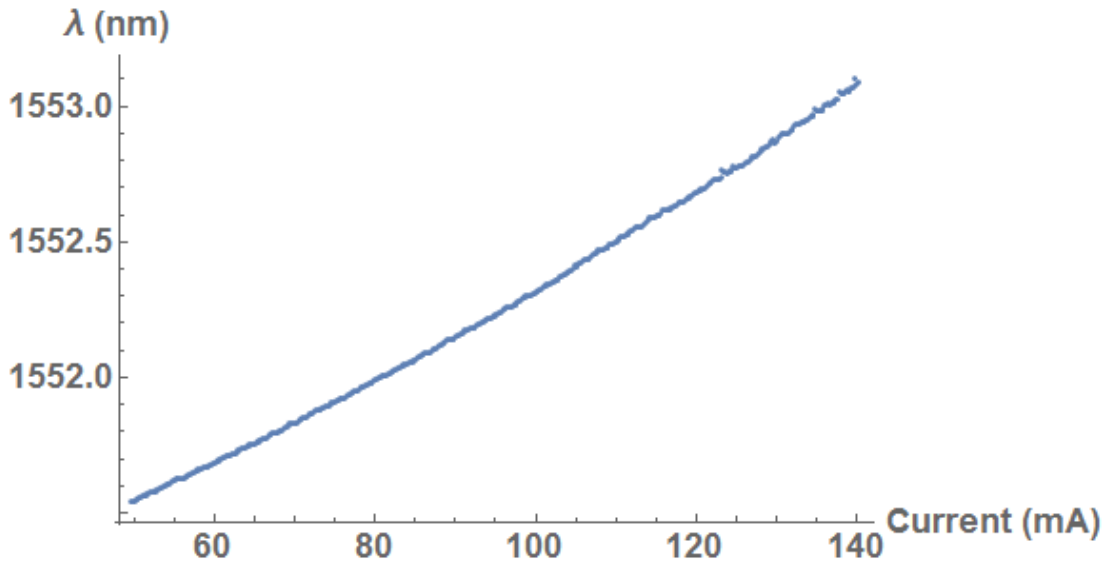


Figure 6.31: Plot of the wavelength of the main mode of the FP device test, versus the current applied.

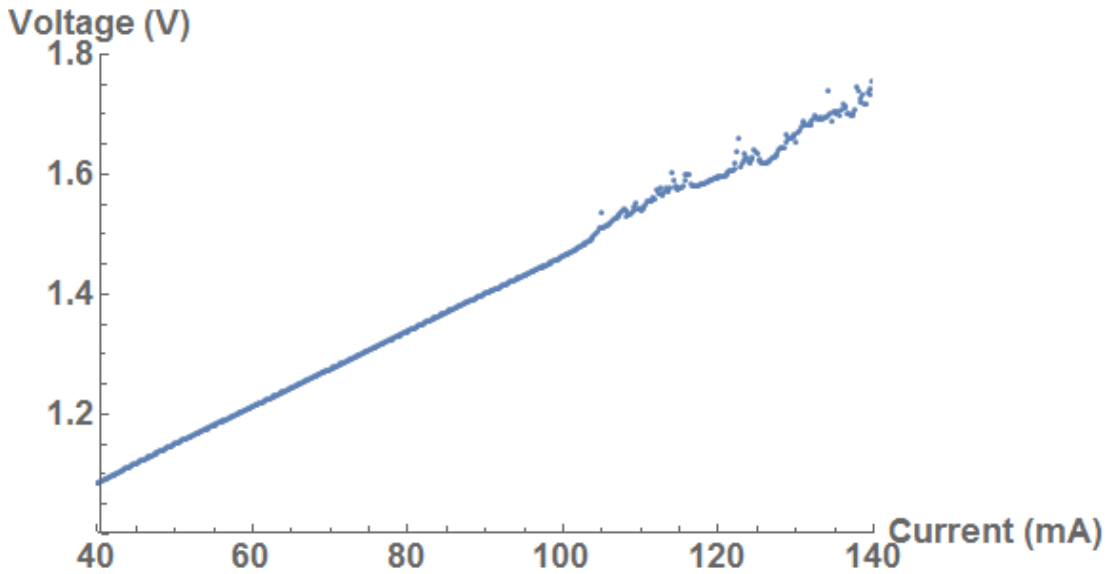


Figure 6.32: Plot of current measured versus voltage applied for the FP device.

$nd$ , of the FP device.

$$\lambda = \frac{2nd}{m} \quad (6.26)$$

Through analysis of the individual trace in figure 6.31, the mode number ( $m$ ) for the main mode was found and by using Eqn. 6.26 the y-axis of figure 6.34 was converted to optical path length. This was then divided by the length of the FP devices to give the change in refractive index,  $n$  (or optical path length

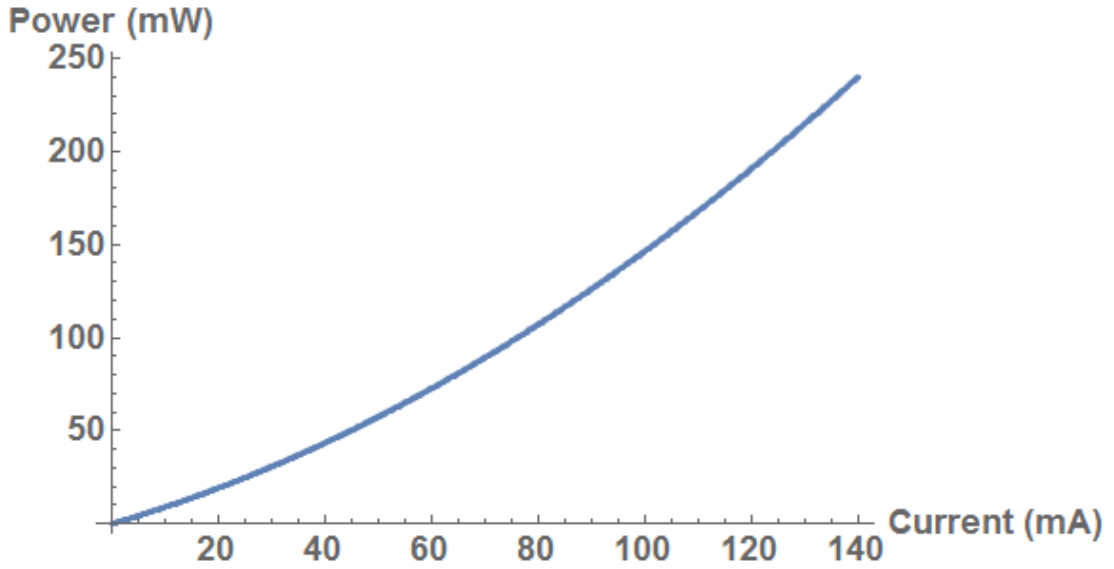


Figure 6.33: Plot of current measured versus power applied for the FP device.

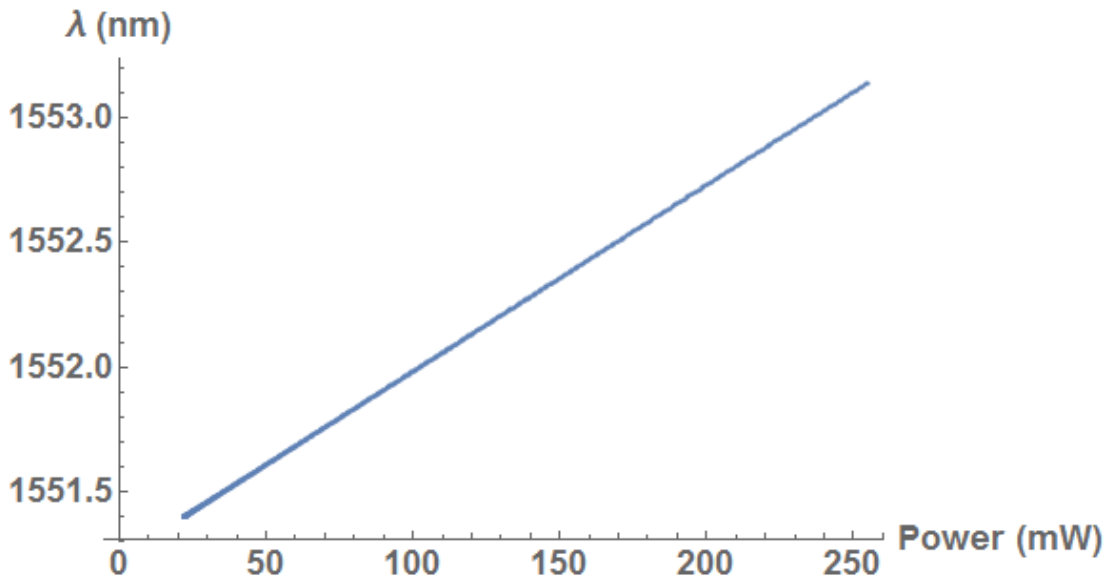


Figure 6.34: Plot of power applied to the FP versus the wavelength of the main mode of the FP device.

per unit length). The result is seen in figure 6.35.

This was then converted to the change in refractive index,  $\Delta n$ , as seen in figure 6.36. This gives a linear relation, which can be fit using  $y = a + bx$ , to get  $\Delta n(P)$ .

Next if the VOA of the MCL devices is assumed to behave as a FP when the is power applied during the voltage sweep of the VOA, using the  $\Delta n(P)$  function found previously and multiplying by the VOA length, the change in optical

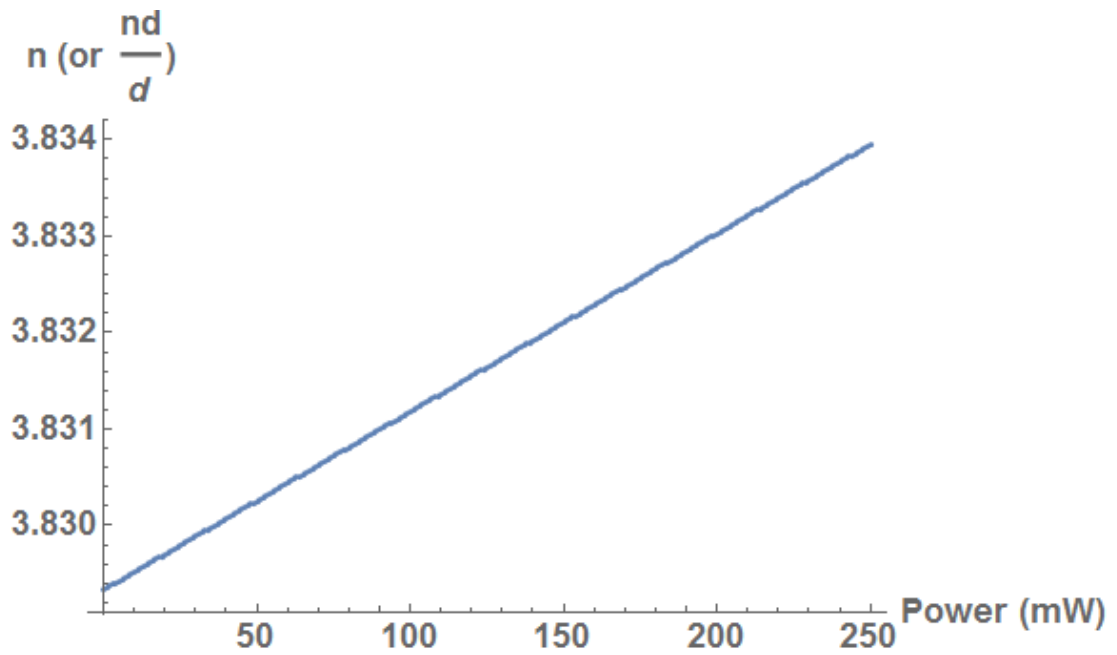


Figure 6.35: Plot of refractive index ( $n$ ) versus power applied to the FP device.

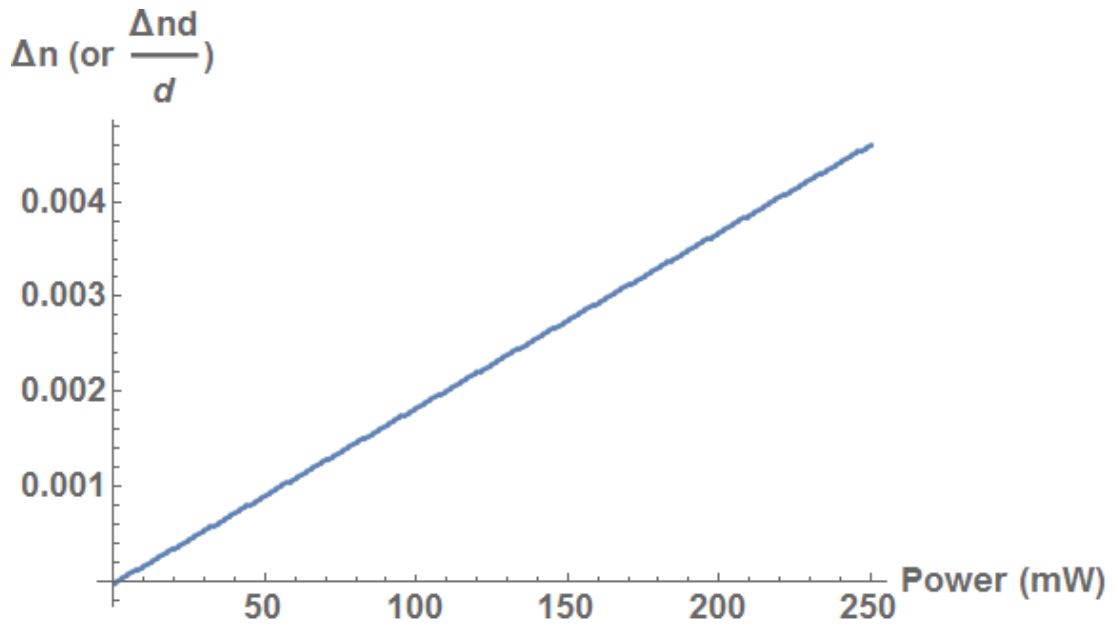


Figure 6.36: Plot of change in refractive index ( $\Delta n$ ) versus power applied to the FP device.

path length with VOA bias can be found. Figure 6.37 shows a series of  $IV$  diagrams for each VOA in the third generation of MCL devices.

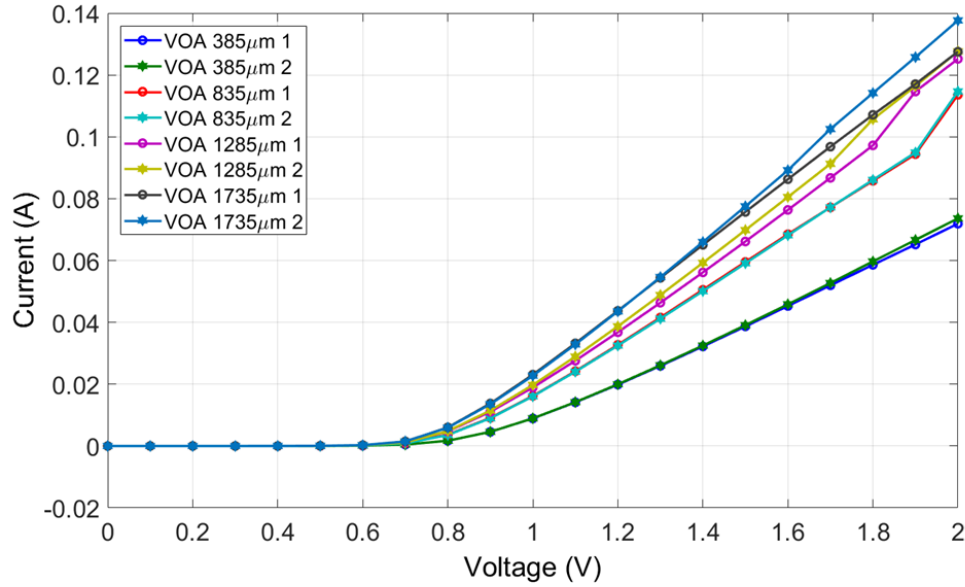


Figure 6.37: Plot of current measured versus voltage applied to the different length VOAs in the third generation MCL devices.

Similar to the process done previously, this was converted to a plot of power versus voltage applied, and then the power was converted to optical path length change, yielding figure 6.38, for the 385  $\mu\text{m}$  VOA device.

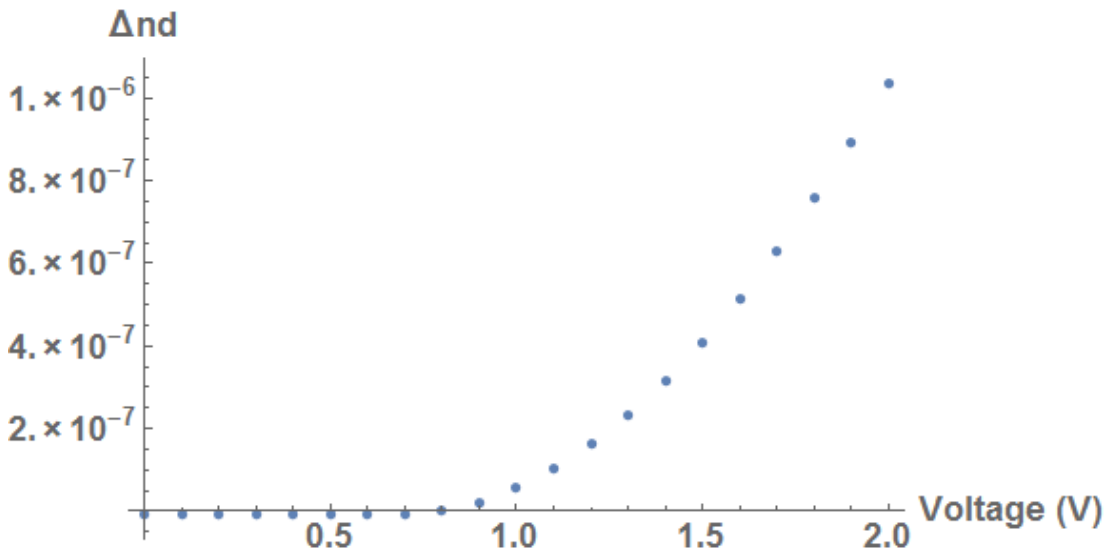


Figure 6.38: Plot of the change in optical path length for the 385  $\mu\text{m}$  VOA device versus the voltage applied.

Using Eqn. 6.27, this can be converted to a phase change. The emission wavelength of the free running laser in the coupling experiment was found to

be 1556 nm. The plot of phase change versus VOA bias can then be seen in figure 6.39.

$$\phi = 2\pi(nd \bmod \lambda) \quad (6.27)$$

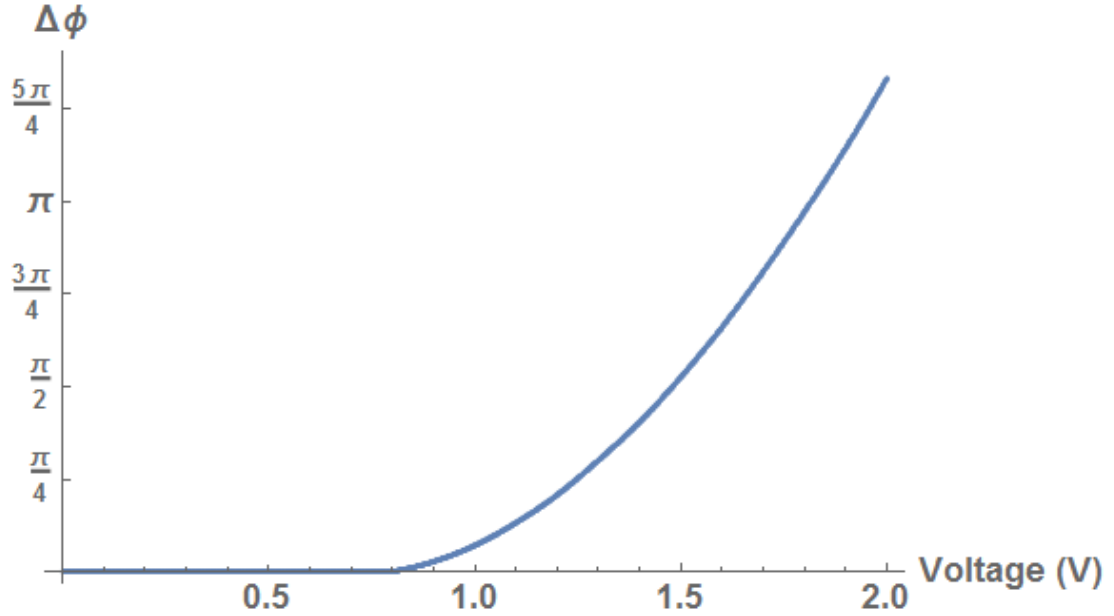


Figure 6.39: Plot of phase change for the 385  $\mu\text{m}$  VOA device versus the voltage applied.

The previous process was repeated for the other VOA lengths for this set of devices, being 835  $\mu\text{m}$ , 1285  $\mu\text{m}$  and 1735  $\mu\text{m}$ . The results can be seen in figure 6.40. One can see that for longer lengths of VOA, the phase can go through a number of  $2\pi$  phase rotations.

For the 385  $\mu\text{m}$  device the  $\phi$  variation with voltage can be combined with the  $\eta$  variation with voltage seen in figure 6.22, to observe the curve in the  $(\phi, \eta)$  space performed during the voltage sweep. This can then be placed over a bifurcation diagram to show what bifurcations would be crossed during this VOA bias sweep. A starting value for  $\phi$  is not possible to find, as only the relative shift in  $\phi$  with voltage was found. Figure 6.41 shows two such curves for two arbitrary start values of  $\phi$ , over the bifurcation diagrams for  $\Delta\omega_{1,2} = 0.05$ . Given the  $\pi$  symmetry of the bifurcations diagrams the diagrams have been restricted from  $0 - \pi$ , and the curves wrap around.

Figure 6.42 shows the logarithmic contour plots of the FFT of  $E_{L_1}$  and  $|E_{L_1}|$  for the two different starting  $\phi$  values outlined in figure 6.41, while following the black lines in  $(\phi, \eta)$  space, in the case of  $\Delta\omega_{1,2} = 0.05$ .



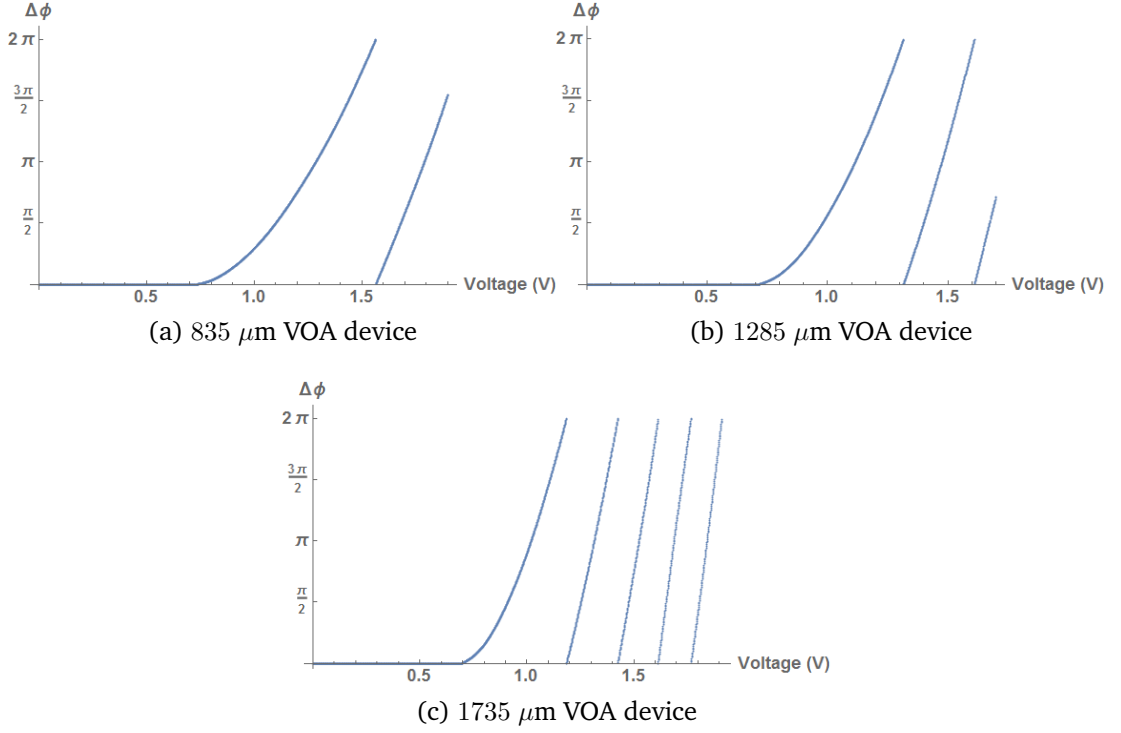


Figure 6.40: Plot of phase change for the various VOA lengths versus the voltage applied.

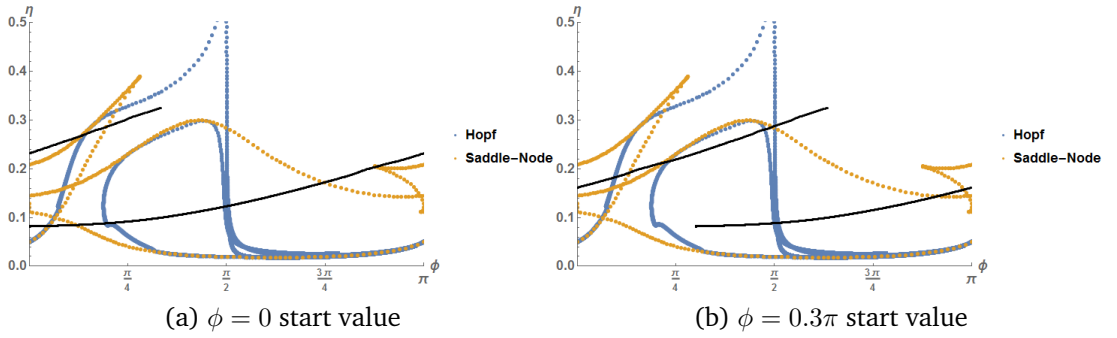


Figure 6.41:  $(\phi, \eta)$  curves found from experimental results (black), placed over the bifurcation diagrams of the multimode model, for  $\Delta\omega_{1,2} = 0.05$ .

Figure 6.42a and 6.42b shows for low VOA bias ( $V < 0.98$ ) the system is in a one colour state (single peak in FFT of  $E_{L_1}$  and featureless space FFT of  $|E_{L_1}|$ ), this transitions to a small region of closely spaced lines in the FFT of  $|E_{L_1}|$  (at  $V \approx 0.98$ ), associated with pulsed behaviour, followed by a two colour state with harmonics with a curving frequency (up to  $V = 1.4$ ). The system then returns to a one colour state (between  $V = 1.4 - 1.9$ ). Finally a small region of harmonic two colour states exist ( $V > 1.9$ ). Based on current experimental results it is seen that there are only small windows of one colour states, and

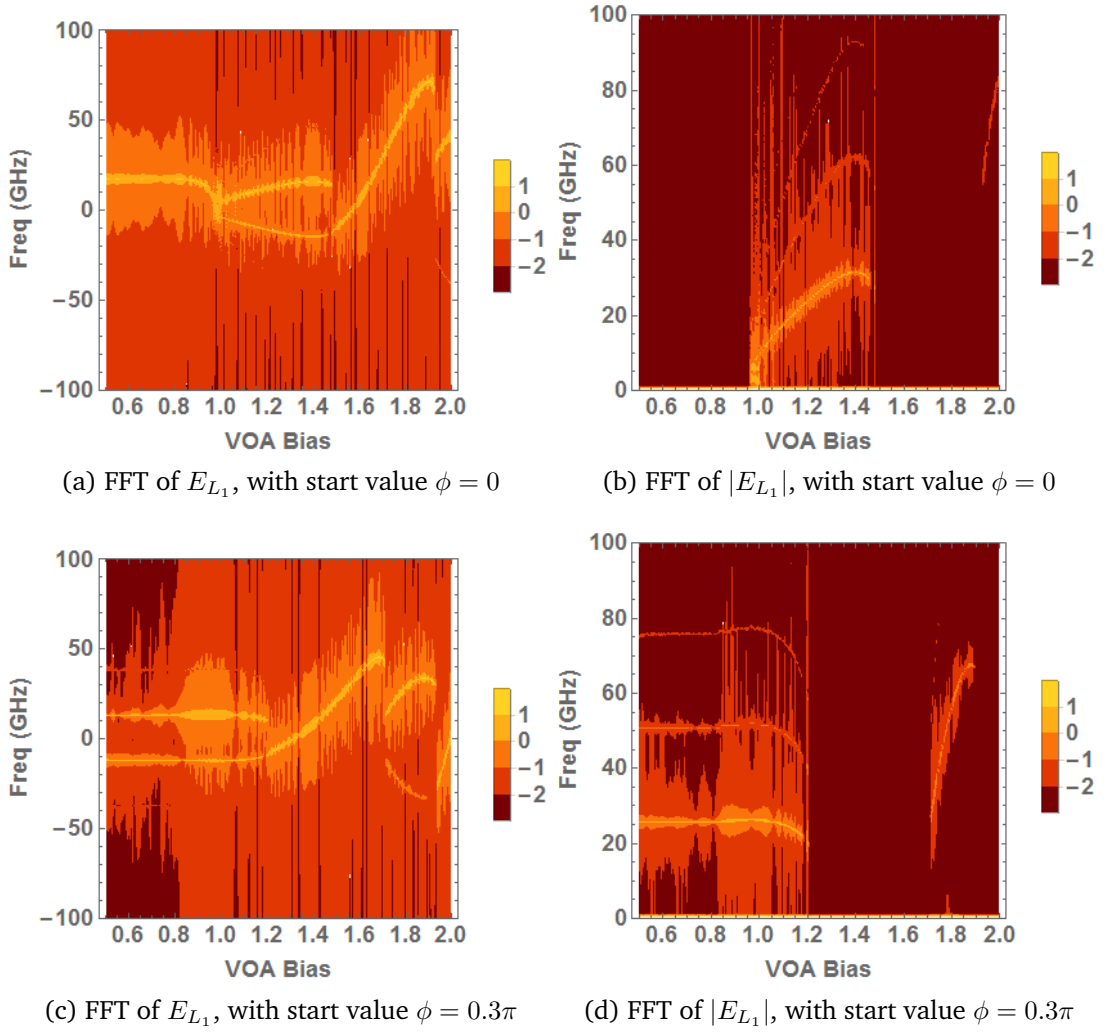


Figure 6.42: Logarithmic contour plots of the FFT of  $E_{L_1}$  and  $|E_{L_1}|$  from the multimode model, for a)  $\phi = 0$  b)  $\phi = 0.3\pi$  start values of the  $(\phi, \eta)$  curves highlighted in figure 6.41.

they do not exist at low VOA bias, so figure 6.42c and 6.42d have starting values that lead to two colour harmonic states initially. However this curve misses the pulsed behaviour region. To have a better chance of encountering complex behaviours  $\eta$  needs to be lower during these  $(\eta, \phi)$  curves. A longer VOA would have a lower initial value of  $\eta$ , and a lower max value of  $\eta$ , and may give a better result. No measurements of  $\eta$  versus voltage for the  $835 \mu\text{m}$  were available, but a good estimate can be made by decreasing the initial and max value of  $\eta$  versus voltage. Making this assumption and combining it with the curve of  $\phi$  versus VOA bias (figure 6.40a), leads to figure 6.43 for the  $(\phi, \eta)$  curve placed over the  $\Delta\omega_{1,2} = 0.05$  bifurcation diagram, with the same two starting values for  $\phi$ .

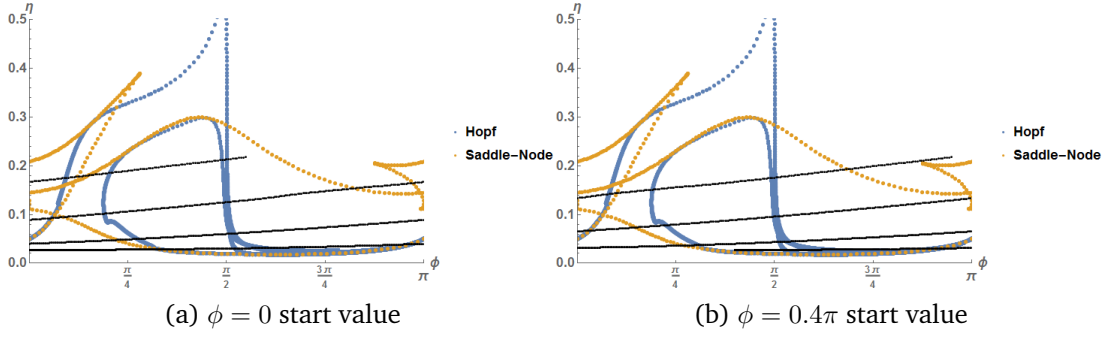


Figure 6.43:  $(\phi, \eta)$  curves found from experimental results (black) for the  $835\mu\text{m}$  VOA device, placed over the bifurcation diagrams of the multimode model, for  $\Delta\omega_{1,2} = 0.05$ .

In figure 6.44 the associated contour plots are shown.

From these diagrams, one can see the general trend that for low VOA bias the system is in an oscillatory behaviour. Intuitively this is caused by two detuned signals being weakly coupled (low  $\eta$ ). These then transition into a region of pulsing behaviour, identifiable by the series of closely spaced lines in the FFT of  $|E|$ . Finally as the VOA bias increases, the system transitions between one and two colour states, based on the phase variation causing the system to wrap around the bifurcation diagrams a number of times. In the next section  $\eta$  and  $\phi$  will be replaced with a single variable, that being the VOA bias, and a bifurcation analysis will be done.

### 6.6.2 Data summary of a collection of VOA sweeps

A number of experimental results were summarised into a single graph, where for each detuning arrangement the different behavioural regimes present had their range of voltage at which they are present saved and then summarised on a single graph (these will be presented in Sec. 6.7). In this graph the x-axis detuning, and the y-axis is VOA voltage. This can be re-created by setting  $\Delta\omega_1 = \Delta\omega_2 = \Delta\omega$ , and replacing  $\phi$  and  $\eta$  with a function of VOA bias. These functions were found by applying a non-linear fit to figure 6.22 and 6.39 for the  $385\mu\text{m}$  VOA devices. Using XPPaut the bifurcation diagrams of the system over the  $(\Delta\omega, \text{VOA bias})$  parameter space were found, for two different initial phase difference values,  $\phi = 0$  and  $\phi = 0.3\pi$ . These diagrams are presented in figure 6.45.

Next, this method was also applied to the  $835\mu\text{m}$  VOA device, using a

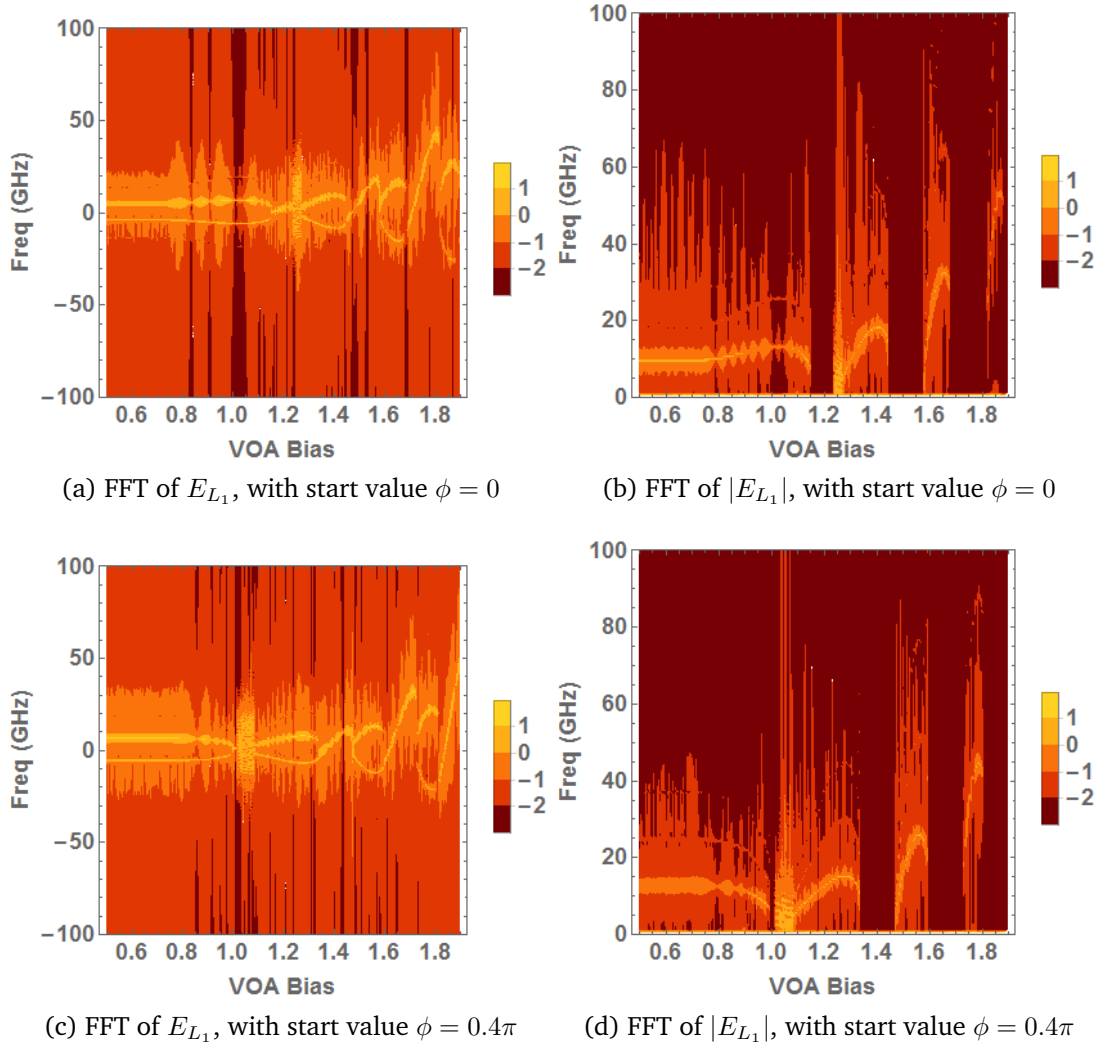


Figure 6.44: Logarithmic contour plots of the FFT of  $E_{L_1}$  and  $|E_{L_1}|$  from the multimode model, for a)  $\phi = 0$  b)  $\phi = 0.4\pi$  start values of the  $(\phi, \eta)$  curves highlighted in figure 6.43 for the  $835\mu\text{m}$  VOA devices.

non-linear fit of figure 6.40a to provide the expression of  $\phi(\text{VOA bias})$  and the same function of  $\eta(\text{VOA bias})$  from figure 6.43a which assumes a reduced  $\eta$  value for the longer VOA. This gives figure 6.46.

In these diagrams the Hopf bifurcations show where the system transitions in and out of oscillatory behaviour. This work will be directly compared in the next section with results obtained experimentally, where a series of different detuning sweeps were summarised in single diagrams.

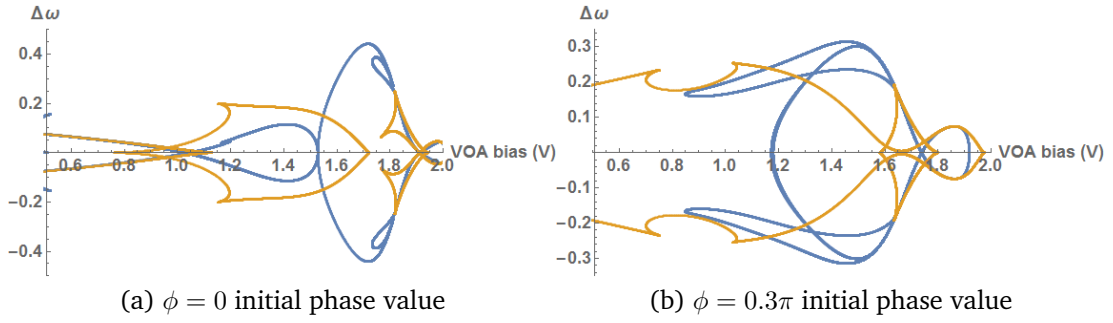


Figure 6.45: Hopf (blue) and saddle-node (orange) bifurcations for the ( $\Delta\omega$ , VOA bias) parameter space for the 385  $\mu\text{m}$  VOA MCL device, for two initial phase values, a)  $\phi = 0$  and b)  $\phi = 0.3\pi$

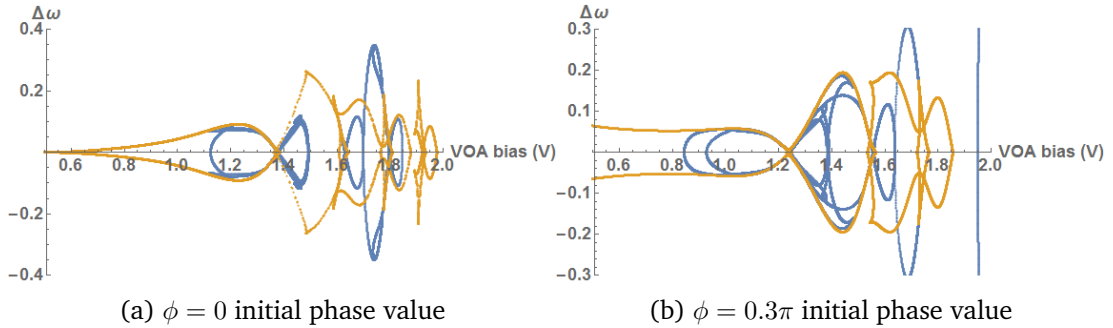


Figure 6.46: Hopf (blue) and saddle-node (orange) bifurcations for the ( $\Delta\omega$ , VOA bias) parameter space for the 835  $\mu\text{m}$  VOA MCL device, for two initial phase values, a)  $\phi = 0$  and b)  $\phi = 0.3\pi$

## 6.7 Comparison with experiment

The two main experimental results that are being compared are figure 5.44b and 5.46 from the second and third generation of MCL devices respectively. These two results are shown again below in figure 6.47 for the reader's convenience. Recall that the main difference between these two devices was an improved coupling percentage between the lasers. The second generation reached a lower maximum coupling strength ( $<10\%$ ) while the third generation achieved values greater than 30%.

Figure 6.47a displays a beat note for low VOA bias equal to the detuning of the lasers, similar to that seen in figure 6.23a. This transitions to a region of complex behaviour between 1.2 V and 1.4 V. At this point a noisy two colour state with harmonics is generated, with the main beat note approximately at 10 GHz. This goes from 1.4 V to 1.8 V, and in places demonstrates what look like sub-harmonics, similar to those seen in figure 6.27. However in this

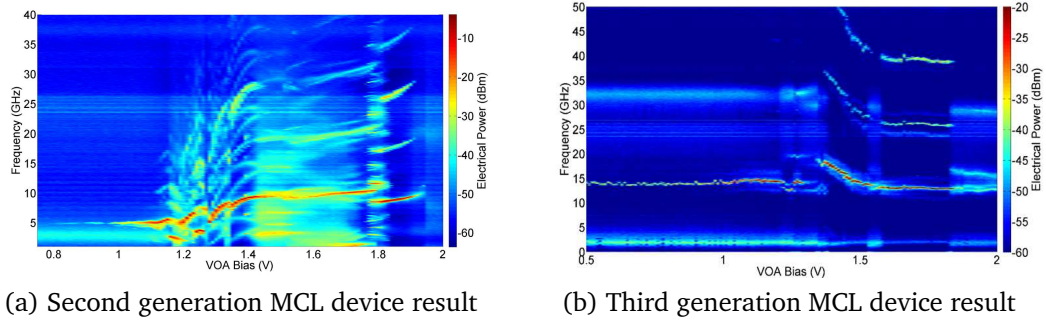


Figure 6.47: ESA contour plots for varying VOA bias for different generation MCL devices

theoretical case this sub-harmonic behaviour is actually part of a more complex behaviour that exhibits features above the highest frequency of the high speed photodiode used in the experiment. At 1.8 V there is a thin region of closely spaced lines on the ESA that corresponds to the behaviour exhibited in figure 6.28a, which is caused by a pulsed behaviour. Finally after this, the system transitions back to a beat note with harmonics with an increasing frequency. In figure 6.23a where when the VOA bias is swept and  $\eta$  increases exponentially at higher VOA bias, the increase in frequency observed is steeper than that observed experimentally. However it is still a two colour harmonic state of increasing frequency, which has been observed theoretically. Overall the multi-mode model does a good job of re-creating each individual dynamical regime observed, except for the complex regime between 1.2 V and 1.4 V. Moving on to the third generation of devices, whose results are shown in figure 6.47b, the single beat note corresponding to the detuning of the lasers for low VOA bias, observed theoretically in figure 6.46a is again observed. This transitions to a harmonic two colour state, which is a common behavioural regime observed theoretically (theoretically it was shown that this frequency only increased with  $\eta$ ). It is however of decreasing frequency, which was not observed theoretically. This is followed by a small window of one colour behaviour, similar to those seen in figure 6.46a. After this the two colour harmonic state is re-established. It is flat corresponding to being in the flat region of figure 6.22 of the VOA bias vs.  $\eta$  graph. As discussed in the previous chapter, at this point the device becomes a compound cavity device, rather than two discrete lasers and a VOA. In this particular result, good agreement is seen with theoretical results, where for a low VOA bias there is a beating between the two detuned signals that are weakly coupled, transitioning to a more complex behaviour. After this the system settles down into transitioning

between harmonic two colour states and one colour states (caused by the phase wrapping around in modulo  $\pi$ ), similar to figure 6.44d. As mentioned previously, a number of sweeps like figure 6.47b, each one for different detuning values, were summarised; the result of which can be seen in figure 6.48.

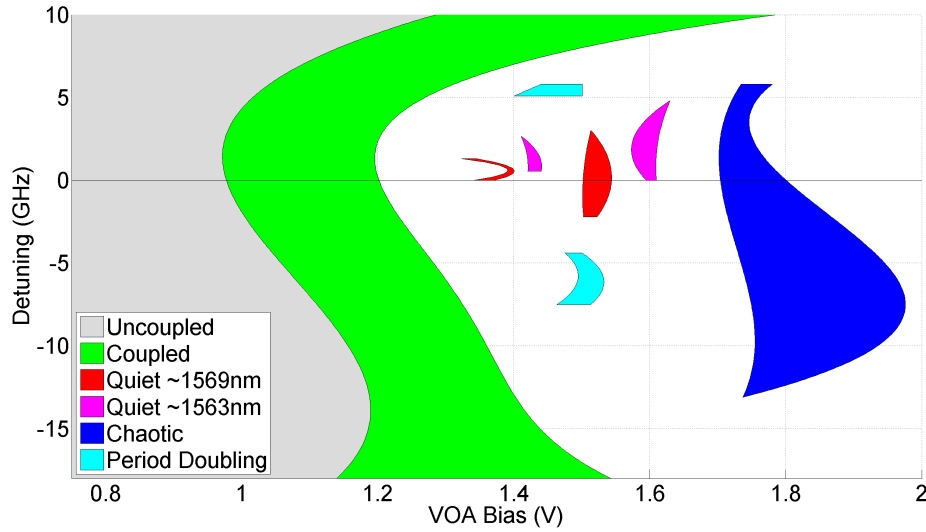


Figure 6.48: Summary of a number of experimental sweeps, where for each sweep, a detuning was fixed and the VOA bias was swept. The different behavioural regimes are given by the colour legend in the plot

This diagram is most comparable to figure 6.46b where for low VOA bias there is an oscillatory behaviour and the Hopf bifurcation diagram has the similar shape to the borders for the uncoupled and coupled regions; except for when the curve bends back at detuning =  $-15$  GHz. Also close to the zero detuning axis there are small windows of locked behaviour (red and pink), similar to the theoretical result in figure 6.46b.

Overall the multi-mode model has re-created theoretically the majority of behaviours observed experimentally, with some more complex behaviours remaining unexplained. The main advancement of this model is that when a two colour state is encountered, it exhibits harmonics, unlike the case of the single mode model, where the pure two colour states resulted in single beat notes in the FFT of  $|E|$ . By studying how the coupling phase varies with the VOA voltage, the regions of alternating between harmonic two colour states and locked behaviour was re-created theoretically. This was caused by the phase wrapping around in modulo  $\pi$ .

## 6.8 Conclusion

In this chapter a new multi-mode model for mutually coupled lasers was created by adapting a previously used version. This was then followed by a rigorous bifurcation study of two, two mode lasers under mutual coupling. This system was studied for various detuning arrangements, and then the detunings were made bifurcation parameters to study their effect on the system. It was found there was a major asymmetry in the effect of the two separate detunings on the model, i.e. changing  $\Delta\omega_1$  had a different effect to changing  $\Delta\omega_2$ . After this the balance of the power of the modes was altered to more accurately model the situation in the experiment. By using the unbalanced mode arrangement, and the measurements of  $\eta$  and  $\phi$  versus VOA bias, the model was made as close to the experiment as possible. It was shown the multi-mode model re-created the majority of the behavioural regimes observed and was an improvement on the single mode model. However the multi-mode model failed in one aspect. That is the phenomena of the lasers jumping to the suppressed modes with the suppression of the original lasing mode as the VOA bias was increased. During all sweeps, the suppressed modes were always lesser in power to the main mode.



## **Chapter 7**

### **Conclusion and future work**

This thesis has provided an experimental and theoretical insight into the dynamics of mutually coupled lasers (MCL) on photonic integrated circuits (PIC). Initially a series of MCL devices were designed and tested. These results provided design refinements for the devices and a good platform for future experimental work. After this the single mode rate equation model was studied for various parameter arrangements analytically where possible. It was found that an analytical bifurcation study was not possible when a frequency difference between the modes of the lasers was included, so numerical methods were used. An algorithm was developed to track the stable solutions of the model and then the simulations were compared with experimental results. This comparison highlighted the shortcomings of the single mode model, and that different approach was needed. Finally a multi-mode model was developed to model two, two mode MCLs. This model proved to be experimentally realistic, and through modelling the parameters of the system in an experimentally realistic manor (measuring how the coupling and phase difference varied in the experiment) results were produced which matched the experiments in a reasonable fashion. In the future this multi-mode model could be expanded to include a high number of modes to accurately recreate the lasers used in experiments. However, this would be difficult due to the increase in the number of equations and would require the calculation of more  $\beta_{mn}$  terms to model the gain. The model could also be adjusted to allow for modes being spectrally closer together, as the model here assumes a large spectral separation between the modes ( $> 200$  GHz). This would more accurately model the lasers on the PICs used. As suggested previously a more experimentally realistic handling of the variable optical attenuator section (VOA) may improve the theoretical results. The models used here presume a passive element between the lasers, however in the PIC environment being considered this is made of active material. Appendix B.1 highlights a possible model to accomplish this.

## 7. CONCLUSION AND FUTURE WORK

## **Appendix A**

### **Breakdown of the epitaxial composition of the wafers used**

A. BREAKDOWN OF THE EPITAXIAL  
COMPOSITION OF THE WAFERS USED

This appendix describes the epitaxial structure of the commercially available wafers used in standard DC PICs. The active region is made using five AlGaInAs quantum wells (layers 6 and 7 are repeated five times to create the quantum well structure), surrounded by P and N doped InP cladding layers.

Table A.1: Epitaxial structure of the material used. A right arrow ( $\rightarrow$ ) indicates a gradient in composition, from lower layer numbers to higher layer numbers.

Layer No.	Material	Composition		Strain (%)	Thickness ( $\mu m$ ) ( $\pm 10\%$ )	C-V doping level ( $cm^{-3}$ ) ( $\pm 30\%$ )	Dopant	Type
		x	y					
16	GaIn(x)As	0.53			0.200	$> 1.5 \times 10^{19}$	Zn	P
15	GaIn(x)As(y)P	0.71	0.62		0.050	$> 3.0 \times 10^{18}$		
14	InP				0.100	$> 1.5 \times 10^{18}$		
13					1.500	$1.0 \times 10^{18}$		
12	GaIn(x)As(y)P	0.85	0.33		0.020			
11	InP				0.050	$7.0 \times 10^{17}$		U/D
10	[Al(x)Ga]In(y)As	0.90	0.53		0.060	$4.0 \times 10^{17}$		
9		0.72 $\rightarrow$ 0.90			0.060			
8		0.44	0.49	-0.3	0.010			
7x5		0.24	0.71	+1.2	0.006			
6x5		0.44	0.49	-0.3	0.010			
5		0.90 $\rightarrow$ 0.72	0.53		0.060		Si	N
4		0.90			0.060			
3		0.86 $\rightarrow$ 0.92			0.010	$1.0 \times 10^{18}$		
2	InP				0.500			
1					0.300	$3.0 \times 10^{18}$		

Table A.2: Epitaxial structure of the substrate on which the material in table A.1 was grown on.

Substrate Details - 2" InP:S						
Orientation	Thickness ( $\mu m$ )	Material	Carrier Concentration ( $cm^{-3}$ )	Flat Specification	EPD ( $cm^2$ )	Finish
(100) $\pm 0.5$	350 $\pm$ 20	InP:S	(1 $\rightarrow$ 8) $\times 10^{18}$	EJ	<1000	P/P

A. BREAKDOWN OF THE EPITAXIAL  
COMPOSITION OF THE WAFERS USED

## **Appendix B**

### **Model for improved handling of VOA section**

From the experimental results in Section 5.4.1 it was determined that a more advanced model was needed to recreate the highly harmonic experimental results observed, two models were proposed, but ultimately only one was tested. In this appendix the unused model will be outlined.

## B.1 Model basis

This model was based on more realistic modelling of the VOA section. The single mode model outlined in Eqn. 4.6-4.9 was developed with there being some sort of attenuating passive element between the lasers, such as a fibre or air gap. However on the PICs used this was not the case. The VOA elements which the light passed through, were made of active material, which while pumped below lasing threshold, would still have the gain and losses associated with the active material. In a previous work a model was developed which model an active region surrounded by absorbing regions [42]. The model can be seen in Eqn. B.1-B.3, with a schematic of the situation being modelled in Fig. B.1. Using this model the study produced pulsating results, so showed promise as a basis to model the devices in this study.

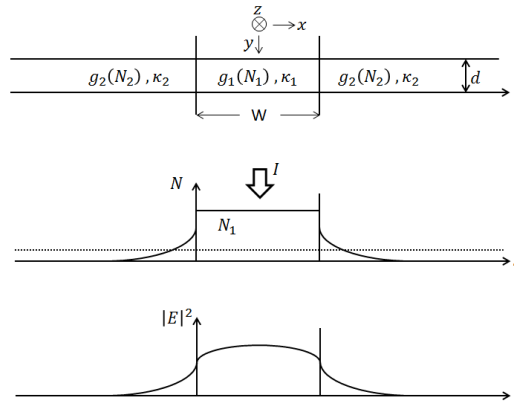


Figure B.1: Schematic of situation modelled by Eqn. B.1-B.3. The middle region is the active region of the laser, labelled 1, and this is surrounded by absorbing regions, labelled 2. The bottom two graphs show the carrier distribution and the power distribution in transition between active and absorbing regions.

$$\frac{dS}{dt} = [a_1\xi_1(N_1 - N_{g1}) + a_2\xi_2(N_2 - N_{g2}) - G_{th}]S + \frac{CN_1V_1}{\tau_s} \quad (\text{B.1})$$

$$\frac{dN_1}{dt} = \frac{-a_1\xi_1}{V_1}(N_1 - N_{g1})S - \frac{N_1}{\tau_s} - \frac{(N_1 - N_2)}{T_{12}} + \frac{I}{eV_1} \quad (\text{B.2})$$



$$\frac{dN_2}{dt} = \frac{-a_2\xi_2}{V_2}(N_2 - N_{g2})S - \frac{N_2}{\tau_s} - \frac{(N_2 - N_1)}{T_{21}} \quad (\text{B.3})$$

## B.2 Adapted model

Here,  $a_i$  is a proportionality constant between the gain coefficient and the electron density in region  $i$ ,  $\xi_i$  is the distribution ration of the optical power in the region  $i$ ,  $N_{gi}$  is transparency carrier density in region  $i$ ,  $G_{th}$  is the threshold gain,  $\tau_s$  is the carrier lifetime,  $C$  is the spontaneous emission coefficient,  $V_i$  is the volume of region  $i$  and  $T_{i,j}$  is a time constant associated with the diffusion of carrier between region  $i$  and  $j$ . By including a second active region to the right of the absorbing region in Fig. B.1, the schematic now resembles an MCL device with two active regions and an absorbing region between them. This yields Fig. B.2.

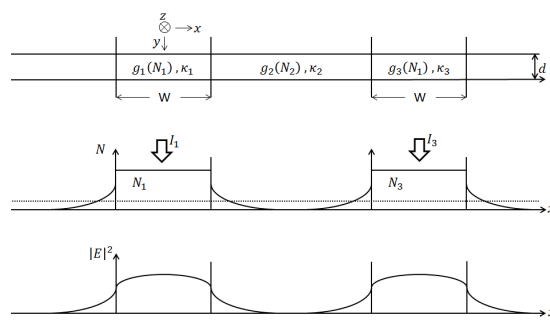


Figure B.2: Schematic of MCL device where the region labelled 1, is one of the active regions and the region labelled 3 is the other, and in between them is the absorbing region, labelled 2. The bottom two graphs show the carrier distribution and the power distribution in transition between active regions and absorbing region.

The equations are adapted by adding another gain term to the  $\frac{dS}{dt}$  equation for the  $N_3$  region, Eqn. B.1, adding another carrier equation, for  $N_3$ , similar in for to that of Eqn. B.2, and adding another diffusion term to the  $\frac{dN_2}{dt}$  equation, Eqn. B.3, to allow for diffusion into the second active region,  $N_3$ . The proposed model can be seen in Eqn. B.4-B.7.

$$\frac{dS}{dt} = [a_1\xi_1(N_1 - N_{g1}) + a_2\xi_2(N_2 - N_{g2}) + a_3\xi_3(N_3 - N_{g3}) - G_{th}]S + \frac{CN_1V_1}{\tau_s} + \frac{CN_3V_3}{\tau_s} \quad (\text{B.4})$$

$$\frac{dN_1}{dt} = \frac{-a_1\xi_1}{V_1}(N_1 - N_{g1})S - \frac{N_1}{\tau_s} - \frac{(N_1 - N_2)}{T_{12}} + \frac{I_1}{eV_1} \quad (\text{B.5})$$

$$\frac{dN_2}{dt} = \frac{-a_2\xi_2}{V_2}(N_2 - N_{g2})S - \frac{N_2}{\tau_s} - \frac{(N_2 - N_1)}{T_{21}} - \frac{(N_2 - N_3)}{T_{23}} \quad (\text{B.6})$$

$$\frac{dN_3}{dt} = \frac{-a_3\xi_3}{V_3}(N_3 - N_{g3})S - \frac{N_3}{\tau_s} - \frac{(N_3 - N_2)}{T_{32}} + \frac{I_3}{eV_3} \quad (\text{B.7})$$

Though no work was done on this model, it was believed to be an interesting alternative to the multi-mode coupled model used in Chapter and could be used in future work.

## **Appendix C**

### **Comb injection rate equation model development**

## C.1 Model development

As a part of another member of the research group's work a rate equation based model to simulate comb injection was attempted. This was a part of another work package of the same research projected that funded this thesis. A diagram of the experimental setup can be seen in Fig. C.1.

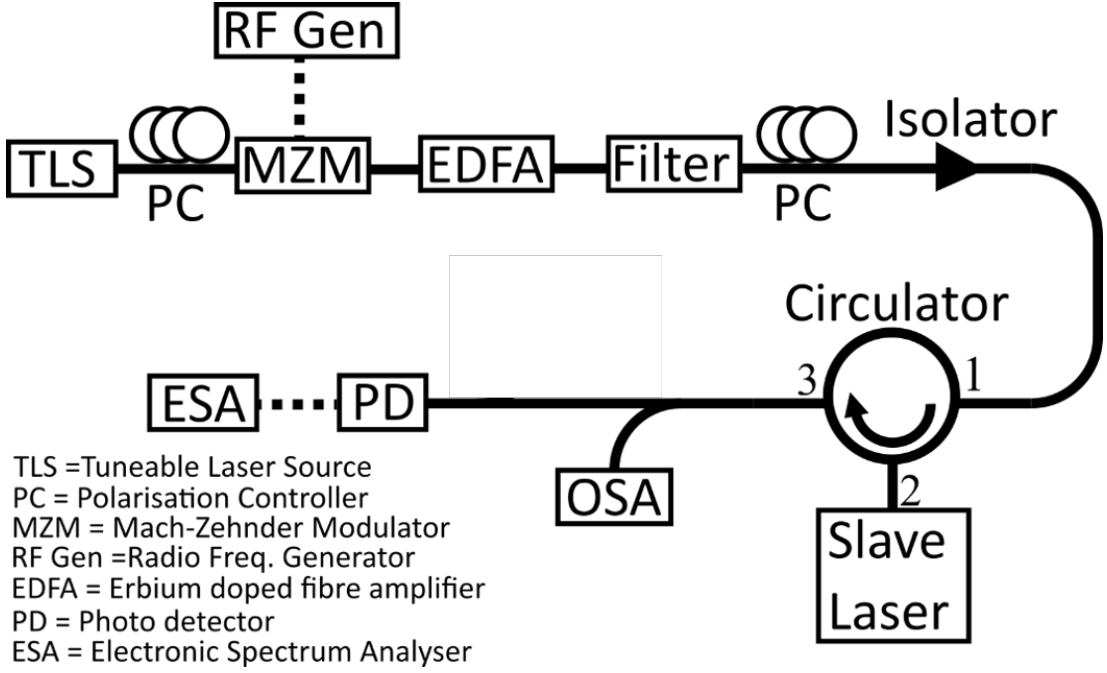


Figure C.1: Experimental diagram for comb injection.

The model was created by adapting the approach used in a previous study [5]. In this work the author developed a model for master/slave injection of two single mode lasers. Firstly the model is laid out in Eqn. C.1 and C.2.

$$\dot{\tilde{E}}_0 = \frac{1}{2}\xi(1 + i\alpha)(N - N_{thr})\tilde{E}_0 + \kappa\tilde{E}_i \quad (\text{C.1})$$

$$\dot{N} = J - \Gamma_N N - (\Gamma_E + \xi(N - N_{thr}))|\tilde{E}_0|^2 \quad (\text{C.2})$$

Where the injected laser field is represented by  $\tilde{E}_i$  and can be written:

$$\tilde{E}_i(\hat{t}) = E_i e^{i(\omega_i - \Omega_{thr})\hat{t}} \quad (\text{C.3})$$

These equations model the field of the injected laser,  $\tilde{E}_0$  and it's carrier density  $N$ .  $\Omega_{thr}$  is the free running frequency of the master laser, and  $\omega_i$  is the frequency of the injected light. However as can be seen in Fig. C.2, in the

three line comb injection case there are three injected fields, labelled  $E_{i1,2,3}$ , each with its free running frequency,  $\omega_{i1,2,3}$ .

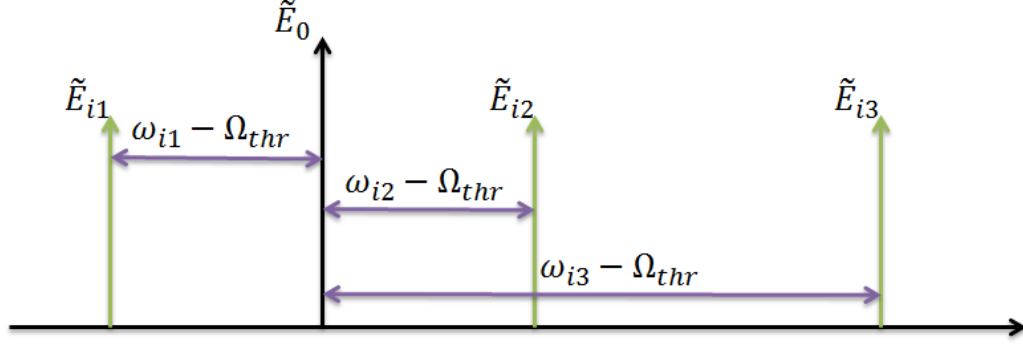


Figure C.2: Frequency space diagram of a three line comb (green) injected into a single mode laser (black), where the frequency difference between each line and the laser is highlighted in purple.

The single line injection model in Eqn. C.1 becomes Eqn. C.4

$$\dot{\tilde{E}}_0 = \frac{1}{2}\xi(1 + i\alpha)(N - N_{thr})\tilde{E}_0 + \kappa(\tilde{E}_{i1} + \tilde{E}_{i2} + \tilde{E}_{i3}) \quad (C.4)$$

Where

$$\tilde{E}_{i_n}(\hat{t}) = E_{i_n}e^{i(\omega_{i_n} - \Omega_{thr})\hat{t}} \quad (C.5)$$

These equations are then written in the reference frame of  $\Omega_{thr}$  and the following rescaling was introduced:

$$\tilde{E} = \tilde{E}_0/E_0^s, n = \xi(N - N_{thr})/\omega_R, t = \hat{t}\omega_R \quad (C.6)$$

Which yields:

$$\dot{\tilde{E}} = \frac{1}{2}(1 + i\alpha)n\tilde{E} + K(e^{i\omega_1 t} + e^{i\omega_2 t} + e^{i\omega_3 t}) \quad (C.7)$$

$$\dot{n} = -2\Gamma n - (1 + 2Bn)(|\tilde{E}| - 1) \quad (C.8)$$

Where the injected frequencies have been re-written in the form

$$\omega_n = (\omega_i - \Omega_{thr})/\omega_R \quad (C.9)$$

All derivatives are now with respect to the rescaled time  $t$  and

$B = \omega_R/2\Gamma_E, \Gamma = \frac{1}{2}(\Gamma_N)/\omega_R + 2B$ . The dimensionless injected field strength

$K = (\kappa E_i)/(\omega_R E_0^s)$ . The spacing between the comb lines is defined as  $d\omega$ . Using this spacing the outer two lines can be written as being offset from the central line by  $\pm d\omega$ . This gives:

$$\dot{\tilde{E}} = \frac{1}{2}(1 + i\alpha)n\tilde{E} + K(e^{i\omega_1 t} + e^{(i\omega_1 - d\omega)t} + e^{(i\omega_1 + d\omega)t}) \quad (\text{C.10})$$

Next the electric field is written in terms of the frequency of the central comb line, via:

$$\tilde{E} = E e^{-i\omega_1 t} \quad (\text{C.11})$$

Through substitution into Eqn. C.10, this yields:

$$\dot{E} = (1 + i\alpha)nE + K(1 + 2\cos(d\omega t)) + iE\omega_1 \quad (\text{C.12})$$

This equation can be separated in real and imaginary parts, giving:

$$\dot{E}_x = n(E_x - \alpha E_y) + K(1 + \cos(d\omega t)) - E_y\omega_1 \quad (\text{C.13})$$

$$\dot{E}_y = n(E_y + \alpha E_x) + E_x\omega_1 \quad (\text{C.14})$$

## C.2 Experimental recreation

In experiments performed within the group, the laser is swept across different comb lines, which is analogous to varying  $\Omega_{thr}$ , or the laser is fixed and the comb is swept across it, which is analogous to varying  $\omega_{i_1}$  in Eqn. C.9. Both methods are equivalent, and for this study it was decided to vary the comb frequencies. For each sweep a different injection strength,  $K$ , and comb spacing was chosen. Fig. C.3 shows a contour diagram of the FFT of  $|E|$  for sweeping the comb across the laser, for a comb spacing of  $d\omega = 2\omega_R \approx 10GHz$  for an injection strength of  $K = 0.1$ .

Fig. C.4 increased the comb spacing to  $3\omega_R$ .

Fig. C.5 shows an experimental result from following the procedure outlined in Fig. C.1, where the temperature of the slave was varied to sweep its frequency across the comb. In this arrangement the comb spacing was set to  $10GHz$ . This shows decent agreement with Fig. C.3, which has a theoretical comb spacing of  $10GHz$ .

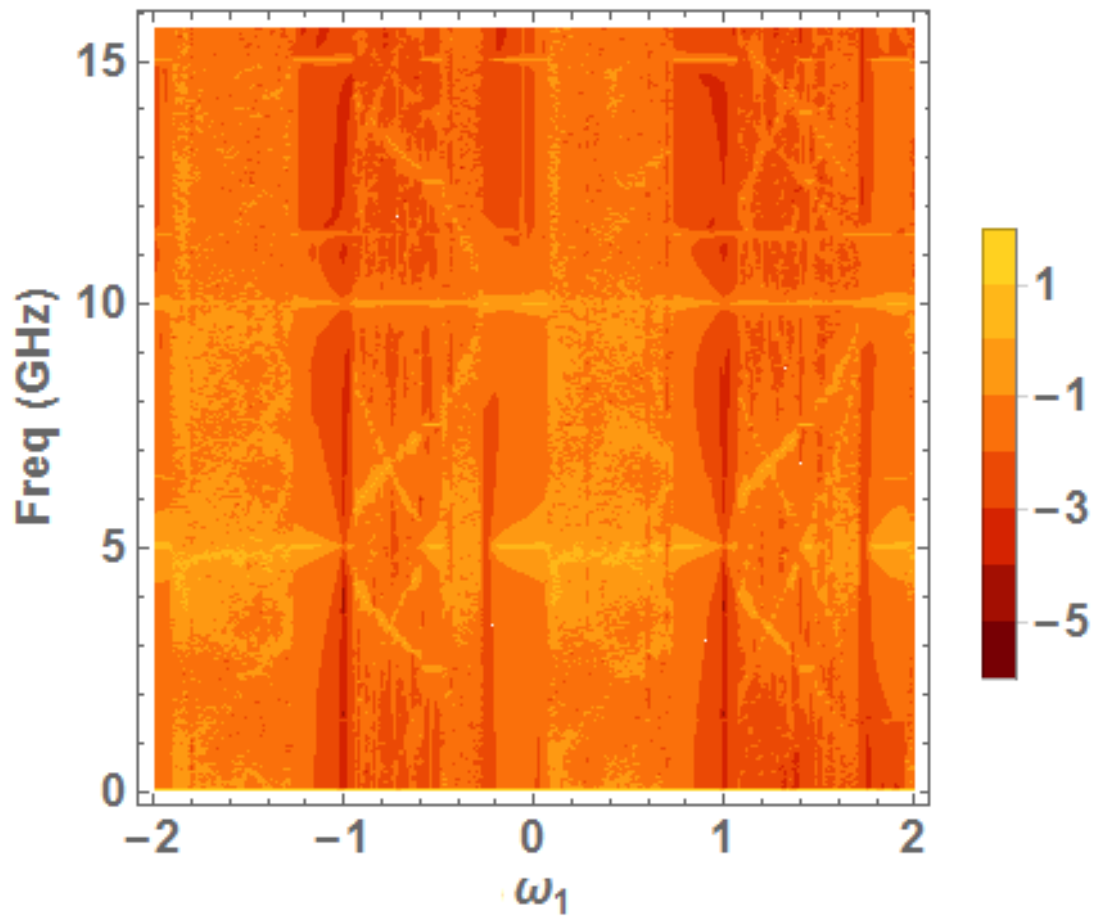


Figure C.3: Contour diagram of the FFT of  $|E|$ , for solving Eqn. C.13 and C.14 with a comb spacing of  $d\omega = 2\omega_R$ , and an injection strength of  $K = 0.1$

In each theoretical case shown a frequency line can be seen at  $d\omega$  corresponding to the beat notes between the comb lines. There are also locked regimes around  $\omega_1 = 0$  and  $\pm\omega_R$ . However in Fig. C.3 at the locking region around  $\omega_1 = 0$  an oscillation can be seen, which splits into higher harmonics in a 1 : 2 fashion, which is also present in the experimental result. Other higher harmonic splitting was also found experimentally. Through further study of the splitting into higher harmonics, by the other authors of this work, a clear devil's staircase structure in both the lasing frequency and the induced oscillations in the electric field amplitude were observed. It was found that the emergence of higher harmonic resonance tongues in the lasing frequency is enabled by the locking of the amplitude oscillations, but also regions of unlocked oscillations in the field amplitude where the optical frequency remains locked were found. Our results show that by proper implementation of an external drive, additional regions of stable frequency locking can be introduced in systems which originally show only a single Adler-type

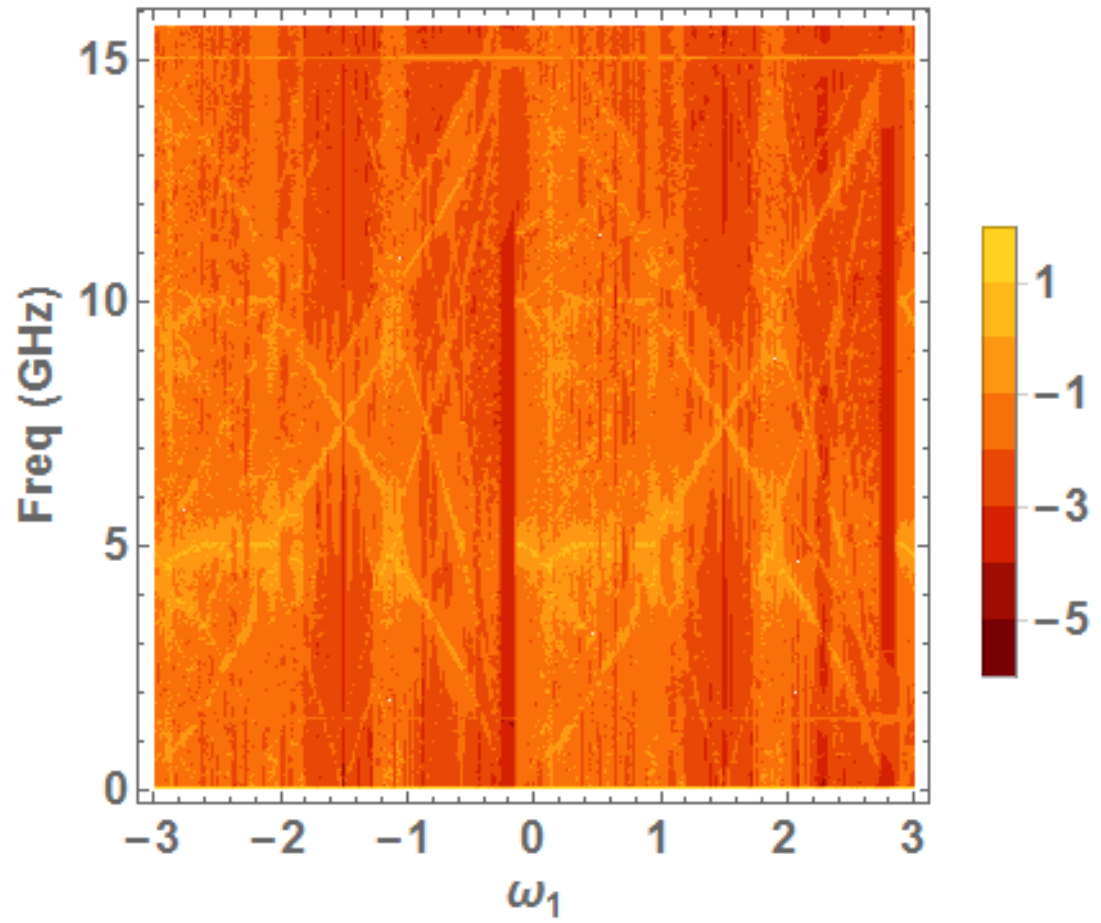


Figure C.4: Contour diagram of the FFT of  $|E|$ , for solving Eqn. C.13 and C.14 with a comb spacing of  $d\omega = 3\omega_R$ , and an injection strength of  $K = 0.1$ .

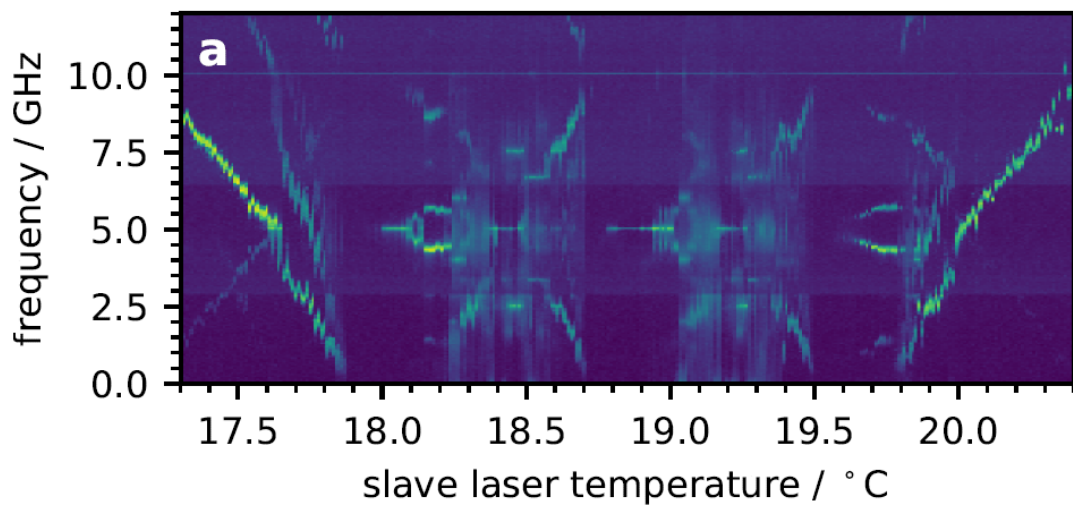


Figure C.5: Contour diagram of ESA traces for a comb spacing of  $10GHz$



resonance tongue.

## References

- [1] L. A. L. A. Coldren, S. W. S. W. Corzine, and M. Mashanovitch, *Diode lasers and photonic integrated circuits*. Wiley, 2012.
- [2] S. K. Mondal, B. Roycroft, P. Lambkin, F. Peters, B. Corbett, P. Townsend, and A. Ellis, “A Multiwavelength Low-Power Wavelength-Locked Slotted Fabry–Pérot Laser Source for WDM Applications,” *IEEE Photonics Technology Letters*, vol. 19, pp. 744–746, may 2007.
- [3] L. Goldberg, A. Yurek, H. Taylor, and J. Weller, “35 GHz microwave signal generation with an injection-locked laser diode,” *Electronics Letters*, vol. 21, no. 18, p. 814, 1985.
- [4] L. Chan, C. Chan, F. Tong, D. Tong, and L. Chen, “Upstream traffic transmitter using injection-locked Fabry-Perot laser diode as modulator for WDM access networks,” *Electronics Letters*, vol. 38, no. 1, p. 43, 2002.
- [5] S. Wieczorek, B. Krauskopf, T. Simpson, and D. Lenstra, “The dynamical complexity of optically injected semiconductor lasers,” *Physics Reports*, vol. 416, pp. 1–128, sep 2005.
- [6] S. H. Strogatz, *Nonlinear Dynamics and Chaos*. Addison-Wesley Publishing Company, 1994.
- [7] A. Hohl, A. Gavrielides, T. Erneux, and V. Kovanis, “Localized Synchronization in Two Coupled Nonidentical Semiconductor Lasers,” *Physical Review Letters*, vol. 78, pp. 4745–4748, jun 1997.
- [8] A. Hohl, A. Gavrielides, T. Erneux, and V. Kovanis, “Quasiperiodic synchronization for two delay-coupled semiconductor lasers,” *Physical Review A*, vol. 59, pp. 3941–3949, may 1999.
- [9] H. Erzgräber, D. Lenstra, B. Krauskopf, E. Wille, M. Peil, I. Fischer, and W. Elsässer, “Mutually delay-coupled semiconductor lasers: Mode

- bifurcation scenarios,” *Optics Communications*, vol. 255, pp. 286–296, nov 2005.
- [10] K. Otsuka, R. Kawai, S.-L. Hwang, J.-Y. Ko, and J.-L. Chern, “Synchronization of Mutually Coupled Self-Mixing Modulated Lasers,” *Physical Review Letters*, vol. 84, pp. 3049–3052, apr 2000.
- [11] N. Gross, W. Kinzel, I. Kanter, M. Rosenbluh, and L. Khaykovich, “Synchronization of mutually versus unidirectionally coupled chaotic semiconductor lasers,” *Optics Communications*, vol. 267, pp. 464–468, nov 2006.
- [12] J. Mulet, C. Masoller, and C. R. Mirasso, “Modeling bidirectionally coupled single-mode semiconductor lasers,” *Physical Review A*, vol. 65, p. 063815, jun 2002.
- [13] T. Heil, I. Fischer, W. Elsässer, J. Mulet, and C. R. Mirasso, “Chaos Synchronization and Spontaneous Symmetry-Breaking in Symmetrically Delay-Coupled Semiconductor Lasers,” *Physical Review Letters*, vol. 86, pp. 795–798, jan 2001.
- [14] E. Wille, M. Peil, I. Fischer, and W. Elsasser, “Dynamical scenarios of mutually delay-coupled semiconductor lasers in the short coupling regime,” vol. 5452, p. 41, International Society for Optics and Photonics, sep 2004.
- [15] D. Arroyo-Almanza, A. Pisarchik, I. Fischer, C. Mirasso, and M. Soriano, “Spectral properties and synchronization scenarios of two mutually delay-coupled semiconductor lasers,” *Optics Communications*, vol. 301-302, pp. 67–73, aug 2013.
- [16] I. Reidler, M. Nixon, Y. Aviad, S. Guberman, A. A. Friesem, M. Rosenbluh, N. Davidson, and I. Kanter, “Coupled lasers: phase versus chaos synchronization,” *Optics Letters*, vol. 38, p. 4174, oct 2013.
- [17] M. P. Vaughan, I. Henning, M. J. Adams, L. J. Rivers, P. Cannard, and I. F. Lealman, “Mutual optical injection in coupled DBR laser pairs,” *Optics Express*, vol. 17, p. 2033, feb 2009.
- [18] D. Liu, C. Sun, B. Xiong, and Y. Luo, “Nonlinear dynamics in integrated coupled DFB lasers with ultra-short delay,” *Optics Express*, vol. 22, p. 5614, mar 2014.

- [19] M. Yousefi, Y. Barbarin, S. Beri, E. A. J. M. Bente, M. K. Smit, R. Nötzel, and D. Lenstra, “New Role for Nonlinear Dynamics and Chaos in Integrated Semiconductor Laser Technology,” *Physical Review Letters*, vol. 98, p. 044101, jan 2007.
- [20] J. Mulet, C. Mirasso, T. Heil, and I. Fischer, “Synchronization scenario of two distant mutually coupled semiconductor lasers,” *Journal of Optics B: Quantum and Semiclassical Optics*, vol. 6, pp. 97–105, jan 2004.
- [21] F. Rogister, D. Pieroux, M. Sciamanna, P. Mégret, and M. Blondel, “Anticipating synchronization of two chaotic laser diodes by incoherent optical coupling and its application to secure communications,” *Optics Communications*, vol. 207, pp. 295–306, jun 2002.
- [22] C. Masoller, D. Sukow, A. Gavrielides, and M. Sciamanna, “Bifurcation to square-wave switching in orthogonally delay-coupled semiconductor lasers: Theory and experiment,” *Physical Review A*, vol. 84, p. 023838, aug 2011.
- [23] V. Flunkert, O. D’Huys, J. Danckaert, I. Fischer, and E. Schöll, “Bubbling in delay-coupled lasers,” *Physical Review E*, vol. 79, p. 065201, jun 2009.
- [24] J. Hu, K. Jia, and J. Ma, “Chaos synchronization and encoding in coupled semiconductor lasers of multiple modulated time delays,” *Optik - International Journal for Light and Electron Optics*, vol. 122, pp. 2071–2074, dec 2011.
- [25] S. Yanchuk and L. Recke, “Dynamics of two mutually coupled semiconductor lasers: Instantaneous coupling limit,” *Physical Review E*, vol. 69, p. 056221, may 2004.
- [26] F. Rogister and J. García-Ojalvo, “Symmetry breaking and high-frequency periodic oscillations in mutually coupled laser diodes,” *Optics Letters*, vol. 28, p. 1176, jul 2003.
- [27] H. Erzgräber, D. Lenstra, B. Krauskopf, and I. Fischer, “Dynamical properties of mutually delayed coupled semiconductor lasers,”
- [28] H. Erzgräber, E. Wille, B. Krauskopf, and I. Fischer, “Amplitude–phase dynamics near the locking region of two delay-coupled semiconductor lasers,” *IOP Publishing Nonlinearity*, vol. 22, pp. 585–600, 2009.

- [29] H. Erzgräber, B. Krauskopf, and D. Lenstra, “Mode structure of delay-coupled semiconductor lasers: influence of the pump current,” *J. Opt. B: Quantum Semiclass. Opt.*, vol. 7, pp. 361–371, 2005.
- [30] H. Erzgräber, S. Wieczorek, and B. Krauskopf, “Dynamics of two laterally coupled semiconductor lasers: Strong- and weak-coupling theory,” *Physical Review E*, vol. 78, p. 066201, dec 2008.
- [31] H. Erzgräber, S. Wieczorek, and B. Krauskopf, “Dynamics of two semiconductor lasers coupled by a passive resonator,” *Physical Review E*, vol. 81, p. 056201, may 2010.
- [32] E. Clerkin, S. O’Brien, and A. Amann, “Multistabilities and symmetry-broken one-color and two-color states in closely coupled single-mode lasers,” *Physical Review E*, vol. 89, p. 032919, mar 2014.
- [33] M. Seifika, A. Amann, and F. H. Peters, “Dynamics of two identical mutually delay-coupled semiconductor lasers in photonic integrated circuits,” *Applied Optics*, vol. 57, p. E37, aug 2018.
- [34] R. Lang and K. Kobayashi, “External optical feedback effects on semiconductor injection laser properties,” *IEEE Journal of Quantum Electronics*, vol. 16, pp. 347–355, mar 1980.
- [35] H. Erzgräber, S. Wieczorek, and B. Krauskopf, “Dynamics of two semiconductor lasers coupled by a passive resonator,” *Physical Review E*, vol. 81, p. 056201, may 2010.
- [36] R. Phelan, W.-H. Guo, Q. Lu, D. Byrne, B. Roycroft, P. Lambkin, B. Corbett, F. Smyth, L. P. Barry, B. Kelly, J. O’Gorman, and J. F. Donegan, “A Novel Two-Section Tunable Discrete Mode Fabry-Pérot Laser Exhibiting Nanosecond Wavelength Switching,” *IEEE Journal of Quantum Electronics*, vol. 44, pp. 331–337, apr 2008.
- [37] V. L. Arnol’d, V. S. Afraimovich, Y. S. Il’yashenko, L. P. Shil’nikov, and N. D. Kazarinoff, “I. Bifurcation Theory Translated from the Russian,”
- [38] P. E. Morrissey, W. Cotter, D. Goulding, B. Kelleher, S. Osborne, H. Yang, J. O’Callaghan, B. Roycroft, B. Corbett, and F. H. Peters, “On-chip optical phase locking of single growth monolithically integrated slotted fabry perot lasers,” *Optics Express*, vol. 21, p. 17315, jul 2013.
- [39] K. Engelborghs, “DDE-Biftool,” 2001.

- [40] G. B. Ermentrout, “XPPAUT.”
- [41] S. Osborne, A. Amann, K. Buckley, G. Ryan, S. P. Hegarty, G. Huyet, and S. O’Brien, “Antiphase dynamics in a multimode semiconductor laser with optical injection,” *Physical Review A*, vol. 79, p. 023834, feb 2009.
- [42] M. Yamada, “A theoretical analysis of self-sustained pulsation phenomena in narrow-stripe semiconductor lasers,” *IEEE Journal of Quantum Electronics*, vol. 29, pp. 1330–1336, may 1993.